UNIVERSITAT
POLITÈCNICA
DE VALÈNCIA

Grid Forming Wind Power Plants: Black start operation for HVAC grids and Diode Rectifier-based Wind Power Plant integration

PhD Dissertation

Author: Jaime Martínez Turégano
Supervisor: Ramón Blasco Giménez
November 24, 2021

Acknowledgements

Este és el resultat d'una part del treball que he pogut desenvolupar durant este temps com investigador de l'Institut d'Automàtica i Informàtica Industrial formant part de l'equip liderat pel professor Ramón Blasco Giménez.

En primer lloc, agrair a Ramón Blasco haver confiat en mi i donar-me l'oportunitat de formar part d'aquest equip. Sense la seua ajuda, els seus consells i la seua visió del tema del qual tracta la tesi, aquest treball haguera sigut molt difícil. Moltes gràcies.

Agrair a tot l'equip i a les persones amb qui he pogut treballar durant este període la seua ajuda i tot el que m'han permés aprendre d'ells. Treballar amb persones com estes sempre és molt enriquidor.

També agrair als amics que he trobat en l'Institut d'Automàtica i Informàtica Industrial que han fet que tot el treball es faça més amé, ja siga prenent cafés, fent esport, o simplement parlant de qualsevol cosa.

Als meus amics Oscar, Pere, Andrea y Noel amb qui sempre ho passes bé i ja són part de la meua família, a Antoniet, Oscar i Toni que saps que sempre pots comptar amb ells, i a la meua família. Finalment, a BRB que m'ha ajudat i m'ha patit en alguns moments d'aquest període.

Jaime Martínez Turégano

València, Novembre 2021

Abstract

The European Union GREEN DEAL aims to make its 27 members climate-neutral by 2050. The decarbonization of the energy sector stands out as one of the proposed actions. To achieve that goal, the target for wind power generation is set at 1,200 GW in 2050, from the 190 GW that was had in 2019.

The closure of power plants based on large synchronous generators and the increase of power electronics based generation such as Wind Power Plants (WPPs) or photovoltaic plants, leads to the use of grid forming controllers for power electronics based renewable energy.

Grid forming control strategies for wind turbines generators (WTGs) must consider active and reactive power sharing control (droop control in synchronous generators) as well as a protection system that allows a quick recovery after fault clearance.

Moreover, a transition from the conventional grid following WPPs to new grid forming WPPs is required. The transition must consider the parallel operation of both technologies for a long time. Thus, it is necessary to study the stability of Wind Power Plants with both technologies, as well as the study of how much grid forming generation is required to keep a mixed grid forming and grid following WPP stable in any situation.

In addition, the use of grid forming WPPs allows different applications such as the energization of HVAC and HVDC grids after a blackout from these WPPs, or the use of diode rectifiers in HVDC links for the off-shore WPPs connection.

An aggregation technique for type-4 WTGs has been proposed in this thesis in order to facilitate the study and design of grid forming WPPs. The aggregation technique allows to reduce the WPP complexity for its study and analysis.

The main contributions of this theses are: A design methodology has been proposed for the parallel operation of grid forming and grid following WTGs. Including the stability analysis of the complete system. Additionally, a fault control strategy is proposed to ensure a fast and safe recovery.

The use of $\mathcal{H}_\infty$ control techniques is also proposed for grid forming controller tuning. Using $\mathcal{H}_\infty$ control techniques for controller design may improve the robustness of the controllers as well as the performance of the controllers.

A procedure to carry out black start operation of HVAC grid from mixed grid forming and grid following WPPs has been proposed. The obtained results validate that the procedure works as expected. Moreover, the results show that the amount of grid-forming generation usually is determined by the load size steps as stability limits are usually less stringent.

Finally, protection strategies have been proposed for the integration of off-shore WWPs in multi-terminal HVDC grids using diode rectifiers. Grid forming WPPs are able to help managing faults. Their use allow lower requirements of the HVDC protection equipment, leading to overall cost reduction and an increment of the system robustness.

Keywords: Grid Forming, black start, Diode Rectifier, aggregation, Off-shore Wind Power Plant.

Resum

La Unió Europea planteja uns reptes al GREEN DEAL per a aconseguir un escenari on els seus membres siguen climàticament neutrals al 2050. Per a aconseguir aquest objectiu es plantegen unes accions entre les quals destaca la de descarbonitzar el sector energètic. D'altra banda, s'ha posat com a objectiu aconseguir una capacitat d'energia eòlica de 1200 GW al 2050, des dels 190 GW que es tenia al 2019.

El tancament de centrals elèctriques basades en grans generadors síncrons juntament amb l'augment en la construcció de centrals elèctriques basades en electrònica de potència com a parcs eòlics o plantes fotovoltaiques, fa necessari la incorporació de controladors *grid forming* en energies renovables que es basan en electrònica de potència.

La integració d'estratègies de control *grid forming* per a turbines eòliques ha de considerar les funcions de repartiment de potència activa i reactiva, així com un sistema de protecció davant faltes que permeta una recuperació ràpida quan s'aïlla la falta.

D'altra banda, en la transició dels actuals parcs eòlics *grid following* que funcionen com a fonts de corrent a parcs eòlics *grid forming* que funcionen com a fonts de tensió, s'ha de considerar que totes dues tecnologies coexistiran conjuntament per molt de temps. Per tant, es fa necessari l'estudi d'estabilitat d'un parc eòlic amb totes dues tecnologies, així com l'estudi del percentatge de generació *grid forming* necessari per a mantindre el parc eòlic estable en qualsevol situació.

A més, l'ús de parcs eòlics *grid foming* permet diferents aplicacions com l'energització de xarxes elèctriques després d'una apagada des d'aquests parcs eòlics, o l'ús de díodes rectificadors en enllaços HVDC per a la connexió de parcs eòlics marins.

Per a facilitar l'estudi i disseny d'aerogeneradors *grid forming*, en la present tesi es proposa una tècnica d'agregació d'aerogeneradors tipus-4. Aquesta tècnica permet reduir la complexitat del parc eòlic per al seu estudi i anàlisi.

La present tesi inclou les segÃ¼ents contribucions: Per al funcionament d'aerogeneradors *grid forming* en paral·lel amb aerogeneradors *grid following* es proposa un mètode de disseny analitzant l'estabilitat del sistema complet. A més, es proposa una estratègia de control davant faltes per a assegurar una recuperació ràpida i segura.

Es proposa l'ús de tècniques de control $\mathcal{H}_\infty$ per a la sintonització de controladors *grid forming.* L'ús d'aquestes tècniques per al disseny de controladors pot millorar la robustesa dels controladors, a mé del rendiment d'aquestos.

Considerant l'aplicació de l'energització de xarxes HVAC des de parcs eòlics, s'ha proposat com dur a terme aquesta maniobra a partir d'un parc eòlic amb aerogeneradors *grid forming* i *grid following.* Els resultats obtinguts validen el funcionament de l'operació. A més, mostren que la quantitat de generació *grid forming* està més relacionada amb la dimensió de les càrregues que ha d'aguantar el parc eòlic, que amb l'estabilitat del sistema que permet un menr percentatge de generació *grid forming.*

Finalment, s'han proposat estratègies de protecció per a la integració de parcs eòlics marins en xarxes multi-punt HVDC utilitzant rectificadors de díodes. Els parcs eòlics *grid forming* poden ajudar a gestionar faltes disminuint els requisits de les proteccions necessàries en l'enllaç HVDC. Això permet una reducció del cost de la instal·lació, a més d'augmentar la robustesa del sistema.

Paraules clau: Grid Forming, black start, Rectificador de diodes, agregació, Plantas Eòicas Marinas.

Resumen

La Unión Europea plantea una serie de retos en el GREEN DEAL para conseguir un escenario donde sus miembros sean climáticamente neutros en 2050. Para ello se plantean unas acciones entre las que destaca la descarbonización del sector de la energía. Por otra parte, se ha puesto como objetivo conseguir una capacidad de energía eólica de 1200 GW en 2050, desde los 190 GW que se tenía en 2019.

El cierre de centrales eléctricas basadas en grandes generadores síncronos junto con el aumento en la construcción de centrales eléctricas con fuentes basadas en electrónica de potencia como parques eólicos o plantas fotovoltaicas, hace necesario la incorporación de controladores *grid forming* en energías renovables basadas en electrónica de potencia.

La integración de estrategias de control *grid forming* en turbinas eólicas debe considerar las funciones de reparto de potencia activa y reactiva (*control droop* en generadores síncronos), así como un sistema de protección ante faltas que permita una recuperación rápida cuando se despeja la falta.

Por otra parte, en la transición de los actuales parques eólicos *grid following* que funcionan como fuentes de corriente a parques eólicos *grid forming* que funcionan como fuentes de tensión se debe considerar que ambas tecnologías van a coexistir conjuntamente por mucho tiempo. Por tanto, se hace necesario el estudio de estabilidad de parques eólicos con ambas tecnologías, así como el estudio de cuanta generación *grid forming* es necesaria para mantener el parque eólico estable en cualquier situación.

Además, el uso de parques eólicos *grid foming* permite diferentes aplicaciones como la energización de redes eléctricas después de un apagón desde estos parques eólicos, o el uso de diodos rectificadores en enlaces HVDC para la conexión de parques eólicos marinos.

Para facilitar el estudio y diseño de aerogeneradores *grid forming*, en la presente tesis se propone una técnica de agregación de aerogeneradores tipo-4. Esta técnica permite reducir la complejidad del parque eólico para su estudio y análisis.

Esta tesis incluye las siguientes contribuciones: Para el funcionamiento de aerogeneradores *grid forming* en paralelo con aerogeneradores *grid following* se propone un método de diseño analizando la estabilidad del sistema completo. Además, se propone una estrategia de control ante faltas para asegurar una recuperación rápida y segura.

Se propone el uso de técnicas de control $\mathcal{H}_\infty$ para la sintonización de controladores *grid forming*. El uso de estas técnicas para el diseño de controladores puede mejorar la robustez de los controladores, así como el rendimiento de estos.

Considerando la aplicación de la energización de redes HVAC desde parques eólicos, se ha propuesto como llevar a cabo dicha maniobra a partir de parque con aerogeneradores *grid forming* y *grid following*. Los resultados obtenidos validan el funcionamiento de la operación. Además, muestran que la cantidad de generación *grid forming* está relacionada con la dimensión de cargas que tienen que aguantar dichas turbinas más que con la estabilidad del sistema con un porcentaje bajo de generación *grid forming*.

Finalmente, se han propuesto estrategias de protección para la integración de parque eólicos en redes malladas HVDC utilizando rectificadores de diodos. Los parques eólicos *grid forming* pueden ayudar a gestionar faltas disminuyendo los requisitos en las protecciones necesarias en el enlace HVDC. Esto permite una reducción del coste de la instalación, además de aumentar la robustez del sistema.

Palabras clave: Grid Forming, black start, Rectificador de diodos, agregación, Parques eólicos marinos.

Contents

List of Figures

Chapter 1

Introduction

This chapter introduces the motivation of the presented research work. It includes a brief description of the current situation of wind energy, wind energy forecast for the next thirty years, and expected future grid with massive integration of power electronic devices. Then, the objectives of this thesis are presented. Finally, this chapter includes a description of the thesis structure and the contents of each chapter.

1.1 Motivation and background

In the last years, governments are taken measures to reduce the effects of climate change. Currently, the new EU *Green Deal* agreement intends to achieve a climate-neutral and sustainable EU by 2050 [1].

The *Green Deal* requires Europe to achieve 1,200 GW of wind capacity by 2050 up from 190 GW in 2019 [2, 3]. This means an offshore wind capacity in Europe of 240-440 GW by 2050, compared to about 22 GW today [4].

Fig. 1.1 shows the current wind power capacity in Europe. In order to achieve the new EU agreement *Green Deal* objectives, 21 GW of additional wind power will be installed every year during the next decade [5].

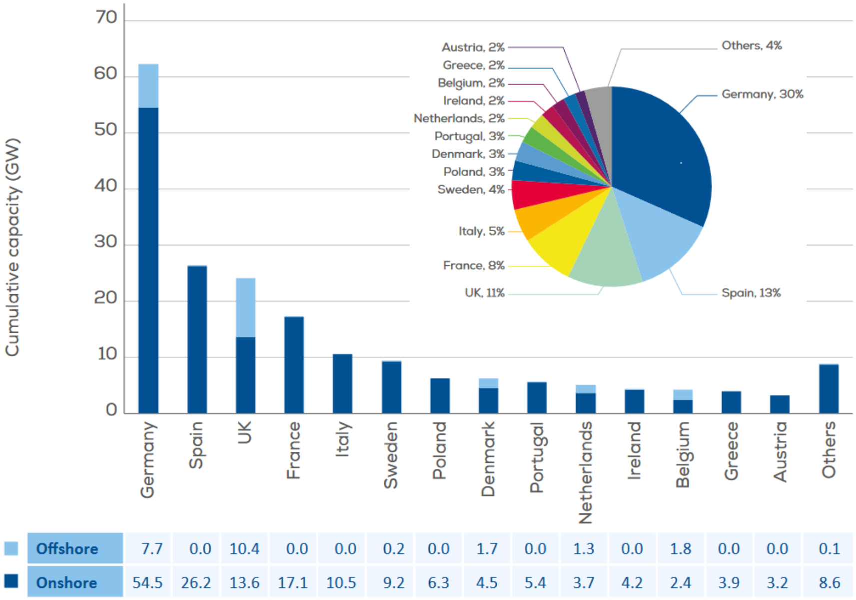

	Germany	Spain	UK	France	Italy	Sweden	Poland	Denmark	Portugal	Netherlands	Ireland	Belgium	Greece	Austria	Others
Offshore	7.7	0.0	10.4	0.0	0.0	0.2	0.0	1.7	0.0	1.3	0.0	1.8	0.0	0.0	0.1
Onshore	54.5	26.2	13.6	17.1	10.5	9.2	6.3	4.5	5.4	3.7	4.2	2.4	3.9	3.2	8.6

Source: WindEurope

Figure 1.1: Cumulative wind power capacity in Europe (EU 27+ UK) as of 1 July 2020 [5].

Considering the presented scenario, the main off-shore wind turbine manufactures are developing new wind turbines with higher rated power to reduce the levelised cost of Electricity (LCoE). Some of the last wind turbine announced by the main manufactures are listed in table 1.1.

Manufacturer	Model	Rated Power (MW)
MVOW	V164-10.0 MW	10.0
SWISS ELECTRIC	YZ190/10.0	10.0
Dongfang	D10000-185	10.0
MingYang	MySE11-203	11.0
GE	Haliade-X 13 MW	13.0
Siemens Gamesa	SG 14-222 DD	14.0
Bewind	BW 14.xM225	14.0

Table 1.1: Wind turbine generators.

Moreover, the optimal technology for the off-shore wind power plant integration to the on-shore grid depends of the distance between the off-shore wind power plant and the onshore grid. Fig. 1.2 shows the investment costs of high-voltage electrical transmission infrastructure. It shows that the investment cost of an AC transmissions grid rises with the distance. Furthermore, Siemens claims that using Diode rectifier based HVDC link, the investment cost of the DC transmission system can be reduced and the new break even distance is approximately 80 km fig. 1.2 [6].

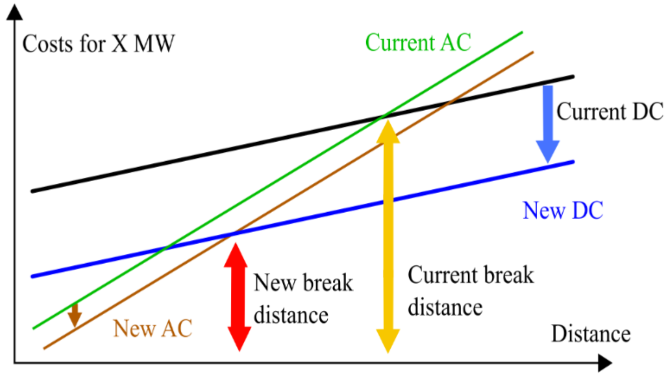

Figure 1.2: AC vs. DC break-even-distance for a large power wind farms [7].

Grid forming WPPs have been identified as a key enabling technology for safe grid operation ans stability, considering the scenario with a massive integration of power electronic converters in the grid and the use of Diode-Rectifier based HVDC link for WPP integration.

1.2 Objectives

This PhD disertation is carried out as a part of the project PROgress on Meshed HVDC Offshore Transmission Networks (PROMOTioN), funded by *H2020-EU.3.3.4. - A single, smart European electricity grid* programmes in the topic *LCE-05-2015 - Innovation and technologies for the deployment of meshed off-shore grids*, under grant agreement No 691714. The PROMOTioN goals are [8]:

- Develop interoperable & reliable network protection.
- Work towards technology interoperability & standardisation.
- Recommendations for EU regulatory & financial framework.
- Deployment plan & Roadmap for implementation up to 2050.
- Full scale technology demonstrations of:
    - HVDC control & protection systems.
    - Wind turbine converter harmonic model validation.
    - HVDC gas insulated switchgear.
    - HVDC circuit breakers.

One of the Work Packages of the PROMOTioN project is *WP3 - Wind Turbine - Converter Interaction*, focused on the identification and the specification of appropriate analyses to demonstrate interoperability of wind turbine and wind power plant controls with two different types of HVDC systems for connecting the wind power plants to the DC network: diode rectifier units (DRU) and Voltage Source Converters (VSC) [9]. Additionally, the identification and the specification of appropriate analyses to demonstrate the off-shore WPPs Self-energization and Black Start capability for HVAC connection were added as another goal of WP3 [10].

The main goal of this Phd dissertation is the study, analysis and design of **Grid Forming Wind Power Plants**, that becomes crucial considering the future massive integration of power electronic devices in the grid and the reduction of conventional power plants. Moreover, it is a requirement for Diode Rectifier-based Wind Power Plants and for Black Start in Wind Power Plans.

Moreover, three secondary goals are identified:

- **WPP Black start operation for HVAC grids**: Considering the future massive integration of power electronic devices in the grid and the reduction of conventional power plants, the black start service shall be carry out by another power plant. Grid forming wind turbines allow that the wind power plant to carry out the black start operation on any grid (or just some part of the grid).
- **Diode Rectifier-based Wind Power Plant integration**: Considering the planned wind power plants in the north sea, the distance of the off-shore wind power plants to shore, and the HVDC grid that will be developed in the north sea, the study of some solutions for the wind power plant integration that make possible a CAPEX and OPEX reduction. Diode Rectifier was proposed as a solution for wind power plant integration that allows up to 30 % cost reductions on the WPP transmission system [6, 11, 12, 13, 14, 15].
- **Aggregation of off-shore Wind Power Plants**: Large off-shore wind power plants (WPPs) with more than one hundred wind turbine generators (WTG) are currently operational or in the planning or approval phases. Simulation studies covering individual WTGs during the design phase are very demanding from the computational point of view. When studying the impact of WPPs in the overall HVDC or HVAC transmission network, very detailed models are not generally required. Therefore, simulation complexity and computing time can be reduced by using aggregated WTG models. However, these aggregated models should provide a faithful representation of the actual WPP dynamics.

1.3 Contibutions of the thesis

This thesis is based on a collection of papers and consists of an introduction, literature review, conclusions and considered papers:

- A WPP aggregation method has been proposed based on a multiobjective optimization technique. It achieves to reduce the error between a detailed model (150 WTGs) and an aggregated model (3 WTGs) up to 10% in comparison with the aggregation techniques presented in the literature.
- A procedure for the design of grid forming controllers using $\mathcal{H}_\infty$ synthesis has been proposed. It includes resonant behaviour for the voltage loop. Moreover, it achieves better performance and robustness than the achieved

using PI controllers. Harmonic magnitude reduction is also achieved as the total harmonic distortion analysis of the current and the voltage shows.

- The controller design and stability analysis of grid forming WTGs in parallel with grid following WTGs has been proposed. The operation of mixed grid forming and grid following off-shore WPPs with diode rectifier link to HVDC grids has been validated for normal and fault operation. Moreover, in the case when there is not enough wind in grid forming WTGs, they can still operate as a STATCOM to control system voltage and frequency.
- A fault recovery procedure for WTGs after faults has been proposed. Communications are not required, so a fast and controlled grid recovery is achieved using a detailed model (a cluster of 50 WTGs in parallel with 2 aggregated clusters).
- A black start procedure from a HVAC-connected off-shore WPP is defined. The WPP may consist of grid following and grid forming WTGs. The black start operation is achieved using a 24% of grid forming power using a detailed model (50 WTGs).
- The use of a diode rectifier based WPP to reduce the protection equipment cost in a multi-terminal HVDC grid has been proposed and validated. The proposed control leads to smaller current requirements of eventual circuit breakers. The WPP is able to detect faults on the HVDC grid without communications, so the WPP can contribute to reduce the voltage to clear the dc fault, and then to resume the normal operation. Moreover, different fault recovery techniques have been included, both with and without communication between the DRU and the WPP is possible. When communication between the DRU and WPP is available, it is possible to minimise the fault impact on the healthy on-shore converter.

1.4 Structure of the thesis

This PhD dissertation is structured as follows:

1. **Introduction**: this chapter presents the background, motivation and scope of this thesis.
2. **Grid forming Wind Power Plants**: This chapter presents the different control purposes for grid forming wind power plants including a background about WPP aggregation techniques.

3. **Application of Grid Forming Wind Power Plants**: This chapter presents the main purposed strategies for Black start operation and the identified issues to consider during the Black start operation, and the different controls strategies for this kind of wind power plants and the different purposes of the diode rectifier integration in HVDC grids.

4. **Conclusions**: A summary of the work carried out in this PhD dissertation is presented, including a detailed discussion of the main contributions and a proposal of future work to continue the presented research.

5. **Publications**: The main journal and conference papers presented in this PhD dissertation are presented.

   Journal papers:

   - Martínez-Turégano, Jaime; Añó-Villalba, Salvador; Bernal-Perez, Soledad; Peña, Ruben; Blasco-Gimenez, Ramon. (2020) Small-signal stability and fault performance of mixed grid forming and grid following offshore wind power plants connected to a HVDC-diode rectifier. IET Renewable Power Generation - . 10.1049/iet-rpg.2019.1264

   - Martínez-Turégano, Jaime; Vidal-Albalate, Ricardo; Añó-Villalba, Salvador; Bernal-Perez, Soledad; Blasco-Gimenez, Ramon. (2020) Protection Strategies for the Connection of Diode Rectifier-based Wind Power Plants to HVDC Interconnectors. IEEE Journal of Emerging and Selected Topics in Power Electronics - . 10.1109/JESTPE.2020.3028780

   - Martínez-Turégano, Jaime; Añó-Villalba, Salvador; Bernal-Perez, Soledad; Blasco-Gimenez, Ramon. (2019) Aggregation of Type-4 Large Wind Farms Based on Admittance Model Order Reduction. Energies, 9 (12), 1 - 21. 10.3390/en12091730

   Conference Papers:

   - Martínez-Turégano, Jaime; Añó-Villalba, Salvador; Bernal-Perez, Soledad; Peña, Ruben; Blasco-Gimenez, Ramon (2018). Mixed Grid-Forming and Grid-Following Wind Power Plants for Black Start Operation. EN 17th International Workshop on Large-Scale Integration of Wind Power into Power Systems as well as on Transmission Networks for Offshore Wind Power Plants. (1 - 6). Stockholm, Sweden.

   - Martínez-Turégano, Jaime; Sala, Antonio; Blasco-Gimenez, Ramon (2019). $\mathcal{H}_\infty$ controller design for grid forming Offshore Wind Power

Plants Connected to a HVDC-Diode Rectifier system. EN 13th International Conference on Modeling and Simulation of Electric Machines, Converters and Systems (ElectrIMACS 2019). Salerno, Italy.

Chapter 2

Grid Forming Wind Power Plants

This chapter presents the background about Grid forming Wind Power Plants. It includes the difference between grid forming and grid following control, grid forming control purposes for parallel connection of wind turbines, fault-ride-through capability, and a study about Aggregation techniques for Wind Power Plants. The use of aggregation WPPs are justifies during the chapter and an introduction about multiobjective optimization to aggregate WPPs is presented.

2.1 Introduction

Considering the European Commission goals for de-carbonisation and the the goal of 100% renewable electricity production by 2050, the grid forming WPPs will became a requirement in order to maintain the grid stable and within its operational limits.

Moreover, black start from grid forming WPPs will be of particular relevant for the grid maintenance tasks, and to speed up service restoration after a black-out of the power grid, or the energisation of new grid installations make compulsory the investigation to carry out the black start operation from grid forming WPPs.

Nowadays, installed WPPs work as grid following. Some researchers proposed solutions to convert a grid following WPP into grid forming by using hybrid solutions [16]. This PhD dissertation considers grid forming WPPs where the WTGs work with grid forming controllers as this solution just requires a controller firmware update.

Finally, for off-shore WPPs where the best solution to transmit the power is the use of HVDC grids, the Diode Rectifier-based Wind Power Plant has been proposed a good alternative to reduce CAPEX and OPEX of off-shore WPP [6, 11, 12, 13, 14, 15].

2.2 Background

Grid forming control applied to power electronic devices has been well studied for microgrids and in some European Commission's projects as MIGRATE or PROMOTioN. The main requirements to consider are the next: parallel connection of VSCs and fault-ride-through. Parallel connection of VSCs shall be considered in order to allow the connection of grid forming WTGs at the same WPP. Fault-ride-through capability is compulsory to safe power electronics.

The main control approaches for the parallel connection of power electronic devices are the following [17]:

1. **Droop control**: The baseline solution to grid forming control is to mimic the speed droop control of a synchronous machine. The droop control was proposed in [18] considering proportional gains for the control of active and reactive power through the frequency and the voltage droop.
2. **Virtual Synchronous Machine**: The solution is based on reproducing the dynamic properties of a real synchronous generator using a voltage source

inverter. It allows to incorporate the advantages of a synchronous generator as inertia or islanding operation [19].

3. **Matching Emulation Control**: It is based on the similarities between the synchronous generator and the voltage source converter. There are dualities between the converter DC link voltage and synchronous generator rotor angular frequency [20].
4. **Virtual Oscillator Control**: It is based on synchronization theory and methods from nonlinear control [21]. It has been well studied in European Commission's project MIGRATE.
5. **ICT/IoT based approach**: It is similar to the Virtual oscillator control, but it uses communication between WTGs in order to improve the results.

Fault-ride-through capability for grid forming converters can be achieved by using cascaded control with an inner control loop to limit the current. Reference conditioning is also an alternative to avoid the inner current loop. This solution is usually presented as virtual impedances that reduces the VSC voltage up to the required to limit the current.

2.3 Grid Forming vs Grid Following

The control strategies that can be implemented in a converter can be divided in 2 types as comented in [22]:

- **Grid Following:** This control strategy makes the WTG behave approximately as a current source as shown in fig. 2.1(a). Is the most extended control strategy for renewable energy sources. Moreover, this kind of converter has been well studied and a lot of modifications in order to improve its behaviour and provide ancillary services have been proposed.
- **Grid Forming:** This control strategy makes the WTG behave approximately as a voltage source as shown in fig. 2.1(b). This kink of controllers became compulsory as the conventional power plants are closing, or if a scenario with 100% renewable energy is considered. It can allow the WPPs to carry out the Black Start operation. Furthermore, it is required for Diode Rectifier-based Wind Power Plants.

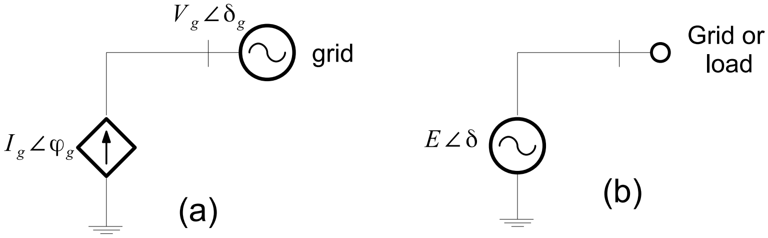

Figure 2.1: Basic concepts of inverter controls: (a) grid-following and (b) grid-forming.

Grid Following	Grid Forming
Controls magnitude and phase angle	Controls voltage magnitude and frequency
Controls active and reactive power	Instantaneously balances loads
as well as fault currents	without coordination controls
Cannot operate standalone	Can operate standalone
PLL is required	PLL is not required
Allow Fault ride through	Allows Fault ride through

Table 2.1: Grid Forming vs Grid Following.

2.4 Power sharing controllers

This section reviews some of the most studied power sharing controls for parallel connection of VSCs that can work in grid connection, as well as islanded mode of operation.

2.4.1 Droop Control

As commented before, this solution is based on emulating the speed-droop control of a synchronous machine. The classical droop control system is often implemented in microgrids.

The behaviour can be described as follows [23]:

$$\omega = \omega^* - G_p(s) \cdot (P - P^*) \tag{2.1}$$

$$E = E^* - G_q(s) \cdot (Q - Q^*) \tag{2.2}$$

Some improvements of the droop control are considered below.

In [24], the droop dynamics are improved introducing power derivative-integral terms into a conventional droop scheme. Control loops to achieve both stable output impedance and proper power balance in VSCs are proposed in [25]. [26] takes the R to X line impedance ratio into account in order to improve the mitigation of voltage harmonics, short-circuit behaviour and the effectiveness of the frequency and voltage control. In [27, 28], a small-signal analysis is presented in order to analyse the system stability, which gives rules to design the main control parameters of the droop control. Hierarchical control levels are presented in [29]. Authors in [30] consider the impedance possibilities for the parallel connection of VSCs analysing the behaviour for pure inductive, pure resistive or complex impedance.

The droop concept is also considered for multiterminal HVDC grids [31, 32, 33, 34].

Moreover, there are some proposals with the aim to improve the reactive power sharing for islanded operation. In [35] is considered the reactive power error to add a compensation to minimise it. Moreover, introduce a voltage increment to recover drop of voltage that the droop causes. In [36, 37] a secondary control structure is proposed to improve the reactive power sharing. Authors of [38] studied the behaviour of the reactive power sharing control considering secondary control after losing communications.

In any case, a real grid is a changing system because the following reasons:

- Number of generation units connected in each moment.
- The connection/disconnection of some elements of the grid in some operations.
- The multiple operation point of power production.

Hence, grid impedance as seen from the converter can show large changes. Therefore, practical controllers should be designed to be robust to the aforementioned grid changes.

2.4.2 Virtual Synchronous Machine

The Virtual Synchronous Machine concept is based on reproducing the dynamic properties of a real synchronous generator using a VSC. It allows to incorporate the advantages of a synchronous generator as inertia or islanding operation. Fig. 2.2. shows how synchronous machines synchronise. Then, the Virtual Synchronous Machine idea consist of implement by software the behaviour of a synchronous machine in the controller of a VSC. Considering two VSC working in parallel, the behaviour of both machines are described below:

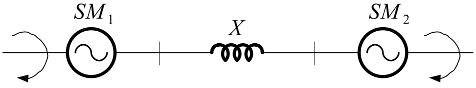

Figure 2.2: Synchronization mechanism between SMs in an ac system.

$$P = \frac{E_1 E_2 sin\theta}{X} \tag{2.3}$$

$$J_1 \frac{d\omega_{m1}}{dt} = T_{m1} - T_{e1} \tag{2.4}$$

$$J_2 \frac{d\omega_{m2}}{dt} = T_{m2} - T_{e2} \tag{2.5}$$

where θ is the electrical angle separating the two emfs E_1 and E_2, J_i is the total inertia of SM_i, ω_{mi} is the rotor speed, and T_{ei} is the electromagnetic torque of SM_i.

In [39] is proposed a method that utilizes the internal synchronization mechanism of an ac system to avoid the instability caused by a standard phase-locked loop in a weak ac-system connection. To that avail, [39] introduces a Power-Synchronization Loop that keeps synchronism between the VSC and the ac system. Moreover, the active power remains controlled by adding an angle increment. The proposed control system also includes the next loops: Automatic-Voltage Controller, Direct-Voltage Controller to control the HVDC voltage, Current-Limitation Controller, and Reactive-Power Controller. The main advantage is that the proposed control has no requirement on the short-circuit ca- pacity of the ac system to be connected. Additionally, the proposed control gives the weak ac system strong voltage support. But the main problem is that the control system shall be tuned with a lower bandwidth to work in very weak grids as authors recommends.

Authors of [40] call synchronverters to inverters mimicking a synchronous generator. The active and reactive power delivered by synchronverters connected in parallel a can be shared using the well-known droop control. Moreover, synchronverters are able of islanded operation. The proposed control strategy includes the droop control and the swing equation. Moreover, the dynamics described below are included:

$$T_e = -M_f i_f \left\langle i, \frac{\partial}{\partial\theta}\widetilde{cos\theta} \right\rangle = -M_f i_f \left\langle i, \widetilde{sin\theta} \right\rangle \tag{2.6}$$

$$e = \dot{\theta} M_f i_f \widetilde{sin\theta} \tag{2.7}$$

$$P = \dot{\theta} M_f i_f \left\langle i, \widetilde{sin\theta} \right\rangle, Q = -\dot{\theta} M_f i_f \langle i, \widetilde{cos\theta} \rangle \tag{2.8}$$

where T_e is the electromagnetic toque, M_f is the mutual inductance, i_f is the rotor excitation current, θ is the rotor angle, and e is the no-load voltage.

In [41] the Virtual Synchronous Machine concept is applied to an VSC-HVDC system to provide inertia response. In this way, frequency support capability is added to WPPs, which is particularly beneficial in low inertia grids. The main problem of this strategy is that some active power and frequency oscillations may appear during load changes.

In [42] the concept is applied to a back-to-back converter in order to achieve a motor-generator pair system that allows power transmission. The proposed control strategy has a dc control loop and a power loop that is transferred between each converter considering the power direction. It achieves a noise reduction of the power. The main disadvantage is that the bandwidth of the controller is reduced as shown in the paper results.

2.4.3 Matching Control

This control strategy is based on the similarities between the synchronous generator and the voltage source converter [20]. Consider the three phase converter model shown in fig. 2.3, which can be described using the following equations:

$$C_{dc}\dot{v}_{dc} = -G_{dc}v_{dc} + i_{dc} - \frac{1}{2}m_{\alpha\beta}^{T}i_{\alpha\beta} \tag{2.9}$$

$$L\dot{i}_{\alpha\beta} = -Ri_{\alpha\beta} - v_{\alpha\beta} + \frac{1}{2}m_{\alpha\beta}v_{dc} \tag{2.10}$$

$$C\dot{v}_{\alpha\beta} = -Gv_{\alpha\beta} + i_{\alpha\beta} - i_l \tag{2.11}$$

where the DC circuit consist of a controllable current source i_{dc}, a capacitance C_{dc} and a conductance G_{dc}, while the AC circuit consist of an inductance L, a resistance R, a capacitance C, a shunt conductance G, $m_{\alpha\beta}$ is de modulation amplitude, and another controllable current source i_l.

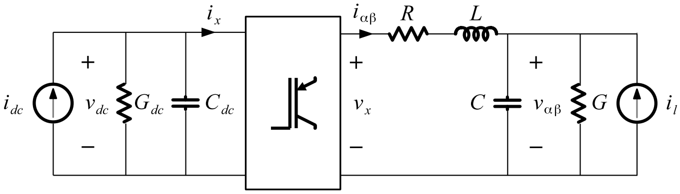

Figure 2.3: Circuit diagram of a 3-phase DC/AC converter.

Now, consider the synchronous machine model defined in [43] with the next equations:

$$M\dot{\omega} = -D\omega + \tau_m + L_m i_f e^{-j\theta} i_{\alpha\beta} \tag{2.12}$$

$$L_s\dot{i}_{\alpha\beta} = -R_s i_{\alpha\beta} - v_{\alpha\beta} - L_m i_f e^{-j\theta}\omega \tag{2.13}$$

$$C\dot{v}_{\alpha\beta} = -Gv_{\alpha\beta} + i_{\alpha\beta} - i_l \tag{2.14}$$

where M is the rotor inertia, D is the damping coeficient, τ_m is the driving mechanical torque, L_m is the stator-to-rotor mutual inductance, L_s the stator inductance, and C is a shunt capacitor to interface the synchronous machine with the grid.

The similarities between equations 2.9, 2.10, 2.11 and 2.12, 2.13, 2.14 are clear. The DC capacitor is similar to the rotor moment of inertia, and the electrical torque and the electromotive force are similar to the switching current and switching voltage. Hence the idea is to match the converter dynamics to a synchronous machine dynamics.

The first step to design the matching controller is to introduce an oscillator mode:

$$m_{\alpha\beta} = \mu e^{-j\theta} \tag{2.15}$$

where μ represents an amplitude for the modulation of the oscillator. Then, the virtual angle θ_v is introduced similar to the synchronous machine rotor angle. The following dynamics are assign to it.

$$\dot{\theta}_v = \eta v_{dc} \tag{2.16}$$

where η is a constant gain to be specified. It could be choice as the ratio between the nominal AC frequency and the DC voltage reference. Then, the converter model is matched to the generator model though the control scheme. The authors define the relation between the average switch voltage and the virtual electromotive force as follows:

$$\mu = -2\eta L_m i_f \tag{2.17}$$

The last step is to define ξ as the controller state and rewrite the controller as the following nonlinear oscillator:

$$\dot{\xi} = \eta v_{dc} \begin{bmatrix} 0 & 1 \\ -1 & 0 \end{bmatrix} \xi, m_{\alpha\beta} = -\mu\xi \tag{2.18}$$

The obtained control loop defined as a generalised form that can be synthesised considering passivity to ensure the stability of the controller. It means that the WTG will provide a stable frequency regulation and power sharing when connected to other WTGs. Moreover, the control strategy manages to regulate voltage and curent within their limits. The disadvantage is that the synthesis of the controller from the passivity point of view could lead to too conservative controllers.

2.4.4 Dispatchable Virtual Oscillator Control

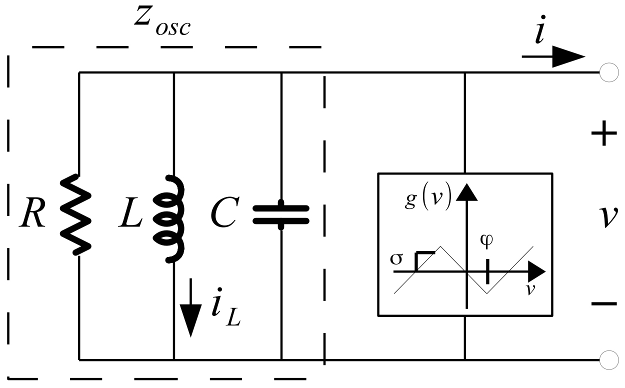

Figure 2.4: Electrical schematic of the dead-zone oscillator.

Virtual Oscillator Control was presented in [21] as a method to synchronise and control parallel connected VSCs. The control is based on the nonlinear dead-zone oscillator model that the VSCs shall emulate. Fig. 2.4 shows the nonlinear dead-zone oscillator model. The impedance z_{osc} is a passive RLC circuit defined as:

$$z_{osc}(s) = R||sL||(sC)^{-1} = \frac{\frac{1}{C}s}{s^2 + \frac{1}{RC}s + \frac{1}{LC}} \tag{2.19}$$

The voltage dependent current source is a static nonlinear function $g(v) = -i_g(v)$. It is parametrised by σ and φ, and defined as

$$g(v) = f(v) - \sigma v \tag{2.20}$$

where $f(v)$ is a dead-zone function with slope 2σ

$$f(v) = \begin{cases} 2\sigma(v-\varphi), & v > \varphi \\ 0, & |v| \leq \varphi \\ 2\sigma(v+\varphi), & v < \varphi \end{cases} \tag{2.21}$$

From that, the dynamics of the oscillator are defined as

$$\frac{dv}{dt} = \frac{1}{C}\left(\sigma - \frac{1}{R}\right) v - f(v) - i_L - i, \quad \frac{di_L}{dt} = \frac{v}{L} \tag{2.22}$$

Using this control strategy the VSCs are able to synchronize and share the load proportionally to their ratings. The problem is that using this control strategy each VSC cannnot be dispatched to track references for the power injection and voltage. It means that the power sharing between sources is not resolved and it is determined by the network conditions.

That issue is resolved in [44]. A dispatchable virtual oscillator control is achieved ensuring that the system is asymptotically stable with respect to set points for the phase shift, frequency, and magnitude. Active and reactive power setpoints are set as follows:

$$u_k = \omega_0 J_{v_k} + \eta \left[K_k v_k - R(k) i_k + \alpha \Phi_k(v_k) v_k\right] \tag{2.23}$$

where J_{v_k} is a 90^o rotation matrix, v_k is the VSC terminal voltage, η is the synchronization gain, α the voltage control gain, and K_k and Φ_k are defined as

$$K_k = \frac{1}{v_k^{*2}} R \begin{bmatrix} p_k^* & q_k^* \\ -q_k^* & p_k^* \end{bmatrix}, \quad \Phi_k(v_k) = \frac{v_k^{*2} - ||v_k||^2}{v_k^{*2}} I_2 \tag{2.24}$$

K_k considers the active and reactive power references that allows to dispatch the power using the virtual oscillator control.

Moreover, the authors in [44] explicit bounds on the controller set-points, branch powers, and control gains are established in order to guarantee global asymptotic stability of the controller in combination with a dynamic model of the transmission network. The main problem of this control strategy is that the inverter dynamics cannot be close to the transmission line dynamics because the inverter could became unstable. Thus, this control strategy is not valid for long ac transmission lines that have low frequency resonant peaks.

2.5 Fault ride through for grid forming converters

As defined in [45], *Fault Ride Through is the ability of Generating Units and Power Park Modules to ride through Supergrid Transmission System faults and disturbances whilst connected to a healthy System circuit.* In other words, the generating units shall remain connected while a fault appear for the grid to recover after the fault clearance.

The grid codes that includes fault-ride-through requirements considered in this PhD dissertation are listed:

- ENTSO-E NC RfG.
- National grid ESO GC0062: Fault Ride Through.

The grid codes define a voltage profile to maintain the voltage when a fault occurs. Fig. 2.5 shows the voltage envelope defined in **ENTSO-E NC RfG**.

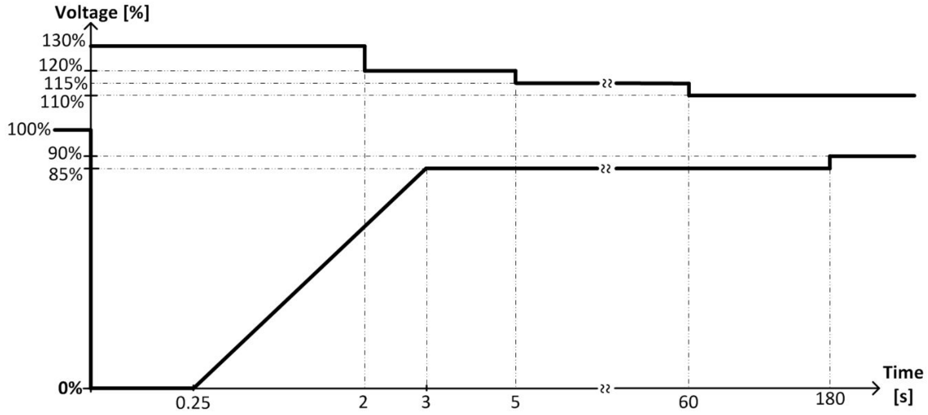

Figure 2.5: Voltage-time profile for offshore AC faults [ENTSO-E NC HVDC, article 38] [ENTSO-E NC RfG Article 16 (3) (a) (i)].

Wind and PV are based on power electronics, so current must be limited to protect the devices.

Hence, some solutions are found in the literature to achieve fault-ride-through by limiting the current. The first of them is based in a cascade control that includes a current controller as a fast inner loop and the second solution without that loop. In some cases, when an inner current loop is not implemented, the control strategy is switched form grid forming to grid following during fault, so the current loop is introduced [46]. Fault ride trough solutions based on current loop and based on reference conditioning will be studied below.

2.5.1 Current control

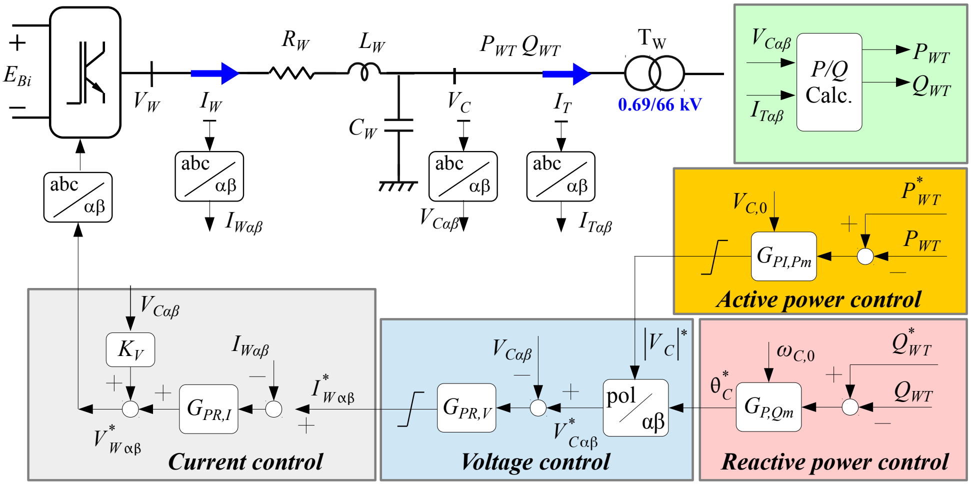

Figure 2.6: Grid forming controller based on stationary reference frame cascade control.

Fault-ride-through capability can be added using a current control loop. For grid forming WTGs, it is used as the inner loop of a cascaded control (Fig. 2.6). The current loop can be designed for stationary reference frame ($\alpha\beta$), as well as for synchronous reference frame (dq). Considering the WTG shown in Fig. 2.6, the dynamics of the WTG for the current control are described below.

$$V_W = R_W I_W + L_W \frac{dI_W}{dt} + V_C \tag{2.25}$$

$$I_W - I_T = C_W \frac{dV_C}{dt} \tag{2.26}$$

$$V_C = R_T I_T + L_T \frac{dI_T}{dt} + V_F \tag{2.27}$$

where V_W is the converter output voltage, I_W is the converter output current, V_C is the capacitor filter voltage, I_T is the transformer current, and R_W, L_W, C_W, R_T and L_T are the filter and transformer parameters.

Transforming the model to design the current control in stationary reference frame ($\alpha\beta$), the following model is obtained:

$$\begin{pmatrix} \dot{I}_{W\alpha\beta} \\ \dot{V}_{C\alpha\beta} \end{pmatrix} = \begin{pmatrix} -\frac{R_W}{L_W} & -\frac{1}{L_W} \\ \frac{1}{C_W} & 0 \end{pmatrix} \begin{pmatrix} I_{W\alpha\beta} \\ V_{C\alpha\beta} \end{pmatrix} + \begin{pmatrix} \frac{1}{L_W} \\ 0 \end{pmatrix} V_{W\alpha\beta} + \begin{pmatrix} 0 \\ -\frac{1}{C_W} \end{pmatrix} I_{T\alpha\beta} \tag{2.28}$$

In [28] a grid forming controller designed in $\alpha\beta$ frame is proposed. It includes measurement and PWM delays for the controller design. The proposed controller is based on a proportional-resonant controller that includes a resonant control for the fundamental frequency and for each harmonic that requires minimisation.

A method to generate proper current and voltage references during asymmetrical faults is proposed in [47]. It is achieved following these steps: first, the amplitude of each component $\alpha\beta$ is calculated from that component and its $\pi/2$ delayed signal. The second step consists of calculating a gain for each component $\alpha\beta$ to ensure that the current is always within limits.

In [48] a Model Predictive Control is designed to avoid overcurrents during asymmetrical faults. The MPC calculates factors for each component $\alpha\beta$ to avoid overcurrents.

Control in d-q frame shows cross-coupling terms:

$$\begin{pmatrix} \dot{I}_{Wd} \\ \dot{I}_{Wq} \\ \dot{V}_{Cd} \\ \dot{V}_{Cq} \end{pmatrix} = \begin{pmatrix} -\frac{R_W}{L_W} & \omega_C & -\frac{1}{L_W} & 0 \\ -\omega_C & -\frac{R_W}{L_W} & 0 & -\frac{1}{L_W} \\ \frac{1}{C_W} & 0 & 0 & \omega_C \\ 0 & \frac{1}{C_W} & -\omega_C & 0 \end{pmatrix} \begin{pmatrix} I_{Wd} \\ I_{Wq} \\ V_{Cd} \\ V_{Cq} \end{pmatrix} + \begin{pmatrix} \frac{1}{L_W} & 0 \\ 0 & \frac{1}{L_W} \\ 0 & 0 \\ 0 & 0 \end{pmatrix} \begin{pmatrix} V_{Wd} \\ V_{Wq} \end{pmatrix} + \\ + \begin{pmatrix} 0 & 0 \\ 0 & 0 \\ -\frac{1}{C_W} & 0 \\ 0 & -\frac{1}{C_W} \end{pmatrix} \begin{pmatrix} I_{Td} \\ I_{Tq} \end{pmatrix} \tag{2.29}$$

Many studies consider the synchronous reference frame (dq) to control the current achieving fault-ride-trough. The use of proportional-integral controller including the current decoupling is the usually selected alternative. In [49], instabilities during faults caused by the droop control are identified and solved adding a sliding mode stabilizer.

[50] resolves the problem of the overcurrents that appear during asymmetrical faults. It includes the negative sequence current control and a system that reduces the current reference in case of any overcurrent. The strategy can work with grid forming and grid following WTGs. The main problem is that the overcurrent problem is not well resolved because during asymmetrical faults the currents exceed the maximum current reference, leading to power electronics over-rating.

In [51] a similar solution is proposed, but the solution is applied in three and four wire systems. In this case, the overcurrent is avoided calculating the current amplitude of each phase and reducing the current reference the required to maintain all the currents within limits.

The authors in [52] calculate a virtual resistor that reduce the voltage reference in function of the converter current in order to maintain the synchronisation during faults.

In [53], a virtual admittance to enhance the stability of the controller and to avoid desynchronisation of the grid forming converter during faults is proposed.

From the proposals above, there are different approaches for grid forming control design. The most commonly used are models based on synchronous reference frame (dq) and models based on stationary reference frame ($\alpha\beta$). The main advantage of designing the current control in stationary reference frame ($\alpha\beta$) is that it is analogous to implement positive and negative sequence in synchronous reference frame (dq). However, steady state references in a stationary frame would be sinusoids.

2.5.2 Reference conditioning

The second way to achieve fault-ride-trough is based on implementing a reference conditioning to the voltage control loop. In this case the current control loop is not implemented. This solution is presented as a virtual impedance that is activated just when the current exceeds the limits [54, 55].

Authors in [56] propose two strategies. The fist strategy consist of applying the measured voltage V_C at the converter terminal V_W. It ensures a current close to zero though the filter inductor L_W. Moreover, the voltage reference is also changed to the measured voltage ($V_C^* = V_C$) in order to avoid controller integration that may cause an uncontrolled recovery. The main problem of this strategy is that the WTG does not provide reactive power during the fault.

The second strategy proposed in [56] adds a V_{FRT} to the voltage that applies to the converter in order to allow the injection of reactive power during faults. The following equation describes that.

$$V_W = V_C + V_{FRT} \tag{2.30}$$

The main problem of this proposal is the WTGs cannot control the injected reactive power, as it depends on the fault location and the kind of fault (symmetrical/asymmetrical).

Authors in [55] propose a virtual impedance that reduces the voltage calculated by a Virtual Oscillator Control when the current overcomes its limit. The proposed strategy consists of a fault detector and an over-current limiter. The fault detector works as follows:

$$x_f = \begin{cases} 0, & |I_T| \leq I_{max} \quad || \quad |V_C| \geq V_{Low} \\ 1, & |I_T| > I_{max} \quad || \quad |V_C| < V_{Low} \end{cases} \tag{2.31}$$

where x_f is a flag to indicate if there is any fault, I_{max} is the maximum allowed over-current and V_{Low} is the low voltage threshold. Then, the current is limited using x_r. From the error between the current $I_T$and its maximum value I_{max}, the converter voltage V_W is decreased applying a virtual impedance as shown below.

$$\Delta Vw = x_r R_0 (I_{max} - I_T) \tag{2.32}$$

where ΔVw is the voltage reduction and R_0 is the virtual impedance.

A virtual impedance that reduces the converter voltage is proposed in [57]. That virtual impedance is activated when the converter current rises a defined value. As the previous proposal, a voltage reduction ΔV_z is calculated using the the current I_W and a virtual impedance R_V and L_W. ΔV_z is calcalated as follows.

$$\Delta V_z = \begin{cases} I_{Wd}R_V + I_{Wq}X_V, & if en = 1 \\ en(I_{Wd}R_V + I_{Wq}X_V), & if 1 > en > 0 \\ 0, & if en = 0 \end{cases} \tag{2.33}$$

$$en = \begin{cases} 1, & if |I_W| > I_{max-2} \\ \frac{|I_W| - I_{max-1}}{I_{max-2} - I_{max-1}}, & if I_{max-2} > |I_W| > I_{max-1} \\ 0, & if |I_W| < I_{max} \end{cases} \tag{2.34}$$

2.6 Wind Power Plant Aggregation

In the last years there are many WPPs with more than one hundred WTGs that are currently operational or in planning or approval phases. During the design phase, simulation studies to check the interoperability between WTGs are important, but the computational requirements are excessive. By using aggregation techniques for some parts of the WPP (as some WTG strings) computing time can be reduced. Aggregation techniques are also useful when real time simulations are required.

Fig 2.7 shows the purpose of the use of aggregation techniques. the figure shows the most extreme case where a entire WPP of fifty WTGs is aggregated in just one WTG, but is possible to aggregate just some strings or some desired part in order to allow the required simulation studies.

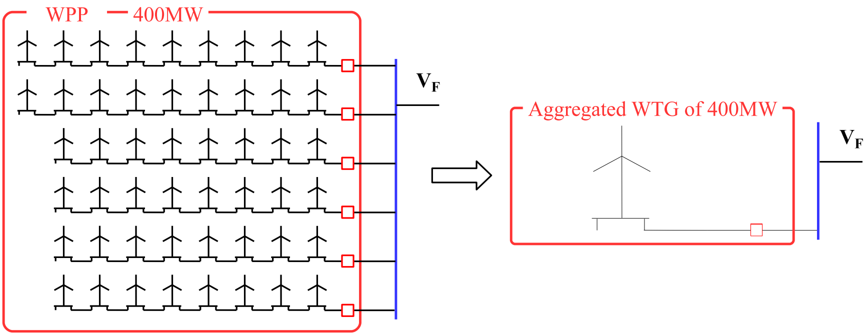

Figure 2.7: WPP aggregation concept.

Additionally, there are a large amount of literature developed on aggregation techniques for different applications [58, 59]. The considered aggregation techniques are listed below.

1. Aggregation technique based on power losses [60]. This technique develops an equivalent representation of a wind power plant collector system for power system planning studies.
2. Aggregation technique to represent the dynamic response of wind farms [61]. This aggregation technique uses the produced power by any WTG to weight its contribution to the aggregated model. Thus, the accuracy on grid disturbance simulations is improved.
3. Aggregation technique for type-1 and type-3 WTGs [62]. This technique is presented as suitable for large power systems simulation. The short-circuit impedance is used to aggregate the WPP grid.
4. Aggregation technique based on voltage drop [63]. This technique was performed as the most appropriate aggregation technique for stability assessment studies.
5. Aggregation technique to represent the whole power system seen from the WTG AC terminals [64].

Considering the commented aggregation techniques above, the main aggregation techniques follow two steps. The fist step consist of aggregating a string of WTGs into an equivalent WTG. This is shown in Fig 2.8. The second step consists of the aggregation of the overall WPP, as Fig 2.9 shows.

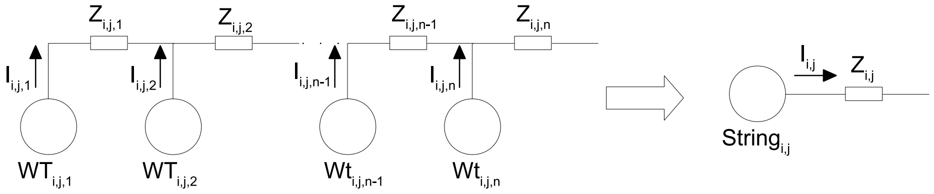

Figure 2.8: Above: String of WTs; bellow: Aggregated serial impedance of string.

The voltage drop and the power loses based techniques can be used to aggregate type-4 WTGs, but the achieved accuracy of the response in comparison with the detailed WPP shall be improved.

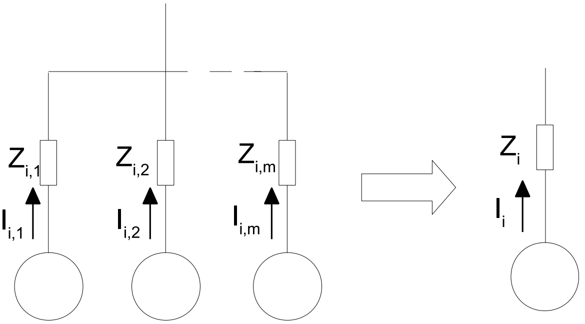

Figure 2.9: Left: Wind power plant; Right: Aggregated model of wind power plant.

2.6.1 Aggregation based on Voltage Drop

Aggregation based on voltage drop, proposed in [63], has been used for stability assessment studies. It considers the frequency response of the WTG grid side converter and the impedance seen from the WTG to study the stability of the system. This technique has been mainly used for grid following WTGs, but the results obtained in [65] shows that it is also valid for grid forming WTGs.

Then, the aggregated model is obtained applying the following steps:

Aggregated serial impedance of the string

The aim of this step consists of reducing a complete string of WTGs or a part of it in a single WTG. As shown in Fig 2.8. Hence, the serial aggregation is carried out using eq (2.35).

$$Z_{ij} = \frac{1}{n}\sum_{k=1}^{n} kZ_{ijk} \tag{2.35}$$

where n is the number of WTGs in the string, k is the position of each WTG, Z_{ijk} is the cable impedance and Z_{ij} is the aggregated cable impedance of the string.

Overall aggregated impedance

In this step an aggregated model as shown in Fig 2.9 is obtained. It consist of obtain an equivalent model of the parallel connection of WTGs. The equivalent model is obtained using the following equation:

$$Z_i = \frac{1}{\sum_{j=1}^{m} \frac{1}{Z_{ij}}} \tag{2.36}$$

where m is the total number of strings, j is the string index, Z_{ij} is the aggregated cable impedance of each string and Z_i is the aggregated cable impedance of the WPP.

Total capacitance calculation

The aggregated capacitance is calculated as follows:

$$C_i = \sum_{j=1}^{m} \sum_{k=1}^{n} C_{ijk} \tag{2.37}$$

where C_{ijk} is the parallel capacitance of the WTG_{ijk} cable.

2.6.2 Aggregation based on Power Losses

Aggregation based on power losses proposed in [60] is commonly used for load-flow studies as well as electromechanical (RMS) stability and was applied to many wind farm projects [58].

The aggregated model can be obtained by applying the following steps:

Aggregated serial impedance of the string

The first step consist of reducing a string of WTGs (or a part of it) to a single WTG, as seen in Fig 2.8. The aggregated WTG can be obtained applying the following equation:

$$Z_{ij} = \frac{1}{n^2} \sum_{k=1}^{n} k^2 Z_{ijk} \tag{2.38}$$

where n is the number of WTGs in the string, k is the position of each WTG, Z_{ijk} is the cable impedance and Z_{ij} is the aggregated cable impedance of the string.

Overall aggregated impedance

This step consist of reducing the parallel connected strings to a single WTG, as seen in Fig 2.9. The equivalent model is obtained using the following equation:

$$Z_i = \sum_{j=1}^{m} \left(\frac{1}{\sum_{k=1}^{n} n_k} \right)^2 Z_{ij} \tag{2.39}$$

where m is the total number of strings, j is the string index, Z_{ij} is the aggregated cable impedance of each string and Z_i is the aggregated cable impedance of the WPP.

Total capacitance calculation

The aggregated capacitance can be calculated as follows:

$$C_i = \sum_{j=1}^{m} \sum_{k=1}^{n} C_{ijk} \tag{2.40}$$

where C_{ijk} is the parallel capacitance of the WTG_{ijk} cable.

2.6.3 Multiobjective Optimization

Analysing the previous aggregation techniques some discrepancies and limitations have been identified. The fist of them is that the presented aggregation techniques consider the current/power of all the WTGs to aggregate are equal. Moreover, some errors in the first resonant peak and the gain at frequency 0 have been detected comparing the frequency response of the overall system and the obtained aggregated models.

On the other hand, multiobjective optimization is a technique that can be used to identify models from its frequency response. Moreover, this technique allows to introduce constraints in the matching of the model parameters [66, 67, 68, 69].

Multiobjective optimization is proposed to be used to obtain an aggregated model that achieves the next goals:

- Matching of the dc gain ($K_{\omega=0}$).
- Matching of the first resonant peak (ω_{peak}).
- Matching of the gain at the grid frequency ($K_{\omega=\omega 0}$).

Moreover, each goal can be weighted in order to obtain proper results. Additionally, constraints of the aggregated model can be introduce to obtain positive values for equivalent resistor, inductances or capacitors.

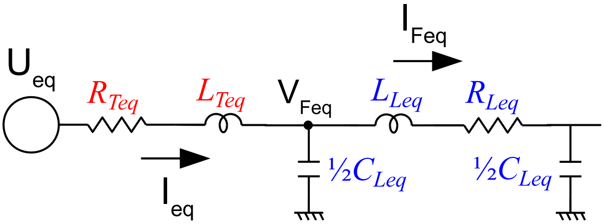

Figure 2.10: Model of an aggregated WPP.

Then, considering the objective to obtain a model as the shown in Fig 2.10, the following constraints are defined:

$$\begin{pmatrix} R_{Teq,min} \\ L_{Leq,min} \\ R_{Leq,min} \end{pmatrix} < \begin{pmatrix} R_{Teq} \\ L_{Leq} \\ R_{Leq} \end{pmatrix} < \begin{pmatrix} R_{Teq,max} \\ L_{Leq,max} \\ R_{Leq,max} \end{pmatrix}$$

2.7 Conclusions

This chapter shows a background about grid forming WPPs. In order to achieve fault ride through, the grid forming controllers presented in the literature are based on PID for synchronous reference frame (dq) models and PR for stationary reference frame ($\alpha\beta$) models. In order to improve the performance of the grid forming controllers, a design procedure based on $\mathcal{H}_\infty$ synthesis has been proposed for ($\alpha\beta$) models. It achieves better performance and robustness than the achieved using controllers based on PI or PR, in addition to harmonic reduction in both voltage and current.

Furthermore, the possibility to build grid forming WPPs close to grid following WPPs should be considered in order to increase the stability of the grid. For that reason, a controller design and stability analysis for mixed grid forming and grid following WPPs has been proposed. It includes a study about how grid forming WTGs can contribute to grid stability when there is not sufficient wind. In addition, a fault recovery procedure for mixed grid forming and grid following WPPs has been proposed in order to ensure a safe grid recovery.

On the other hand, the chapter shows the background about aggregation techniques for WPPs. The existing alternatives present some errors in the final aggregated model as some of them show dc gain errors, or first resonant peak frequency errors or impedance errors at the fundamental frequency. For that reason, a WPP aggregation method based on a multiobjective optimization has been proposed to reduce the error between detailed models and an aggregated models up to 10% in comparison with the aggregation techniques presented in the literature.

Chapter 3

Application of Grid Forming Wind Power Plants

This chapter presents two applications of Grid Forming Wind Power Plants. The first of them is the black start operation of HVAC grids using grid forming WPPs. For that a background about black start operation carried out from a Wind Power Plant is presented. The main operational requirements and the main issues regarding black start operation is also presented. The second application is the diode rectifier-based WPPs. In this case a background is also presented, in addition to the proposed control strategies for this kind of WPPs and the Diode Rectifier-based WPP integration proposals.

3.1 Introduction

The grid forming WPPs means a great progress considering their applications, as well as their importance to carry out the de-carbonisation of the world. One of the applications of grid forming WPPs is carry out the black start operation. Another applications is the diode rectifier-based WPPs.

As defined in entso-e NC RfG, *"black start capability" means the capability of recovery of a power-generating module from a total shutdown through a dedicated auxiliary power source without any electrical energy supply external to the power-generating facility.*

In order to provide black start capability, some power stations have small diesel generators which can be used to start larger generators. Often hydroelectric power plants are designated as black-start sources to restore network interconnections. Then, hydroelectric power plants can provide enough power very quickly to allow start-up of fossil-fuel or nuclear stations.

Moreover, the use of battery energy storage system with grid forming capability has been validated in [70] where black start operation of the system was carried out.

Furthermore, black start operation also has been validated using MMC converters [71].

In any case, the energy source which carry out black start operation shall be able to accept instantaneous loading of demand blocks, ideally in the range 35 to 50 MW, and controlling frequency and voltage levels within acceptable limits during the block loading process [72].

Renewable power plants with grid forming capability to provide black start sevices are required in a context of coal power plant reduction [73]. Large WPP are a good alternative to incorporate that functionality. Authors of [74] studied the decrease of rotor speed produced by a block load connection, so it validates the capability of the WPP to carry out black start operation if there is enough wind.

Moreover, some works are presented proposing WPPs as potential energy sources for black start operation. In [75], the authors proposes to carry out black start operation from a WPP with a 26% of grid forming WTGs. The percentage of required grid forming is identified as the maximum block loads that the WPP shall support. In [76], a review about the current status to use WPPs to carry out black start operation is presented. In [77], the authors compares the behaviour of the WPP during black start operation depending of the implemented grid forming control. Fig 3.1 shows a scenario considered to carry out black start operation from a WPP.

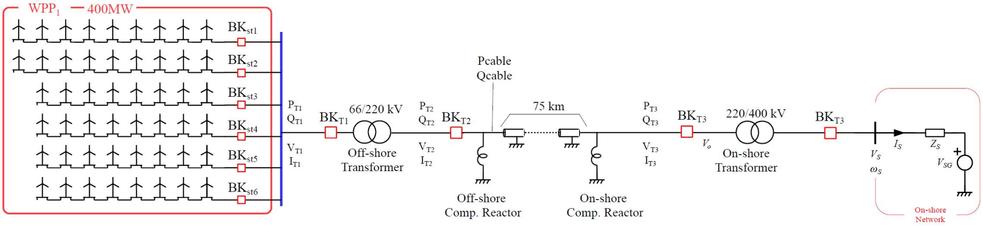

Figure 3.1: Baseline scenario for HVAC Connected Off-shore Wind Power Plant [10].

On other hand, the use of Diode Rectifiers HVDC link was proposed in [78, 79, 80]. This alternative increases the robustness and reduces the installation costs and the power losses of the complete connection system. Since the Diode rectifier is a passive device the WPP should be able to control the off-shore grid frequency and voltage magnitude, i.e. operate in grid forming mode.

In [12], the use of Diode Rectifiers HVDC link was proposed for the connection of off-shore WPPs, including an on-shore LCC converter for on-shore grid connection. Different grid forming control strategies for Diode Rectifiers HVDC link WPPs have been proposed. Moreover, different structures to integrate Diode Rectifiers HVDC link WPPs have been proposed. A small review of the proposed control strategies is done in [81].

The Europen project PROMOTioN studied the use of Diode rectifiers for the connection of off-shore WPPs from the proposed studies as [12, 14, 15, 6]. Fig. 3.2 shows an example of a Diode Rectifier based WPP.

3.2 Black Start Operation

This section shows some proposals about black start operation carried out from voltage source converters and, in some cases, from WPPs. Moreover, it shows the stability and operation requirements proposed in PROMOTioN European project.

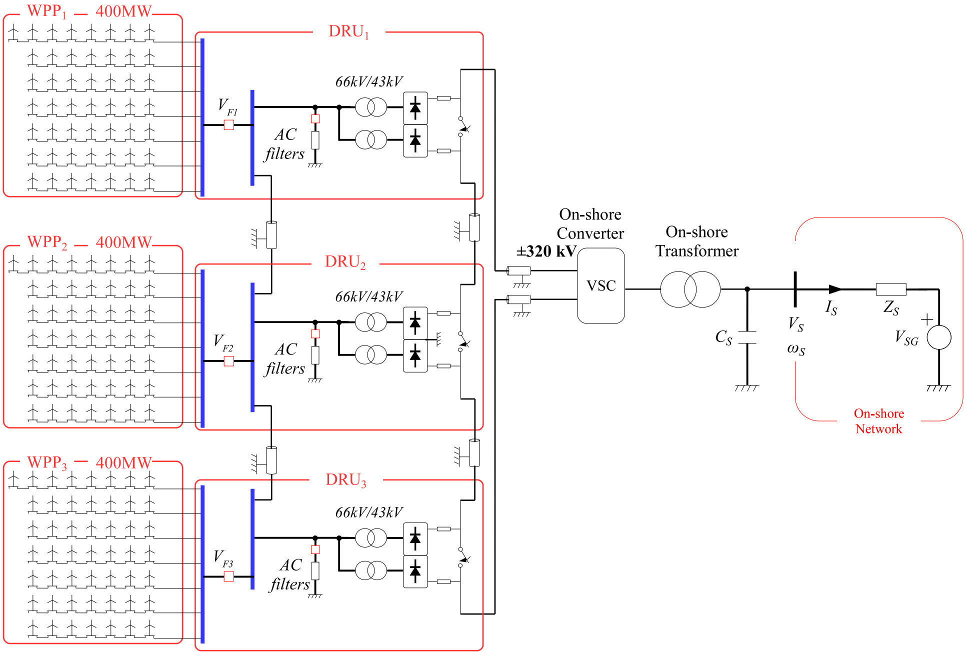

Figure 3.2: Diode Rectifiers based WPP.

3.2.1 Proposals of Wind Power Plants for Black Start Operation

For HVAC connected WPPs, there are several configuration strategies for implementing self start capability in the WF design as presented in [76]. The authors in [82] present a review about the ongoing research on black start service integrated with offshore wind power plants. It identifies the requirements that National Grid ESO and ELIA grid codes specify to carry out black start operation. That requirements are listed in Tab. 3.1:

Grid forming capability is required to comply the requirements that Tab. 3.1 shows, to provide voltage control, frequency control, block loading, reactive power control and grid inertia. Moreover, black start capability requires self start of the power plant.

Some alternatives to include self start capability to WPPs have been proposed in the literature. The review done in [76] considers the following alternatives to implement the self start capability:

Category	National grid ESO	ELIA
Self-start	Yes	Yes
Time to connect	$\leq 2h$	$1.5 - 3h$
Service availability	$\geq 90\%$	Depending on provider
Voltage control	$\pm 10\%$	Time dependent, see [76]
Frequency control	$47.5Hz - 52Hz$	$49Hz - 52Hz$
BS service resiliency of supply	$\geq 10h$	
BS auxiliary unit(s) resiliency of supply	$\geq 72h$	$\geq 72h$
Block loading capability	$\geq 20MW$	$\geq 10MW$
Reactive capability	$\geq 100MVAr$ leading	Depending on provider
Sequential start-ups	≥ 3	≥ 3
Inertia value	$\geq 800MVA.s.$	

Table 3.1: List of black-start requirements by ELIA and National Grid ESO [82].

- Diesel generator: It requires fuel provision. Moreover, another equipment as STATCOM or synchronous condenser may be required.
- Battery energy storage: The capability depends of the stored energy.
- Wind turbine: Its internal power supply allows WTGs their self start. Considering grid forming WTGs, the WPP self start is possible without any additional equipment.

At the end of the WPP self energisation, the WPP is in islanded operation and it is able to carry out the restoration of a grid.

In [83], a hierarchical model predictive control distributed in a WPP control and a WTG control is proposed. The approach consists of two control modes: frequency regulation mode and reserve recovery mode. The fist of them generates power references for each WTG according to the proportion of single WTG reserve. An energy storage system is connected in case of insufficient power during black start procedure in order to eliminate frequency deviations. The frequency dynamics of the proposed system is shown below:

$$\Delta \dot{f} = \frac{P_{WPP} + P_{ESS} + \Delta P_L}{2H_{sys}} - \frac{D}{2H_{sys}} \tag{3.1}$$

where H_{sys} is the system inertia constant, D is the damping coefficient, P_{WPP} is the WPP active power, P_{ESS} is the energy storage system active power, and ΔP_L is the disturbance from the load side.

The reserve recovery mode aims to reserve a certain proportion of WPP available power to manage potential frequency disturbances in the future. Authors propose a model predictive control that tries to minimise two objectives. The fist of them is the power reference tracking error:

$$minW_1 \left(P^*_{WPP} - \sum_{i=1}^{N} P^*_{WTi} - P^*_{ESS} \right) \tag{3.2}$$

where P^*_{WPP} is the WPP active power reference, P^*_{WTi} is the active power reference of each WTG-i, P^*_{ESS} is the energy storage system active power reference and W_1 is the weight coefficients to minimise the power reference tracking error. The second objective to minimise is the power output rate of WTGs and ESS. It is minimised as follows:

$$minW_2 \left(\sum_{i=1}^{N} \Delta P_{WTi} \right)^2 + W_3 \left(\Delta P_{ESS} \right)^2 \tag{3.3}$$

where ΔP_{WTi} is the change of each WTG output power, ΔP_{ESS} is the change of the energy storage system output power, and $W2$ and $W3$ are weight coefficients for these two terms of objective, respectively. Moreover, a model predictive control is implemented for each WTG in order to minimise the mechanical loads of the blades. However, this work did not consider energisation of large transformers and long cables nor investigated control performance in weak grids.

Authors in [84] propose a decentralized control system that allows WPPs to carry out the black start operation. The proposed control strategy consist of the following modules:

- Current control in dq axis.
- Voltage control to maintain Vq to 0.
- Active power sharing control that consist of a proportional control when the WPP is islanded, and a direct power control the the WPP is connected to any grid.
- Reactive power synchronization control to synchronise all the WTGs.

The proposed power control is a P/V Q/f droop control. The main problem of this control strategy is its operation with inductive or capacitive loads. The connection of these kind of loads may produce a reactive power step which can cause undesirable frequency deviations. This control only works when the grid or the connected loads are mainly resistive.

3.2.2 Operational and Stability requirements

The PROMOTioN European project achieved to define Operational and Stability requirements for black start operation. Those requirements were obtained analysing existing grid codes and proposing solutions in the case of absence of requirements. Those operational and stability requirements for HVAC and HVDC scenarios were proposed in [10] and are listed below:

- **FREQUENCY RANGES:** The frequency range defined is understood to be the maximum frequency excursion during block load connection/disconnection when the considered wind power plant is the only generation operating in a given island. The frequency range in this specification should not be understood as allowing the WTG to trip if frequency lays outside the frequency range. Therefore, the frequency range stated in this section is a design parameter for the grid-forming wind turbine frequency control, and does not apply for situations other than the WPP being the only generator in an islanded system.

  The considered maximum frequency range during block load connection and disconnection is 49-52Hz as required by Elia (NGESO and NC RfG consider larger frequency ranges, so the considered requirements are relatively stringent on the WTG and WPP control). The studies performed should include the maximum load ramp rate which would keep the frequency within the considered range.

- **FREQUENCY CONTROL WILL INCLUDE A SELECTABLE DROOP WHICH COULD BE SET AT BETWEEN 2 AND 12% AND THE DEAD BAND OF WHICH CAN BE SET AT BETWEEN 10 TO 200 MHZ. VOLTAGE RANGES:** Consider initially ±10% voltage variation during block loads as per NGESO requirements. The test case studies will show if these limits should be changed in light of the results.

  Voltage control will include a selectable V-Q droop up to 12% with an optional deadband.

- **BLOCK LOAD SIZE:** Block load size is selected to be a maximum of 30 MW, with capability to handle ±30 MW instantaneous load change. The simulation test results will show what is the maximum ramp rate achievable, considering the stated maximum voltage and frequency limits.

- **REACTIVE POWER CAPACITY:** No specific requirement is set for reactive power capacity. Nevertheless, the results will investigate the reactive power needed to perform black-start for different scenarios.
- **DYNAMIC VOLTAGE CONTROL:** The black-start capable wind power plant should be able to control the voltage at the PCC within its operational limits and respond to voltage references.
- **FREQUENCY CONTROL CAPABILITY:** The black-start capable wind power plant should be able to control the frequency at the PCC within its operational limits and respond to frequency references.
- **HARMONIC DISTORTION:** Voltage distortion requirements for black-start capable units the same as for normal connected units. In this way, equipment compatibility is ensured, as well as making easier synchronisation with other islands during system recovery.
- **LOW VOLTAGE RIDE-THROUGH:** Low voltage ride through profiles will be kept the same as existing profiles as a starting point, with the following considerations: During black start it is not clear that current can be controlled the way it is specified in grid codes. A recommendation will be issued based on the results of the study. Transmission system fault clearing times might be larger than usual, as wind power plants will limit their current contribution to the fault to protect themselves and hence relays will see lower fault currents than expected. This issue will also be studied. It is likely that alternative settings to protective relays will have to be used for black-start using WPPs.
- **OVER-VOLTAGE RIDE THROUGH:** Consider Over Voltage Ride Through according to VDE AR-N-4120: i.e 130% for 100 ms and 125% for 60 s. This OVRT requirement is in line with overvoltage events, particularly in HVDC connected wind power plants.
- **POWER SHARING BETWEEN WIND TURBINES:** Wind turbines should be able to share both active and reactive power amongst themselves, with selectable contribution factors. Note this is not a grid compliance requirement. This is rather an operational requirement for the WPP so all WTG contribute to active and reactive power requirements within their operational limits.

- **SYNCHRONISATION CAPABILITY:** Capability to synchronise to another island when the frequency difference is less than 0.1Hz, the angle difference is less than 20° and the voltage difference is less than 1%.
- **INERTIA RESPONSE:** During houseload and black-start operation, inertia response is indirectly set by the block load size, rise time and operational frequency requirements. Therefore, no specific value is set for these cases. Inertia response might be useful once the WPP island has been synchronised to another (weak) island. In this case, specific TSO requirements will apply.

3.2.3 Black start operation procedure

Considering the scenario shown in fig. 3.1 a sequential black start operation procedure consists of:

1. Energisation of transformer of WT1-1 from WT1-1.
2. Energisation of string cable 1 from WT1-1.
3. Sequential synchronisation of the rest of WTs connected to string 1 (first energisation of the transformer from the string and then synchronisation of the WT).
4. Sequential energisation of the rest of strings and synchronisation of the WTs. The sequence to energise the next string consist of:
    (a) Energise a string from energised strings.
    (b) Energise the WT transformers from the energised strings.
    (c) Synchronisation of the WTs.
5. Energisation of the off-shore substation.
6. Energisation of the export cable.
7. Energisation of the off-shore substation.
8. Power block delivery.

Moreover it can include the synchronisation to any external grid. A flow chart of black start operation procedure is shown in Fig. 3.3.

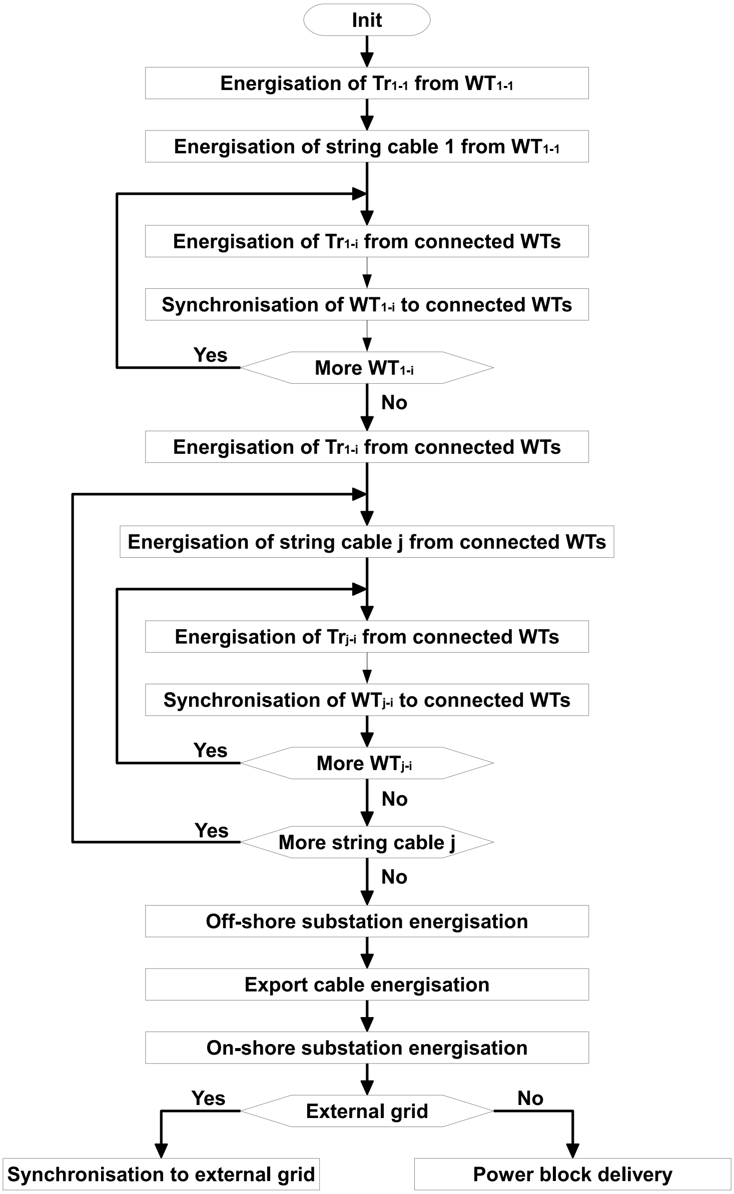

Figure 3.3: General control structure for modern wind distributed power-generation systems.

The most challenging issues during black start procedure are the energisation of substations, the energisation of the export cable, and the synchronisation to any far away grid that can produce instabilities if the WPPs controller is not properly tuned.

3.2.4 Transformer energisation

The substation energisation for HVAC systems as the shown in Fig. 3.1 consists of the energisation of transformers and auxiliary loads. It is known that some issues appear in the energisation of transformers that may cause large in-rush currents and overvoltages [85]. The transformer core may saturate when a brusque change of voltage to it is applied. The transformer absorbs magnetization current when it is saturated.

Moreover, when a transformer is energised from a grid with other transformers a sympathetic interaction may appear. Sympathetic interaction has been identified for parallel connection or for series connection as presented in [86]. In the scenario shown in Fig. 3.1, the series connection appears as the on-shore substation is energised when the transformer of the off-shore substation is working.

The re-energisation of transformers also shall be considered because in this case the initial fluxes of the transformers may not be zero, so it is a case study that can reduce the effectiveness of the in-rush current mitigation techniques.

The main solutions to mitigate the in-rush current are based on the installation of pre-insertion resistors (PIR) and the use of independent-pole breaker controlling the instant to close each pole known as point-of-wave (POW), but there are other alternatives.

1. **Use of Pre-insertion Resistors in the Circuit Breaker Energizing the Transformer**:

   The use of pre-insertion resistors can mitigate the in-rush currents during the transformer energisation. The main problem using this technique to mitigate the in-rush current is the required area for the resistor because large resistors use to be required.

   Furthermore, the resistor value and the resistor bypassing time shall be well select to achieve properly mitigation of the in-sush current.

2. **Use of Point-Of-Wave Circuit Breaker Energizing the Transformer**:

> Using point of wave the in-rush current can be almost deleted, at least theoretically. This technique requires a single pole operation breaker. Closing a pole of the breaker at the maximum voltage phase, and the other two poles 1/4 cycle later the inrush current can be almost deleted. The main problem of this technique is that the breaker open/close each pole using a mechanical system and the time between the command to close the breaker pole and when it occurs may vary for each pole. Moreover, a not properly maintenance may produce a completely uncordinated pole close.

Fig. 3.4 shows current during the energisation of a 460 MVA transformer. The results show the energisation current without any in-rush current mitigation technique, using pre-insertion resistors and using point-of-wave. The transformer has been energised from an 66 kV ideal source. As the figure shows, using any mitigation techniques the overcurrent is avoided. Using point-of-wave technique the obtained result seams to be better, but no error at the closing breaker pole has been introduced, so the in a real transformer energisation using point-of-wave error in the instant of close eache pole shall be considered.

There are another techniques to mitigate the in-rush current during the transformer energisation. Some of them are listed:

- Adjusting the On-load Tap Before Energizing the Transformer.
- Reducing the System Voltage Before Energizing the Transformer.
- Energizing the Transformer using Air-break Disconnect Switches.
- De-fluxing the Transformer Core Before Energization.
- Inrush mitigation strategy based on a pre-insertion neutral resistor. This technique is however restricted to star grounded transformers.

3.2.5 Export cable energisation

Energisation of long HVAC cables is challenging, due to overvoltages during cable energisation, current zero-missing, parallel resonances between cables and shunt reactors, Ferranti effect and more [87].

1. **Ferranti Effect**: It is the increase in voltage occurring at the receiving end of a long AC cable when the load es very small or no load is connected. The capacitive behaviour of the cable produces this effect.

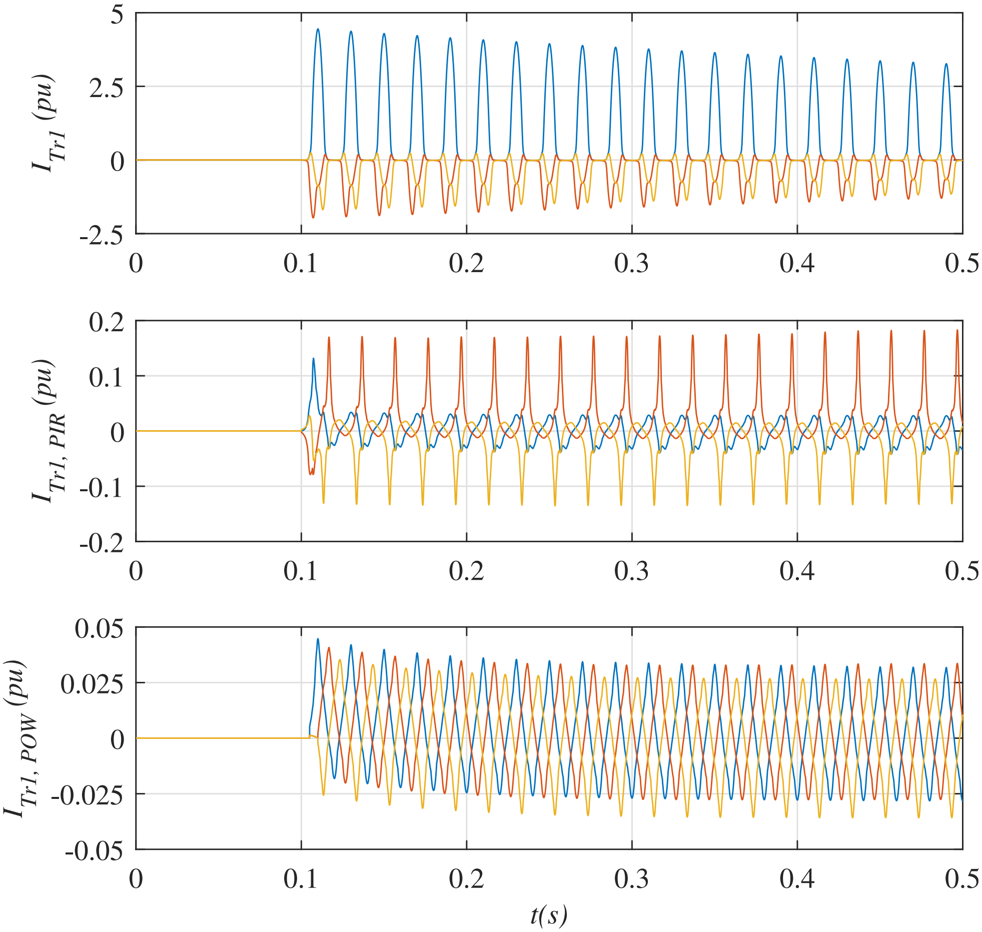

Figure 3.4: Current during the transformer energisation: (a) closing the three poles of breaker at the same time; (b) using pre-insertion resistors; (c) using point-of-wave to close the breaker poles.

2. **Overvoltages during the Cable Energisation**: The cable energisation may originate a transitory overvoltage depending of the instant that the cable is connected. The overvoltages will be maximum if the cable is connected at the peak voltage, and minimum if it is connected at zero voltage.

3. **Zero-missing of currents during the Cable Energisation**: In order to minimize losses, cables shall be compensated using shunt reactors connected in parallel. The problem is that zero-missing of currents may occur during

the energisation of the cable if the reactive power of the cable is compensated more than 50% using shunt reactors. The zero-missing phenomena may open the poles of a circuit breaker. In case of any fault, the effect prevent hazardous.

4. **Transformer inrush currents**: The overvoltages produced during the cable energisation can saturate transformers of the grid. The harmonic content of the inrush currents will be propagated to the cable producing a non desired voltage and current transitory.

In order to avoid those problems, the next shall be considered:

- The level of compensation of the cable shall be considered before cable energisation.
- The use of pre-insertion resistors may reduce the overvoltages during cable energisation.
- The use of point-of-wave circuit breakers with independent control pole may reduce overvoltages during cable energisation.

3.3 Diode Rectifier-based Wind Power Plants

3.3.1 Control Strategies

This section includes a revision of published control strategies for HVDC diode rectifier connected WPPs.

The first control strategy for this purpose was proposed in [12] and is shown in Fig. 3.5 and Fig. 3.6. As shown in both figures, this control strategy controls the system in dq frame, and allows to control the PCC voltage, the PCC frequency and the current of each WTG. The voltage at PPC_F (see Fig. 3.5) permits to control the active power using the voltage amplitude V_{Fd}, and the grid frequency ω_F using the current I_{Wq}. The voltage control consist of a proportional distributed loop and an integral centralised loop. Moreover, the distributed control allows to limit each WTG power production depending of the available wind. The centralised integral loop ensures that the voltage reference is followed during islanding operation and is not active during normal operation.

The main problem of this control strategy is that the voltage that controls each WTG is the same (V_F in Fig. 3.5). That voltage is not a local measure of each WTG, so high speed communications might be required. Another problem to consider is that the voltage angle is obtained using a polar transformation from the measured voltage. Voltage disturbances are transmitted to the voltage angle. It can produce undesired distortion in the off-shore grid voltage.

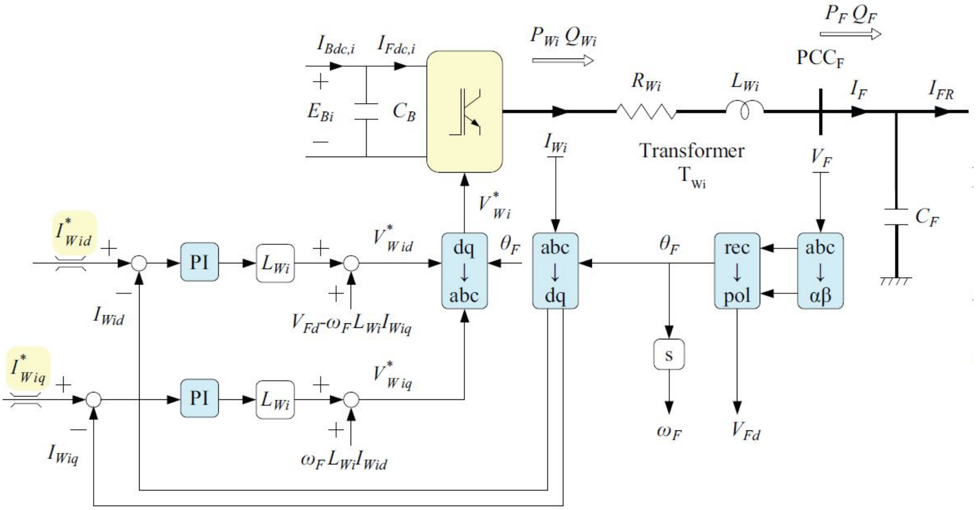

Figure 3.5: Control Scheme 1: Offshore I_{Fdi} and I_{Fqi} current control loops [12].

Another proposed control strategy is shown in Fig. 3.7 that was proposed in [88]. In this control strategy, the voltage and the current loop are in $\alpha\beta$ frame. Both positive and negative sequence are controlled using resonant controllers [89]. Moreover, this control strategy includes P/ω Q/V droop control in order to improve the power sharing between WTGs. In addition, a centralised controller is included to control the transmitted power by the diode rectifier and to control the active and reactive power of any ac grid connected to the off-shore grid. The main problem of this control strategy is that requires communications to control the WPP power transmission.

In [90], another alternative was proposed. This alternative includes a distributed PLL to synchronise each WTG with the ac grid. Moreover, the proposed control strategy controls the negative sequence of the current, the active and the reactive power and the frequency. Some functions to provide fault-ride through are included. Using PLLs to synchronise WTGs during the connection tu any grid is required, but during the normal operation WTGs can maintain synchronised just with the active and reactive control, so the PPL introduce complexity and a instability source to the control strategy [91, 92].

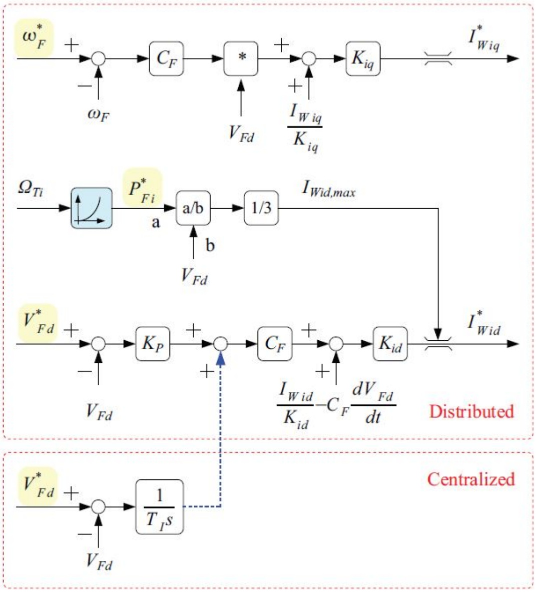

Figure 3.6: Control Scheme 1: Offshore ac-grid voltage control [12].

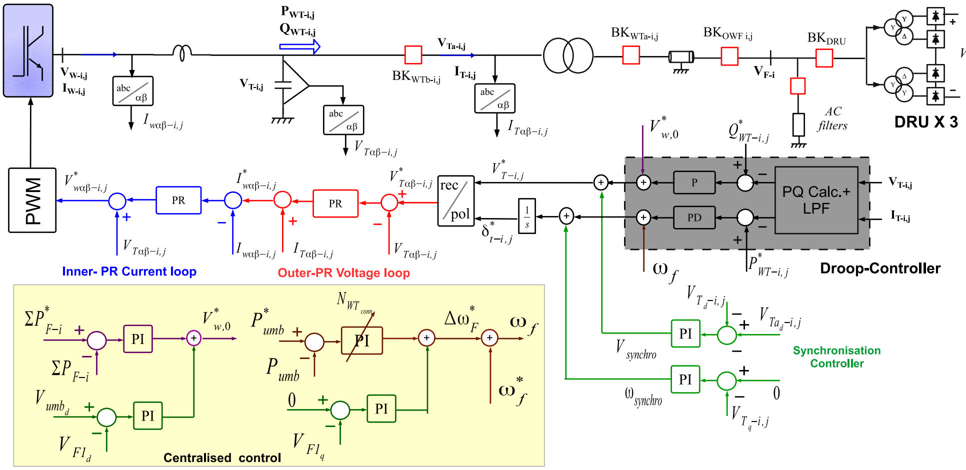

Figure 3.7: Control Scheme 2: Grid forming control [88].

Furthermore, other control strategies have been proposed. A stable operation in AC and DC mode including a smooth transition between modes was presented in [94]. The proposed control calculates a voltage magnitude and a voltage phase

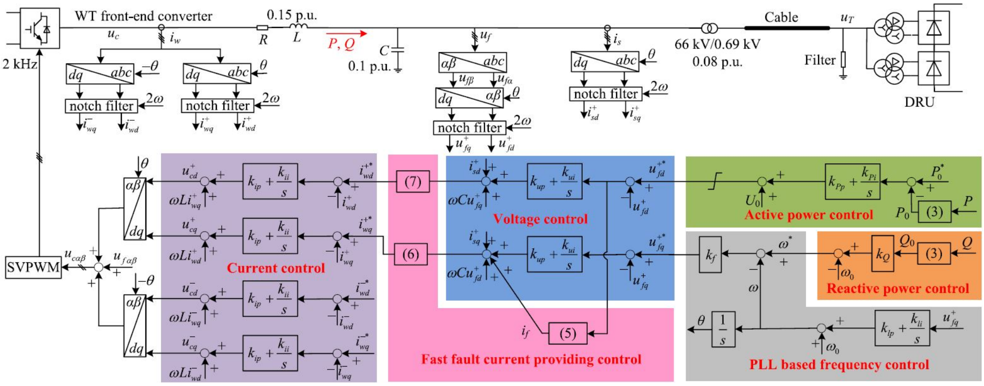

Figure 3.8: Control Scheme 3: Offshore I_{Fdi} and I_{Fqi} current control loops [93].

increment to control the power of each WTG and to maintain the voltage and frequency of the off-shore ac-grid. The authors present the functions that the control strategy shall include, but implementation of the solution is not presented. A fault-ride-though strategy is neither included.

The use of a fixed reference system synchronised via GPS time in all grid connected inverters was proposed in [95]. This purpose requires an onshore auxiliary converter that maintains the off-shore ac-grid stable when the WPP is not producing power. The on-shore auxiliary converter is connected to the off-shore ac-grid throug an umbilical cable. In this solution, the WTGs do not have the capability to work in island mode, nor they have self start capability (on-shore auxiliary converter required).

In [96] a decentralised reactive power control that acts on the off-shore frequency is proposed. The authors identify a frequency deviation using its control strategy that is solved using a master control implemented in one of the WTGs that send an increment of Vq to the other WTGs. This solution requires fast communication between WTGs.

None of the proposed controllers have been validated working in parallel with any grid following WPP.

3.3.2 Diode Rectifier-based Wind Power Plant Integration

Point to Point HVDC grids

There are different alternatives to integrate Diode Rectifier-based WPPs. The first of them was proposed in [12, 13] for a point to point HVDC grid. It proposes the use of an on-shore LCC converter to connect the Diode Rectifier-based WPP to the main grid. Moreover, a significant reduction of the HVDC rectifier filter banks was proposed if WTGs with fully rated converters are used.

As shown in Fig. 3.9, the use of on-shore MMC converters was proposed in [97, 14], including a technical feasibility study. Additionally, the development and validation of a dynamic model suitable for control design and stability analysis was proposed in [98].

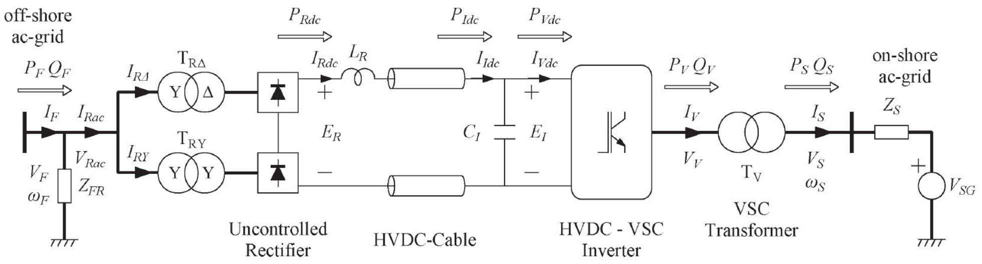

Figure 3.9: HVDC link (uncontrolled rectifier and VSC inverter) and onshore ac grid [14].

Another purpose is the proposed in [99], that increase the frequency of the off-shore ac grid from 50 to 100-400 Hz that allows the reduction of the off-shore transformer size. The main problem is how the off-shore equipment shall be modified in order to operate as expected, and cables need to be overdimensioned due to increased capacitive currents and increased skin effect, which reduces effective cable section.

In [100] a STATCOM with active filter function is included in the off-shore ac grid to remove the diode rectifier filters. In [101] a reactive power balance at the DR station is used to control the frequency. The main problem is the cost increase in comparison with the passive filters of the diode rectifier.

Multi-terminal HVDC grids

The use of diode rectifier for the power plants integration in multi-terminal HVDC grids was proposed in [79]. Moreover it defines the operation mode of each connection of the HVDC grid. It defines that just one of the connections shall woks as a voltage source to maintain the voltage of the HVDC grid ans the others shall work as current sources.

The application for diode rectifier-based WPPs was proposed in [102] as Fig. 3.9 shows. It proposes the integration of a diode rectifier-based WPP in an existing point to point HVDC grid with two MMCs. In this configuration one of the MMC works as a voltage source and the diode rectifier-based WPP ans the second MMC work as current source. Moreover the the detailed modeling and small-signal stability analysis for a multi-terminal HVDC system that includes diode rectifier-based WPP is proposed in [103].

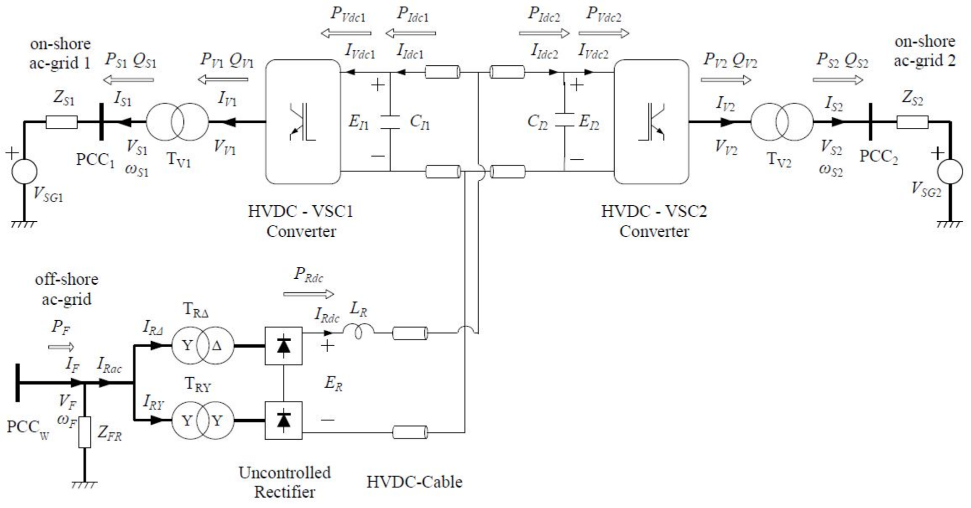

Figure 3.10: Multi-terminal HVdc link consisting of two VSC inverters and a off-shore WPP connected through an uncontrolled rectifier [102].

Considering the benefits of using diode rectifier-based WPPs in the integration of off-shore WPPs, this system was studied in the European's project PROMOTioN. In [104] the system shown in Fig. 3.9 is also studied. Moreover, it is extended to a system including 3 MMCs and 1 diode rectifier-based WPP.

Other Diode Rectifier based Wind Power Plant Integration Solutions

The use of diode rectifier based WPPs requires grid forming WTGs. In order to avoid the use of grid forming WTGs and reduce the cost of an off-shore MMC some solutions has been proposed. The connection of a MMC in serie with a 12-pulse diode rectifier for the HVDC link of a WPP was proposed in [105]. That configuration is shown in Fig. 3.11. This configuration reduces the power losses of the converter and allows to control the active power transmitted by the diode rectifier controlling the off-shore ac grid voltage and the HVDC voltage from the MMC. The problem is that the WPP just can transmit power if the MMC is in operation, and the solution is to use grid forming strategy for the WTGs. Moreover, if there are any fault in the diode rectifier the HVDC voltage will be halved.

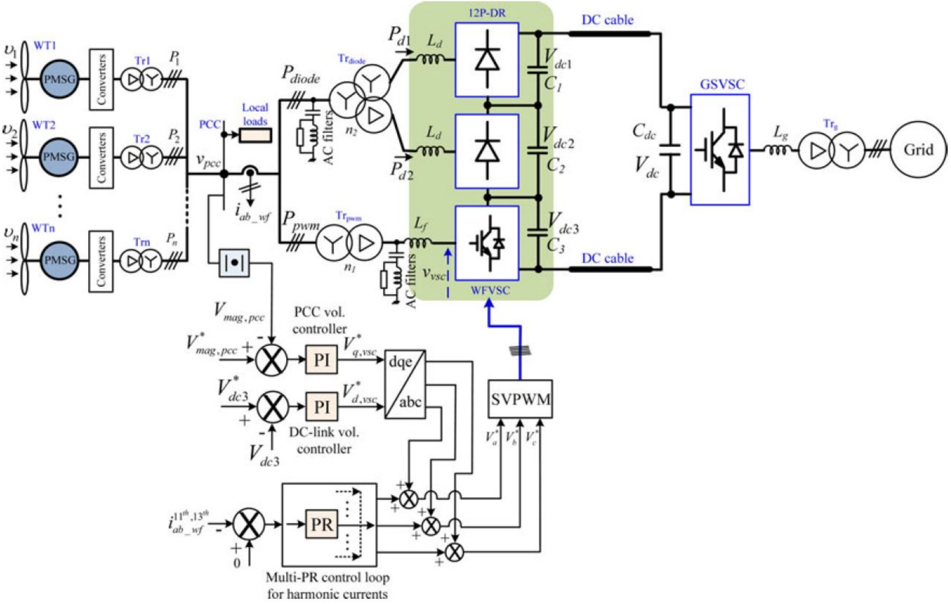

Figure 3.11: Single-line diagram and control scheme of the proposed HVDC link for integrating the off-shore WPP with the grid [105].

In [106] a similar solution was proposed, but in this case two diode rectifiers are connected in series with the MMC. The authors also use the MMC to compensate the ripple of the current that diode rectifiers introduce to the HVDC grid. It means the use of smaller dc inductors. The proposed solution is validated in a reduced power setup. In any case, it presents the same problems described above.

Using the same configuration, [107] includes a thyristor valve at the dc side of the MMC to prevent potential overcharge during faults. Moreover, it validates the operation during faults, although the presented dc current values during faults (up to 6 pu) requires oversizing of diode rectifier converters and MMCs.

A parallel connection of the MMC and the diode rectifier is proposed in [108]. It allows the proper energisation of the WPP and reduce harmonics that the diode rectifier produce. Moreover, the parallel connection of both converters reduce the installation cost in comparison with a full power MMC converter.

In any case, the majority of the active power is transmitted through the diode rectifier as it has lower losses then the MMC. Moreover, the MMC includes active filter function that allows the dc and ac filter bank reduction. However, this alternative is too complex and voids the use of a simple diode rectifier.

3.4 Conclusions

This chapter presents two applications of grid forming WPPs. The first of them is the *black start operation for HVAC grids from WPPs.* The current grid codes, as entso-e NC RfG, National grid ESO or ELIA, are presented to analyse the defined operational and stability requirements. Additionally, the operational and stability requirements proposed in PROMOTioN project [10] have been taken into account.

Moreover, a black start operation procedure has been presented. The energisation of big transformers and the energisation of long HVAC cables has been considered as the most challenge issues that may appear during the black start operation. Even though some previous researchers studied black start operation using grid forming WPPs, none of them considered the black start operation from a mixed grid forming and grid following WPP. Including the study of the percentage of grid forming in the WPP and the strategies for the contribution to the procedure of the grid following WTGs.

The second presented application of grid forming WPPs is the *diode rectifier-based WPPs.* A background about its integration in HVDC grids has been presented. The main grid forming control strategies proposed for diode rectifier based WPPs have been considered. All of them are based on cascade control loops that controls the current as faster loop in order to limit it, a voltage loop, and any kind of droop control or similar. Moreover, some of the presented control strategies include centralised control, so that control strategies requires communication between

WTGs and the centralised controller (the communication velocity depends of the required dynamics of the control system).

Additionally, the proposed configurations to integrate diode rectifier based WPPs are listed. It includes the integration of off-shore WPPs using on-shore LCC or MMC converters, the integration in MMC mult-terminal HVCD grids, and the use of diode rectifiers in serie or in parallel with MMC in order to reduce the cost of the off-shore substation based on a full MMC converter.

All the proposed control strategies for the integration of diode rectifier based WPPs consider that all the WTGs of the WPP have the same controller. Mixed grid forming and grid following WPPs shall be considered because new grid forming WPPs may be built near to any grid following WPP and diode rectifier based HVDC link is an attractive for the power transmission to on-shore.

Moreover, the integration of diode rectifier-based wind power plant in meshed HVDC grids shall be considered because it means an important cost reduction while the robustness of the system is enhanced. Additionally, the grid forming WPP may help in the recovery of the system after faults reducing the requirements of dc circuit breakers.

Chapter 4

Conclusions

This chapter presents the conclusions of this PhD dissertation, its contributions and the proposed future research for grid forming WPPs and Diode Rectifier HVDC connection of WPPs.

4.1 Research gaps

Grid forming Control strategies for diode rectifier connected WPPs and black start operation.

- There are various power sharing controller for the parallel connection of VSCs that allows islanded operation. The power sharing is achieved using the well known *Droop Control* that shares the active and reactive power with increments in the operational voltage and frequency, the *Virtual Synchronous Machine* that emulates the behaviour of a synchronous generator, the *Matching Control* that is based on the equation similarities between a synchronous generator and a VSC, or the *Dispatchable Virtual Oscillator Control* that is based on the nonlinear dead-zone oscillator model.

- The main grid forming control strategies have been described. Those control strategies use models based on synchronous reference frame (dq) and models based on stationary reference frame ($\alpha\beta$). A current loop use to be included in order to provide fault ride through, though reference conditioning is also used with the same purpose and allows to not include the current loop.

- The grid forming controllers shall include fault ride through capability. It shall includes a current limitation to save the power electronics converters and a recovery strategy to achieve a fast grid recovery considering the grid codes. Then, considering the current limitation strategies as to include a current loop or a reference conditioning to maintain the current within its limits, grid forming controls with better performance that the achieved using a classical PID control shall be studied.

- The stability analysis of grid forming WPPs is required during the design phase. The eigenvalue-based stability can be used for the analysis and allows to detect what is causing instabilities or low damping in a system. Moreover, it is also valid for mixed grid forming and grid following WPPs.

Type-4 WPP aggregation.

- The use of aggregation techniques for WPPs is a tool that can help during the design phase of WPPs. Using aggregated WPPs allows the time reduction of the simulation studies. Moreover, hardware-in-the-Loop controler validation as well as Power-in-the-Loop validation of some parts of the system becomes necessary in order to detect mistakes during the design process that can cause an increment cost in the WPP commissioning process. In large WPPs, the use of aggregated models is compulsory to achieve real time simulations required for that tests.

- There are some alternatives to aggregate WPPs. Each of them was presented in the literature with different purpose. In any case, all of them presents some errors in the aggregated models in comparison with the frequency response of the detailed WPP.
- The study to carry out will determine the level of aggregation that can be used in order to not miss desired information about the WTG behaviour.

Black start procedure from WPPs.

- WPPs with grid forming capability are able to carry out black start operation. The main European grid codes have been analysed to define the operational and stability requirements that shall satisfy a WPP.
- The main issues during the black start procedure have been identified, considering the energisation of large transformers and long ac cables as the most challenging issues. The grid distortion produced during the energisation of transformers and ac cables may be reduced using preinsertion resistor or breakers that allows point-of-wave.
- Mixed grid forming and grid following WPPs allows to carry out black start operation. The percentage of required grid forming is determined by the loads that will be connected during black start operation. Then, the grid required power could generated by the grid following WTGs to liberate the grid forming WTGs for the connection of other loads.

Integration of Diode rectifier based WPPs.

- The use of diode rectifier may be combined with MMCs in order to reduce the investment cost of the MMCs. In any case, if the WPP has grid forming capability, the use of just Diode rectifier for the connection of the WPP to any HVDC grid will reduce the investment cost in comparison with any combination of MMC and diode rectifiers.
- Diode rectifier based WPPs may be integrated in point-to-point grids or in multi-terminal HVDC grids. In both case, the contribution of the grid forming WPP during faults can reduce the protection equipment cost.
- WTGs are able to detect faults on the HVDC grid without communications. It allows the design the protection strategies with the contribution of the WPP.

- Mixed grid forming and grid following WPPs is a good option to convert some of WTGs that are in operation in WPPs. It can provide grid forming capability to the WPP with just a software update.

4.2 Contributions

The contributions of this PhD dissertation are the following:

- A WPP aggregation method has been proposed based on a multiobjective optimization technique. It achieves to reduce the error between a detailed model and an aggregated model up to 10% in comparison with the aggregation techniques presented in the literature.
- A procedure for the design of grid forming controllers using $\mathcal{H}_\infty$ synthesis has been proposed. It includes resonant behaviour for the voltage loop. Moreover, it achieves better performance and robustness than the achieved using controllers based on PI. An harmonic reduction is also achieved as the total harmonic distortion analysis of the current and the voltage shows.
- The controller design and stability analysis of grid forming WTGs that works in parallel with grid following WTGs have been proposed. The operation of mixed grid forming and grid following off-shore WPPs with diode rectifier link to HVDC grids has been validated for normal and fault operation. Moreover, in the case of there is not enough wind in grid forming WTGs, the operation is guaranteed because the grid forming WTGs can works as an statcom.
- A fault recovery procedure for WTGs after faults has been proposed. Communications are not required, so a fast and controlled grid recovery is achieved.
- A black start procedure from an off-shore WPP that is connected to on-shore with an HVAC cable is defined. The WPP may consist of grid following and grid forming WTGs. The black start operation is achieved using a 24% of grid forming power.
- The use of a diode rectifier based WPP to reduce the protection equipment cost in a multi-terminal HVDC grid has been proposed and validated. It achieves to reduce the required power of the dc circuit breakers. The WPP is able to detect faults on the HVDC grid without communications, so the WPP can contribute to reduce the voltage to clear the dc fault, and then to resume the normal operation. If communications are considered, the WPP

may ensure that the remaining converters connected to the HVDC grid continue exporting the same power they were delivering before the fault.

4.3 Future Research

The work done during this PhD dissertation may be continued with the following tasks:

- Proposals for grid forming control design in order to ensure stability with large degree of uncertainty considered. The uncertainty shall consider changes of the grid structure, as well as the connection of unknown active elements.
- Study of fault ride through strategies when WTGs of a WPP are controlled using a distributed controller (one controller that controls all the WTGs).
- The design of distributed control strategies for WPPs considering the available fast communications. Using just a centralised controller is possible to control all the WTGs of a WPP. It may mean a performance increment of the WPP in any operation carried out in a WPP.
- The study of the ratio of grid forming to grid following in a WPP to ensure stability and to ensure the capability to carry out some operations such as black start.
- Control strategies that estimate in-rush currents during the black start procedure and achieves a fast mitigation of the in-rush current.
- New functionality proposal for diode rectifier WPPs in order to reduce the required protection equipment in point to point and multi-terminal HVDC grids.

Chapter 5

Small-signal stability and fault performance of mixed grid forming and grid following offshore wind power plants connected to a HVDC-diode rectifier

Note: this chapter proposes a controller design procedure for mixed grid forming and grid following diode rectifier based WPPs. It includes the small-signal stability analysis and a fault performance study. The chapter contents are published on:

Martínez-Turégano, Jaime; Añó-Villalba, Salvador; Bernal-Perez, Soledad; Peña, Ruben; Blasco-Gimenez, Ramon. (2020) Small-signal stability and fault performance of mixed grid forming and grid following offshore wind power plants connected to a HVDC-diode rectifier. IET Renewable Power Generation - . 10.1049/iet-rpg.2019.1264

Abstract

This paper aims at validating the simultaneous operation of grid following and grid forming wind power plants when connected to a common Diode Rectifier based HVDC link. The controllers for both grid forming and grid following wind turbines include fault-ride-through capability with soft restoration of the off-shore ac-grid. Current and voltage controllers are developed in the stationary $\alpha\beta$ reference frame. The presented control and soft restoration strategies are based on local measurements only and do not require communication between wind turbine generators. The small signal stability analysis of the mixed system in multiple d-q axis using detailed string models is carried out in order to show the sensitivity to grid following PLL gains and to grid forming droop gains. Interoperability between grid forming and grid following wind turbines during transients is shown by means of detailed simulation during symmetric faults in different locations of the off-shore grid.

5.1 Introduction

The use of HVDC Diode Rectifier (DR) stations has been proposed by the authors as a technical solution for a significant cost reduction for the grid connection of distant off-shore wind farms (OWFs), while increasing the efficiency and robustness of the overall system [11, 12, 13, 14, 15]. It is claimed by Siemens that the use of HVDC diode rectifier stations can lead to up to a 30% cost reduction for the electrical connection of large off-shore wind power plants (WPP) [6, 109].

However, as the DR station is a passive converter, wind turbine generators (WTGs) are required to create the off-shore ac-grid, and control the power delivered through the HVDC link. Several control strategies have been proposed to such avail [11, 12, 13, 105, 6, 109, 90, 93, 110, 81]. These grid forming control strategies for DR connected WTGs are based on the fact that off-shore ac-grid voltage is effectively capped by the HVDC-link voltage when the diode rectifiers are conducting and also on the fact that off-shore ac-grid frequency has a strong dependency on the reactive power delivered by the WTGs due to the large system capacitance from cables and capacitor banks [11].

Current industrial standard WTGs are grid following and hence cannot be used directly for diode rectifier (DR) connection. Solutions allowing operation of standard WTGs with a diode rectifier connection are of particular industrial importance, as it would allow the DR connection of existing certified grid following WTGs from different manufacturers. In [105], a series connection of the Diode

Rectifier and a voltage source converter for the HVDC-link has been proposed which allows the use of standard WTGs, at the expense of needing additional equipment. The connection of standard grid following WTGs to Line Commutated Converters (LCC) is also shown in [111], however this solution required an additional STATCOM and a controlled LCC rectifier.

None of the previous published work addressed the issue of joint connection of grid forming and grid following wind turbine generators (WTGs) to HVDC Diode Rectifier stations. To validate the technical feasibility and interoperability of the HVDC DC connection of mixed grid forming and grid following OWFs, this paper includes the small signal stability and fault-ride-through performance of the proposed system. The study of such a system has been carried out by means of detailed PSCAD simulations.

The proposed control strategy for both grid forming and grid following WTGs does not require communication for normal and fault operation. Moreover, the presented strategy shows an excellent behaviour of the complete system during off-shore ac-grid short-circuits, again, without requiring communication between WTGs.

This paper is organized in four sections and includes the description of the system to be analysed, a description of both grid forming and grid following control strategies, the stability analysis of the detailed system, a fault-ride-through study and the corresponding discussion and conclusions.

5.2 System Description

Fig. 5.1 shows the diagram of the complete system, based on the distributed Diode Rectifier Station proposed in [6]. Therefore, three 400 MW off-shore wind power plants have been considered, connected via a diode-based HVDC link to a full-bridge on-shore Modular Multi-level Converter (MMC). Each OWF consists of fifty Type-4 8 MW rated WTGs. Each OWF is modeled by considering one detailed string of 9 WTGs, whereas the rest of the strings are modeled by using an aggregated wind turbine for each string, as shown in Fig. 5.1. WTGs have been aggregated as per [112]. Therefore, the considered system shows a great level of granularity, so results can be obtained at the wind turbine and string levels, at a reasonable computational cost. Wind turbine transformer models consider saturation.

The DR converter consists of six 12-pulse diode rectifier units (DRU) of 200 MW each, parallel connected on the ac-side, series connected on the dc-side and dis-

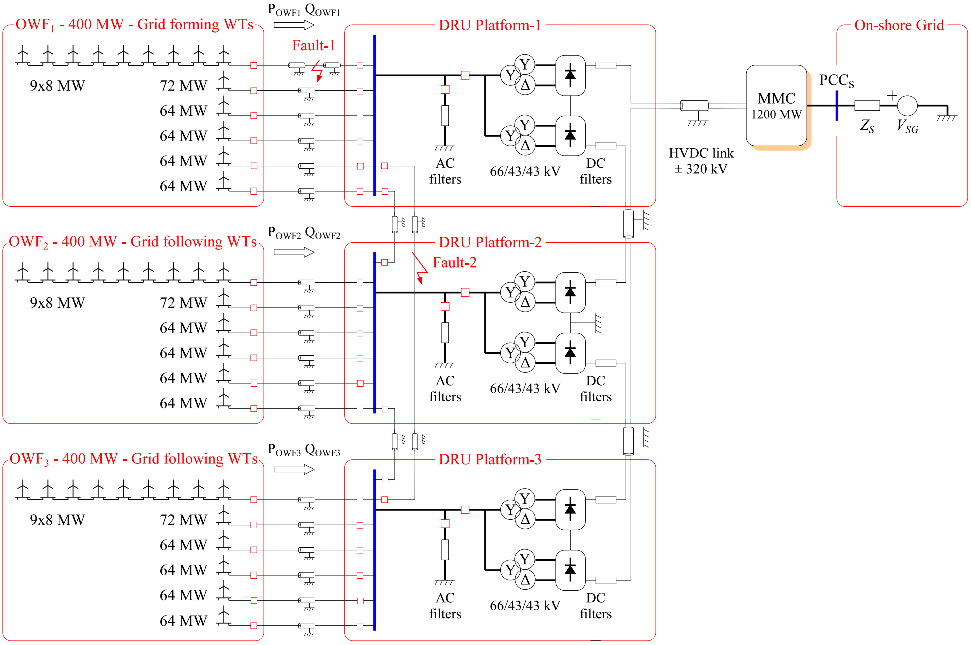

Figure 5.1: OWFs connected to the on-shore ac-grid via a diode-based HVDC link. Grid forming WTGs: OWF$_1$; grid following WTGs: OWF$_2$ and OWF$_3$.

tributed in three platforms [6], albeit the installation in a single platform is also possible.

In this topology, each off-shore wind farm OWF-i ($i = 1, 2, 3$) is connected to the corresponding DRU platform-i. An ac-ring bus connects the ac-side collector buses of the three DRU platforms. Each platform includes the corresponding ac and dc filters. The ac-grid is modelled using lumped π-parameters.

In the considered system, OWF$_1$ consists of DR-capable grid forming WTGs, whereas OWF$_2$ and OWF$_3$ consist of standard grid following WTGs.

The HVDC submarine cable connects the dc-side of the DRU platforms to the on-shore MMC converter, which exports the energy to the on-shore ac-grid. The HVDC cable is modelled using a distributed model with frequency dependent parameters. The grid forming WTGs could be used for black-starting the complete system provided that the WTG has an energy storage system that allows the WTG to yaw to the wind and that there is enough wind to compensate system losses.

System parameter values are shown in the Appendix 1.

5.3 Control Strategy

This section presents the proposed control strategies for DR-enabled grid forming and traditional grid following WTGs. Both control strategies are implemented as decentralised controllers using only local signals for feedback. Therefore, communications between WTGs are not required (other than general wind farm controller communications). Moreover, both control strategies include fault-ride-through capability.

The on-shore MMC controls the dc-voltage of the HVDC link and the reactive power injected to the on-shore ac-grid, albeit the MMC responses are not analyzed in this paper.

Control parameter values are shown in Appendix 1.

5.3.1 Grid Following Wind Turbines

Fig. 5.2 shows the control strategy used for the grid following WTGs (blocks labeled (1) and (2) are part of the fault-ride-through strategy and are described in section 5.5.1). The grid following control consists of standard cascaded control loops, the inner loop controlling active and reactive currents (I_{W_d}, I_{W_q}), whereas the outer loop controls the back-to-back converter DC-link voltage (E_B) and the WTG reactive power (Q_{WT}) [89]. A PLL is used to provide grid synchronization. Additionally, the control strategy includes a fault detection algorithm for fault-ride-through operation using the grid admittance Y_T seen by the WTG. A more detailed description of the controllers is included as follows.

Current Control

Standard P+R $\alpha\beta$ stationary frame current controllers have been used for both grid following and grid forming controllers (Figs. 5.2 and 5.3):

$$V_{W\alpha\beta} = R_W I_{W\alpha\beta} + L_W \frac{dI_{W\alpha\beta}}{dt} + V_{C\alpha\beta} \tag{5.1}$$

where L_W and R_W are the parameters of the choke in Fig. 5.2, V_W is the voltage applied by the WTG inverter, and I_W is the current through the choke.

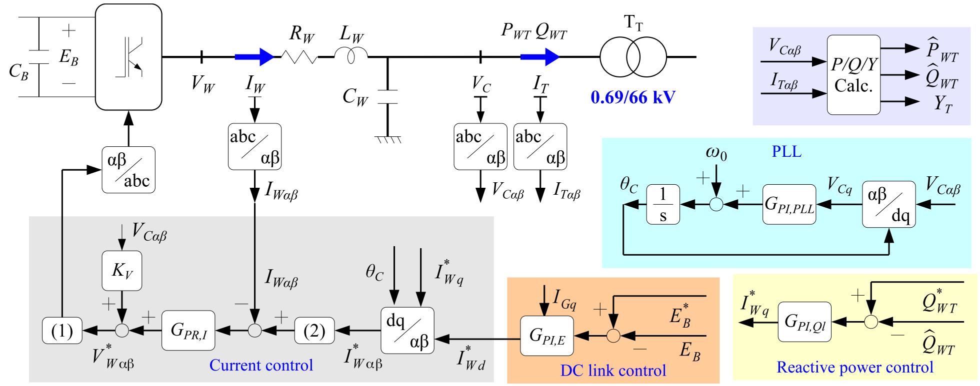

Figure 5.2: Control strategies for grid following WTGs.

From (5.1), the grid side converter current $I_{W\alpha\beta}$ is controlled by means of stationary frame proportional-resonant controllers (PR) with a weighed feed-forward voltage term. The weighted voltage feed-forward term improves controller performance, particularly during faults [89, 113]. The output of the regulator $V^*_{W\alpha\beta}$ is:

$$V^*_{W\alpha\beta}(s) = G_{PR,I}(s)(I^*_{W\alpha\beta}(s) - I_{W\alpha\beta}(s)) + K_V V_{C\alpha\beta}(s) \tag{5.2}$$

where K_V is the V_W feedforward gain and $G_{PR,I}$ is the current PR controller [114, 115]:

$$G_{PR,I}(s) = K_{P,I} + \frac{K_{R,I} \cdot s}{s^2 + \omega_0^2} \tag{5.3}$$

where $K_{P,I}$ and $K_{R,I}$ are the proportional and resonant parameters of the PR controller.

The PR controller has been designed by stationary frame transformation of an equivalent d-q PI controller based on the synchronous plant equivalent of (5.1) [89, 116]. The controller is designed in order to achieve a bandwidth of 180 Hz. Clearly, this bandwidth is compatible with the considered 4 kHz grid-side converter switching frequency.

DC voltage control

The DC voltage of the back-to-back converter of the WTG is controlled by the front-end converter. This controller calculates the direct current reference $I^*_{W_d}$. Neglecting R_W losses, dc-link voltage dynamics can be expressed as:

$$C_B \frac{d}{dt} E_B = \frac{3}{2\sqrt{2}} (m_{GSC} I_{W_d} - m_{MSC} I_{G_q}) \tag{5.4}$$

where C_B is the DC-link capacitance and m_{GSC} and m_{MSC} are the PWM modulation indexes for grid-side and machine-side converters, respectively.

The voltage controller is based on a PI regulator. The output of the regulator I^*_{Wd} is

$$I^*_{Wd}(s) = G_{PI,E_B}(s)(E^*_B(s) - E_B(s)) + \frac{m_{MSC}}{m_{GSC}} I_{G_q} \tag{5.5}$$

where $G_{PI,E_B}(s)$ is

$$G_{PI,E_B}(s) = K_{P,E_B} + \frac{K_{I,E_B}}{s} \tag{5.6}$$

PLL

The grid following controller includes a PLL in order to allow the synchronization of the WTGs to the ac-grid. Additionally, the PLL helps the WTGs to be synchronized during faults. The implemented PLL is based on the well-known SRF-PLL [90, 117, 118]. So, the phase angle of V_C is calculated as

$$\theta_C(s) = \left(\left(K_{P,PLL} + \frac{K_{I,PLL}}{s} \right) (0 - V_{Cq}(s)) + \omega_0 \right) \frac{1}{s} \tag{5.7}$$

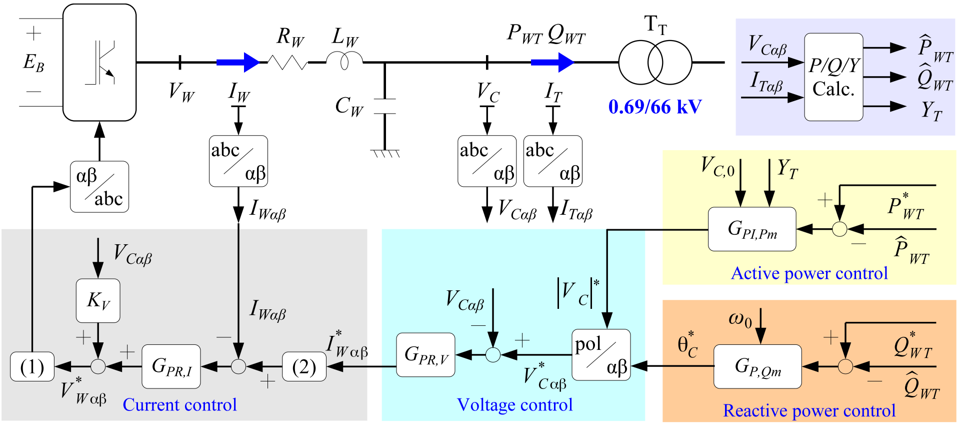

Figure 5.3: Control strategies for grid forming WTGs.

5.3.2 Grid Forming Controllers

Fig. 5.3 shows the control strategy used for the grid forming WTGs. The control strategy consists of cascaded controls for the wind turbine current I_W, ac-filter capacitor voltage V_C, and active and reactive powers P_{WT} and Q_{WT}. Additionally, the control strategy includes a fault detection algorithm for fault-ride-through operation using the grid admittance Y_T seen by the WTG. The description of the grid forming wind turbine controllers is included below.

Current Control Loops

The current control loops for the grid forming WTGs are exactly the same as the ones used for the grid following WTGs, i.e. PR controllers designed for a 180 Hz bandwidth including a weighted $V_{C\alpha\beta}$ feedforward term [89, 28].

Voltage Control

The wind turbine ac-filter capacitor voltage V_C dynamics can be expressed, in the stationary $\alpha\beta$ reference frame, as

$$C_W \frac{dV_{C\alpha\beta}}{dt} = I_{W\alpha\beta} - I_{T\alpha\beta} \tag{5.8}$$

Therefore, the voltage controller also is based on a PR regulator [89, 119]. The output of the regulator I_W^* is

$$I_{W\alpha\beta}^*(s) = G_{PR,V}(s)(V_{C\alpha\beta}^*(s) - V_{C\alpha\beta}(s)) \tag{5.9}$$

where $G_{PR,V}(s)$ is

$$G_{PR,V}(s) = K_{P,V} + \frac{K_{R,V} \cdot s}{s^2 + \omega_0^2} \tag{5.10}$$

The parameters of the voltage regulator have been obtained by designing a synchronous frame PI controller, aiming at a 40 Hz closed loop bandwidth, and transforming the parameters to obtain the equivalent stationary frame PR controller [89, 116].

Power Control

When the diode rectifier is conducting, the active power transmitted by the DRUs depends on the voltage levels of both off-shore ac-grid (V_{Fd}) and HVDC grid (V_{Rdc}) and on the equivalent impedance between these points, [120],

$$V_{Rdc0} - V_{Rdc} = \frac{3}{\pi} B\omega_0 L_{TR} I_{Rdc} + 2BL_{TR}\frac{dI_{Rdc}}{dt} \tag{5.11}$$

here $V_{Rdc0} = \frac{3\sqrt{6}}{\pi}BNV_{Fd}$, V_{Fd} is the off-shore ac-grid voltage magnitude, B is the number of rectifier bridges, N and L_{TR} are the diode rectifier transformer ratio and leakage reactance, respectively. In practice, the resistive term $R_{eq} = \frac{3}{\pi}B\omega_0 L_{TR}$ is relatively large, as the diode rectifier leakage reactance is around 0.18 pu.

Therefore, the active power sent by the OWF through the DRUs depends on the voltage levels of the off-shore ac-grid and the HVDC grid

$$P_{Rdc} = \frac{(V_{Rdc0} - V_{Rdc})\, V_{Rdc}}{R_{eq}} \tag{5.12}$$

A similar behaviour is shown in [25, 30] for a mostly resistive line impedance.

Therefore, a decentralized P/V PI control and Q/θ droop control is proposed:

$$|V_C^*|\,(s) = \left(K_{P,Pm} + \frac{K_{I,Pm}}{s}\right)(P_{WT}^*(s) - \widehat{P}_{WT}(s)) \tag{5.13}$$

$$\theta_C^*(s) = K_{P,Qm}(Q_{WT}^*(s) - \widehat{Q}_{WT}(s)) + \frac{1}{s}\omega_0 \tag{5.14}$$

The parameters of the active and the reactive power control are designed in order to achieve a bandwidth of 8 Hz. Active and reactive powers measurements are first order filtered, with a cut-off frequency of 314.16 rad/s ($\widehat{P}_{WT}$ and $\widehat{Q}_{WT}$ in Fig. 5.3).

5.4 Decentralised Control Analysis

The controllers have been tuned assuming aggregated converters, therefore, this section includes the analysis of the complete system dynamic model, including local synchronouos frames of reference and local controllers. The model is developed considering complex variables and includes the stationary frame model of the electric system and the α-β part of the controllers:

$$\dot{x}^{\alpha\beta} = Ax^{\alpha\beta} + Bu^{\alpha\beta} \tag{5.15}$$

The control input $u_i^{\alpha\beta}$ is not calculated in fixed coordinates, but rather in local synchronous coordinates alined to angle θ_i:

$$u_i^{dq} = u_i^{\alpha\beta} e^{-j\theta_i}; \qquad i = 1 \ldots m \tag{5.16}$$

where θ_i is the angle of the $i-$th frame of reference and m is the number of inputs.

The following rotation matrices are defined:

$$\begin{aligned} \Theta_u &= diag\left\{e^{-j\theta_1}, e^{-j\theta_2}, \cdots, e^{-j\theta m}\right\} && (5.17)\\ u^{dq} &= \Theta_u u^{\alpha\beta} \rightarrow u^{\alpha\beta} = \Theta_u^{-1} u^{dq} && (5.18) \end{aligned}$$

and:

$$\Theta = diag\left\{e^{-j\theta_1}, e^{-j\theta_1}, e^{-j\theta_2}, e^{-j\theta_2}, \cdots, e^{-j\theta m}\right\} \quad (5.19)$$

$$x^{dq} = \Theta x^{\alpha\beta} \rightarrow x^{\alpha\beta} = \Theta^{-1} x^{dq} \quad (5.20)$$

where one or more $\alpha\beta$ state variables are transformed to each dq frame. Therefore:

$$\dot{x}^{dq} = \dot{\Theta} x^{\alpha\beta} + \Theta \dot{x}^{\alpha\beta} \quad (5.21)$$

$$\Theta \dot{x}^{\alpha\beta} = \dot{x}^{dq} - \dot{\Theta} x^{\alpha\beta} \quad (5.22)$$

Transforming (5.15) to the new coordinates:

$$\Theta \dot{x}^{\alpha\beta} = \Theta A x^{\alpha\beta} + \Theta B u^{\alpha\beta} \quad (5.23)$$

$$\dot{x}^{dq} = \left(\Theta A + \dot{\Theta}\right) x^{\alpha\beta} + \Theta B u^{\alpha\beta} \quad (5.24)$$

$$\dot{x}^{dq} = \left(\Theta A \Theta^{-1} + \dot{\Theta}\Theta^{-1}\right) x^{dq} + \Theta B \Theta_u^{-1} u^{dq} \quad (5.25)$$

where $\Theta B \Theta_u^{-1} = B$ if all inputs are local and $\dot{\Theta}\Theta^{-1} = -j\Omega_l$. Ω_l is a diagonal matrix with its elements being the angular speed of each state dq-reference frame ($\omega_i = \frac{d}{dt}\theta_i$):

$$\Omega_l = diag\left(\dot{\theta}_1, \dot{\theta}_1, \dot{\theta}_2, \dot{\theta}_2, \ldots, \dot{\theta}_m\right) \quad (5.26)$$

Therefore:

$$\dot{x}^{dq} = \left(\Theta A \Theta^{-1} - j\Omega_l\right) x^{dq} + B u^{dq} \quad (5.27)$$

The local dqi synchronous frame control for each converter will be:

$$\theta_i = f_{\theta i}\left(x_{ci}^{dqi}, x_1^{dqi}, x_2^{dqi}, \ldots, x_{ni}^{dqi}\right) \quad (5.28)$$

$$\dot{x}_{ci}^{dqi} = f_i\left(\theta_i, x_{ci}^{dqi}, x_1^{dqi}, x_2^{dqi}, \ldots, x_{ni}^{dqi}, u_{refi}^{dqi}\right) \quad (5.29)$$

$$u_i^{dqi} = g_i\left(\theta_i, x_{ci}^{dqi}, x_1^{dqi}, x_2^{dqi}, \ldots, x_{ni}^{dqi}, u_{refi}^{dqi}\right) \quad (5.30)$$

where θ_i is the angle of the i-th dq reference framce, x_{ci}^{dqi} are the local controller states, u_{refi}^{dqi} are the local input references and $\left(x_1^{dqi}, x_2^{dqi}, \ldots, x_{ni}^{dqi}\right)$ are the local feedback state variables, which, as previously mentioned, are all expressed in the local dqi-frame.

5.4.1 Local d-q Controllers

The grid following PLL dynamics according to (5.28) to (5.30), consi-dering the filtering of V_{cqi}:

$$\begin{aligned} \dot{\theta}_{Ci} &= -K_{P,PLL}\widehat{V}_{cqi} - K_{I,PLL}x_{2i} + \omega_0 && (5.31)\\ \dot{x}_{2i} &= \hat{V}_{cqi} && (5.32)\\ \dot{\widehat{V}}_{cqi} &= -\omega_a\widehat{V}_{cqi} + \omega_a V_{cqi} && (5.33) \end{aligned}$$

Regarding the Grid Forming wind turbines, the P-V and Q-ω control droops using the filtered active and reactive power will be:

$$\begin{aligned} \dot{\theta}^*_{Cj} &= K_{P,Qm}(\dot{Q}^*_{WTj} + \omega_c\widehat{Q}_{WTj} - \omega_c Q_{WTj}) + \omega_0 && (5.34)\\ \dot{\widehat{P}}_{WTj} &= -\omega_c\widehat{P}_{WTj} + \omega_c P_{WTj} && (5.35)\\ \dot{\widehat{Q}}_{WTj} &= -\omega_c\widehat{Q}_{WTj} + \omega_c Q_{WTj} && (5.36)\\ \dot{x}_{3j} &= P^*_{WTj} - \widehat{P}_{WT} && (5.37)\\ V^*_{Cdj} &= K_{P,Pm}(P^*_{WTj} - \widehat{P}_{WTj}) + K_{I,Pm}x_{3j} && (5.38) \end{aligned}$$

where the i, j subscripts refer to grid following and grid forming WTGs, respectively, ω_a and ω_c are the voltage and power filter cut-off frequencies, x_{2i}, x_{3j} are auxiliary variables and $\widehat{V}_{cqi}$, $\widehat{P}_{WTj}$ and $\widehat{Q}_{WTj}$ are the corresponding filtered variables.

5.4.2 Small Signal Analysis

A small signal analysis is carried out to find up to which extent the design of local controllers is valid for the complete system and the sensitivity to PLL and droop gains. Due to the size of the system, a detailed grid forming string and a detailed grid following string, with 9 WTGs each, have been considered. This approach allows for the model to keep both intra-string and inter-string dynamics. The considered system has 370 states and has been linearised according to Appendix 2.

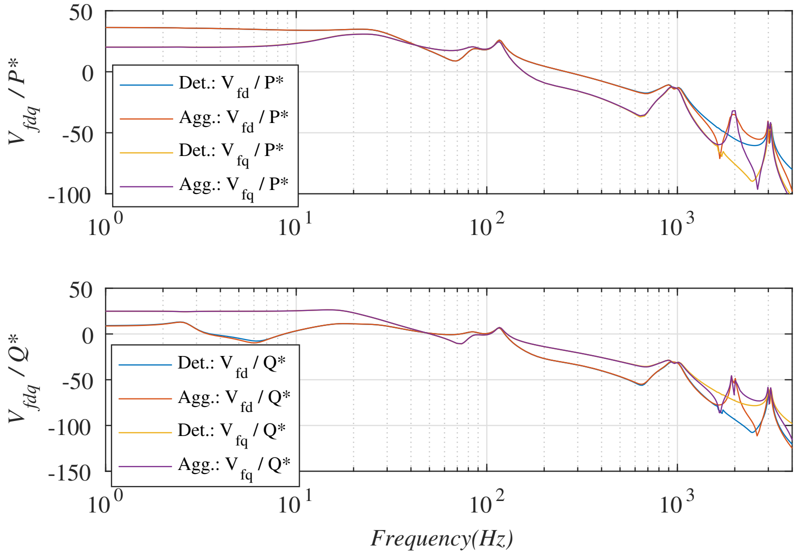

Figure 5.4: Frequency response from P^* and Q^* to the DR substation busbar voltage (V_f)

Response of aggregated and detailed systems

Fig. 5.4 shows the frequency response of the aggregated and detailed systems. The graph shows the frequency response from the active and reactive power references (P^*, Q^*) to the diode rectifier busbar voltage (V_f). In order to allow the comparison superposition principle has been applied to show the frequency response of the detailed string.

The frequency response shows that both the aggregated and detailed system have almost an identical response up to 1.2 kHz. The overall behaviour of both detailed and aggregated WTGs is very similar in the frequency range of interest, hence, a controller tuning based on aggregated WTGs will give a reasonable approximation to the dynamic response of the detailed system. Nevertheless, discrepancies do exist and a distributed control design should be used if the aggregated tuning does not lead to the expected performance.

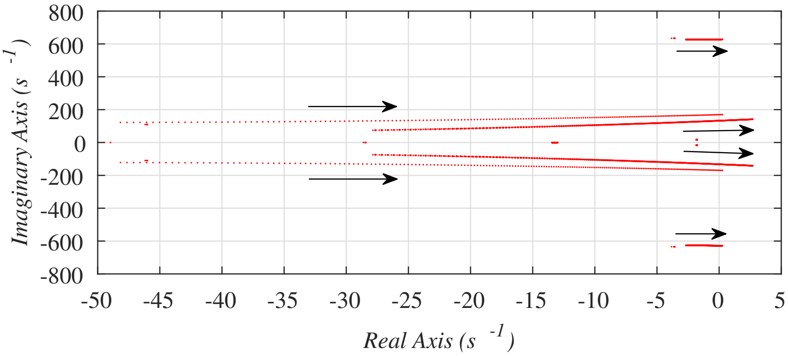

Figure 5.5: Root locus when $K_{I,Pm}$ increases from 105 to 630

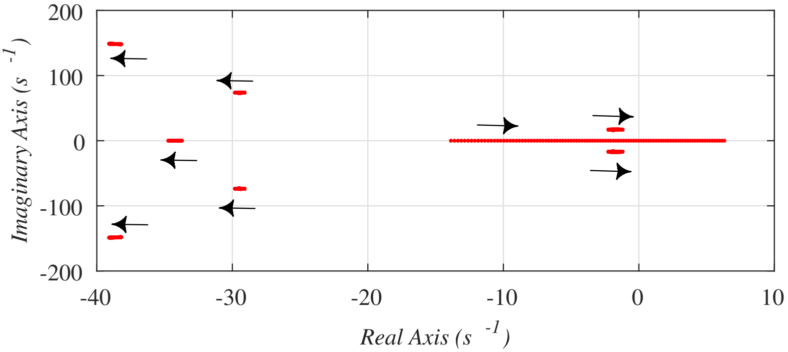

Figure 5.6: Root locus when $K_{P,Qm}$ increases from 1 to 1.375

Sensitivity to PLL and droop gains

Clearly, the grid forming Q-ω droop and the grid following PLL show a very similar structure [121], as their main purpose is grid synchronisation.

Therefore, figs. 5.5 to 5.7 show the sensitivity of the detailed grid forming and grid following system to changes in the corresponding PLL and droop gains $K_{I,Pm}$, $K_{P,Qm}$ and $K_{I,PLL}$.

Fig. 5.5 shows how the position of the dominant poles when $K_{I,Pm}$ increases from 105 to 630 (keeping $K_{P,Qm}$ and $K_{I,PLL}$ at their nominal values). The system shows oscillations around 150 rad/s when the value of $K_{I,Pm}$ exceeds 598.

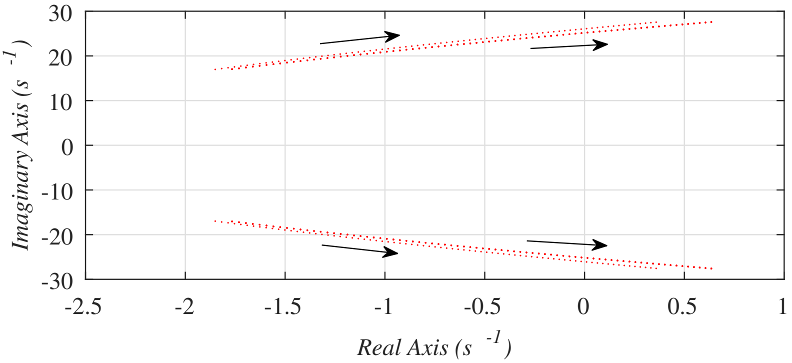

Figure 5.7: Root locus when $K_{I,PLL}$ increases from 40 to 120

Fig. 5.6 shows how the position of the dominant poles when $K_{P,Qm}$ increases from 1 to 1.375 (with constant $K_{I,Pm}$ and $K_{I,PLL}$). The system becomes unstable for $K_{P,Qm} > 1.19$.

Similarly, fig. 5.7 shows how the position of dominant poles when $K_{I,PLL}$ increases from 40 to 120, while keeping $K_{I,PLL}$ constant. When $K_{I,PLL}$ exceeds 100.2 the WPP becomes unstable, showing a sub-synchronous oscillation of approx. 26 rad/s.

From these figures, it is clear that changes in $K_{I,PLL}$ affect mainly the poles at $s = -1.8 \pm j17$, changes in $K_{I,Pm}$ affect mainly the poles at $s = -30 \pm j70$ and $s = -38 \pm j150$ whereas changes in $K_{K,Qm}$ mainly influence the pole at $s = -14$. Therefore, it is possible to tune these three parameters almost independently in order to modify the damping ratio of the corresponding poles.

5.5 Fault Ride Through

Fault behaviour and recovery is paramount for the correct co-ordination of HVDC-Diode Rectifier connected grid forming and grid following WTGs. This section includes the detailed faul-ride-through study to faults in a grid forming WTG string and also in the off-shore ring-bus.

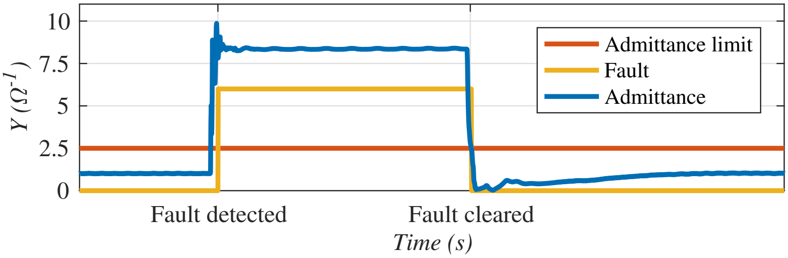

Figure 5.8: Off-shore fault detection using impedance measured by WTG.

5.5.1 Fault-ride-through Strategy

Both the grid forming and the grid following WTGs make use of the control blocks (1) and (2) shown in Fig. 5.2 and Fig. 5.3. These control blocks are proposed to improve the system response to off-shore ac-grid faults.

In addition, both types of WTGs implement a short-circuit detection function Y_{fault} using the admittance Y_T which is calculated using local measurements

$$Y_T \angle \varphi = \frac{I_T \angle \theta_{IT}}{V_C \angle \theta_C} \tag{5.39}$$

When the magnitude of the admittance exceeds a threshold, the WTG considers that a fault has occurred, Fig. 5.8. The fault signal is used in the control blocks (1), and (2)which are explained as follows.

- Block-(1): V_W^* *dynamic saturation:* During the short-circuit ($Y_{fault} = 1$), the limit of V_W^* is reduced to $\widehat{V_C} + 0.05$ pu, where $\widehat{V_C}$ is the filtered voltage V_C with a time constant of 100 ms. When the fault is cleared, the V_W^* limit increases to 1.1 pu following a 10 pu/s ramp. This ramp is used to improve the transient voltage recovery, as WTGs might detect the fault clearance at different times, depending on the distance to the fault.

- Block-(2): I_W^* *dynamic saturation:* During the short-circuit, the limit of I_W^* is 1.1 pu to provide correct relay protection. At short-circuit clearance (Y_{fault} negative edge) the limit of I_W^* is reduced to 0.05 pu during 25 ms to allow WTGs resynchronization with limited currents. Then it is increased to 1.1 pu at a rate of 10 pu/s.

The fault-ride-through control strategies described previously have been validated using detailed PSCAD simulations. Both grid forming and grid following control strategies have been implemented as digital controllers with a sampling time of 250 μs. For the following tests, the 400 MW OWF$_1$ consists of grid forming WTGs, whereas the two remaining OWFs of 400 MW each, consist of grid following WTGs. As described previously, each OWF is modeled by a total of 14 WTGs (9 individual WTGs in a single string and further 5 aggregated WTGs for each remaining string in the OWF, see Fig.5.1).

Several scenarios have been considered to check the integration of grid forming and grid following WTGs during off-shore short-circuits (Fig. 5.1). The first scenario is a short-circuit at a string of the grid forming wind farm (OWF$_1$). This scenario is important in order to validate that system remains stable if it loses a sizeable amount of grid forming power.

The second scenario is a short-circuit in one of the ring bus cables, as a worst case scenario.

A third scenario is considered in order to check adequate steady state and fault-ride-through operation without active power generation from grid forming WTGs. The third scenario includes the fault-ride-through response to a cable fault in one of the grid forming strings.

In all three scenarios, the breakers at both ends of the short-circuited cable clear the fault in 200 ms.

5.5.2 Grid Forming OWF String Cable Fault

Figs. 5.9 to 5.12 show the behaviour of both grid forming and grid following WTGs during a grid forming OWF string short-circuit. The short-circuit occurs at $t = 50$ ms and is cleared at $t = 250$ ms.

Fig. 5.9 shows the instantaneous active and reactive powers of each of the grid forming and grid following WTGs. As seen in Fig. 5.9, at the short-circuit onset, the instantaneous active power peak is higher in WTGs that have the short-circuit nearer. This is because the impedance of the grid, as seen from WTGs, decreases when the short-circuit is closer. Moreover, during the short-circuit, the injected active power is lower for WTGs nearer to the fault as their voltage is smaller while current limits are the same for all WTGs.

Note that, since there is no active power transmitted through the HVDC link and because of the solid fault, most part of the short-circuit current is, effectively reactive, as shown in fig. 5.9.

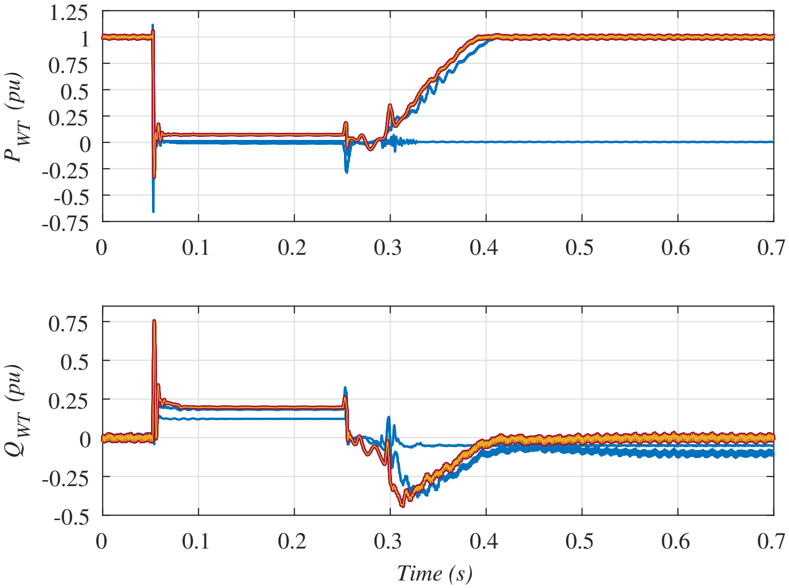

Figure 5.9: WTG active and reactive powers during a string short-circuit: OWF$_1$ (blue), OWF$_2$ (red), OWF$_3$ (yellow).

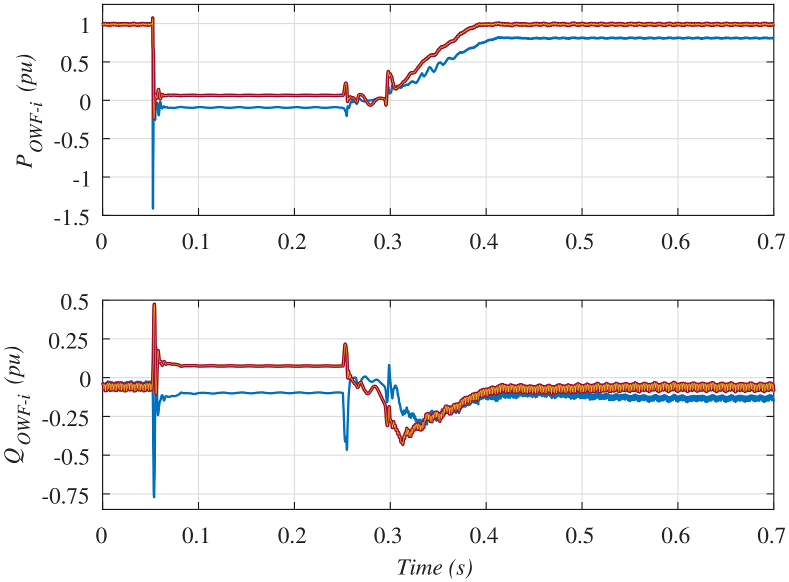

Figure 5.10: OWFs active and reactive powers during a string short-circuit: OWF$_1$ (blue), OWF$_2$ (red), OWF$_3$ (yellow).

When the fault is cleared, the system remains controlled and stable with reduced grid forming power. After approximately 50 ms, active power injection is resumed, hence the DRUs are conducting. Full power transmission is resumed at approx. 150 ms after the fault is cleared.

At the same time, the WTGs in the isolated string also power and bring-up the now islanded string. Note the active power delivered by the islanded WTGs is very small and their reactive power shows spikes caused by the in-rush current due to the wind turbine transformer saturation, [122].

During recovery, the off-shore ac-grid is over compensated because of the DRU-filters are connected and the active power being transmitted by the DRUs is still zero or very small. Therefore, the WTGs will absorb the reactive power over-compensation until nominal active power transmission is resumed. As DRU filters are rated around 0.4 pu, the grid forming WTGs (one third of installed power) cannot absorb enough reactive power, therefore, the grid following WTGs help restoring the system by absorbing reactive power during the recovery.

Fig. 5.10 shows the total instantaneous active and reactive powers from each OWF (Fig. 5.1). The initial power peak is higher in OWF_1 than in the other WPPs, as the short-circuit is at one string of OWF_1. The -1 pu active power surge corresponds to the discharge of cable and DRU filter capacitance and lasts less than 2 ms. However, most of that active power is fed to the short-circuit and the grid forming WTGs do not have to withstand such a large power surge (as seen in fig. 5.9).

During the short-circuit, clearly OWF_2 and OWF_3 contribute to the short-circuit active and reactive currents. DRU filters absorb around 0.35 pu reactive power, therefore reactive power contribution from all OWFs is required. During fault recovery, grid following WTGs inject maximum allowed reactive current, until the DRU starts conducting. From that point onwards, the WTG reactive power set-point is reduced to its pre-fault value with a 10 pu/s ramp rate (Fig. 5.10).

Fig. 5.10 also shows system restoration after the fault is cleared. OWF_1 active power is lower after the fault is cleared as one of its 72 MW (0.18 pu) strings has been disconnected. Therefore total transmitted power is reduced by 72 MW and additional reactive power from the grid-forming WTGs is needed to offset the DRU filter reactive power over-compensation.

Fig. 5.11 shows the instantaneous voltage V_C and the current I_W of grid forming and grid following WTGs. The voltage of the grid forming and grid following WTGs are similar, so only the voltage of the grid forming is shown.

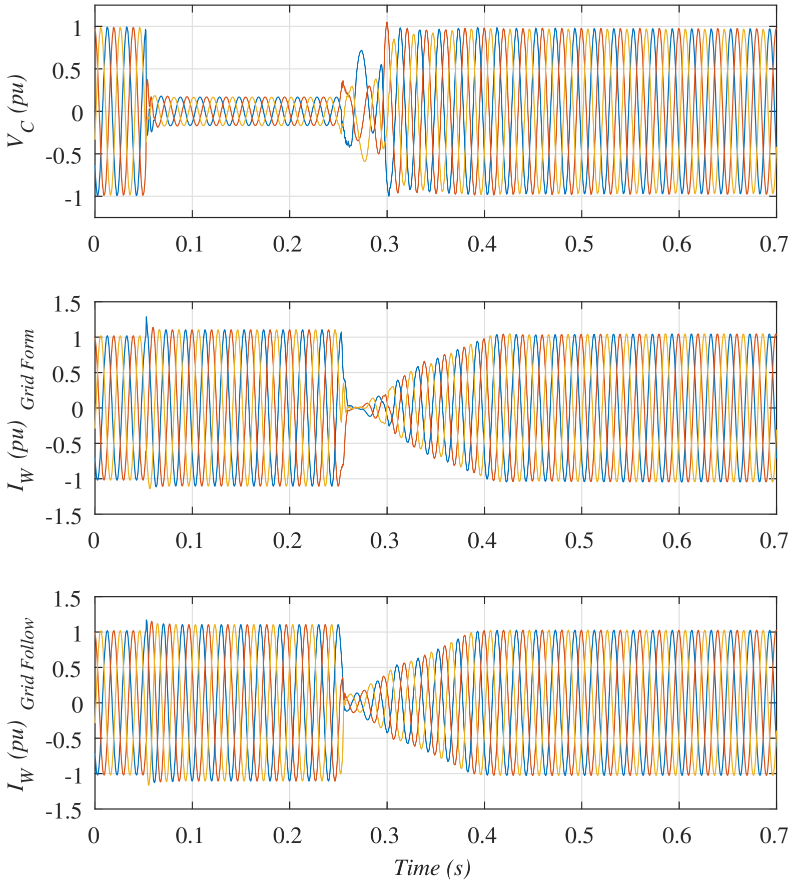

Figure 5.11: WTG voltages and currents during string short-circuit.

The voltage distortion after the short-circuit clearance is caused by the breaker arc of each pole being extinguished at the zero crossings of the pole fault current.

The current surge at the beginning of the fault is lower than 1.3 pu during 2 ms, which compares favourably to commercial IGBTs which can withstand peak collector current up to 2 pu during 1 ms [123]. Note all WTGs deliver 1.1 pu current during the short-circuit. When the fault is cleared ($t = 0.25$ s), there is a voltage transient due to the sudden increase in system impedance. Moreover, during approx. 50 ms, the WTGs self-synchronize. At $t = 0.33$ ms, the off-shore grid voltage has completely recovered and OWF_1 resumes active power production at $t = 0.37$ ms, i.e. 120 ms after the fault has been cleared. The final OWF_1 current

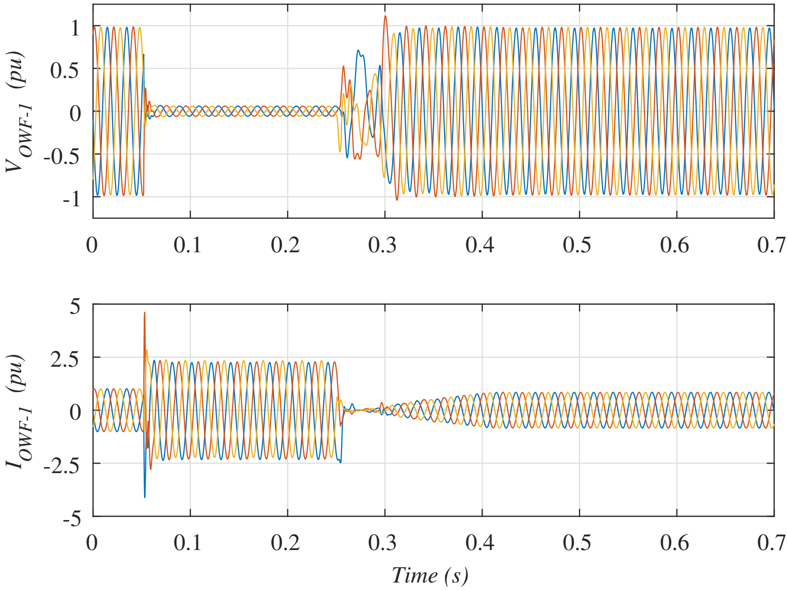

Figure 5.12: DRU Platform-1 AC voltages and currents during a string short-circuit.

is smaller than its pre-fault current, as one of its strings has been disconnected to clear the fault (see fig. 5.12).

Fig. 5.12 shows the voltage at DRU Platform-1 and the current from OWF_1 (Fig. 5.1). During the short-circuit the voltage drop at DRU Platform-1 is higher than the voltage drop at WTGs (see Fig. 5.11), because the impedance from the short-circuit to the WTGs (cable plus WTG transformer) is higher than the impedance to the DRU Platform-1 (only the cable). Moreover, the short-circuit current is above 2 pu during the short-circuit, due to the contribution of the other two wind farms.

5.5.3 Short-Circuit at Off-shore ac-Ring bus

Figs. 5.13 to 5.16 show the response of the system to a fault in the off-shore ac-grid ring bus (see Fig. 5.1).

Figs. 5.13 and 5.14 show active and reactive powers response in WTGs and off-shore wind farms, respectively, whereas figs. 5.15 and 5.16 show instantaneous currents and voltages in WTGs and off-shore wind farms.

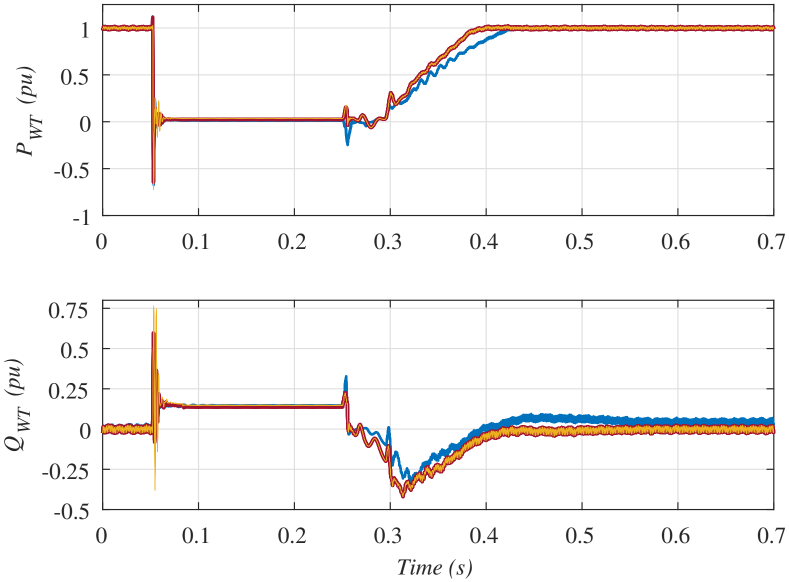

Figure 5.13: WTG active and reactive powers during ac-ring-bus short-circuit: OWF_1 (blue), OWF_2 (red), OWF_3 (yellow).

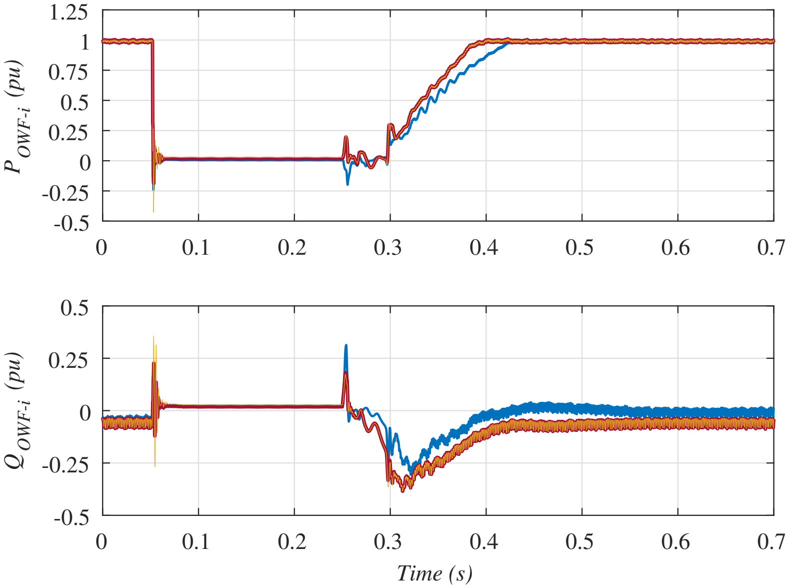

Figure 5.14: OWFs active and reactive powers during ac-ring-bus short-circuit: OWF_1 (blue), OWF_2 (red), OWF_3 (yellow).

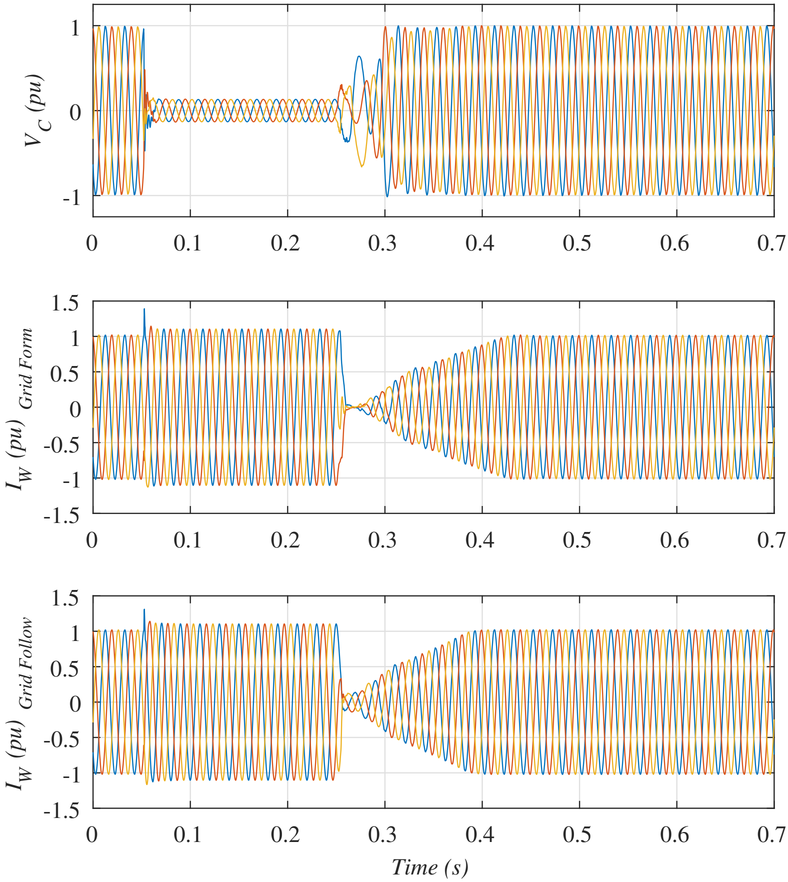

Figure 5.15: WTG voltages and currents during ac-ring-bus short-circuit.

The results are very similar to those shown for the string short-circuit, with a much smaller WPP voltage at the DRU platform connection point as the fault is now electrically closer.

In addition, the cable that connects OWF1 and OWF2 has been disconnected to clear the short-circuit. So, after the short-circuit, the grid forming WTGs produce more reactive power to compensate the contribution of the disconnected cable (see fig. 5.13).

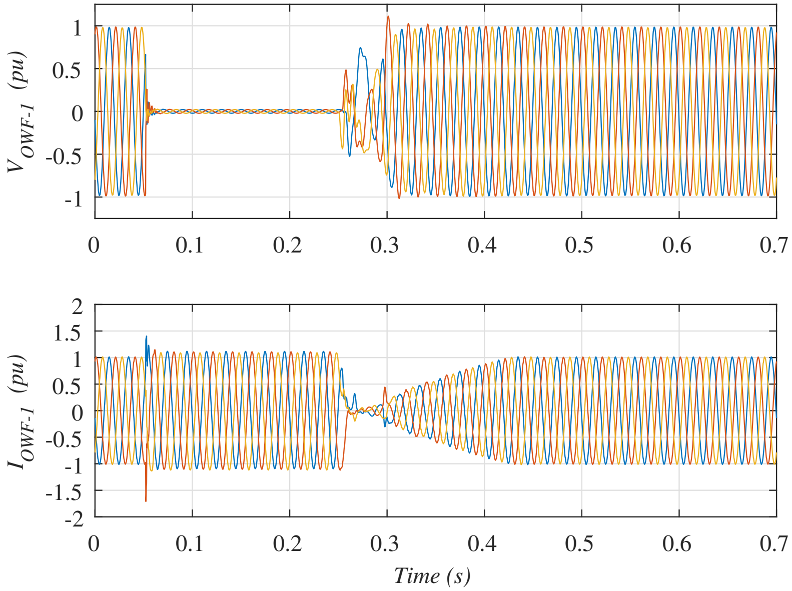

Figure 5.16: DRU Platform-1 AC voltages and currents during ac-ring-bus short-circuit.

5.5.4 Grid Forming WPP String Fault when it is Generating Zero Active Power

As the grid forming WPP is responsible to keep the DRU operational, an important concern is both steady state and fault operation when the grid forming WPP is not generating any active power due to low wind conditions.

Figs. 5.17 and 5.18 show the response to a grid forming WPP string fault (fault-1 in fig. 5.1) when grid forming WTGs are not generating active power.

Fig. 5.17 shows grid forming and grid following WTG active and reactive powers response, whereas fig. 5.18 shows WTG instantaneous currents and voltages.

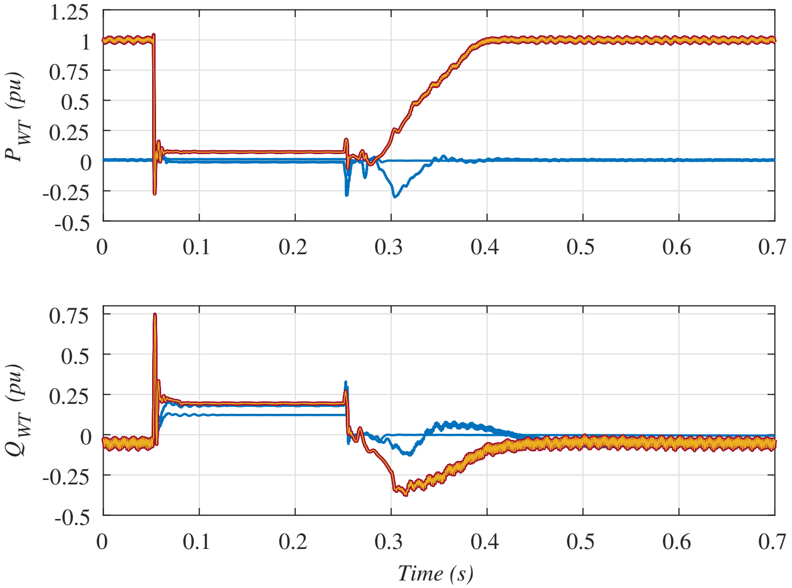

Figure 5.17: WTG active and reactive powers during a string fault: OWF_1 (blue), OWF_2 (red), OWF_3 (yellow)

The results show adequate steady state and fault operation. The behaviour in this scenario is similar to the short-circuit when the grid forming WTGs are generating the maximum active power (Figs. 5.9 to 5.12). In this scenario one third of the DRU capacitor and filter banks have been disconnected to prevent reactive power over-compensation.

Therefore, it has been shown that adequate fault-rid-through operation is possible with the grid forming WTGs generating only a peak of 100 MW (0.08 pu of rated 1.2 GW) and 40 MVAr (0.03 pu) during voltage recovery.

5.6 Discussion and Conclusions

This paper has presented the interoperability of grid forming and grid following WTGs when connected to a diode rectifier based HVDC link.

The considered control for the grid forming WTGs does not require communication for proper operation and does not require the use of phase-locked-loops or frequency-locked-loops for their operation.

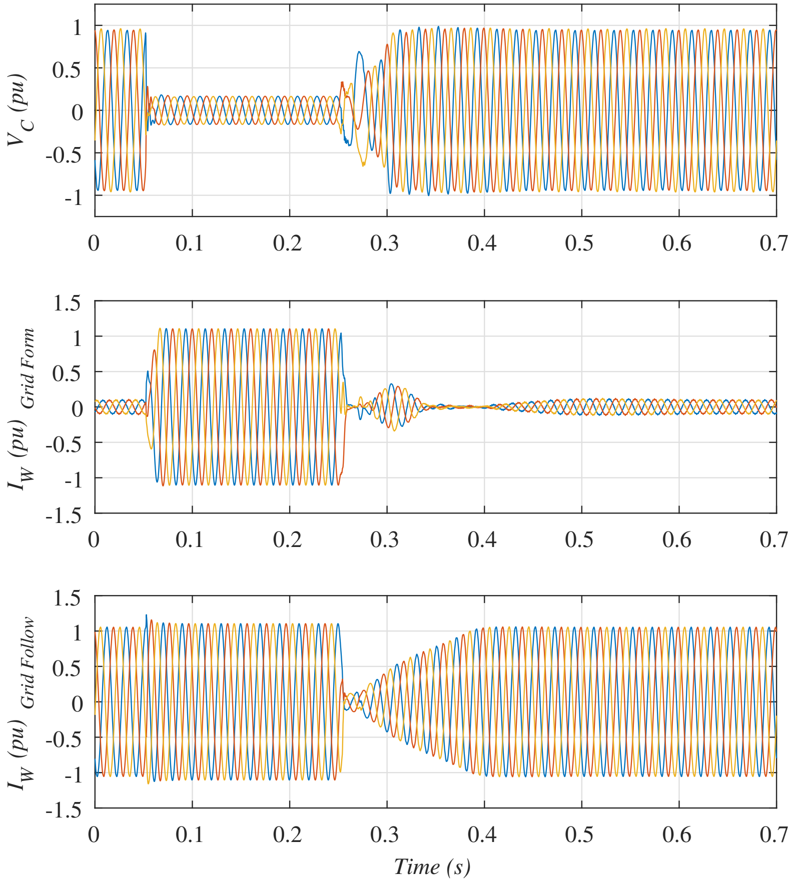

Figure 5.18: WTG voltages and currents during a string fault

The small signal stability analysis of the mixed system, considering detailed strings, has been carried out. The comparison of the frequency response of the aggregated and the distributed plants has been carried out, with good agreement in a wide range of frequencies.

It has been shown that an increase in either PLL or droop gains would lead to worse dominant pole damping and even to instability. It has been found that dominant poles are affected independently by either PLL or droop gains.

Particular attention has been paid to adequate joint response during transients. The same fault-ride-through strategy has been implemented in both grid forming and grid following WTGs. Fault onset and fault clearance detection is carried out by the individual WTGs.

The proposed control strategies has been shown to keep wind turbine active, reactive, current and voltage magnitudes within their operational levels during faults.

It has been shown that the system can operate with 328 MW grid forming WTGs and 800 MW grid following WTGs, which represent a percentage of 29% wind forming WTGs with respect to total delivered power.

Furthermore, it has been shown that grid forming WTGs are capable of controlling the off-shore grid even when they are not generating active power, while showing adequate fault response and fault recovery. This is particularly important as it shows that the grid following WPP can operate with very low or no power production in the grid forming WPP.

Appendix 1

Table 5.1 shows the parameters values of the system components. Table 5.2 shows the parameters values of the control strategies.

Appendix 2. Linearization

This section includes the linearization procedure being carried out for the small signal analysis of the complete system:

$$\dot{x}^{dq} = \Theta A \Theta^{-1} x^{dq} - j\Omega x^{dq} + B u^{dq} \tag{5.40}$$

$$\dot{\theta}_i = f_{\theta i}\left(x_{ci}^{dqi}, x_1^{dqi}, x_2^{dqi}, \ldots, x_{ni}^{dqi}\right) \tag{5.41}$$

$$\dot{x}_{ci}^{dqi} = f_i\left(\theta_i, x_{ci}^{dqi}, x_1^{dqi}, x_2^{dqi}, \ldots, x_{ni}^{dqi}, u_i^{dqi}\right) \tag{5.42}$$

$$u_i^{dqi} = g_i\left(\theta_i, x_{ci}^{dqi}, x_1^{dqi}, x_2^{dqi}, \ldots, x_{ni}^{dqi}, u_{refi}^{dqi}\right) \tag{5.43}$$

Table 5.1: System Parameters

Wind Turbines
Grid-side converter: 8 MW, 1.2 kVcc, 690 Vac, 50 Hz
Grid-side filter: $R_T = 476.1\ \mu\Omega$, $L = 18.94\ \mu$H, $C = 2674\ \mu$F
Transformer: 9.2 MVA, 0.69/66 kV, $R_W = 0.004$ pu, $X_W = 0.1$ pu, Saturable
Off-shore ac-grid
WTG to WTG distance: 2 km
WTG to ring-bus distance: 4 km
Distance between platforms: 10 km
String cable sections: C = 150 mm^2, B = 185 mm^2, A = 400 mm^2
String with 8 WTGs: C-C-B-B-B-B-B-A
String with 9 WTGs: C-C-B-B-B-B-B-A-A
DRU Platform
Filter and compensation filter bank according to [124]
Transformer: 215 MVA, 66/43/43 kV, $R_{TR} = 0.004$ pu, $X_{TR} = 0.27$ pu
dc-smoothing reactor: 66.67 mH
On-shore full-bridge MMC
MMC: 1400 MW, ±320 kVcc, 370 kVac, 50 Hz
MMC arm reactor: 50 mH
MMC reactor: 1.25 mH, 1 Ω
Transformer: 1400 MVA, 370/230 kV, $X_V = 0.1$ pu

Table 5.2: System Control Parameters

Common Controls
Current control: $G_{PR,I}$: $K_{P,I} = 1.75$, $K_{R,I} = 360.0$; $K_V = 0.843$
Grid Forming Controls
Voltage control: $G_{PR,V}$: $K_{P,V} = 0.28$, $K_{R,V} = 360.0$
Active power control: $G_{PI,Pm}$: $K_{P,Pm} = 1.95$, $K_{I,Pm} = 105.0$
Reactive power control: $G_{P,Qm}$: $K_{P,Qm} = 1.0$
Grid Following Controls
PLL: $G_{PI,PLL}$: $K_{P,PLL} = 1.0$, $K_{I,PLL} = 40.0$
Active power control: $G_{PI,Pl}$: $K_{P,Pl} = 0.5$, $K_{I,Pl} = 64.0$
Reactive power control: $G_{PI,Ql}$: $K_{P,Ql} = 0.5$, $K_{I,Ql} = 64.0$

The following vectors are defined: $\theta = (\theta_1, \theta_2, \ldots, \theta_m)^T$, $x_c^{dq} = \left(x_c^{dq1}, x_c^{dq2}, \ldots, x_c^{dqm}\right)^T$, $u_{ref}^{dq} = \left(u_{ref}^{dq1}, u_{ref}^{dq2}, \ldots, u_{ref}^{dqm}\right)^T$.

Also, the following functional vectors are defined:

$$\Omega = (f_{\theta 1}, f_{\theta 1}, f_{\theta 2}, f_{\theta 2}, \cdots, f_{\theta m})^T \tag{5.44}$$

$$G = (g_1, g_2, g_3, \cdots, g_m)^T \tag{5.45}$$

$$F = (f_1, f_2, f_3, \cdots, f_m)^T \tag{5.46}$$

$$F_\theta = (f_{\theta 1}, f_{\theta 2}, f_{\theta 3}, \cdots, f_{\theta m})^T \tag{5.47}$$

In the steady state operating point:

$$f_{\theta 10} = f_{\theta 20} = \cdots = f_{\theta m0} = \omega_0 \tag{5.48}$$

And the linearised system will be

$$\begin{aligned} \Delta \dot{x}^{dq} &= \left(\Theta A \Theta^{-1} - j \frac{\partial \left(\Omega x^{dq} \right)}{\partial x^{dq}} \right) \Delta x^{dq} - j \frac{\partial \left(\Omega x^{dq} \right)}{\partial x_c^{dq}} \Delta x_c^{dq} \\ & \left(B - j \frac{\partial \left(\Omega x^{dq} \right)}{\partial u^{dq}} \right) \Delta u^{dq} + \frac{\partial \left(\Theta A \Theta^{-1} x^{dq} \right)}{\partial \theta} \Delta \theta \end{aligned} \tag{5.49}$$

$$\Delta \dot{\theta} = \frac{\partial F_\theta}{\partial x^{dq}} \Delta x^{dq} + \frac{\partial F_\theta}{\partial x_c^{dq}} \Delta x_c^{dq} + \frac{\partial F_\theta}{\partial \theta} \Delta \theta \tag{5.50}$$

$$\Delta \dot{x}_c^{dq} = \frac{\partial F}{\partial x^{dq}} \Delta x^{dq} + \frac{\partial F}{\partial x_c^{dq}} \Delta x_c^{dq} + \frac{\partial F}{\partial \theta} \Delta \theta + \frac{\partial F}{\partial u^{dq}} \Delta u^{dq} \tag{5.51}$$

$$\Delta u^{dq} = \frac{\partial G}{\partial x^{dq}} \Delta x^{dq} + \frac{\partial G}{\partial x_c^{dq}} \Delta x_c^{dq} + \frac{\partial G}{\partial \theta} \Delta \theta + \frac{\partial G}{\partial u_{ref}^{dq}} \Delta u_{ref}^{dq} \tag{5.52}$$

where $\frac{\partial F}{\partial x}$ is the Jacobian of vector field F with respect to vector x evaluated at the steady state operating point.

Chapter 6

Protection Strategies for the Connection of Diode Rectifier-based Wind Power Plants to HVDC Interconnectors

Note: this chapter studies how diode rectifier based WPPs can contribute during fault to multi-terminal HVDC grids. Moreover, a comparative study about five different protection strategies is included. The chapter contents are published on:

Martínez-Turégano, Jaime; Vidal-Albalate, Ricardo; Añó-Villalba, Salvador; Bernal-Perez, Soledad; Blasco-Gimenez, Ramon. (2020) Protection Strategies for the Connection of Diode Rectifier-based Wind Power Plants to HVDC Interconnectors. IEEE Journal of Emerging and Selected Topics in Power Electronics - . 10.1109/JESTPE.2020.3028780

Abstract

The connection of diode rectifier (DR) based wind power plants to existing or planned High Voltage dc (HVdc) interconnectors can lead to important savings on cost and system robustness. Since the DR station usually operates in a bipolar configuration, its connection to symmetric monopoles is particularly challenging. However, there are no published detailed studies on the protection of DR connection wind power plants to symmetric monopole interconnectors or even to bipolar interconnectors.

This paper includes the comparative study of five different protection strategies for such systems, including both solid and resistive DR station grounding and strategies with and without the use of dc-circuit breakers. An analytical study allows for the calculation of fault current during fault on-set for both half-bridge and hybrid Modular Multi-level Converter (MMC) stations. Using detailed Electromagnetic Transient (EMT) simulation studies, the different protection strategies are evaluated in terms of current, voltage and isolation requirements of each element, as well as the need for dc-circuit breakers, fast communication or larger surge arresters. Moreover, a distance fault detection algorithm is included for the wind turbine converters to distinguish between local ac-grid and dc-cable faults.

From the simulation results it is possible to conclude that DR high impedance grounding, together with wind turbine distance protection can be used for the protection of DR based off-shore wind power plants connected to symmetric monopole interconnectors without requiring dc-circuit breakers.

6.1 Introduction

Diode Rectifier (DR) stations have been proposed for the connection of off-shore Wind Power Plants (WPPs) to High Voltage dc (HVdc) links, [12, 6]. The main benefits of diode rectifier stations when compared to Voltage Source Converter (VSC) stations are lower cost and footprint, and higher efficiency and robustness [125]. Transmission losses can be reduced by 20% with respect to VSC links [14, 126]. Manufacturers claim that the total cost of the transmission system can be reduced by 30% whereas the total topside volume can be reduced by 80%, compared to existing VSC-HVdc transmission systems [127].

On the other hand, particularly in Northern Europe, a large number of interconnectors are planned in close proximity to off-shore wind power plant development sites. Therefore, the use of the HVdc interconnectors for both energy trading and WPP connection can lead to important installation savings while increasing overall system redundancy.

DC faults in Modular Multi-level Converter (MMC) based HVdc links have been extensively studied, mainly by means of simulation models [128, 129]. [128] compares the use of ac and dc breakers to isolate dc faults and [129] proposes to use full bridge (FB) cells to interrupt the fault currents at the expense of higher losses during normal operation. Mathematical models have been proposed to estimate the maximum fault currents and their steady-state value for both monopolar symmetrical [130, 131] or bipolar [131, 132] HVdc links. [130] and [132] provide analytical expressions to obtain the value of the fault currents, however, the overvoltages that can appear in the system, specially in pole-to-ground faults in symmetrical monopolar grids, are not studied. Moreover, none of them considered the effect of Diode Rectifier Units (DRUs) on HVdc faults. Even though half bridge (HB) MMCs behave as a diode rectifier when blocked, they use ac side point-star reactors for grounding, whereas Line Commutated Converter (LCC) rectifier stations typically use dc-side low impedance grounding. Therefore, these works did not consider the effects of specific station grounding or wind power plant control on over-currents and over-voltages during faults.

Specific studies have been carried out for hybrid LCC-VSC systems. Operation and fault ride through studies of hybrid LCC-VSC systems, such as the Wudongde multi-terminal project, have been presented in [133, 134, 135]. A monopolar configuration, consisting on a single LCC rectifier station and two MMC inverter stations, used high power diodes to prevent the half-bridge MMC stations from feeding the faults [133]. Fault currents were cleared by acting on the commutation angle of the LCC rectifier station. This study was extended from a single LCC station to a bipolar system including two MMC inverter stations, an LCC rectifier station and an LCC inverter stations. The protection strategy also included the use of high power diodes and fault current blocking by the thyristor rectifier stations [136]. These strategies are not applicable to interconnectors since the MMC stations should operate with bi-directional power flows, therefore diode protection is not feasible and the LCC diode rectifier stations cannot be used to clear the fault currents.

The protection strategies for the Wudongde project includes the use of fast disconnectors and hybrid full-bridge half-bridge MMC stations with fault blocking capability in a bipolar configuration, considering a single LCC rectifier station and two MMC inverter stations [134, 135]. The combined use of hybrid MMC stations and LCC station phase angle control, allow for fast fault current reduction during dc-faults, at the expense of higher system losses. However, since the

Wudonge project uses overhead lines, the likelihood of dc faults is much larger than when using submarine cables, so the use of hybrid MMC stations is justified.

The aforementioned studies considered bipolar systems, however, most VSC interconnectors are symmetric monopoles. In these installations, fault response is particularly challenging, as pole to ground faults lead to large healthy pole overvoltages [137]. Moreover, pole re-balancing is needed due to the use of high impedance grounding for the MMCs [138]. The authors of [139] did show the technical viability of a protection and pole re-balancing system consisting of dc-circuit breakers (dcCB) and dc choppers using actual control and protection replicas for all the elements, including converter stations control replicas. However, the use of dc choppers and dcCBs, is very costly, particularly for off-shore HVdc stations. Moreover, it would undermine the simplicity and robustness of the use of a diode rectifier station.

Faults in hybrid LCC-VSC HVdc systems with Diode Rectifier-connected Wind Power Plants (DR-WPP) have been previously studied [14, 140, 141, 93]. However, [14] considered mainly the efficiency studies, with only marginal fault studies in monopolar point-to-point systems. This work was extended to multi-terminal bipolar systems [140]. In both cases, averaged models of the VSC converters were used and the fault studies carried out did not include any new proposal for fault response co-ordination between different elements. Other studies used either full bridge converters [141] or hybrid MMC stations [93]. The use of fault blocking converters makes fault handing relatively easier, at the expense of higher costs and losses, moreover [93] only considered off-shore ac faults.

Therefore, existing literature did not cover in detail the protection of WPP-DR wind power plants when connected to HVdc interconnectors. Moreover, the effects of DR station grounding or Wind Turbine Generator (WTG) distance protection to distinguish between local ac-grid and HVdc cable faults has not been covered in existing literature.

Therefore, the contributions of this paper are:

- Proposal and comparative evaluation of different protection strategies for the connection of DR-WPP to HVdc interconnectors (i.e. a type-1 HVdc station connected to either type-3 or type-4 on-shore stations [137]).
- Study of high impedance grounding on the LCC diode rectifier station when connecting to symmetric monopolar MMC stations.

- Develop a WTG distance protection strategy that allows WTGs to detect if a fault is located in the off-shore ac-grid or in the HVdc cables and act accordingly.

This paper includes the study of 5 different strategies for the protection of the combined HVdc interconnector and DRU-connected wind power plant against HVdc faults, namely:

1. Solid DRU grounding. Baseline scenario with MMCs connected as a symmetric monopole and the DRU with a solid connection to ground. Fault clearing using dcCBs.
2. Resistive DRU-HVdc grounding. Resistive grounding to limit fault currents. Fault clearing using dcCBs.
3. Grounding resistor and WPP blocking. Includes WTG detection of HVdc faults and WPP blocking. Fault clearing using dcCBs.
4. WTG distance protection and MMC blocking. Includes WTG detection of HVdc faults and WPP and HVdc blocking. dcCBs not used.
5. Hybrid MMC with full fault blocking capability. Bipolar configuration. No dcCBs required.

These alternatives are analysed regarding the overvoltage and overcurrent in cables and converters, surge arrester dissipated energy and fault clearing times. It is shown that option 4 is the less costly option, at the expense of somehow larger clearing times and higher energy dissipated in surge arresters.

6.2 Interconnector with Intermediate WPP

The proposed system is shown in Fig. 6.1 and consists of a typical HVdc interconnector with an additional DR-based terminal for the connection of the off-shore WPP. The other two terminals of the HVdc system are two symmetrical monopolar MMC converters (HB) to connect to the corresponding two on-shore grids for protection strategies 1-4, whereas two hybrid bipolar MMC converters are used for strategy 5. The on-shore stations are controlled using standard master-slave control, where one of the stations controls the interconnector HVdc voltage and the other operates on active power reference.

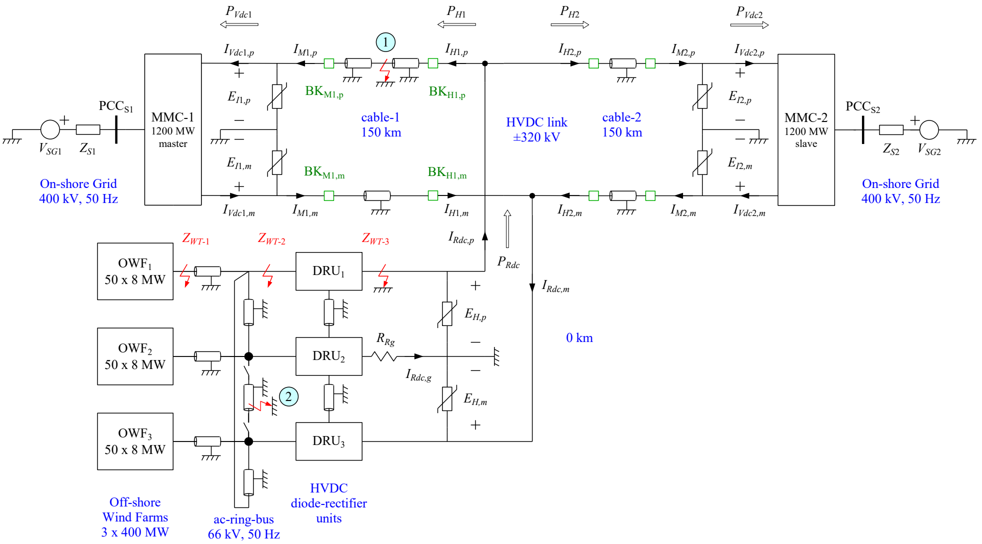

Figure 6.1: Overall system diagram including main components, location of faults (1) and (2), and apparent impedances Z_{WT}.

The off-shore WPP consists of three clusters with fifty 8 MW-rated wind turbines (400 MW each WPP). The wind turbines are of variable speed with fully-rated converters. The diode rectifier HVdc station consists of three platforms. Each platform has two series connected 12-pulse diode based rectifiers with the corresponding ac and dc filters. The WTGs are all grid forming and include P-V and Q-ω droops, commonly used for distributed control of grid forming WTGs when connected to DR stations [12].

The considered scenario has enough complexity, so the results are representative of a realistic fault response. The interconnector is a VSC-HVdc 300km, ±320kV and 1.2GW. Power and voltage ratings correspond to recently completed HVdc projects. The total cable length (300km) is based on the CobraCable link, and represents some of the longest HVdc interconnectors in Europe, therefore, considered cable charge is in the upper limit of existing installations. The DRU system consists of a three platform installation, with parallel ac connection and series dc connection, including an ac ring bus cable [125]. Diode rectifier valves include the effects of snubbers and grading resistors. The DR ac-filters and the surge arresters are also included in the model, as their behaviour is important during fault onset and fault recovery.

Table 6.1: MMC data

Parameter	**Value**	**Parameter**	**Value**
dc voltage (kV)	±320	ac-grid voltage (kV)	400
Active power (MW)	1200	T_R (kV)	333/400
Reactive power (MVAr)	415	T_R power (MVA)	1300
Levels	401	L_{T_R} (pu)	0.18
Arm inductance (mH)	41.7	R_{T_R} (pu)	0.01
C (mF)	14.5	L_g (H)	5000
v_c (kV)	1.6	R_g (Ω)	5000

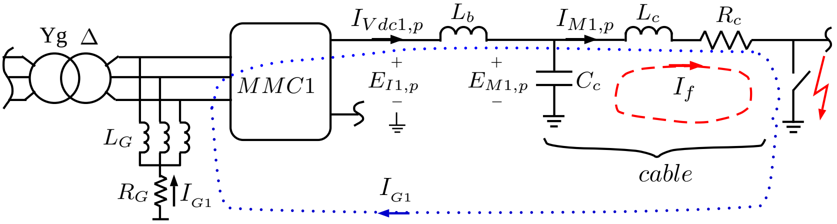

Figure 6.2: Equivalent circuit of the on-shore MMC stations.

The studied dc-faults are located in cable-1, i.e. the section connecting the DR station to the voltage controlling MMC. This is a more challenging scenario regarding dc faults. As for off-shore ac-grid faults, a ring bus fault is considered, as it is a location that would lead to the highest fault currents within the off-shore ac-grid.

The HVdc link, with a symmetrical monopolar configuration, uses a star-point reactor connected on the ac-side to provide a ground reference. The MMCs parameters, which are based on the France-Spain link [142], are presented in Table 6.1.

6.3 Analytical Study of MMC-DR System DC Faults

This section includes the analytical study of dc-fault currents and voltages for hybrid DR-VSC systems considering DR dc-side impedance grounding and both monopolar and bipolar MMC converter stations.

The behaviour of MMC-1 to a solid pole-to-ground cable-1 fault is analysed considering the equivalent circuit in Fig. 6.2, where MMC-1 is not blocked. During the first milliseconds, the response is mainly influenced by cable discharge (red path), since the contribution of the ac-side current is limited by the inductive

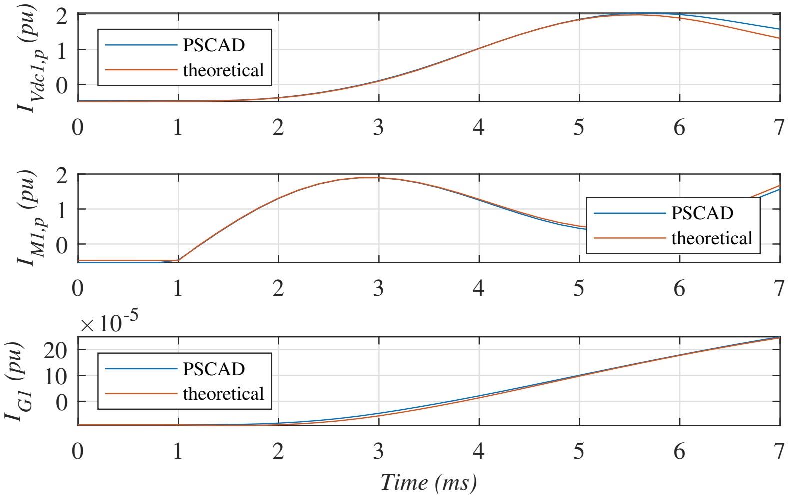

Figure 6.3: Comparison of the theoretical and PSCAD currents when the MMC is not blocked. From top to bottom: MMC-1 dc-current (positive pole); cable-1 current (positive pole); MMC-1 star-point reactor current.

components of the ac-grid (lines, transformers), the MMC arm reactors and the dc-breaker reactor. Additionally, the dc-side neutral voltage is no longer zero but is displaced towards negative values which provokes that a fault current starts flowing through the ac-side star-point reactor as shown with the blue path.

This study is only valid for the first 5-7 ms, i.e., when the system response is hardly influenced by the system controls due to both fault detection delays and control delay times. However, this analysis can help estimating the maximum fault currents that the power stations, cables and dc-breaker need to withstand.

From Fig. 6.2, we have:

$$E_{M1,p} = \left(-L_c C_c \frac{d^2 E_{M1,p}}{dt^2} - R_c C_c \frac{dE_{M1,p}}{dt}\right) + \left(L_c \frac{dI_{Vdc1,p}}{dt} + R_c I_{Vdc,p}\right) \quad (6.1)$$

where the first term corresponds to the cable discharge and the second to the MMC contribution. The cable discharge dynamics are [143]:

$$I_f = \frac{E_{M1,p0}}{\omega_c L_c} e^{-\frac{R_c}{2L_c} t} sin\left(\sqrt{\frac{1}{L_c C_c} - \left(\frac{R_c}{2L_c}\right)^2}\, t\right) \quad (6.2)$$

where $E_{M1,p0}$ is the initial pole-to-ground voltage. The dynamics of MMC contribution in (6.1) are (assuming it is not blocked):

$$L_b \frac{dI_{Vdc1,p}}{dt} = E_{I1,p} - E_{M1,p} = -R_G I_{G1} - L_G \frac{dI_{G1}}{dt} + V_{cap} - E_{M1,p} \tag{6.3}$$

where $E_{I1,p}$ is the dc voltage at the MMC dc-side and V_{cap} is the dc-voltage inserted by the upper MMC arms, which can be obtained from the submodule capacitor discharge dynamics:

$$C_{eq} \frac{dV_{cap}}{dt} = I_{Vdc1,p} - I_{Vdc1,p0} \tag{6.4}$$

where C_{eq} is the equivalent capacitance of the MMC and $I_{Vdc1,p0}$ is the current at the moment of the fault onset.

The dynamics of I_{G1} are:

$$E_n = L_G \frac{dI_{G1}}{dt} + R_G I_{G1} \approx E_{I1,p0} - E_{I1,p} \tag{6.5}$$

where $E_{I1,p0}$ is the nominal pole-to-ground voltage and E_n is the dc-side neutral voltage($E_n = E_{I1,p} - E_{I1,n} \approx E_{I1,p0} - E_{I1,p}$ during the fault). Cable, MMC arm and dc-breaker impedances have been neglected as ac-side grounding impedance can be three to four orders of magnitude greater.

Fig. 6.3 shows the comparison between theoretical and simulation fault currents, showing an underdamped response whose frequency is given by (6.2).

If dcCBs are used as protection system, the surge arrester of the dcCB includes a voltage-dependent resistance in the circuit which is added to R_G in (6.3) and (6.5). Fig. 6.4 shows both the theoretical and PSCAD response when the dc-breaker isolates the fault at $t = 5.3$ ms approximately. In the theoretical study, a constant average value has been considered, for this reason, the steady-state values of I_{G1} differ. Notwithstanding, the analytical expressions allow for a good representation of maximum fault currents and voltages.

If the MMC is blocked as a protection system, it behaves like an uncontrolled half-wave rectifier that creates the following dc voltage.

$$E_n = E_{blk} = \frac{3}{\pi\sqrt{2}} V_v \tag{6.6}$$

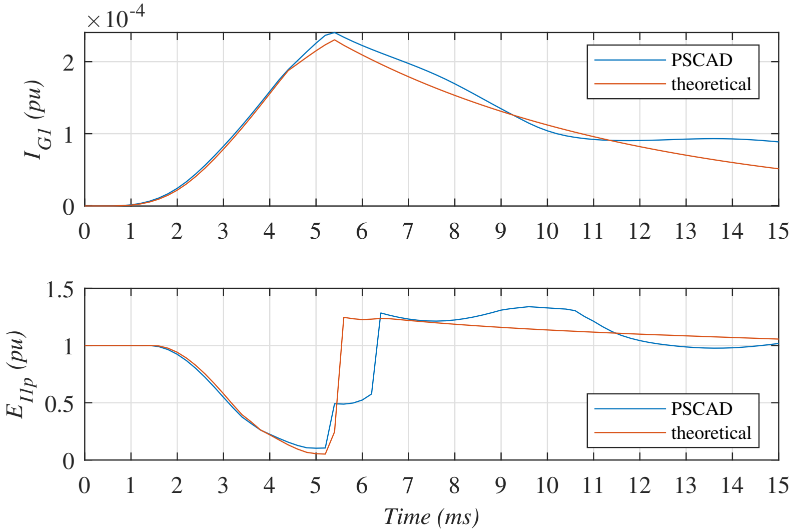

Figure 6.4: Comparison of the theoretical and PSCAD results when the dc-breaker is opened. From top to bottom: MMC-1 star-point reactor current; MMC-1 dc-voltage (positive pole).

where V_v is the rms value of the voltage at the ac-side of the MMC. In steady-state, the grounding fault current is:

$$I_{G1} = \frac{E_{blk}}{R_G} \tag{6.7}$$

Although the MMC behaves as a rectifier and keeps feeding the fault, the current I_{G1} is limited to small values when a high-impedance grounding is used, [142]. Fig. 6.5 shows the grounding fault current I_{G1} and the MMC ac-side voltages V_{v1}, which present a common mode voltage after blocking the converter. Due to the fault, the positive dc pole voltage is zero; therefore, the dc voltage is displaced towards negatives values. This, in turn, provokes a common mode voltage on the MMC ac-side, which is not solidly grounded (see Fig. 6.2).

The previous analysis can be extended to the other MMC station and to the DRU, Fig. 6.6. The cable voltage is:

$$E_{H1,p} = \left(-L_cC_c\frac{d^2E_{H1,p}}{dt^2} - R_cC_c\frac{dE_{H1,p}}{dt}\right) + \left(L_c\frac{dI_{H1,p}}{dt} + R_cI_{H1,p}\right) \tag{6.8}$$

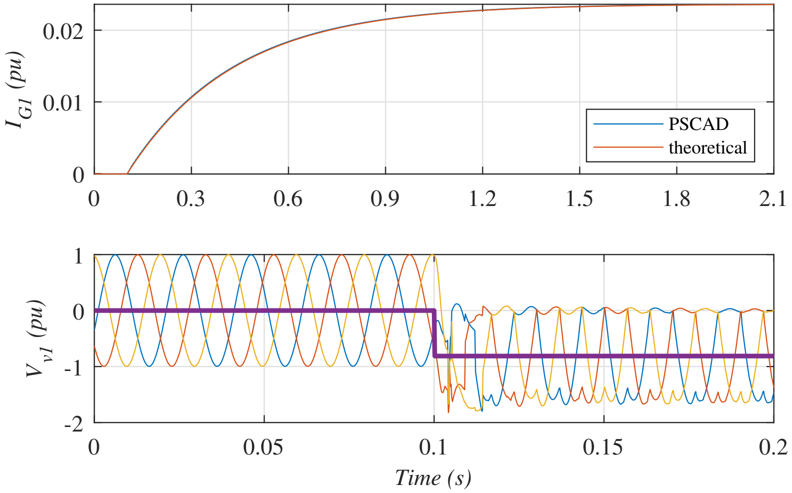

Figure 6.5: Comparison of the theoretical and PSCAD results when the MMC is blocked. From top to bottom: MMC-1 star-point reactor current; MMC-1 ac-voltage.

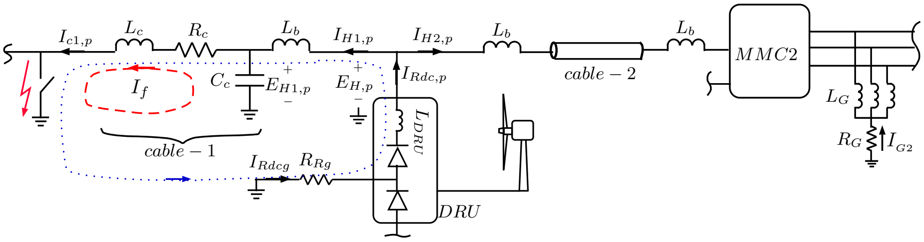

Figure 6.6: Equivalent circuit of the DRU station.

where the first terms correspond to the cable discharge and the second terms correspond to the contribution of the DRU and the MMC-2, where $I_{H1,p}$ is:

$$I_{H1,p} = I_{Rdc,p} - I_{H2,p} \tag{6.9}$$

The current $I_{H2,p}$ due to the discharge of the cable-2 and the contribution of the MMC-2 can be obtained as per (6.2). The WPP fault current $I_{Rdc,p}$ is computed considering the WPP as a constant current source that feeds the fault current:

$$I_{Rdc1,p} = I_{Rdc1,p0} + I_{Rdc,g} \tag{6.10}$$

where $I_{Rdc1,p0}$ is the DRU current at the fault onset and $I_{Rdc,g}$ is the fault current flowing through the DRU grounding resistor. The voltage at the DRU terminals is:

$$E_{H,p} = E_{H1,p} + L_b \frac{dI_{H1,p}}{dt} \tag{6.11}$$

During normal operation, the dc-side neutral voltage $E_{n,DRU} = E_{H,p} - E_{H,n}$ is zero, as both poles have the same voltage. However, after the fault onset, the voltage of the positive pole drops whereas the voltage of the negative pole increases. This causes a fault current $I_{Rdc,g}$ to flow through the DRU grounding (blue loop in Fig. 6.6):

$$E_{n,DRU} = (R_c + R_{Rg})\, I_{Rdc,g} + (L_c + L_b + L_{DRU})\, \frac{dI_{Rdc,g}}{dt} \tag{6.12}$$

$$E_{n,DRU} \approx E_{H,p0} - E_{H,p} \tag{6.13}$$

where $E_{H,p0}$ is the nominal pole-to-ground voltage.

Fig. 6.7 shows the evolution of the cable discharge current, the DRU fault current and the DRU dc-side grounding fault. During the first six milliseconds the theoretical and the PSCAD results present a good agreement. After that time, the error increases since the response of the MMC and WPP controllers has not been taken into account in the analysis.

For a bipolar HVdc system, which has two MMCs with midpoint grounded at each converter node, a pole-to-ground fault collapses the dc voltage to zero since

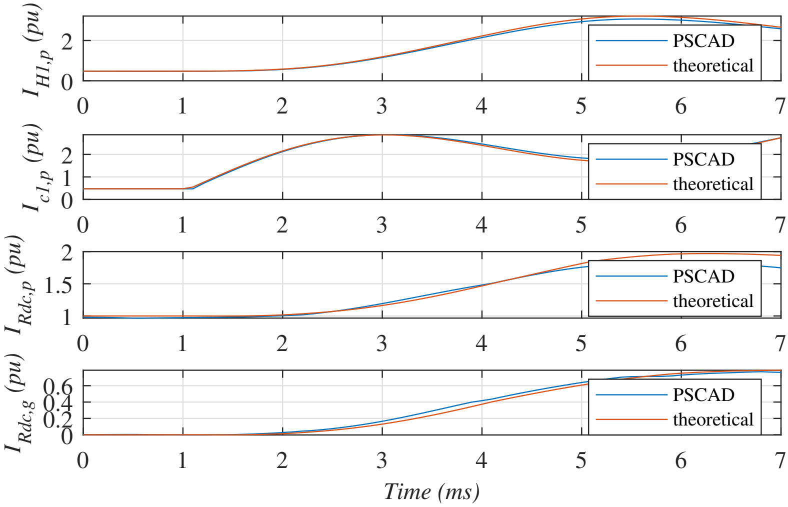

Figure 6.7: Comparison of the theoretical and PSCAD currents of the DRU. From top to bottom: DRU to cable-1 dc-breaker current (positive pole); cable-1 current; DRU dc-current (positive pole); DRU ground current.

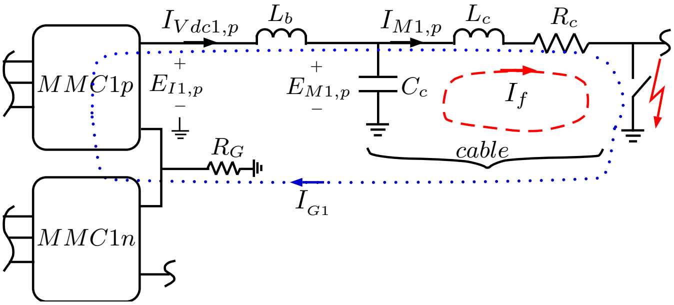

Figure 6.8: Equivalent circuit of the on-shore MMC stations for a bipolar HVdc grid.

it is a short-circuit between the MMC dc terminals, Fig. 6.8. As in the symmetrical monopolar configuration, two fault paths can be identified. The red path in Fig. 6.8 corresponds to the cable discharged, which has already analyzed in (6.1) and (6.2). The second current path (blue loop) corresponds to the fault fed from the ac-side. Same analysis as in the case of monopolar symmetrical configuration can be carried out (equations (6.3)-(6.5)). However, bipolar HVdc grids are usually solidly grounded ($R_G = 0$) so the cable resistance and inductance cannot be neglected as in the previous case [144]. Therefore, (6.3)-(6.5) become:

$$L_b \frac{dI_{Vdc1,p}}{dt} = E_{I1,p} - E_{M1,p} = -R_G I_{G1} - L_{MMC} \frac{dI_{G1}}{dt} + V_{cap} - E_{M1,p} \tag{6.14}$$

where L_{MMC} is the equivalent MMC inductance ($L_{MMC} = 2L_{arm}/3$), being L_{arm} the inductance of each MMC arm.

$$C_{eq} \frac{dV_{cap}}{dt} = I_{Vdc1,p} - I_{Vdc1,p0} \tag{6.15}$$

$$E_{I1,p} - L_c \frac{dI_f}{dt} - R_c I_f = (L_c + L_{MMC}) \frac{dI_{G1}}{dt} + (R_G + R_c) I_{G1} \tag{6.16}$$

Fig. 6.9 shows the comparison between theoretical and simulated fault currents when no actions are taken to limit the fault currents.

The fault current could be limited by using a high impedance grounding on the dc-side. Alternatively, the MMC can control the dc current by adjusting the dc voltage at the MMC terminals. In this case, a hybrid MMC using HB and FB cells is needed given that the MMC arms have to generate negative voltages. For this purpose, the dc voltage reference is changed to zero and the MMC changes to dc current current control. In this case, the voltage $E_{I1,p}$ changes to 0 in the previous analysis once the fault is detected. Fig. 6.10 shows the results when a hybrid MMC is used to block the fault currents.

This section has included the theoretical analysis for the fault current and fault voltages for systems consisting on Diode Rectifiers with resistive grounding and for both symmetrical and bipolar MMC stations. The expressions have been validated by means of EMT simulations and allow to calculate maximum fault currents and voltages for the considered configurations.

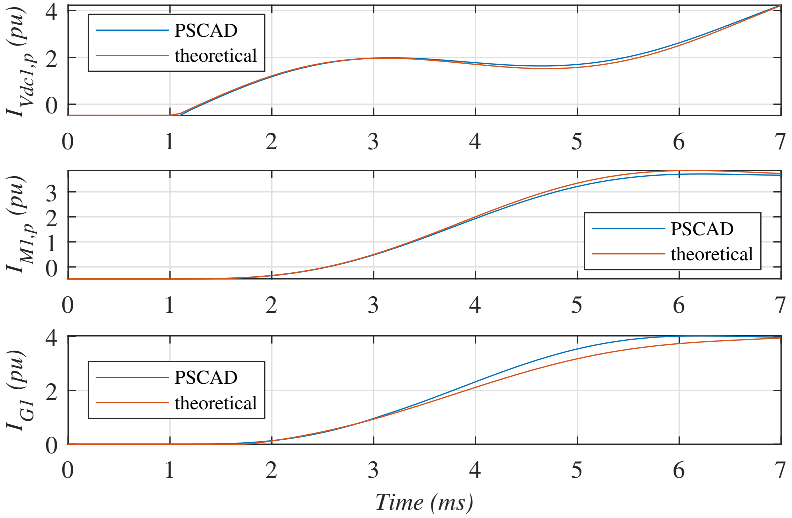

Figure 6.9: Comparison of the theoretical and PSCAD currents for a bipolar HVdc grid. From top to bottom: MMC-1 dc-current (positive pole); cable-1 current (positive pole); MMC-1 ground current.

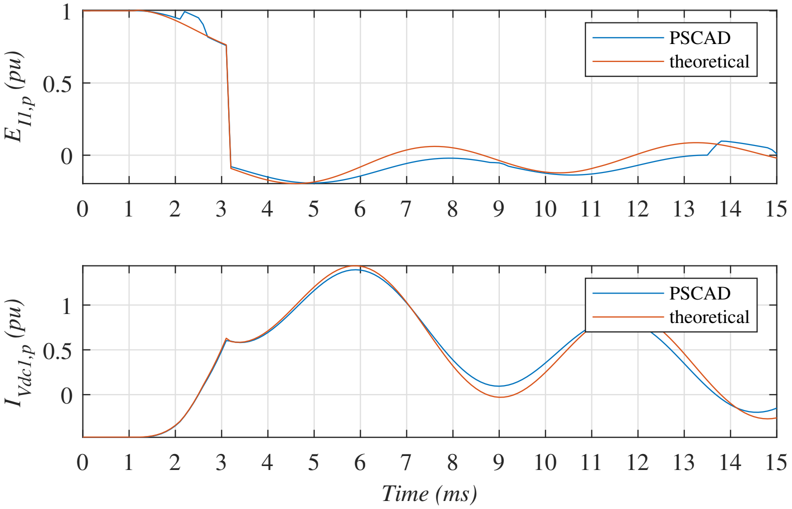

Figure 6.10: Comparison of the theoretical and PSCAD currents for a bipolar HVdc grid using hybrid MMCs. From top to bottom: MMC-1 dc-voltage (positive pole); MMC-1 dc-current (positive pole).

6.4 WTG Distance Protection

This section includes a description of the proposed distance protection strategy so WTGs can distinguish, by using only local measurements, if a fault is located at the off-shore ac grid or at the dc-cable.

WTG control can contribute to reducing overcurrents and overvoltages during faults [143, 93, 145]. However, WTG control needs to distinguish between off-shore ac-grid faults and HVdc faults. The reason being that, for off-shore ac-grid faults, the WTGs are feeding the fault and, hence, they can detect when the fault is cleared. However, for HVdc faults, the WTGs will reduce the ac-grid voltage so the diode rectifier stops conducting and the WTG does not contribute to steady state HVdc fault currents. Therefore, the WTGs cannot know, by themselves, that the HVdc fault has been cleared and they will require a command from the protection co-ordination system to resume active power injection.

Fig. 6.11 shows the apparent impedances ($\frac{V_{WTG}}{I_{WTG}}$) seen from a WTG when the fault is located at different places: high voltage side of the WTG transformer (Z_{WT-1}), DRU station ac-side (Z_{WT-2}), and DRU station dc terminals (Z_{WT-3}), as shown in Fig. 6.1. At 50 Hz, there is a clear difference between the apparent impedance seen by the WTGs for closest and furthest off-shore ac-grid short circuits and HVdc grid short circuits. Therefore, the WTG can distinguish between off-shore ac faults and HVdc faults. From Fig. 6.11, the corresponding detection limits are:

- Off-shore ac grid: apparent admittance $|I_{WTG}| \, / \, |V_{WTG}|$ larger than 4 pu.
- HVdc grid: apparent admittance between 1.25 pu and 3.5 pu.

However, the impedance difference between short circuits in different parts of the off-shore ac-grid is very small. The same can be said about short circuits in different locations of the HVdc cables. Therefore, while detecting if the fault is in the ac-grid or in the dc-grid is relatively straight forward, detecting the exact location of ac or HVdc faults using the proposed method is not.

6.5 HVdc Fault Protection Strategies

This section includes the study of the 5 different strategies for HVdc cable fault protection and recovery, which have been listed in the Introduction. The first 4 strategies consider a symmetric monopole, whereas the last one considers a bipolar configuration.

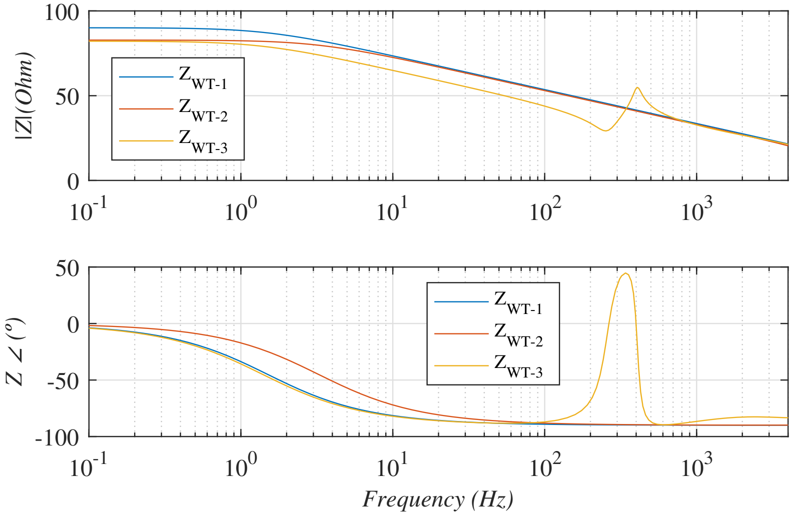

Figure 6.11: Impedance seen by the WTGs for different fault locations.

The performance of each protection strategy is evaluated by means of detailed EMT simulations. To ensure results as close as possible to an actual HVdc system, the EMT simulations carried out used HVdc frequency dependant cable models based on a geometry verified by manufacturers. WTG converter models have also been validated to behave in the same way as current commercial type-4 WTG converters, controllers use a control-software-in-the-loop approach, so delays and possible numerical issues are representative of an actual wind turbine converter controller. MMC simulations include transformers, grounding and individual cell modelling based on existing operational interconnectors. System parameters are included in Appendix 6.7.

The dcCBs are located at both HVdc cable ends and are shown as green squares in Fig. 6.1. The fault current at any of the DRU poles (I_{Rdc}) is cleared when the corresponding cable current I_H is cleared. For the scenarios where dcCBs are not used, they are substituted by disconnectors placed at the same locations as the dcCBs.

All dc cable fault studies assume a fault at the mid-point of the positive pole cable connecting MMC1 to the DRU-HVdc converter, which corresponds to fault 1 in Fig. 6.1.

MMC-1 is initially controlling the HVdc voltage (master), whereas MMC-2 and the OWPP are controlled to follow an active power set point. Once the fault is cleared, MMC-2 switches to voltage control mode.

For all the following fault studies, the DRU connected WPP is initially generating a 1 pu power, whereas MMC-2 has an active power setpoint equal to 0.5 pu and, hence, MMC-1 is drawing the remaining 0.5 pu power being injected by the WPP. When the fault is detected, the dc-breakers disconnect the faulty DC cable (both poles) isolating MMC-1, and MMC-2 turns to control the DC voltage (E_{I2}). At this stage, the WPP curtails its active power production to 0.5 pu, in this way the impact of a cable-1 fault on on-shore ac grid 2 is minimised. The DR station can easily detect if the fault has been in cable-1 or cable-2 and then send the corresponding power curtailment signal to the WPP controller.

The total clearing time for the considered dcCBs is 5 ms from fault onset to zero dc current [139, 146].

6.5.1 Fault response with solid DRU-MMC grounding

In symmetric monopole configurations, the high ac-side grounding impedance of the MMC stations lead to relatively small short-circuit currents, at the expense of healthy pole overvoltage, that might require the use of dc-choppers for pole voltage re-balancing [139].

The use of a solid ground for the DRU station does away with the need of dc-chopper for pole voltage re-balancing, at the expense of much larger short-circuit currents.

Fig. 6.12 shows the voltages at the terminals of each converter for a positive pole-to-ground fault at t=0.02s. The fault is detected and the corresponding dcCBs ($\mathrm{BK_{M1,pm}}$ and $\mathrm{BK_{H1,pm}}$ in Fig. 6.1) clear the fault in 5 ms and both cable poles are disconnected permanently. At this stage, MMC-2 switches to voltage control mode and both MMC-2 and DRU voltages return to their pre-fault values in less than 100 ms.

Fig. 6.13 shows the cable voltages at both ends of each cable. The top graph corresponds to the cable from MMC-1 to DRU and clearly shows that the voltage of the positive pole goes to zero as a result of the fault. The negative pole voltage is limited by the surge arrester and reaches -1.4 pu when the dcCBs are opened. On the other hand, the cable from the DRU to MMC-2 returns to ±1 pu voltage once the fault is cleared.

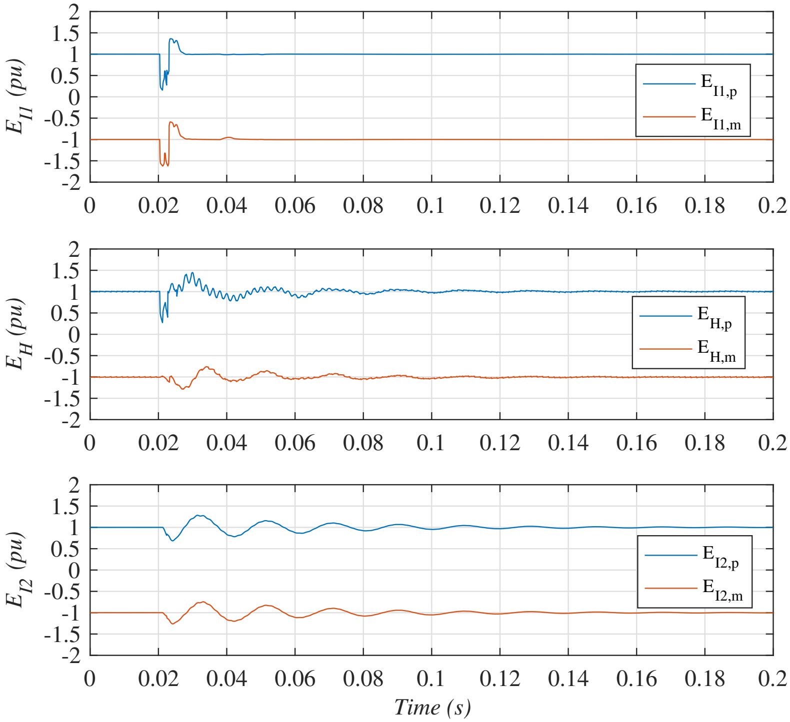

Figure 6.12: Strategy 1: Converter terminal voltages (pu). From top to bottom: MMC-1 dc-voltages; DRU dc-voltages; MMC-2 dc-voltages.

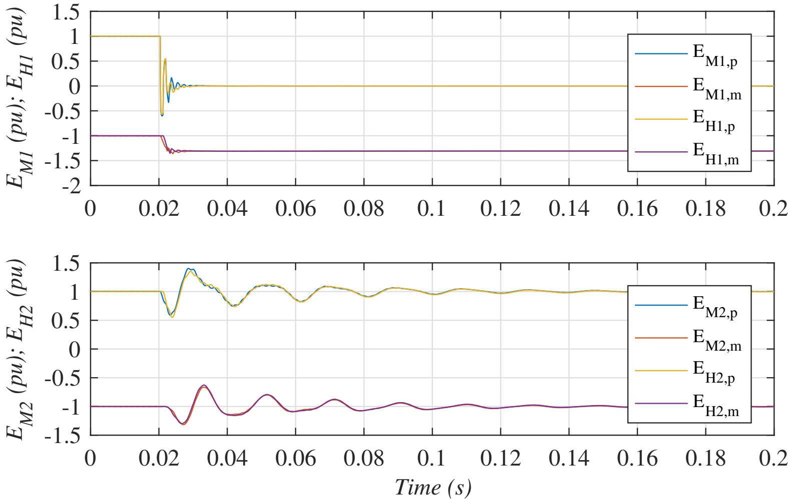

Figure 6.13: Strategy 1: Cable voltages (pu). From top to bottom: cable-1 voltages; cable-2 voltages.

The currents during the short circuit are shown in Fig. 6.14. The MMC-1 dc-side current I_{Vdc1} becomes negative, as it is flowing now through the HB cell diodes. After approximately 3 ms, the dcCB opens and the current now flows through the dcCB surge arresters until it reaches zero.

The dc-side DRU pole current ($I_{Rdc,p}$) reaches a peak value of 2 pu, which is well within the overcurrent capability of the diode rectifiers. The large ground fault current through the diode rectifier ground ($I_{Rdc,g}$) can also be clearly seen, with a value larger than -1.5 pu. On the other hand, the MMC-2 dc side current (I_{Vdc2}) reaches a value of 1.4 pu during fault recovery.

6.5.2 Fault response with resistive DRU-HVdc grounding

By using resistive grounding for the DRU converter, it is possible to limit the short circuit transient currents to adequate levels. However, resistive grounding could cause DRU converter overvoltages which would lead to somehow higher isolation requirements and higher stress to sourge arresters.

To analyze the effect of the resistive DRU grounding, a sensitive analysis has been carried out when a mid-point cable fault occurs between MMC-1 and DRU station. Fig. 6.15 shows the reduction of the maximum dc-fault current as a function of

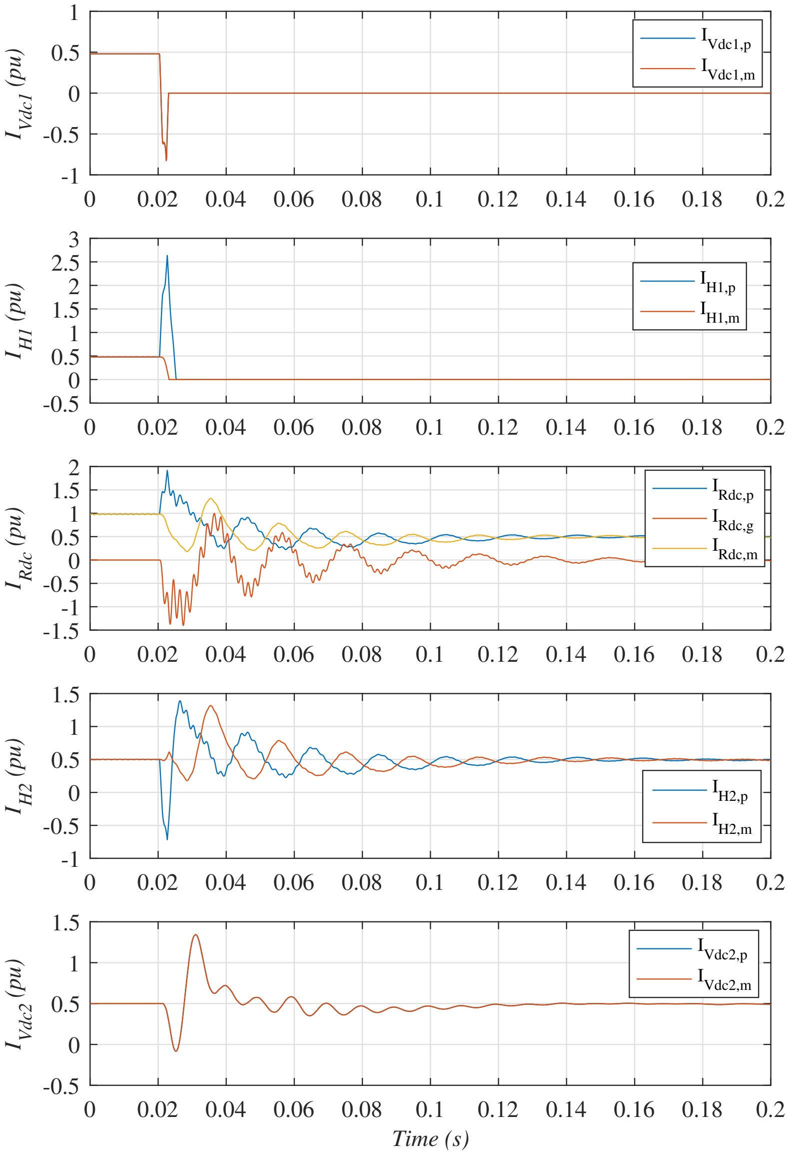

Figure 6.14: Strategy 1: HVdc currents (pu). From top to bottom: MMC-1 dc-currents; DRU to cable-1 dc-breaker currents; DRU dc-currents; DRU to cable-2 dc-breaker currents; MMC-2 dc-currents.

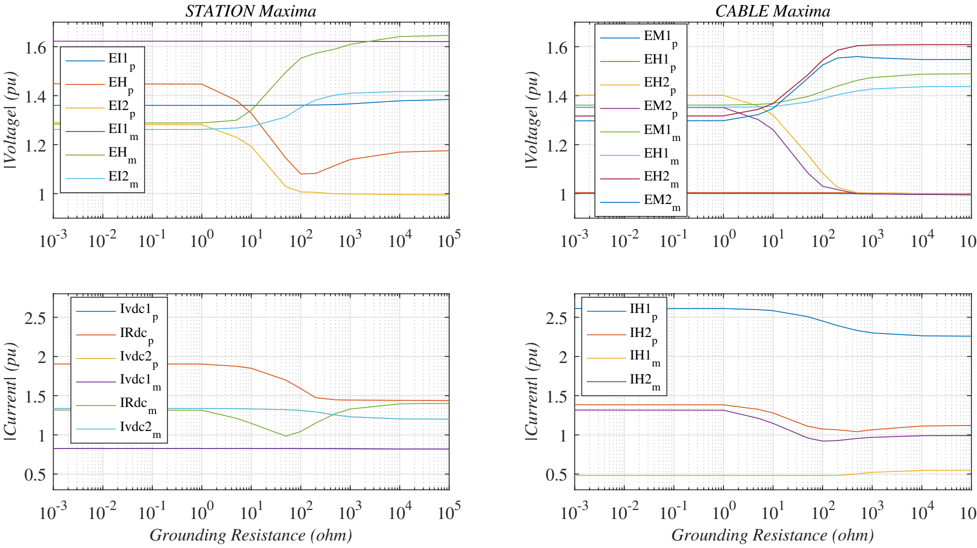

Figure 6.15: MMC-1-DRU cable short-circuit: HVdc voltages (pu) as a function of DRU grounding resistance.

the DRU grounding resistance (R_{DG}). This reduction occurs when $R_{DG} > 1\ \Omega$ and ceases when surge arresters increase their conduction at $R_{DG} > 1000\ \Omega$.

Fig. 6.15 also shows the increase of the maximum dc-voltages as a function of R_{DG}. Now dc-voltages increase from $R_{DG} = 1\ \Omega$ to $R_{DG} = 1000\ \Omega$. Therefore, based on the sensitivity analysis, a resistance value of $R_{DG} = 100\ \Omega$ has been chosen.

With $R_{DG} = 100\ \Omega$, pole-to-pole voltages at MMC-1 and MMC-2 are below 1.1 pu, and shows a 1.3 pu overvoltage at DRU station. Surge arrester energies are bellow 500 kJ, except the surge arresters of the dc-breaker which opens the cable current $I_{H1,p}$, (Fig. 6.1). This surge arrester has a total dissipated energy of 2700 kJ.

Figs. 6.16 to 6.17 show the dc-side voltages and currents for the same fault as the one considered in the previous section but including a DRU grounding resistor.

Maximum voltage values shown in Fig. 6.16 are almost the same as those in Fig. 6.12. However, Fig. 6.16 does not show the voltage oscillations seen in Fig. 6.12.

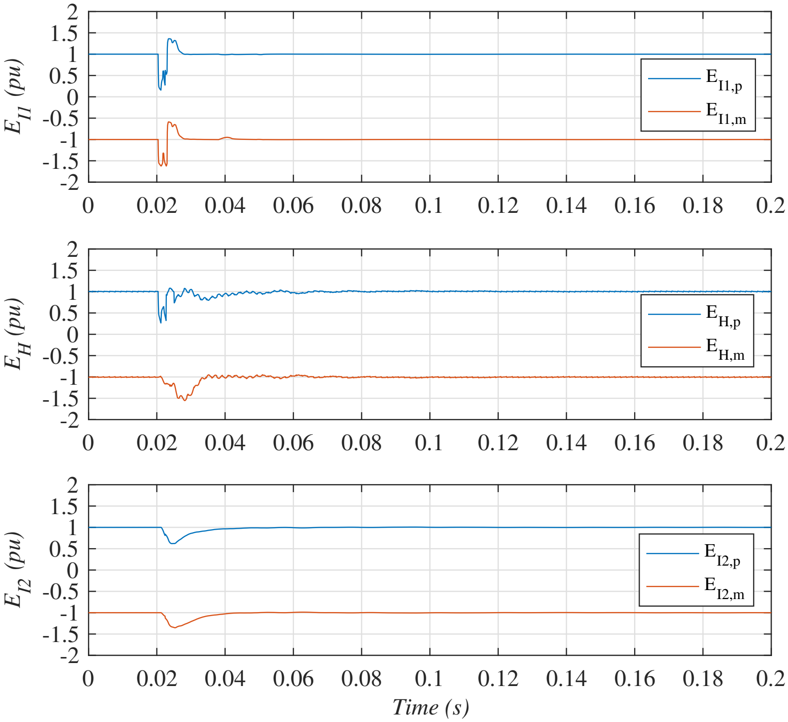

Figure 6.16: Strategy 2: Converter voltages (pu). From top to bottom: MMC-1 dc-voltages; DRU dc-voltages; MMC-2 dc-voltages.

Fig. 6.17 also does away with the oscillations seen in Fig. 6.14, particularly in I_{Rdc}, so clearly the grounding resistor cancels those oscillations. However, the use of a grounding resistor has only limited influence on the peak voltages and currents seen by the converters.

6.5.3 Fault response with grounding resistor and WPP blocking

This test case includes the use of a DRU grounding resistor and WPP reducing its production to zero once the dc-short circuit is detected by the WTGs. Once the short circuit is cleared, the WPP resumes production. The results are shown in Figs. 6.18 and 6.19.

Converter voltages in Fig. 6.18 do not show substantial differences from the previous two cases. However, Fig. 6.19 shows that currents I_{Rdc} go to zero when the WPP is blocked (i.e. its voltage is reduced so the HVdc-DRU does not conduct). Moreover the peak value of MMC-2 converter current (I_{Vdc2}) is greatly reduced. Power through MMC-2 resumes 100 ms after the fault onset, however, in the previous two cases, active power is resumed in less than 20 ms after the fault onset.

6.5.4 dcCB-less Strategy for Symmetric Monopole

The fourth strategy consists on the use of WTG distance protection and MMC blocking without using dcCBs. Clearly, this strategy is the most cost efficient, as relatively costly dcCB are substituted less expensive dc disconnectors. Fault currents are drawn to zero by a combination of MMC converter and WPP blocking. Fault energy is partly absorbed by MMC capacitors, and partly dissipated in the DRU grounding resistor and system surge arresters. Once fault currents are zero (or very near to zero), the fast dc disconnectors are opened and a signal is sent to the WPP to resume power production.

The results for the same fault as that in previos sections are shown in Figs. 6.20 and 6.21. Fig. 6.20 shows that fault currents take longer than in the previous case to reach zero and hence fault clearing times are larger in this case. However, the rest of the currents are similar to those in previous cases. Fig. 6.21 shows that voltages are also very similar to previous cases.

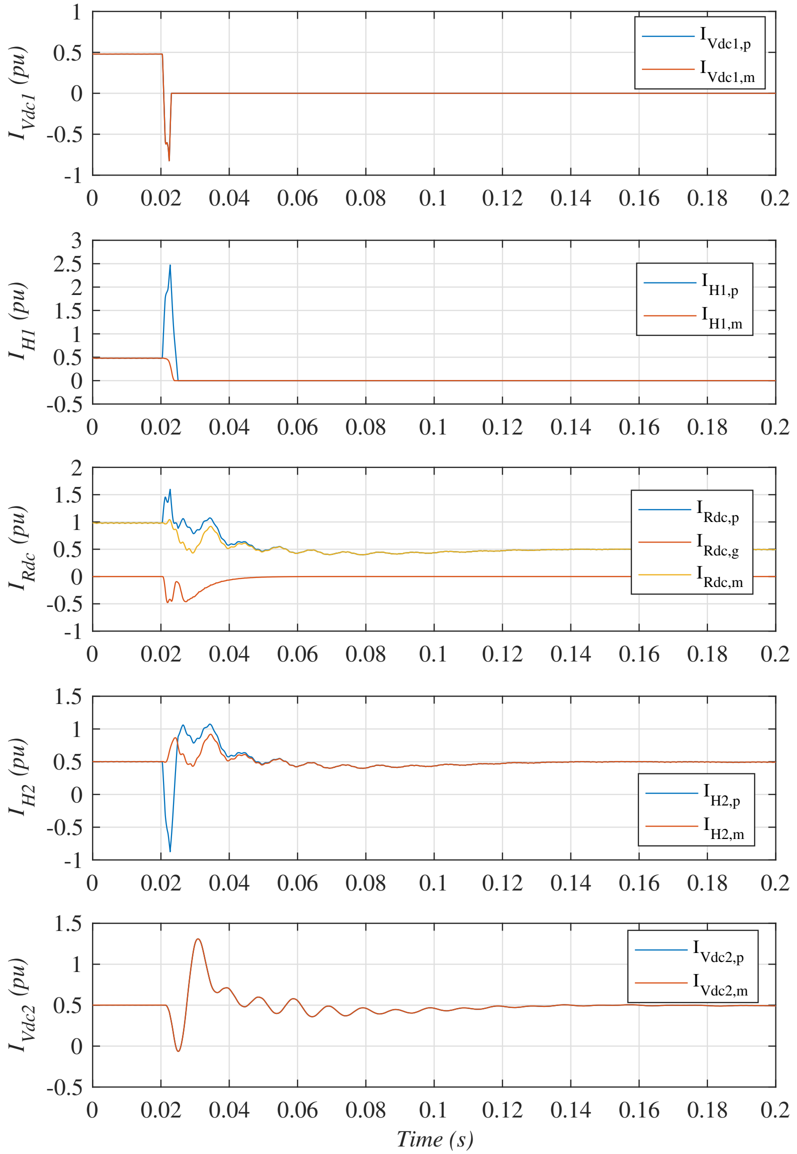

Figure 6.17: Strategy 2: HVdc currents (pu). From top to bottom: MMC-1 dc-currents; DRU to cable-1 dc-breaker currents; DRU dc-currents; DRU to cable-2 dc-breaker currents; MMC-2 dc-currents.

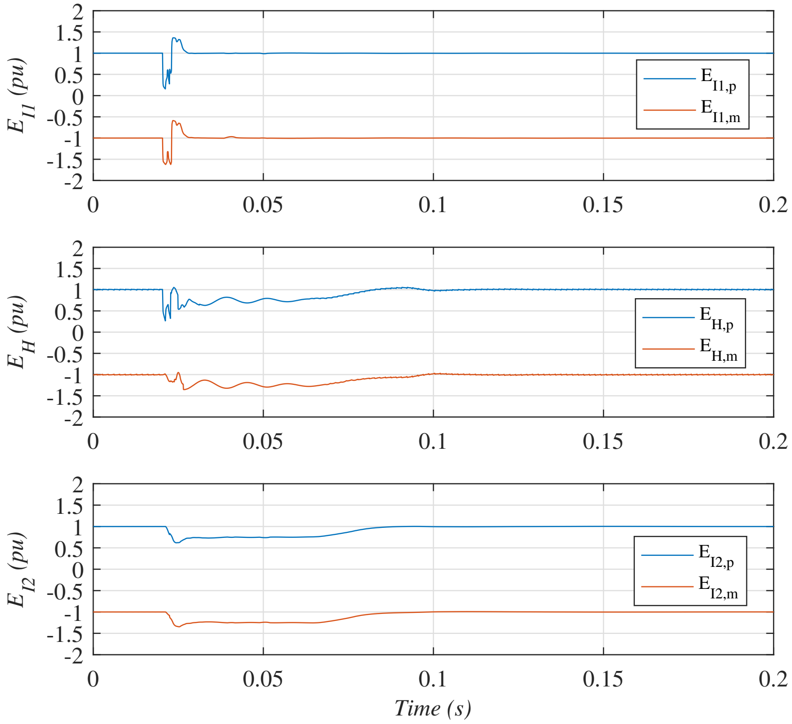

Figure 6.18: Strategy 3: Converter terminal voltages (pu). From top to bottom: MMC-1 dc-voltages; DRU dc-voltages; MMC-2 dc-voltages.

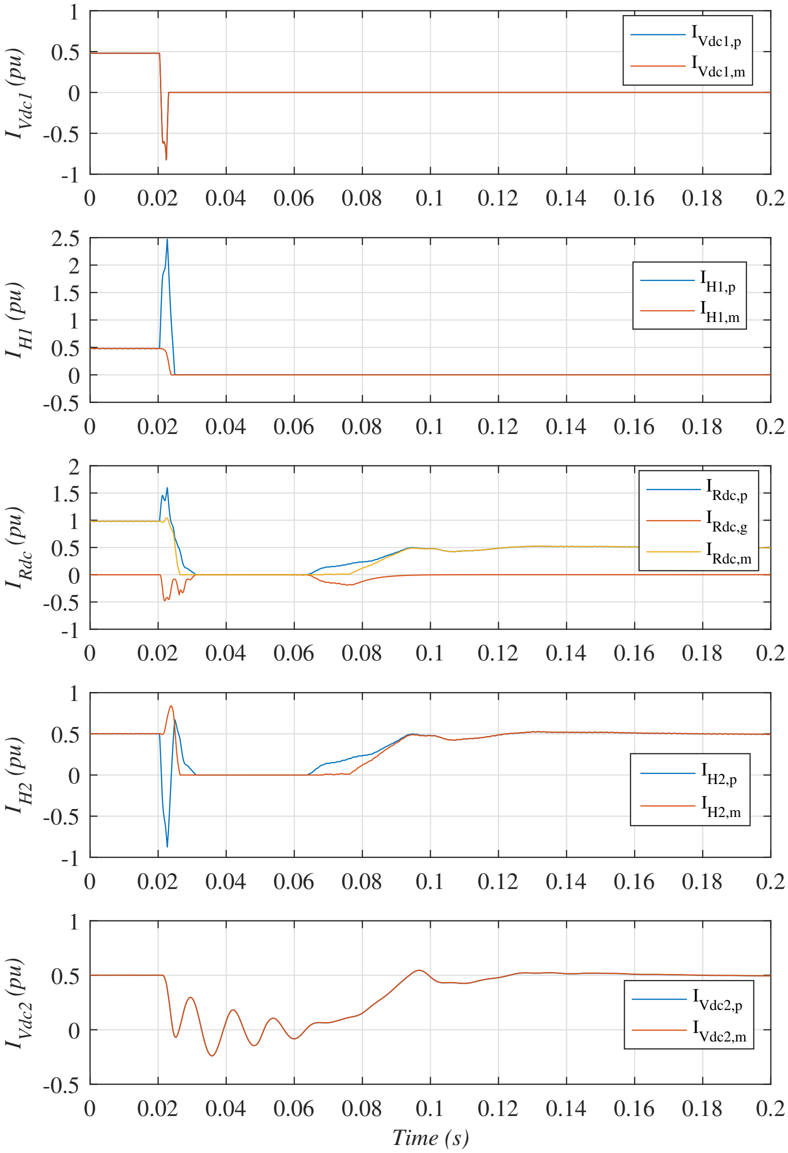

Figure 6.19: Strategy 3: HVdc currents (pu). From top to bottom: MMC-1 dc-currents; DRU to cable-1 dc-breaker currents; DRU dc-currents; DRU to cable-2 dc-breaker currents; MMC-2 dc-currents.

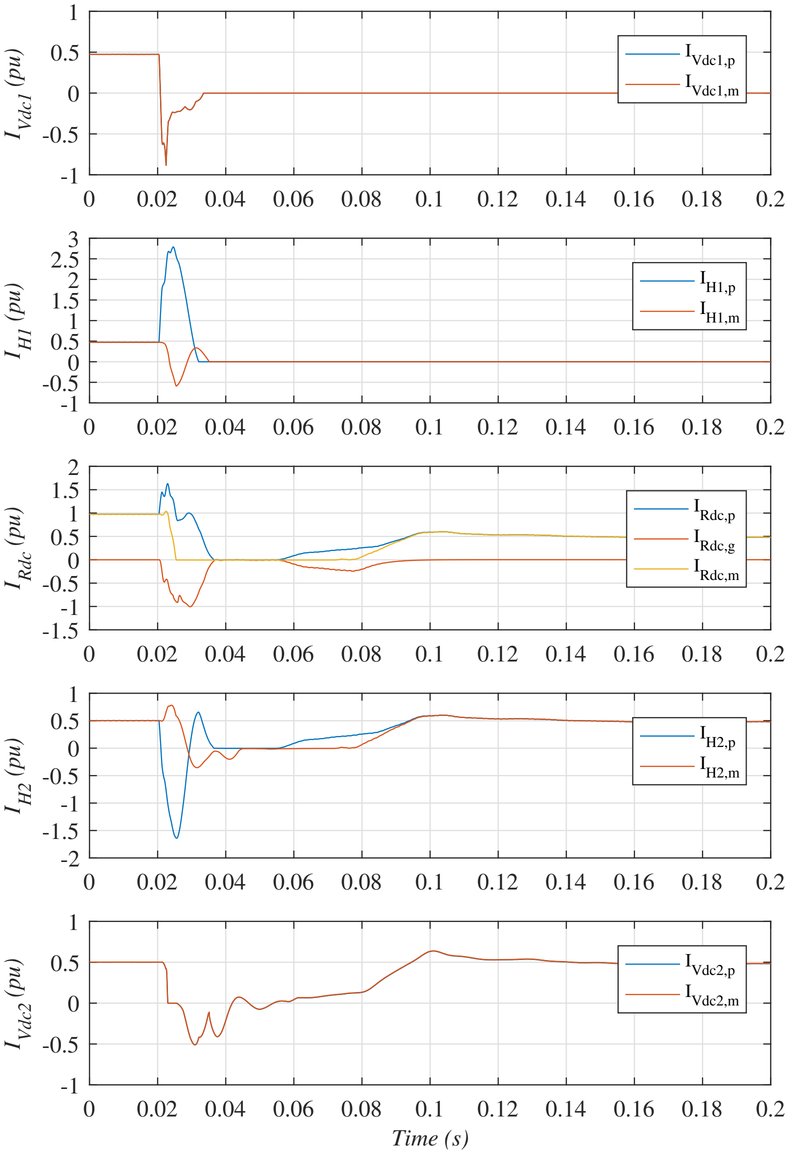

Figure 6.20: Strategy 4 (dcCB-less): HVdc currents (pu). From top to bottom: MMC-1 dc-currents; DRU to cable-1 dc-breaker currents; DRU dc-currents; DRU to cable-2 dc-breaker currents; MMC-2 dc-currents.

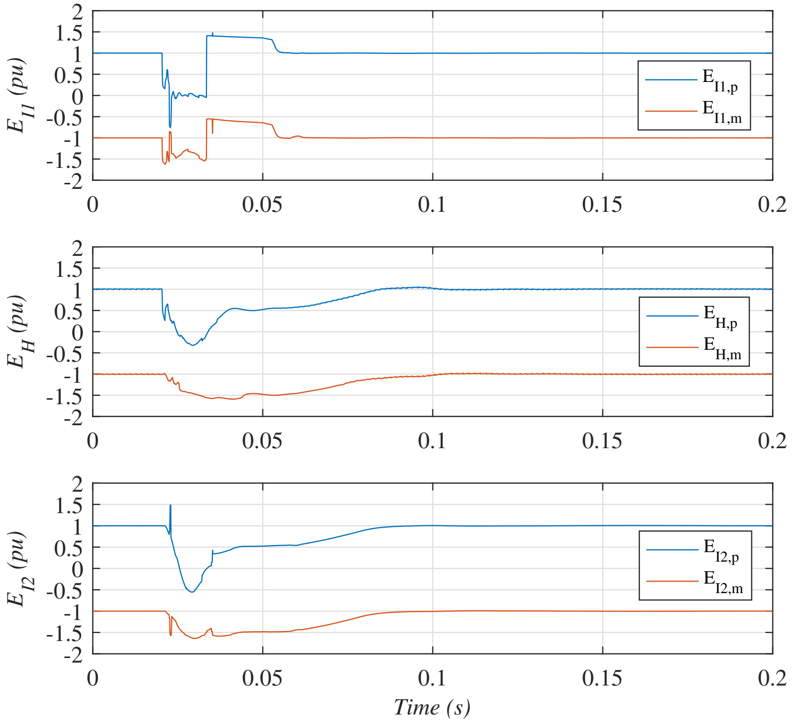

Figure 6.21: Strategy 4 (dcCB-less): HVdc voltages (pu). From top to bottom: MMC-1 dc-voltages; DRU dc-voltages; MMC-2 dc-voltages.

Table 6.2: Maximum pole voltage values (pu)

	$E_{I1,p}$	$E_{I1,m}$	$E_{H,p}$	$E_{H,m}$	$E_{I2,p}$	$E_{I2,m}$	V_{WT}
Solid DRU-MMC ground	1.36	-1.62	1.45	-1.28	1.27	-1.26	1.1
Resistive DRU-HVdc grounding	1.36	-1.62	1.08	-1.55	1.01	-1.35	1.04
Grounding resistor and WPP blocking	1.36	-1.62	1.06	-1.34	1.01	-1.35	1.0
WTG distance protection and MMC blocking	1.4	-1.62	1.06	-1.59	1.49	-1.64	1.07
Bipolar	1.0	-1.06	1.3	-1.06	1.04	-1.05	1.0

6.5.5 Bipolar HVdc Fault Blocking with Hybrid MMCs

Figs. 6.23 and 6.22 shows the response of the system in the event of a dc fault when the HVdc grid has a bipolar configuration. In this case, the HVdc grid is rigidly grounded at the dc-side and hybrid MMCs with 50% of FB-SMs are used. Similarly to the previous cases, the MMC-2 is in power control mode and the MMC-1 regulates the HVdc voltage. When a pole-to-ground occurs at the positive pole at $t = 0.02\ s$, the dc voltage of the positive pole collapses, Fig. 6.22. However, due to the use of FB-SMs, the MMCs can continue their operation and avoid large overcurrents. As soon as the fault is detected, the MMC-2 connected of the positive pole changes its current reference to zero. Moreover, the MMC-1 of the positive pole changes to power control mode with a current reference of zero too. In this way the fault current fed from both MMC stations drops to zero as seen in the first and fifth graphs of Fig. 6.23. Additionally, the WPP also stops injecting power to the HVdc grid so none of the three power stations feeds the fault (third graph). At this time, the dc switches are opened to isolate the faulty cable. Next both MMC-2 converters change to dc voltage control and the MMC-1 connected to the negative pole change to power control and the WPP resumes its operation. With this configuration, the negative pole is continuously in operation so ac grid 1 is not completely disconnected form the HVdc grid. Therefore, there is not a complete loss of power as in the monopolar configuration.

6.6 Comparison of Considered Strategies

The comparison of the considered strategies is carried out in terms of maximum pole-to-ground and pole-to-pole voltages, maximum currents during the fault, surge arrester dissipated energy and fault recovery times.

Table 6.2 shows the maximum pole voltage values for the each fault clearing strategy. The maximum pole voltage is 1.62 pu for the four symmetric monopole cases. It is worth noting that the DRU healthy pole voltage reaches 1.59 pu.

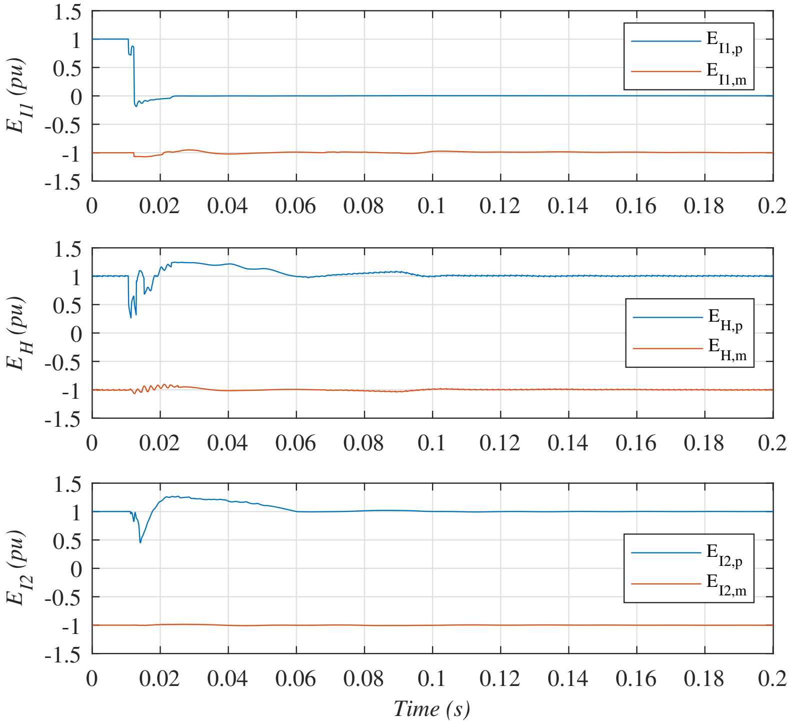

Figure 6.22: Strategy 5 (Bipolar). MMC-1 short-circuit: voltages (pu). From top to bottom: MMC-1 dc-voltages; DRU dc-voltages; MMC-2 dc-voltages.

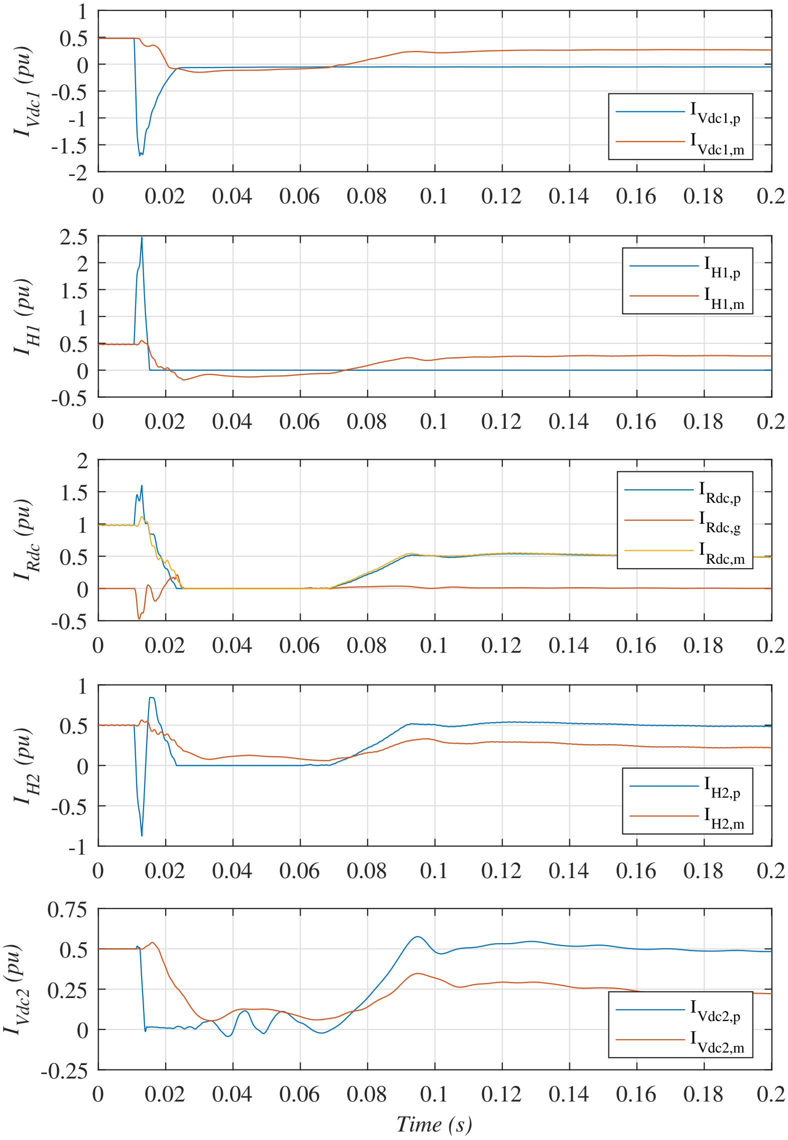

Figure 6.23: Strategy 5 (Bipolar). MMC-1 short-circuit: currents(pu). From top to bottom: MMC-1 dc-currents; DRU to cable-1 dc-breaker currents; DRU dc-currents; DRU to cable-2 dc-breaker currents; MMC-2 dc-currents.

Table 6.3: Maximum pole-to-pole voltage values (pu)

	E_{I1}	E_H	E_{I2}
Solid DRU-MMC ground	1.1	1.32	1.04
Resistive DRU-HVdc grounding	1.1	1.32	1.04
Grounding resistor and WPP blocking	1.1	1.15	1.02
WTG distance protection and MMC blocking	1.18	1.07	1.52
Bipolar	1.0	1.13	1.02

Table 6.4: Maximum current values (pu)

	$I_{Vdc1,p}$	$I_{Vdc1,m}$	$I_{H1,p}$	$I_{H1,m}$	$I_{Rdc,p}$	$I_{Rdc,g}$	$I_{Rdc,m}$	$I_{H2,p}$	$I_{H2,m}$	$I_{Vdc2,p}$	$I_{Vdc2,m}$	I_{WT}
Solid DRU-MMC ground	-0.81	-0.81	2.55	0.5	1.9	-1.4	1.31	1.38	1.32	1.34	1.34	1.2
Resistive DRU-HVdc grounding	-0.82	-0.82	2.5	0.5	1.6	-0.48	1.04	1.08	0.91	1.31	1.31	1.19
Grounding resistor and WPP blocking	-0.8	-0.8	2.5	0.5	1.6	-0.48	1.04	-0.88	0.83	0.6	0.6	1.33
WTG distance protection and MMC blocking	-0.88	-0.88	2.61	-0.59	1.62	-1.0	1.0	-1.64	0.78	0.62	0.62	1.17
Bipolar	-1.67	0.5	2.39	0.5	1.55	-0.47	1.11	0.77	-0.52	0.95	0.95	1.1

Clearly, the different parts of the system should be designed for the isolation levels in Table 6.2. The WTG voltages are within limits in all cases (up to 1.1 pu).

Table 6.3 shows the maximum pole-to-pole voltages, which determine the number of required diodes for the DRU valves (E_H). The sum of the cell voltages of each MMC arm is equal to the pole-to-pole voltage, therefore, the MMC power switches can withstand up to 2 pu pole-to-pole voltage without increasing the number of cells, albeit with increased isolation requirements. The voltage E_H shows that the DRUs valves need to be rated to 1.32 pu voltage for the first two strategies and only by a 7% for the dcCB-less strategy.

Table 6.4 shows the maximum values of currents for the considered test cases. The currents $I_{Vdc1,p,m}$ and $I_{Vdc2,p,m}$ show the current peak levels that the MMCs shall support in order to avoid damage. $I_{H1,p,m}$ and $I_{H2,p,m}$ show the maximum currents through the HVdc cables. The worst results (2.61 pu) are obtained for strategy 4. In any case, the duration of the peak current is shorter than 5 ms which is not enough to damage the cable. $I_{Rdc,p,g,m}$ show the peak current levels at DRU terminals. The largest fault current through the DRUs is obtained for the solid DRU grounding. However, a 1.9 pu current for a diode rectifier for a short period of time (13 ms) is perfectly acceptable. The maximum current peak of WTGs I_{WT} is 1.33 pu for strategy 3. The overcurrent lasts for a few milliseconds, and is within the short time overload capability of high power IGBTs. However, this possible overcurrent should be taken into account when designing the WTG converter.

Table 6.5: Surge Arrester Dissipated Energy (kJ)

	$W_{I1,p}$	$W_{I1,m}$	$W_{M1,p}$	$W_{M1,m}$	$W_{H1,p}$	$W_{H1,m}$	$W_{H2,p}$	$W_{H2,m}$	$W_{M2,p}$	$W_{M2,m}$	$W_{I2,p}$	$W_{I2,m}$
Solid DRU-MMC ground	0.3	332.6	242.4	126.52	3279	0.0	0.0	0.0	0.0	0.0	35.8	36.2
Resistive DRU-HVdc grounding	0.3	333.5	242.3	125.7	2690	0.0	0.0	0.0	0.0	0.0	35.8	36.2
Grounding resistor and WPP blocking	0.3	333.5	242.3	125.7	2626	0.0	0.0	0.0	0.0	0.0	35.8	36.2
WTG distance protection and MMC blocking	4.09	276.7	2.9	0.0	0.0	0.0	0.0	0.0	0.0	0.0	34.7	2316
Bipolar	0.2	0.2	0.0	0.0	2764	0.0	0.0	0.0	0.0	0.0	0.2	0.2

Table 6.6: Fault Recovery Times

	Time from fault detection to fault clearing (ms)	Time to recover previous power generation (ms)
Solid DRU-MMC ground	3	80
Resistive DRU-HVdc grounding	3	80
Grounding resistor and WPP blocking	2	70
WTG distance protection and MMC blocking	10.5	87
Bipolar	3	80

Table 6.5 shows the surge arrester dissipated energy. In any configuration, the surge arresters disipate energy in order to maintain the voltages in safe limits. The worse case is the symmetric monopole with solid ground (3279 kJ). When the DRU grounding resistor is used, there is a reduction on surge arrester energy. In any case, it is worth noting that different strategies lead to subtantially different surge arrester use.

Finally, table 6.6 shows the fault recovery times for each strategy. As expected, the longest clearing time (13 ms) is obtained with a symmetric monopole with both WPP and MMC blocking. In this case, HVdc fault clearing time is 13 ms, with relatively fast power recovery (80 ms), which is within the limits fixed in “(ENTSO-E) Network Code for HVdc connections” (0.14 s).

6.7 Conclusions

This paper includes the study of five protection strategies. Three of them require the use of dcCBs for the symmetric monopole connection. When both WPP and MMC converters are blocked, dcCBs can be substituted by fast disconnectors (or dcCBs of a much smaller rating). For this approach, it is required that the WTGs include distance protection features to distinguish between ac-collector faults and HVdc faults. For the sake of completeness, a case including hybrid MMCs in a bipolar configuration with full blocking capability have also been studied.

Table 6.7: Advantages and disavantages of the considered configurations

	Advantages	Disadvantages
Solid DRU-MMC ground	well known in literature Communication to WPP to clear faults not required	requires 35% extra DRU isolation dc-circuit breaker required
Resistive DRU-HVdc grounding	extra DRU isolation not required Communication to WPP to clear faults not required	dc-circuit breaker required
Grounding resistor and WPP blocking	extra DRU isolation not required	Communicatiion to WPP to clear faults required dc-circuit breaker required
WTG distance protection and MMC blocking	dc-circuit breaker not required	longer clearing times Communication to WPP to clear faults required
Bipolar	dc-circuit breaker not required additional redundancy	Increased cost requires 20% extra DRU isolation

For each strategy, the maximum voltages, currents, surge arrester energy and fault clearing times have been studied. The comparative advantages and disadvantages of each approach are shown in table 6.7.

Moreover, this paper has been shown that it is possible to use a protection strategy for symmetric monopole connectors without use of dcCBs, at the expense of longer clearing times and higher energy dissipated in surge arresters. This solution is particularly attractive as it is the less costly and allows active power flow through the healthy cable in a relatively short period of time after the fault.

APPENDIX

System Parameters

Table 6.8 shows the parameters values of the system components.

Table 6.8: System Parameters

Wind Turbines
Grid-side converter: 8 MW, 1.2 kVcc, 690 Vac, 50 Hz
Grid-side filter: $R_T = 476.1\ \mu\Omega$, $L = 18.94\ \mu$H, $C = 2674\ \mu$F
Transformer: 9.2 MVA, 0.69/66 kV, $R_W = 0.004$ pu, $X_W = 0.1$ pu, Saturable
Off-shore ac-grid
WTG to WTG distance: 2 km
WTG to ring-bus distance: 4 km
Distance between DRU platforms: 10 km
String cable sections: C = 150 mm^2, B = 185 mm^2, A = 400 mm^2
String with 8 WTGs: C-C-B-B-B-B-B-A
String with 9 WTGs: C-C-B-B-B-B-B-A-A
DRU Platform
Filter and compensation filter bank according to [124]
Transformer: 215 MVA, 66/43/43 kV, $R_{TR} = 0.004$ pu, $X_{TR} = 0.27$ pu
dc-smoothing reactor: 66.67 mH

Chapter 7

Aggregation of Type-4 Large Wind Farms Based on Admittance Model Order Reduction

Note: this chapter proposes an aggregation technique for type-4 based WPPs. Its contents are published on:

Martínez-Turégano, Jaime; Añó-Villalba, Salvador; Bernal-Perez, Soledad; Blasco-Gimenez, Ramon. (2019) Aggregation of Type-4 Large Wind Farms Based on Admittance Model Order Reduction. Energies, 9 (12), 1 - 21. 10.3390/en12091730

Abstract

This paper presents an aggregation technique based on the resolution of a multi-objective optimisation problem applied to the admittance model of a wind power plant. The purpose of the presented aggregation technique is to reduce the order of the wind power plant model in order to accelerate WPP simulation while keeping a very similar control performance for both the simplified and the detailed models. The proposed aggregation technique, based on the admittance model order reduction, ensures the same DC gain, the same gain at the operating band frequency and the same resonant peak frequency as the detailed admittance model. The proposed aggregation method is validated considering three 400 MW grid-forming type-4 WPPs connected to a Diode Rectifier HVDC link. The proposed aggregation technique is compared to two existing aggregation techniques, both in terms of frequency and time response. The detailed and aggregated models have been tested using PSCAD-EMT simulations, with the proposed aggregated model leading to a 350-fold reduction of simulation time with respect to the detailed model. Moreover, for the considered scenario, the proposed aggregation technique offers simulation errors which are, at least, three times smaller than previously published aggregation techniques.

Keywords: Off-shore wind farms; wind farm aggregation; admittance model order reduction; HVDC Diode Rectifiers, Grid Forming Wind Turbines.

7.1 Introduction

Large off-shore wind power plants (WPPs) with more than one hundred wind turbine generators (WTG) are currently operational or in planning or approval phases. Simulation studies covering individual WTGs during the design phase are very demanding from the computational point of view. When studying the impact of WPPs in the overall HVDC or HVAC transmission network, very detailed models are not generally required. Therefore, simulation complexity and computing time can be reduced by using aggregated WTG models. However, these aggregated models should provide a faithful representation of the actual WPP dynamics.

This is particularly important if the WPP consists of grid forming converters, such as when using Diode Rectifier (DR) based HVDC stations for the connection of the offshore WPP. The use of DR HVDC stations can reduce significantly Capital Expenditure (CAPEX) and Operational Expenditure (OPEX) by increasing the efficiency and robustness of the overall system [6, 11, 12, 13, 14, 15]. However, a large number of case studies are required in order to verify the correct integration of DR-connected WPPs.

Therefore, this paper is focused on the procedure to obtain an aggregated WTG model for large type-4 WPPs that allows the verification of grid forming WTG controllers for DR HVDC station connection. The presented aggregation technique aims at reducing the computational requirements of such verification, while achieving better simulation accuracy than current state-of-the-art aggregation techniques.

A large amount of literature has been developed on aggregation techniques for different applications [58, 59]. For example, [60] presented an aggregation technique based on power losses, while [61] presented an aggregation technique for grid disturbances studies. Reference [62] included a method for type-3 and type-1 WTG aggregation suitable for large power systems simulation. In this case, the WPP grid was aggregated using a short-circuit impedance method. In [63], an aggregated method based on voltage drop assumptions was performed as the most appropriate aggregation method for stability assessment studies. On the other hand, in [64] an aggregation method was proposed in order to represent the whole power system seen from the WTG AC terminals. Finally, an improvement on the aggregation method based on power losses for off-shore WPP with a diode-based HVDC link was proposed in [65].

However, none of previous methods are based on a model order reduction of the total WPP admittance model. The proposed model order reduction leads to better matching between the dynamic behaviour of the aggregated and full WPP models, as the aggregated system keeps the original dc admittance, fundamental frequency admittance and first resonance peak characteristics of the original system.

The paper is organised as follows. The second section shows the procedure to obtain the full admittance model of a typical WPP, consisting of a number of radially connected WTG strings, as this is the typical topology used in WPPs. Other WPP topologies (i.e. with different degree of meshing) can also be aggregated with the proposed method, by suitable modification of the analytical admittance calculation. The third section explains how to apply the proposed aggregation technique. The fourth section describes the system that is used in the fifth section to compare the proposed aggregation technique with other existing aggregation techniques found in the literature. The sixth section compares aggregated and detailed model of a WPP using PSCAD simulations, considering three different cases. The last sections includes the discussion of the proposed aggregation technique compared with other existing aggregation algorithms.

7.2 Full Order Admittance System Modelling

The proposed model aggregation technique is based on the resolution of a multi-objective optimisation problem applied to a full WPP admittance model. This section includes the analytical development of the WPP admittance model. The inputs to the model are the individual WTG voltages and its output is the WPP current at the point of common coupling (PCC).

Each considered WPP consists of n radial-connected strings, with each string consisting of m_i cascaded connected WTGs. This topology corresponds to the great majority of existing WPPs, as ring-connected strings are always exploited radially. In any case, it is very easy to modify the proposed analytical model to calculate the overall grid-admittance of other WPP topologies.

Fig. 7.1 shows the WTG-j ($j = 1, 2, ..., m_i$) in the string-i ($i = 1, 2, ..., n$) of the WPP. U_{ij} is the WTG grid-side converter, and (L_{Tij} and R_{Tij}) represents the WTG transformer. Several alternatives have been considered to model the array cables, e.g. [147] adds parallel L-R branches to a PI-model in order to represent the frequency dependent impedance of the cable. This model has been used in [148, 149] to obtain a state-space model and reduce the order of the cable model. Additionally, a frequency dependent Pi model of a three core submarine cable is studied in [150].

In the presented study case, PI-sections will be used to represent the cable dynamics (C_{Lij}, L_{Lij} and R_{Lij}), since the cable length between WTGs is less than 3 km with its resonant peak in frequencies higher than 1000 Hz. The use of PI-models offers a good trade-off between complexity and accuracy.

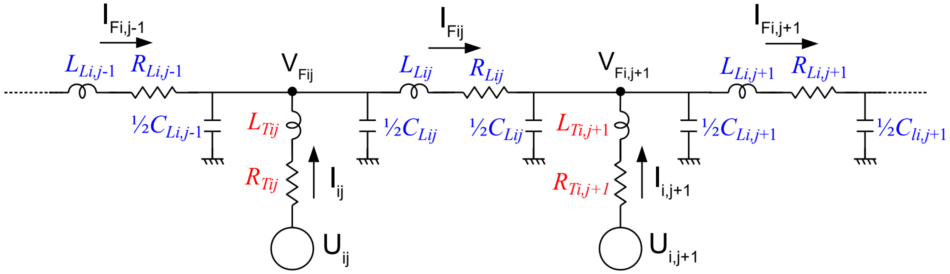

Figure 7.1: WTG-j ($j = 1, 2, ..., m_i$) in the string-i ($i = 1, 2, ..., n$) of the WPP.

7.2.1 String admittance model

The dynamics of the WTG-j ($j = 1, 2, ..., m_i$) and cable shown in fig. 7.1, can be written as:

$$U_{ij} = R_{Tij} \cdot I_{ij} + L_{Tij} \cdot \frac{dI_{ij}}{dt} + V_{Fij} \tag{7.1}$$

$$I_{Fi,j-1} + I_{ij} - I_{Fij} = \left(\frac{C_{Li,j-1}}{2} + \frac{C_{Lij}}{2} \right) \cdot \frac{dV_{Fij}}{dt} \tag{7.2}$$

$$V_{Fij} = R_{Lij} \cdot I_{Fij} + L_{Lij} \cdot \frac{dI_{Fij}}{dt} + V_{Fi,j+1} \tag{7.3}$$

where I_{ij} is the current from WTG-j, V_{Fij} is the voltage at the secondary side of the transformer, and I_{Fij} is the current through the cable. Note that for $j = 1$ (leftmost WTG) the current $I_{Fi,j-1}$ does not exist, and for $j = m_i$ (rightmost WTG) the voltage $V_{Fi,j+1}$ is the PCC voltage (V_F) which is considered a disturbance.

From equations (7.1), (7.2) and (7.3), the state-space admittance model of string-i ($i = 1, 2, ..., n$) can be calculated as:

$$\dot{x}_{st,i} = A_{st,i} \cdot x_{st,i} + B_{st,i} \cdot u_{st,i} + W_{st,i} \cdot V_F \tag{7.4}$$

$$y_{st,i} = C_{st,i} \cdot x_{st,i} \tag{7.5}$$

where the state vector $x_{st,i}$ and the input vector $u_{st,i}$ are:

$$x_{st,i} = \begin{pmatrix} I_{i1} & V_{Fi1} & I_{Fi1} & I_{i2} & V_{Fi2} & I_{Fi2} & \dots & I_{i,m_i} & V_{Fi,m_i} & I_{Fi,m_i} \end{pmatrix},$$
$$u_{st,i} = \begin{pmatrix} U_{i1} & U_{i2} & \dots & U_{i,m_i} \end{pmatrix}^T.$$

Matrices $A_{st,i}$, $B_{st,i}$ and $C_{st,i}$ are the state, input and output matrices respectively:

$$A_{st,i} = \begin{pmatrix} \frac{-R_{Ti1}}{L_{Ti1}} & \frac{-1}{L_{Ti1}} & 0 & 0 & 0 & 0 & 0 & 0 & 0 \\ \frac{2}{C_{Li1}} & 0 & \frac{-2}{C_{Li1}} & 0 & 0 & 0 & 0 & 0 & 0 \\ 0 & \frac{1}{L_{Li1}} & \frac{-R_{Li1}}{L_{Li1}} & 0 & \frac{-1}{L_{Li1}} & 0 & 0 & 0 & 0 \\ 0 & 0 & 0 & \frac{-R_{Ti2}}{L_{Ti2}} & \frac{-1}{L_{Ti2}} & 0 & 0 & 0 & 0 \\ 0 & 0 & \frac{2}{C_{Li1}+C_{Li2}} & \frac{2}{C_{Li1}+C_{Li2}} & 0 & \frac{-2}{C_{Li1}+C_{Li2}} & 0 & 0 & 0 \\ 0 & 0 & 0 & 0 & \frac{1}{L_{Li2}} & \frac{-R_{Li2}}{L_{Li2}} & 0 & 0 & 0 \\ & & & & & & \ddots & & \\ 0 & 0 & 0 & 0 & 0 & 0 & \frac{-R_{Ti,m_i}}{L_{Ti,m_i}} & \frac{-1}{L_{Ti,m_i}} & 0 \\ 0 & 0 & 0 & 0 & 0 & 0 & \frac{2}{C_{Li,m_i-1}+C_{Li,m_i}} & 0 & \frac{-2}{C_{Li,m_i-1}+C_{Li,m_i}} \\ 0 & 0 & 0 & 0 & 0 & 0 & 0 & \frac{1}{L_{Li,m_i}} & \frac{-R_{Li,m_i}}{L_{Li,m_i}} \end{pmatrix}$$

$$B_{st,i} = \begin{pmatrix} \frac{1}{L_{Ti1}} & 0 & 0 \\ 0 & 0 & 0 \\ 0 & 0 & 0 \\ 0 & \frac{1}{L_{Ti2}} & 0 \\ 0 & 0 & 0 \\ 0 & 0 & 0 \\ & \ddots & \\ 0 & 0 & \frac{1}{L_{Ti,m_i}} \\ 0 & 0 & 0 \\ 0 & 0 & 0 \end{pmatrix}, \quad C_{st,i} = \begin{pmatrix} 0 & 0 & 0 & 0 & 0 & 0 & \dots & 0 & 0 & 1 \end{pmatrix}$$

and:

$$W_{st,i} = \begin{pmatrix} 0 & 0 & 0 & 0 & 0 & 0 & \dots & 0 & 0 & \frac{-1}{L_{Li,m_i}} \end{pmatrix}^T$$

7.2.2 Overall Admittance model

The admittance model of the complete WPP is obtained by the radial connection of the n strings to the PCC (represented by voltage V_F). The state space dynamics of the overall system are:

$$\dot{x}_o = A_o \cdot x_o + B_o \cdot u_o + W_o \cdot V_F \tag{7.6}$$

$$y_o = C_o \cdot x_o \tag{7.7}$$

where A_o, B_o and C_o are the state, input and output of the overall system obtained by combining the string state space equations:

$$A_o = \begin{pmatrix} A_{st1} & 0 & & 0 \\ 0 & A_{st2} & & 0 \\ & & \ddots & \\ 0 & 0 & & A_{st,n} \end{pmatrix}, \quad B_o = \begin{pmatrix} B_{st1} & 0 & & 0 \\ 0 & B_{st2} & & 0 \\ & & \ddots & \\ 0 & 0 & & B_{st,n} \end{pmatrix}$$

$$C_o = \begin{pmatrix} C_{st1} & C_{st2} & \dots & C_{st,n} \end{pmatrix}$$

and:

$$W_o = \begin{pmatrix} W_{st1} & W_{st2} & \dots & W_{st,n} \end{pmatrix}^T$$

7.3 Aggregation Technique

The structure of the aggregated equivalent WPP is shown in fig. 7.2. At this point, the aggregation technique based on multi-objective optimisation is carried out by following these steps:

- Input reduction.
- Multi-objective optimisation problem statement.
- Multi-objective optimisation problem solution.

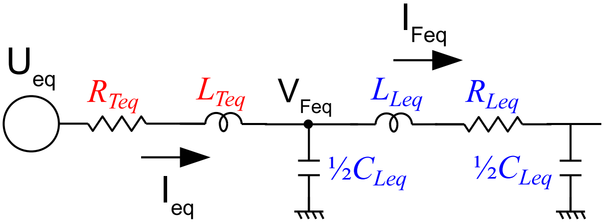

Figure 7.2: Model of an aggregated WPP.

7.3.1 Input Reduction

The proposed admittance model has a total of n voltage inputs that should be reduced to a single voltage input. Using the admittance model of the overall system, the superposition principle can be applied in order to obtain a single-input single-output model. The equivalent single input voltage source is obtained by introducing the vector σ in equations (7.6) and (7.7), leading to equations (7.8) and (7.9):

$$\dot{x} = A \cdot x + B \cdot \sigma \cdot u \tag{7.8}$$

$$y = C \cdot x + D \cdot \sigma \cdot u \tag{7.9}$$

σ is a vector with values 1 for connected WTGs or 0 for disconnected WTG:

$$\sigma = (\sigma_{1,1}, \sigma_{1,2}, \cdots, \sigma_{i,j}, \cdots, \sigma_{n,m_i})^T$$

The obtained SISO system has a single equivalent voltage input (u) and the WPP PCC current as an output ($I_F = I_{F1,m_1} + I_{F2,m_2} + ... + I_{Fn,m_n}$), and has a total of $3 \cdot n$ states, with n equal to number of WTGs in the WPP.

7.3.2 Multi-Objective Optimisation problem statement

The target aggregated model is shown in fig. 7.2, with dynamics:

$$\dot{x}_{eq} = A_{eq} \cdot x_{eq} + B_{eq} \cdot u_{eq} \tag{7.10}$$

$$y_{eq} = C_{eq} \cdot x_{eq} + D_{eq} \cdot u_{eq} \tag{7.11}$$

where the inputs of the aggregated WTG model u_{eq} are the aggregated voltage source (U_{eq}) and the voltage at the point of common coupling (V_F). The model output is the WPP current (I_{Feq}), and the state variables are I_{eq}, V_{Feq} and I_{Feq} as shown in fig. 7.2.

Matrices A_{eq}, B_{eq}, C_{eq} and D_{eq} are given below:

$$A_{eq} = \begin{pmatrix} -\frac{R_{Teq}}{L_{Teq}} & \frac{-1}{L_{Teq}} & 0 \\ \frac{1}{\frac{C_{Leq}}{2}} & 0 & \frac{-1}{\frac{C_{Leq}}{2}} \\ 0 & \frac{1}{L_{Leq}} & -\frac{R_{Leq}}{L_{Leq}} \end{pmatrix} \qquad B_{eq} = \begin{pmatrix} \frac{1}{L_{Teq}} & 0 \\ 0 & 0 \\ 0 & -\frac{1}{L_{Leq}} \end{pmatrix}$$

$$C_{eq} = \begin{pmatrix} 0 & 0 & 1 \end{pmatrix} \qquad D_{eq} = \begin{pmatrix} 0 & 0 \end{pmatrix}$$

The reduced order model in equations (7.10) and (7.11) has 5 parameters to be identified (L_{Teq}, R_{Teq}, L_{Leq}, R_{Leq} and C_{Leq}). In order to formulate the multi-optimisation problem properly, the following considerations are made:

- The aggregated capacitance C_{Leq} is considered as the sum of the total shunt capacitance in the WPP grid [60].
- The factor X_T/R_T of the WTG transformer shall be maintained in the aggregated transformer ($X_{Ti}/R_{Ti} = X_{Teq}/R_{Teq}$).

At this point, three objectives are proposed to identify the remaining 3 parameters for the aggregated model, namely:

- Minimise the error between the DC gain of aggregated ($K_{\omega=0Hz}$) and the high order SISO system ($K^*_{\omega=0Hz}$).
- Minimise the error between the gain of the aggregated WTG model at the grid frequency ($K_{\omega=\omega_0 Hz}$) and that of the high order SISO system ($K^*_{\omega=\omega_0 Hz}$).
- Minimise the error between the frequency of the resonant peak (ω_{peak}) of the aggregated WTG model and the frequency of the first resonant peak of the high order SISO system (ω^*_{peak}).

Finally, we shall consider that the WTG model parameters to identify always shall be positive and within a defined range ($R_{Teq,min} < R_{Teq} < R_{Teq,max}$, $R_{Leq,min} < R_{Leq} < R_{Leq,max}$, and $L_{Leq,min} < L_{Leq} < L_{Leq,max}$).

From the assumptions above, the following multi-objective optimisation function is defined for the aggregated model:

$$f(R_{Teq}, L_{Leq}, R_{Leq}) = \begin{pmatrix} \omega_{peak}(R_{Teq}, L_{Leq}, R_{Leq}) \\ K_{\omega=0}(R_{Teq}, L_{Leq}, R_{Leq}) \\ K_{\omega=\omega 0}(R_{Teq}, L_{Leq}, R_{Leq}, \omega_0) \end{pmatrix} \tag{7.12}$$

The goal function (f^*) obtained from the system described in equations (7.8) and (7.9). Therefore, the aim of the optimisation problem is to minimise the maximum of

$$W_i(f(R_{Teq}, L_{Leq}, R_{Leq}) - f^*) \tag{7.13}$$

where W_i is a diagonal matrix containing the weights to scale each function of $f(R_{Teq}, L_{Leq}, R_{Leq})$. Additionally, the minimisation problem shall satisfy the constraints:

$$\begin{pmatrix} R_{Teq,min} \\ L_{Leq,min} \\ R_{Leq,min} \end{pmatrix} < \begin{pmatrix} R_{Teq} \\ L_{Leq} \\ R_{Leq} \end{pmatrix} < \begin{pmatrix} R_{Teq,max} \\ L_{Leq,max} \\ R_{Leq,max} \end{pmatrix}$$

The multi-objective optimisation problem is solved by the Goal Attainment Method described in [66, 67, 68, 69]. The criteria used to choose the initial parameter and weight estimates is included in section 7.5.1.

7.4 HVDC Diode Rectifier-connected Wind Power Plant

The system under study is shown in Fig. 7.3. It consists of three 400 MW WPPs connected to the on-shore network through a diode rectifier based HVDC link [6, 65].

Each WPP consists of 50 type-4 WTGs rated at 8 MW each one. Each WTG generator has a full scale back-to-back converter, a PWM filter and a WTG transformer that are connected to the 66 kV off-shore AC grid.

Each one of the three WPPs ($k = 1, 2, 3$) is composed of 50 WTGs, distributed in $n = 7$ strings ($i = 1, 2, ..n$) with m_i wind turbines per string ($j = 1, 2, ..m_i$).

Finally, the rectifier station consists of three Diode Rectifier platforms, dc-side series connected. The rectifier stations are connected by means of the HVDC cable to the onshore VSC station, as shown in fig. 7.3. Each DR station consists

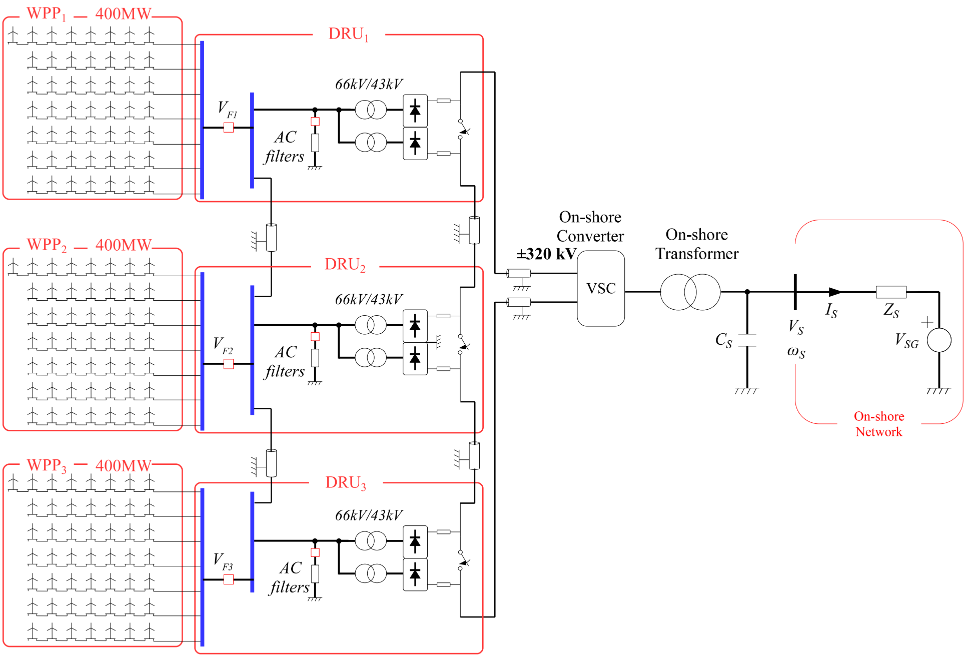

Figure 7.3: Off-shore WPP with 3 WPPs of 400 MW each one connected to the on-shore grid through a diode based HVDC link.

of two 12-pulse DR bridges, together with the corresponding transformers and ac-filters [65].

The implemented control is shown in fig. 7.4. The control consists of a centralised controller for the total delivered active power P_{OWPP}:

$$P_{OWPP} = \sum_{k=1}^{3} \sum_{i=1}^{n} \sum_{j=1}^{m_i} P_{WTG,ijk}$$

and a distributed controller based on a standard P/ω, Q/V droop controller.

The centralised controller is based on a PI controller operating at 20 ms sampling time. Using the total optimum power reference from the WTGs (P^*_{OWPP}) and the actual power being generated by the WPP (P_{OWPP}), the controller calculates the reference voltage (U^*_0) to be used by each individual WTG droop controller. ω^*_F is the grid frequency reference. A communication delay of 40 ms is considered

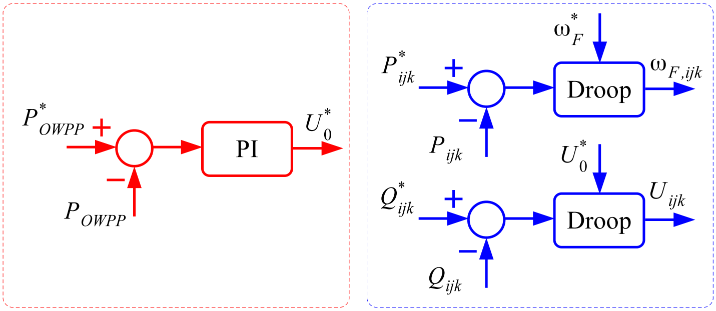

Figure 7.4: Left: Centralized power control; Right: Distributed droop controls

for the WPP active power controller. The WPP active power controller has a bandwidth of 4 Hz.

Each WTG implements a distributed P/ω and Q/V droop controller. The droop controller calculates the frequency ω_{Fijk} and the voltage U_{ijk} of the WTGs grid side converters (GSC) using the measured and reference active power P_{ijk} and the reactive power Q_{ijk} respectively. Local P_{ijk} and Q_{ijk} measurements are filtered with a 10 rad/s low pass filter. More advanced controllers can also be implemented for P and Q sharing amongst wind turbines [29].

The ac-cable parameters, as well as all those of the system in fig. 7.3 are listed in the appendix.

7.5 Wind Power Plant Aggregation

This section includes the application of the proposed technique to the described case, and its comparison with two well established aggregation strategies.

7.5.1 Aggregation based on multi-objective optimisation

The state space admittance model of each one of the wind power plants is obtained following the procedure explained in section 7.2, including input reduction with σ equals to a vector of ones. The state space model thus obtained is of order 150.

Before carrying out the multi-objective optimisation, it is important to ensure that the full system can be reduced to a system with only with three states (according to equations (7.10) and (7.11)). To this avail, the contribution of each state has been analysed obtaining the *Hankel Singular Values* of the system. Fig. 7.5 shows that the dynamics of the complete system are mainly dominated by three states, therefore, a third order reduced system can effectively capture most of the dynamic behaviour of the full order system.

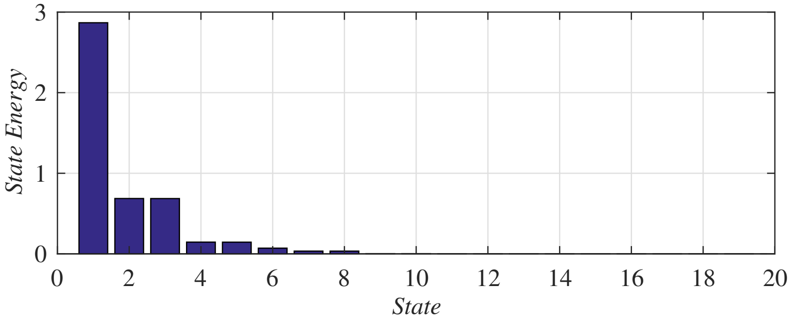

Figure 7.5: Hankel Singular Values (State Contributions; first 20 states are shown).

To carry out the multi-objective optimisation problem, the weights W_i and the restrictions on R_{Teq}, L_{Leq} and R_{Leq} need to be defined. To properly set the weights W_i, it is important to notice that the first objective used in the optimisation function (7.12) is related to a frequency while the other two are related to gains. Therefore, the weight W_i related to the first optimisation objective is 1000 times higher than the other two weights. The selected weights W_i is shown in the Appendix.

The parameters R_{Teq}, L_{Leq} and R_{Leq} are restricted to be always positive. Moreover, their limits can be further refined. Restriction on the equivalent resistance can be obtained from the objective $K^*_{\omega=0}$. Analysing the circuit of the Fig. 7.2, we know that the sum of $R_{Teq} + R_{Leq}$ shall be equal to $1/K^*_{\omega=0}$. So, the maximum value of the addtion of both resistors is $1/K^*_{\omega=0}$.

The restrictions on L_{Leq} are calculated by considering the simplified expression for the cable first resonant frequency:

$$\omega_{res} = \sqrt{\frac{1}{LC}} \rightarrow L_{ini} = \frac{1}{C_{eq}\omega_{res}^2} \tag{7.14}$$

where C_{eq} is the total array cable capacitance and ω_{res} is the first cable resonance frequency obtained from the detailed state space admittance model. Therefore, the restrictions for L_{Leq} are set to $[0.01L_{ini}, 100L_{ini}]$. The selected parameter ranges are shown in the Appendix.

When all the restrictions set, the multi-objective optimisation problem is solved, and the obtained parameters are shown in Table 7.1. Figure 7.6 shows the admittance of the obtained aggregated model as a function of frequency.

7.5.2 Aggregation based on Voltage Drop

The voltage drop aggregation method presented in [63] is proposed in order to simplify frequency response analysis for WTG interaction with the grid. The following equations are a summary of the aggregation method in [63]. When WTGs are connected in a string, the total equivalent string impedance is:

$$Z_{ik} = \frac{1}{m_i} \sum_{j=1}^{m_i} j Z_{ijk} \tag{7.15}$$

where Z_{ik} is the equivalent R-L impedance corresponding to the i-th string of the k-th WPP and Z_{ijk} is the cable R-L impedance between WTGs j and $j+1$. Equation (7.16) is used for the parallel connection of several strings.

$$Z_k = \frac{1}{\sum_{i=1}^{n} \frac{1}{Z_{ik}}} \tag{7.16}$$

where Z_k is the equivalent impedance of WPP k. The aggregated capacitance of the system is obtained as follows:

$$C_k = \sum_{j=1}^{m_i} \sum_{i=1}^{n} C_{ijk} \tag{7.17}$$

where C_{ijk} is the cable capacitance between WTGs j and $j+1$. Additionally, the WTG transformer impedance and PWM filter are scaled by using their per unit values and taking into consideration how many WTGs are in operation.

Following these steps, an aggregated model of the system has been calculated. Obtained values are shown in Table 7.1.

7.5.3 Aggregation based on Power Losses

WTG aggregation based on power losses is used for load-flow studies and also in electromechanical (RMS) stability. Moreover, this aggregation technique has been applied successfully in many real-life wind farm projects [58].

The power loss aggregation technique proposed in [60] is based on the following equations:

$$Z_{ik} = \frac{1}{m_i^2} \sum_{j=1}^{m_i} j^2 Z_{ijk} \tag{7.18}$$

$$Z_k = \frac{\sum_{i=1}^{n} m_i^2 Z_{ik}}{[\sum_{i=1}^{n} m_i]^2} \tag{7.19}$$

$$C_k = \sum_{j=1}^{m_i} \sum_{i=1}^{n} C_{ijk} \tag{7.20}$$

where Z_{ik} is the equivalent R-L impedance corresponding to the i-th string of the k-th WPP, Z_{ijk} is the R-L cable impedance between WTGs j and $j+1$, C_{ijk} is the cable capacitance between WTGs j and $j+1$ and C_k is the total capacitance of WPP k.

In the same way as the voltage drop based aggregation, WTG transformer impedance and PWM filter are scaled from their pu values, taking into consideration how many turbines are in operation.

The values obtained for this aggegation method applied to the considered case study are shown in Table 7.1.

7.5.4 Analytical Frequency Response of Different Aggregation Techniques

Table 7.1 shows the resulting parameters of aggregated models obtained with the proposed aggregation technique and with two alternative state-of-the-art techniques.

Figure 7.6 shows the WPP grid admittance as a function of frequency of the complete 150 state SISO model, as well as that of each one of the aggregated models (multi-objective optimisation, voltage drop and power losses aggregation). All

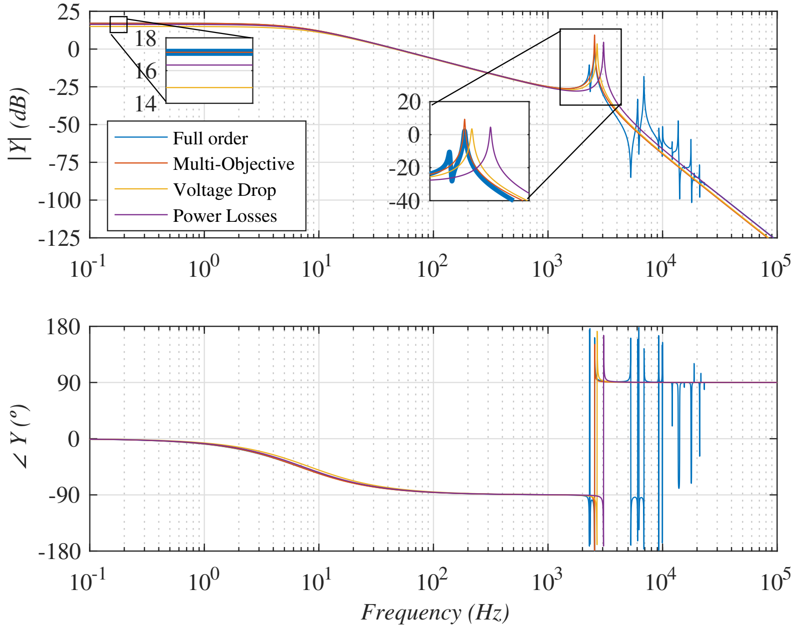

Figure 7.6: WPP grid admittance as a function of frequency: Blue: 150 order system; red: multi-objective optimisation; yellow: voltage drop; purple: power loses.

Table 7.1: Equivalent parameters obtained from different aggregation methods

	V. Drop	**P. Losses**	**Sys. red.**
$\mathbf{L}_T$ (mH)	3.0143	3.0143	2.825483
$\mathbf{R}_T$ (Ω)	0.094696	0.094696	0.088765
$\mathbf{C}_L$ (μF)	18.135	18.135	18.135
$\mathbf{L}_L$ (mH)	0.41342	0.31412	0.509834
$\mathbf{R}_L$ (Ω)	0.08384	0.057677	0.059011

aggregation techniques show a relative good agreement with the detailed model admittance for a wide range of frequencies.

However, the proposed technique shows a much closer match of low frequency admittance values and, more importantly, an excellent match of both main resonant peak frequency and amplitude. It is worth noting that both voltage drop and power loss based aggregation show main resonant peak frequencies that are far off from the actual resonant peak. The largest error is obtained from the power loss error, which leads to a resonant peak frequency more than 500 Hz higher than its actual value.

Additionally, different WPP topologies have been studied, in order to verify that the proposed aggregation technique is valid for different WPP configurations. The studies covered different number of connected strings and also different numbers of connected WTGs per string. In all cases, the multi-objective aggregation technique always showed a better admittance frequency response match that the other two considered aggregation techniques.

Clearly, the results in Fig. 7.6 represent small signal operation, however, the proposed aggregation technique has a very good agreement with the actual grid admittance for a very wide range of frequencies, including the main resonant peak. Therefore, the proposed aggregation technique is expected to show dynamic characteristics very close to the detailed 150 state system. The dynamic response of the proposed and state-of-the-art techniques is covered in section 7.6.

7.6 Results

The frequency results in fig. 7.6 suggest that the proposed aggregation method should be able to represent the full system dynamics with less error than the other two considered aggregation techniques. Therefore, the EMT simulation of the considered test cases are carried out in order to verify the dynamic behaviour of each aggregation method.

Four scenarios have been considered, one with full detail models of each cluster (considering the full 150 WTGs of 8 MW each), and considering an aggregated equivalent for each one of the three 400 MW cluster (with multi-objective optimisation, voltage drop and power losses aggregation methods).

The PSCAD-EMT simulations for the system shown in fig. 7.3 have been carried out in all the four scenarios considered. However, for the sake of clarity, only the full simulation results corresponding to the detailed and multi-objective aggregated model are shown in the simulation section. The results corresponding to the other two aggregation methods are shown as errors with respect to the detailed model simulations.

The validation of the aggregated models has been carried out by comparing the active and reactive power, voltage and current (P_{Fk}, Q_{Fk}, V_{Fk}, I_{Fk}) responses at the points of common coupling of each one of the wind power plants (busses $\text{PCC}_{1,2,3}$ in fig. 7.3).

Three test cases have been considered:

- Fast changes in active power reference.
- Disconnection of one of the three wind power plants.
- Disconnection and re-connection of Diode Rectifier Station ac-filters.

Finally, a study of the computational load of each alternative has been carried out.

7.6.1 Simulation Results

Case 1: Fast changes in active power reference

The three wind power plants are initially operated in islanding mode (DR not conducting) with a voltage reference of 0.87 pu. From this state, the active power reference is ramped up from 0 to 1 pu in 150 ms of all three WPPs at the same time. Once all the WPPs reach their steady state operation, several step transients on active power reference are applied from 1 down to 0.5 pu, by sequentially reducing the active power reference P_{Fk}^{*} of each individual wind power plant.

Fig. 7.7 shows the behaviour of the active power P_{Fk}. Initially, the active power reference P_{Fk}^{*} rises to 1 pu at $t = 0.2$ s, but power production does not increase until currents begin to flow through the DR at $t = 0.25$ s. The reason for this is that the ac-side DR voltage has to be higher than 0.9 pu for the DR station to start conducting. Then, at $t = 0.8$ s the active power reference P_{Fk}^{*} is decreased to 0.5 pu in each cluster every 0.7 s. Such rapid active power transients might not be realistic, but have been chosen as a extreme case for validation purposes. Fig. 7.7 clearly shows that both aggregated and detailed models lead to very similar active power dynamic results.

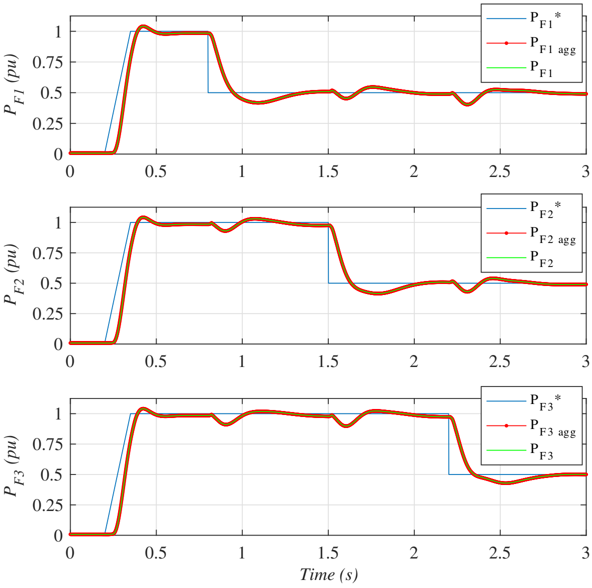

Figure 7.7: Case 1. Active Power P_{Fk} at PCC-k of each diode rectifier platform for detailed and aggregated models.

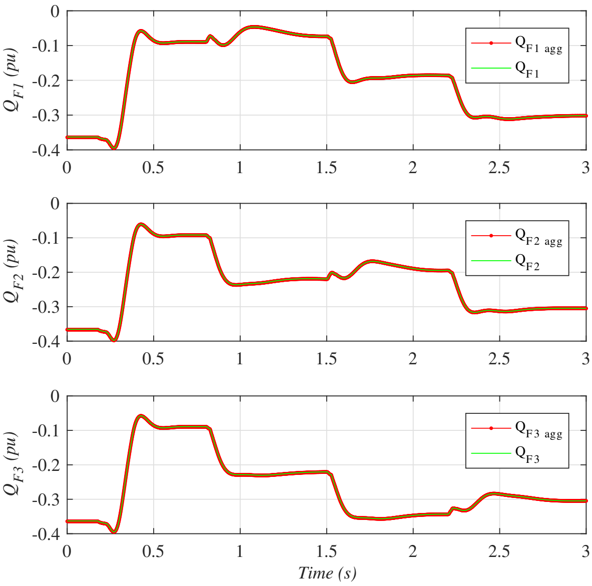

Figure 7.8: Case 1. Rective Power Q_{Fk} at PCC-k of each diode rectifier platform for detailed and aggregated models.

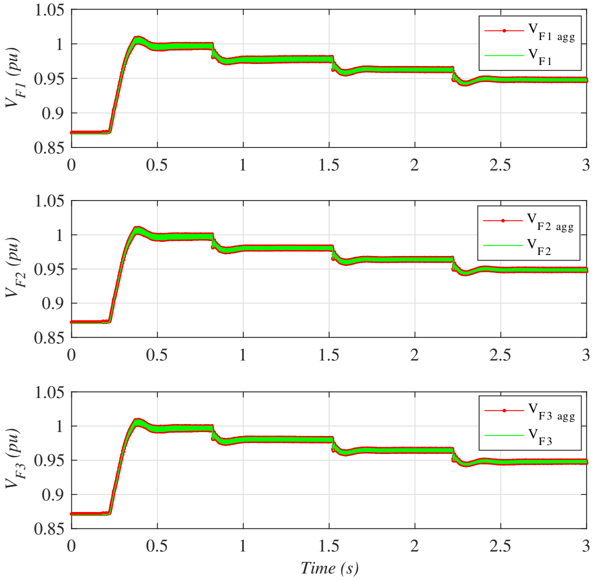

Figure 7.9: Case 1. Voltage amplitude at the PCC of each WPP (V_{Fk}) for detailed and aggregated models.

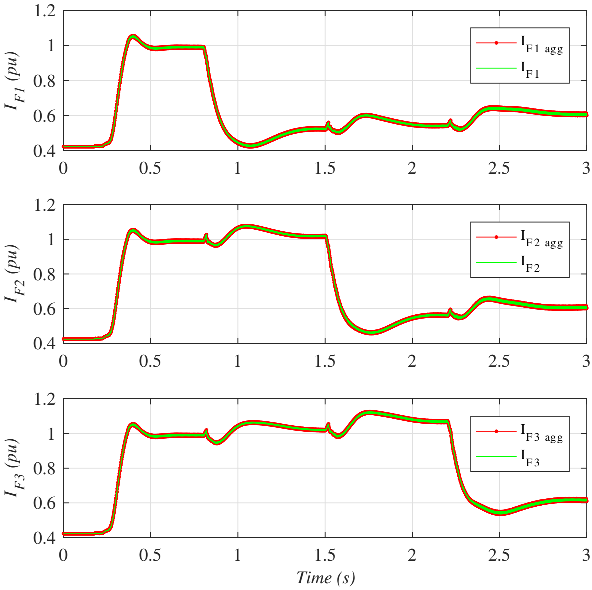

Figure 7.10: Case 1. Current amplitude at the PCC of each WPP (I_{Fk}) for detailed and aggregated models.

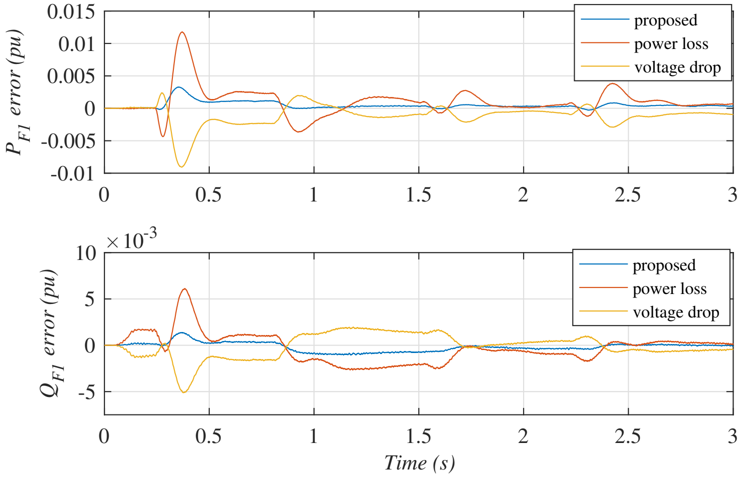

Figure 7.11: Case 1. Simulation errors for different aggregation techniques: Top: $P_{F1Detailed} - P_{F1Agg}$; bottom: $Q_{F1Detailed} - Q_{F1Agg}$.

Fig. 7.8 shows the reactive power responses for each WPP Q_{Fk}. The reactive power produced by the ac-filters is compensated by the WTGs while DRs are not delivering power. Conversely, when the DRs start conducting, the capacitor and ac-filter banks reactive power compensates that absorbed by the DRs and hence the reactive power Q_{Fk} delivered by the wind farms is reduced to a value very close to zero. Reactive power (Q_{Fk}) responses are also very similar for both aggregated and detailed models.

Fig. 7.9 shows the behaviour of the voltage V_{Fk} at the PCC of each WPP. It shows clearly how active power flow by DRs depends of the voltage V_{Fk}. Fig. 7.10 shows the magnitudes of current I_{Fk} at the PCC of each WPP. The current behaviour is similar to that of the active power P_{Fk}. Figs. 7.9and 7.10 clearly show that the voltage and current dynamics from the aggregated and detailed models agree to a great extent.

Three aggregation methods have been used to simulate the fast active power transients considered in case 1. The results are shown in fig. 7.11, which shows the active and reactive power simulation errors between aggregated and detailed models at PCC-1, i.e. ($P_{F1Detailed} - P_{F1Agg}$) and ($Q_{F1Detailed} - Q_{F1Agg}$). Only the traces corresponding to PCC-1 is shown, as the other PCCs show a very similar behaviour.

The simulation error obtained using the proposed multi-objective optimisation aggregation technique (in blue in fig. 7.11) is clearly lower than those with the alternative aggregation techniques.

The maximum active power simulation error with the proposed technique is about 0.3%, whereas the maximum simulation error for the reactive power simulation is approx. 0.2%. For the power loss technique, the active and reactive power maximum simulation errors are 0.9% and 0.5%, respectively. Whereas for the voltage drop technique the maximum simulation, the corresponding errors are 1.2% and 0.7%. Therefore, the proposed technique clearly shows a more accurate simulation during transients.

Moreover, for the complete case, the error variance using the multi-objective optimisation aggregation technique is 0.0423, whereas the error variance with the voltage droop and power losses techniques are 0.4094 and 0.3120, respectively. Therefore the error variance for the proposed technique is up to 9.5 better than the other aggregation techniques.

Case 2: Wind Power Plant disconnection

The second test case consists on the disconnection of WPP3, by opening the breaker at V_{F3} in Fig. 7.3 at t=0.05 s. Initially, all WPPs are generating 0.5 pu rated power. Figures 7.12 and 7.13 show the behaviour of the WPP voltage and current magnitude at the PCC of each Wind Power Plant.

After disconnection, WPP3 voltage remains at its 0.8 pu reference value, as all considered WTGs are grid forming (Fig. 7.12). After the transient, the voltage of the WPPs that remain connected settle to a slightly smaller voltage, as the power transmitted through the diode rectifiers is now reduced by one third [14].

From Figs. 7.12 and 7.13 it is clear that voltage and currents obtained from the detailed and from the proposed aggregated models show an excellent agreement during the transient.

The same WPP3 disconnection case shown in Figs. 7.12 and 7.13 has been repeated considering two alternative aggregation techniques (power loss and voltage drop). The results are shown in Figs. 7.14 and 7.15, which show the difference between the detailed simulation and each one of the three considered aggregation techniques. Simulation errors are expressed as per unit with respect to rated values.

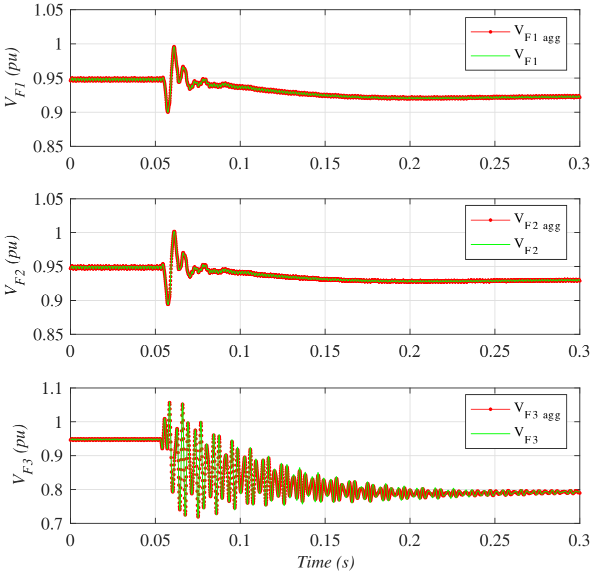

Figure 7.12: Case 2. Comparison of detailed and proposed aggregated simulations. WPP voltage V_{Fk}.

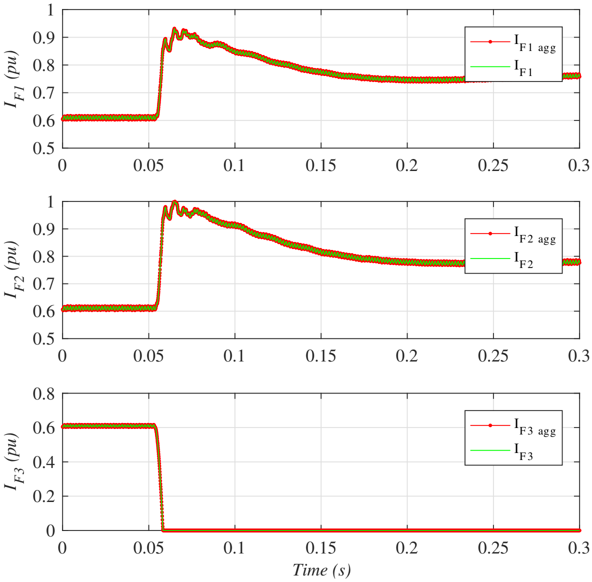

Figure 7.13: Case 2. Comparison of detailed and proposed aggregated simulations. WPP current I_{Fk}.

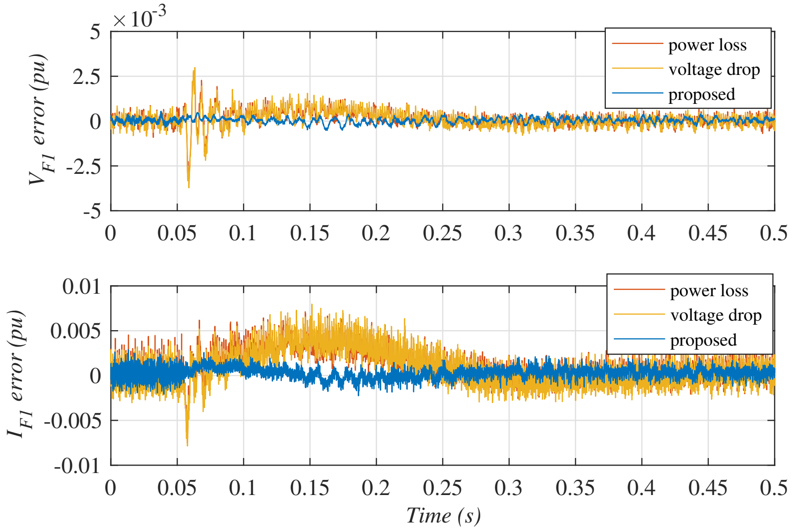

Figure 7.14: Case 2. Simulation errors for different aggregation techniques: top: $V_{F1Detailed} - V_{F1Agg.}$; bottom: $I_{F1Detailed} - I_{F1Agg.}$

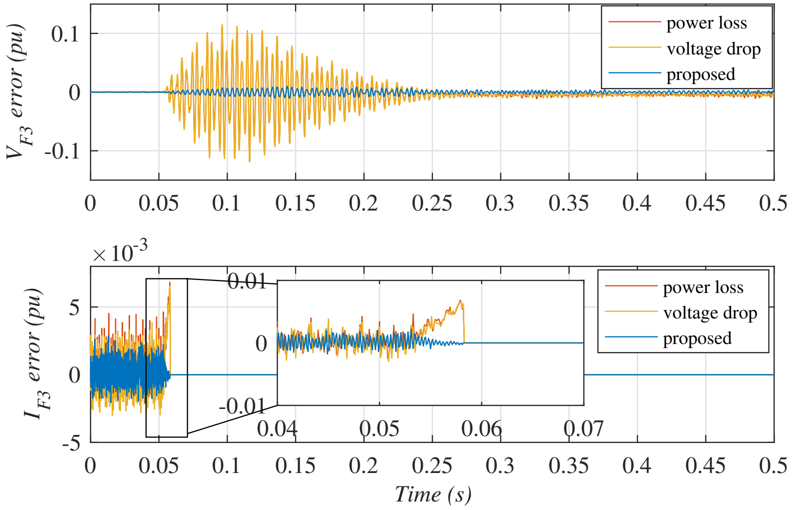

Figure 7.15: Case 2. Simulation errors for different aggregation techniques: top: $V_{F3Detailed} - V_{F3Agg.}$; bottom: $I_{F3Detailed} - I_{F3Agg.}$

Figure 7.14 shows the errors on the simulated voltages and currents for the detailed and aggregated models, $(V_{F1Detailed} - V_{F1Agg.})$ and $(I_{F1Detailed} - I_{F1Agg.})$ respectively. These voltages and currents correspond to one of the two WPP which are not disconnected (WPP1). The proposed aggregation technique (in blue) clearly shows a better performance than existing aggregation techniques, although all aggregation techniques show relatively small V_{F1} and I_{F1} simulation errors.

However, the voltage and current transients are much larger in the disconnected WPP3, as previously shown in Figs. 7.12 and 7.13. The top graph of Fig. 7.15 shows that the V_{F3} simulation error for the proposed aggregation method is much smaller than that of the existing aggregation methods (which even reach simulation errors larger than 10%).

On the other hand, the I_{F3} simulation errors are very small for all aggregation techniques, with only a small deviation just at the instant of WPP3 disconnection (Fig. 7.15 bottom graph).

Case 3: Disconnection and re-connection of Diode Rectifier ac-filters

The third case consists on the disconnection and re-connection of the ac capacitor and filter banks of DRU_3 (Fig. 7.3). The capacitor and filter banks of each DRU are rated at 0.4 pu (160 MVAr) and are connected in several steps. However, this transient considers the connection and disconnection of the full ac filter banks, in order to validate the dynamic performance of the aggregated models.

The voltages and current output of each WPP during this test case are shown in Figs. 7.16 and 7.17. The DRU_3 ac filter banks are disconnected at t=0.1s and re-connected at t=0.8s. Clearly, the harmonic contents of both voltage and current increase when the filter banks are disconnected. Moreover, voltage and current distortion is larger for WPP3, as it is electrically closer to the DRU station with no ac filters connected. WPP1 shows relatively small voltage and current ripple when the filters are disconnected, whereas WPP2 shows intermediate harmonic contents.

In any case, there is a very large agreement between detailed and aggregated simulations during the complete transient, except for the large current peak during ac filter bank reconnection in I_{F3} at t=0.8s (Fig. 7.17), where the aggregated model overestimated the I_{F3} current peak.

The comparison of the proposed aggregation technique with existing techniques is shown in Figs. 7.18 and 7.19. These figures show the simulation errors for

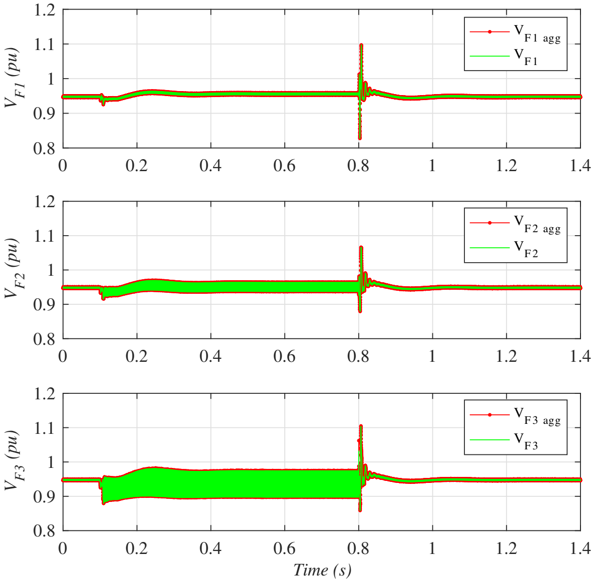

Figure 7.16: Case 3. Comparison of detailed and proposed aggregated simulations. WPP voltage V_{Fk}.

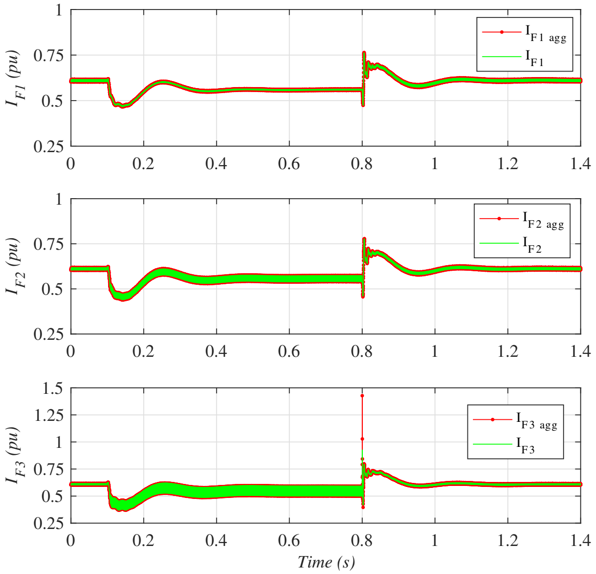

Figure 7.17: Case 3. Comparison of detailed and proposed aggregated simulations. WPP voltage I_{Fk}.

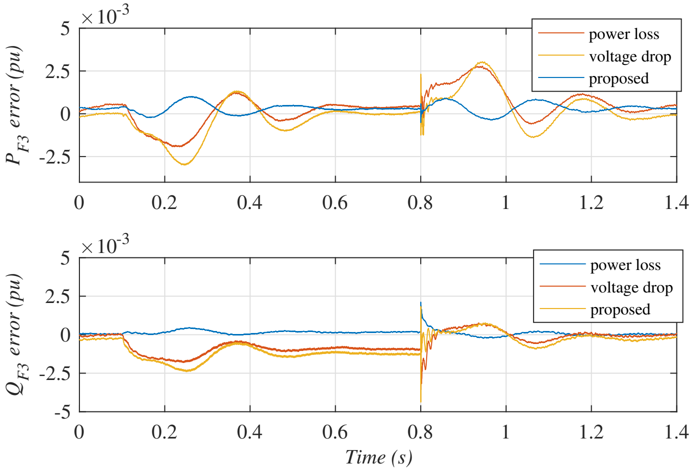

Figure 7.18: Case 3. Simulation errors for different aggregation techniques: top: $P_{F3Detailed} - P_{F3Agg.}$; bottom: $Q_{F3Detailed} - Q_{F3Agg.}$

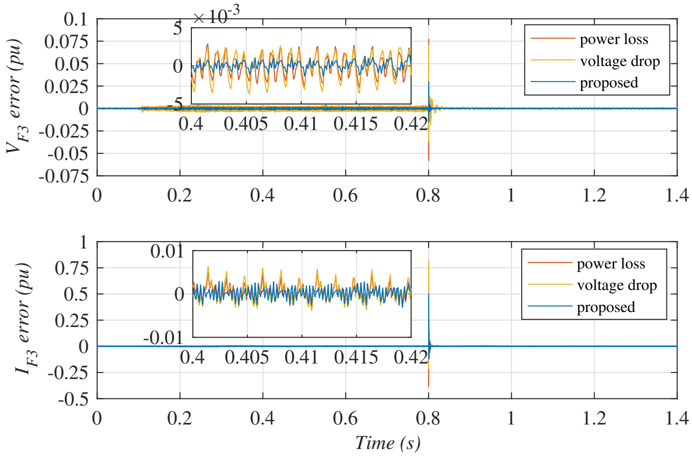

Figure 7.19: Case 3. Simulation errors for different aggregation techniques: top: $V_{F3Detailed} - V_{F3Agg.}$; bottom: $I_{F3Detailed} - I_{F3Agg.}$

the three aggregation techniques, during the DRU_3 ac filter disconnection and re-connection transient considered in this section.

Figure 7.18 shows the error on WPP3 active and reactive powers (P_{F3} and Q_{F3}) when simulated with each one of the considered aggregation techniques. All aggregation models adequately simulate the steady state active and reactive power delivered by WPP3. However, it is clear that, during the transients, the proposed aggregation technique (shown in blue) shows a smaller simulation error than existing techniques.

Figure 7.19 (top graph) shows that the proposed aggregation technique also shows a smaller V_{F3} error than other techniques when the filters are disconnected (i.e. between t=0.1 and t=0.8s). Clearly, the proposed technique is relatively better at simulating V_{F3} voltage harmonics.

On the other hand, Fig. 7.19 (bottom graph) shows that current I_{F3} simulation errors between t=0.1 and t=0.8s are very similar for the three considered techniques, around 0.5% (albeit the proposed technique error is slightly better).

It is worth noting that all aggregation techniques show relatively large simulation errors for V_{F3} and I_{F3} when the ac-filter banks are re-connected at t=0.8s (Fig. 7.19). However, the proposed technique performs clearly better than voltage drop and power loss aggregation techniques.

7.6.2 Simulation performance

The simulations of all considered cases have been carried out with a 3.3 GHz Intel Core i7 PC with 16 GB DDR3 memory, SSD hard drive and MS-Windows 7.

Considering a simulation run time of 3 seconds, table 7.2 shows the complexity and simulation times of both detailed and aggregated models. The detailed simulation takes 2 hours, whereas the aggregated simulation is more than 350 times faster.

Therefore, the use of the proposed aggregated models for large type-4 wind power plants is validated considering the similarity of obtained results and the improvement on simulation times.

Table 7.2: Simulation times

	WTGs	**nodes**	**Simulation time**
Detailed	150	2450	117 minutes
Aggregated	3	174	20 seconds

7.7 Discussion and Conclusions

This paper has presented an aggregation approach based on model order reduction using a multi-objective optimisation technique. The proposed method consists on first obtaining full admittance model of the WPP (in our case using state space techniques), then the inputs to the system are reduced to a single input applying the superposition principle and, finally, multi-objective optimisation has been used to reduce the order of the system. The proposed aggregation technique considers voltage source WTGs line side converters, therefore, it is also applicable to current-controlled voltage source converters.

Using the multi-objective optimisation aggregation technique, the achieved aggregated admittance model has the same DC gain, main resonant frequency and the same gain at the operating frequency than the detailed admittance model.

The proposed aggregation technique has been validated considering the PSCAD/EMTDC simulation of a 1.2 GW HVDC DR-connected system, consisting of three 400 MW WPP of 50 type-4 grid forming WTGs each. Hence, the detailed system consists of 150 individual wind turbines and 2450 nodes.

The proposed aggregation technique and two commonly used aggregation strategies have been used to reduce the WPPs to only 3 aggregated WPPs (each one equivalent to 400 MW).

The comparison has been carried out considering three different test cases, namely, fast active power reference changes, disconnection of a Wind Power Plant and disconnection and re-connection of DRU ac-filter banks. These cases cover a wide range of dynamic and transient conditions.

The response against active power changes achieved by using the proposed aggregation method shows a worst case error 3 times and an error variance 9.5 times better than aggregation techniques as based on voltage drop or on power losses.

During WPP disconnection, all aggregation techniques show relatively good PCC voltage and current simulation accuracy for the two wind power plants that remain connected. However, for the disconnected WPP, the proposed method shows voltage simulation accuracy 10 time better than standard methods, during the disconnection transient.

During disconnection and re-connection of one of the DRU ac-filter banks, the proposed technique also shows better simulation accuracy regarding PCC voltage, active and reactive power.

Finally, it has been shown that the aggregated simulations are 350 times faster than its detailed counterpart.

Therefore, when only the behaviour at the points of common coupling is of interest, the proposed aggregated model provides important simulation time savings while delivering accurate results and preserving the main resonant characteristics of the full array system.

Appendix

SYSTEM PARAMETERS
Wind Turbines
Grid-side VSC: 1.2 kVcc, 690 Vac, 50 Hz PWM filter: $R_W = 0.008$ pu, $L_W = 0.18$ pu, $C_W = 20$ pu.
Transformer $\mathrm{T_R}$: 8 MVA, 50 Hz, 0.69/66 kV (L-L rms), $X_T = 0.18$ pu, $R_T = 0.01$ pu
Off-shore AC grid
Base voltage V_F: 66 kV, 50 Hz
Distance between WTs: 1.5 km
Distance from cluster to DR platform: 3 km
Cable section: a = 150 mm^2, b = 185 mm^2, c = 400 mm^2,
String with 8 WT: a-a-a-b-b-b-c-c
String with 7 WT: a-a-a-b-b-b-c
DR stations
Base voltage of rectifier transformer: 66/43 kV
Filter and reactive power compensation bank for the 12-pulse rectifier according to CIGRE benchmark [124].
HVDC system
Base voltage of HVDC system: ±320 kV, 150 km

Controllers		
PI Power Controller:	$K_P = 0.00006$	$T_I = 380$
Proportional frequency droop:	$m_P = 0.00125$ Hz/MW	
Proportional amplitude droop:	$n_P = 0.01$ V/MVAr	

Multi-objective optimisation parameters	
Optimisation objectives f_i^*:	[16015.38 rad/s, 7.17725, 0.85227]
Weights W_i:	[1000.0, 1.0, 1.0]
R_{Teq} range:	[0.001, 0.139329] Ω
R_{Leq} range:	[0.001, 0.139329] Ω
L_{Leq} range:	[0.00215, 21.5] mH

Chapter 8

Mixed Grid-Forming and Grid-Following Wind Power Plants for Black Start Operation

Note: this chapter proposes a brack start procedure from a mixed grid forming and grid following WPP. How the grid following WTGs can contribute to the black start operation is studied. The chapter contents are published on:

Martínez-Turégano, Jaime; Añó-Villalba, Salvador; Bernal-Perez, Soledad; Peña, Ruben; Blasco-Gimenez, Ramon (2018). Mixed Grid-Forming and Grid-Following Wind Power Plants for Black Start Operation. EN 17th International Workshop on Large-Scale Integration of Wind Power into Power Systems as well as on Transmission Networks for Offshore Wind Power Plants. (1 - 6). Stockholm, Sweden.

Abstract

Grid forming wind turbines allow for additional services to be provided by wind power plants. These additional services include self-start operation, islanding operation of off-shore ac-grids and contribution to system restoration after a black-out. As the complete electric system will consist of both grid-following and grid-forming wind power plants, the aim of this paper is to study possible interactions between grid forming and grid following wind turbines during black-start operation. The presented case study includes a 400 MW off-shore wind power plant connected by means of a 75km HVac cable to the on-shore transmission grid. The results show adequate islanded and black-start operation with less than 25% grid forming power for step block loads of 0.1pu and a maximum of 10% voltage sag.

8.1 Introduction

Currently installed grid scale wind power plants are almost uniquely based on grid following control strategies, both for type-3 and type-4 wind turbines.

However, wind turbine grid side converters can also be controlled to be grid forming, i.e. capable of controlling their ac-side frequency and voltage, with adequate active and reactive power sharing and adequate load rejection. These converters are hence capable of performing some of the power system control tasks normally assigned to synchronous generators. Islanding operation and load sharing control of both type-3 and type-4 wind turbines has been reported in the past [151, 152, 153, 154].

The use of grid forming wind turbines is the key component of transmission technologies such as the use of HVDC Diode Rectifier stations in off-shore wind power plants (OWPPs) [6, 155, 14, 15, 102, 13, 12].

Recently, a large interest has been placed into the ability of off-shore wind power plants to be able of islanding and black-start operation, so more inefficient traditional back-up generation becomes redundant.

OWPPs consisting of grid forming converters can perform some or all of the aforementioned services. Nevertheless, existing OWPPs consist of grid following converters. Therefore, this work aims at studying the joint operation of grid forming and grid following wind turbines during black-start operation. Particular stress will be paid to issues that affect the minimum percentage of grid-forming wind turbines required for a particular scenario.

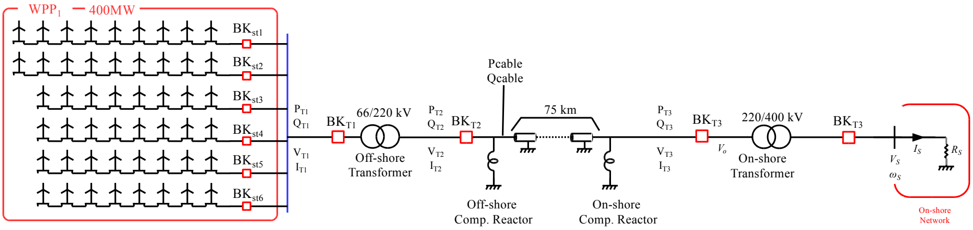

Figure 8.1: Considered HVAC Connected Off-shore Wind Power Plant

8.2 System Description

Figure 8.1 shows the system under consideration. The considered off-shore wind farm consists of 50 wind turbines of 8 MW each, totalling 400MW. The wind turbines are arranged in six strings, connected to a 66 kV collector bus, which, in turn is connected to a 66/220kV substation. The 220kV HVac export cable is 75km long and is shunt compensated at both ends.

To achieve reasonable simulation times, the 9 wind turbines of the first string are considered in detail, whereas the rest of the wind power plant is simulated by considering aggregated wind turbines for each one of the remaining strings.

Of the first string, wind turbines WT_{1-1}, WT_{1-2} and WT_{1-3} are grid forming, as well as all the wind turbines of string 2 (WT_2), totalling 12 grid forming wind turbines (96 MW).

The remaining wind turbines of the first string WT_{1-4}, to WT_{1-9} are all grid following, as well as all those in strings 3 to 6. Therefore, the considered system includes 38 grid following wind turbines with a combined power of 304MW.

8.3 Grid following and grid forming wind turbines

8.3.1 Grid Following Wind Turbines

A grid following wind turbine is defined as one that requires an already powered ac-grid to operate. Specifically, it is assumed that the grid side converter is used for control of the dc-link voltage and to follow a reactive current or reactive power set-point. This definition includes most of the type-4 large scale grid connected wind turbines currently in the market.

Figure 8.2 shows the control scheme of the considered grid following wind turbines. A PLL is used for orientation angle detection and also in order to provide a clean angle estimate during low voltage fault-ride-through events. The dc-link voltage E_{Bi} control loop includes a PI controller that provides the I_{Wd} current reference to the inner current loop. The dc-link voltage controller includes standard feedforward terms (not shown in the figure).

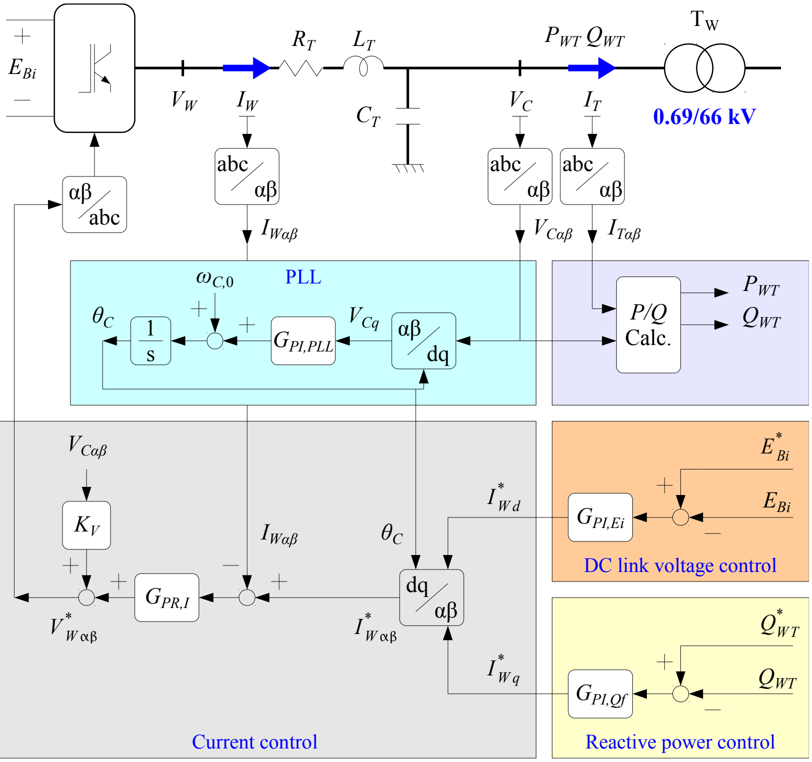

Figure 8.2: Basic Control Structure of a Grid Following Grid Side Converter

On the other hand, the reactive current reference (I_{Wq}^{*}) is obtained from the reactive power control loop. The active and reactive reference currents are then transformed to the $\alpha\beta$ stationary frame and then fed to a proportional+resonant controller. Obviously, standard *dq* synchronous frame current controllers can be used, noting that the PR controller is equivalent to positive and negative sequence PI synchronous frame controllers[156].

The reactive power reference and active power limit is set by the wind power plant controller.

8.3.2 Grid Forming Wind Turbine

In the context of this paper, a grid forming wind turbine is the one that has the following capabilities:

- is able to fully control voltage and frequency of the ac-grid to which it is connected (within its operational limits) even if the ac-grid is not initially energised by other equipment.
- it is capable to share the control effort (e.g. in terms of active and reactive power) with other grid-forming converters or generators connected to the same ac-grid.

Clearly, most advanced wind turbines can contribute to control ac-grid frequency and/or voltage, through different mechanisms, albeit they cannot operate if the ac-grid has not been energised by other converter or generator. Therefore, a large extent of already installed grid-following wind turbines are capable to perform grid support roles (voltage control, frequency support, etc).

As the two degrees of freedom of the grid forming converters are used for ac-grid control, the converter dc-link voltage is now controlled by the machine side converter, as shown in fig. 8.3. The torque producing current I_{Gq} is used as a control action to regulate the dc-link voltage E_{Bi}, with some additional compensation terms. Optimal C_p is now achieved by setting the reference for P_{WT}^{*} [157].

In practice, grid forming converters behave, up to some extent as voltage sources (or synchronous generators), with additional features to limit overcurrents (inner current loops).

The basic control structure of a grid forming converter is shown in fig. 8.4. The inner current control loops are the same as those used for the grid following wind turbine in fig. 8.2. Conversely, the outer P+R voltage loop calculates the required current references, so as to control the voltage V_c to certain voltage magnitude ($|V_C^{*}|$) and phase (δ^{*}).

Active and reactive power is shared amongst grid forming converters by means of droop control:

$$|V_C^{*}|(s) = V_0 + K_q \left(Q_{WT}^{*}(s) - \frac{1}{1+\frac{s}{\omega_{cq}}} Q_{WT}(s) \right) \tag{8.1}$$

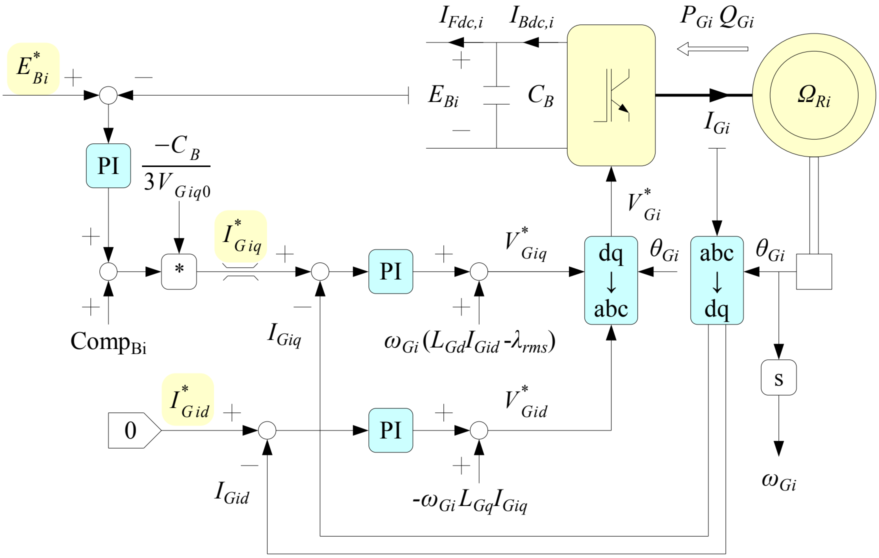

Figure 8.3: Machine side and dc-link voltage control

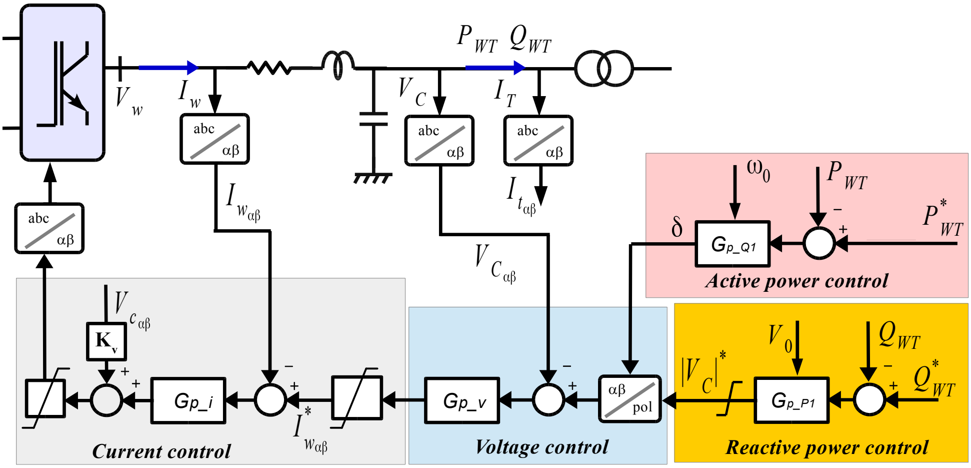

Figure 8.4: Basic Control Structure of a Grid Forming Converter

$$\epsilon(s) = P^*_{WT}(s) - \frac{1}{1+\frac{s}{\omega_{cp}}} P_{WT}(s) \tag{8.2}$$

$$\theta^*_C(s) = \left(\frac{k_i}{s} + k_p + k_i s\right)\epsilon(s) + \frac{1}{s}\omega_0 \tag{8.3}$$

8.4 Black-start Sequence

It is assumed that, at least, one grid forming wind turbine is capable of self-starting, i.e., run its own auxiliaries, align itself to the wind and charge the converter dc-link capacitors. From this point onwards, the black-start sequence is as follows.

8.4.1 Array Energisation

1. First grid forming wind turbine in an array energizes its own transformer and the string cable.
2. Second grid forming wind turbine transformer is connected to the grid created by the first wind turbine, after the transient, the second wind turbine synchronises itself to the grid and starts sharing voltage and frequency control with the first wind turbine.
3. The third grid forming wind turbine in the string is connected, in the same way as the second.
4. The six remaining (grid following) wind turbines in the string are then sequentially connected to the string cable. Grid following wind turbines contribute to overall reactive power sharing through the wind farm voltage controller.
5. Once the first string is up, the second string, consisting of 9 grid forming wind turbines is connected to the collector bus.
6. The rest of the wind turbines are connected to the collector bus string by string.

8.4.2 Export Cable Energisation

7. Off-shore ac-grid voltage is reduced to 0.2 pu.
8. Off-shore sub-station transformer is energised by closing breaker BK_{T1}.
9. On-shore substation transformer is connected to the cable by closing breaker BK_{T3}
10. Export cable and on-shore transformer station are energised by closing breaker BK_{T2}.
11. Finally, the on-shore load is connected by closing BK_{T4}

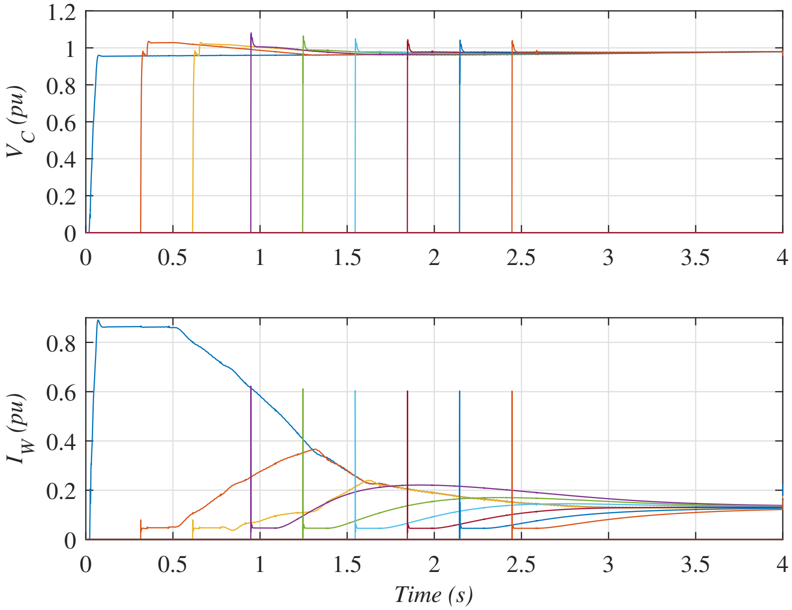

Figure 8.5: String energisation. Wind turbine voltage and current magnitudes

During the complete procedure, all grid following wind turbines active power reference is set to zero.

8.4.3 Results: String Energisation

Figures 8.5 and 8.6 show the energisation of the first string of the wind power plant. Initially, the first grid forming wind turbine energises its transformer and then the string cable. Once the string cable is energised, the second and third grid forming grid turbines are energised, followed by the remaining grid following wind turbines, as per the array energisation sequence explained before.

The grid forming wind turbines naturally share the reactive power needed to bring up the string cable. Moreover, the WPP controller also changes the Q^*_{WT} set points of the grid following wind turbines in order to contribute to reactive power sharing. It has been assumed that WPP controller communication delay is 25 ms. Wind turbine connection has been carried out at 0.3 s intervals, in order to keep simulation times within reasonable limits.

The string cable is not compensated and, in this particular case, it can be energised by a single wind turbine.

Once the first string is energised, the rest of the strings are energised sequentially.

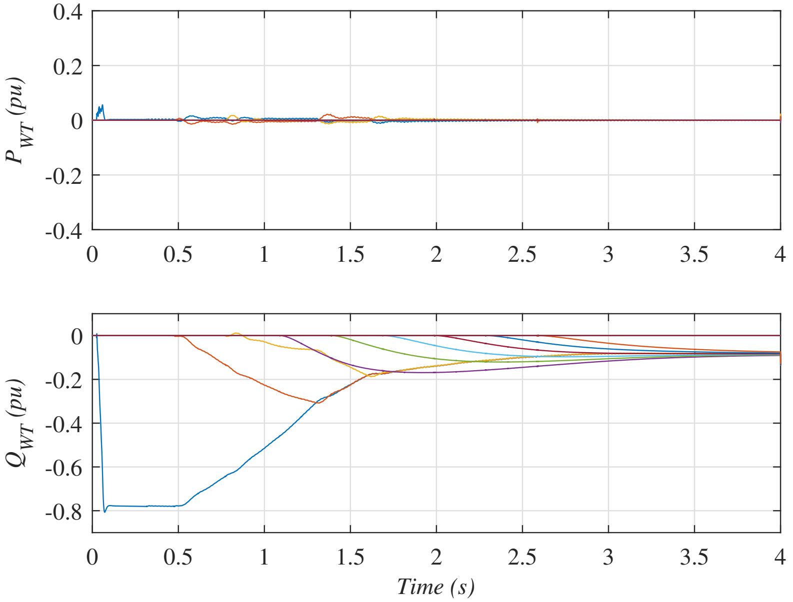

Figure 8.6: String energisation. Wind turbine active and reactive power

8.4.4 Results: Export cable energisation

Figures 8.7 to 8.10 show the procedure carried out for export HVac cable energisation.

Interaction between cable capacitance and transformer saturation during substation and export cable energisation might lead to large in-rush currents, overvoltages and oscillations [158, 159, 160]. Mitigating solutions such as pre-insertion resistors and point-of-wave breakers can be used in order to reduce the aforementioned effects. In this case, the presented solution consists on low voltage connection of transformers and cables, so both saturation and in-rush currents are greatly diminished.

Therefore, once the complete wind power plant is energised, the off-shore ac-grid voltage reference is set to 0.2 p.u. and the off-shore ac-substation is connected by closing breaker BK_{T1}. Then the export cable and on-shore transformer station are energised at the same time, by closing first BK_{T3}, then BK_{T2} and, finally, ramp up the voltage to 1 pu in about 1 second. For the cable compensation, only the on-shore reactor is connected.

Clearly, as the connection of the complete system is carried out at reduced voltage, transformer in-rush currents are kept to a minimum. However, remanent flux or dc-flux created during the connection are present in the transformer core. As the voltage is increased, so it is the transformer flux and then, eventually, existing dc-flux in the transformer will lead to saturation and to overvoltage caused by interaction between transformer saturation and cable capacitance. These effects can clearly be seen in figs. 8.7 to 8.10, at $t = 9.14$ s approx-

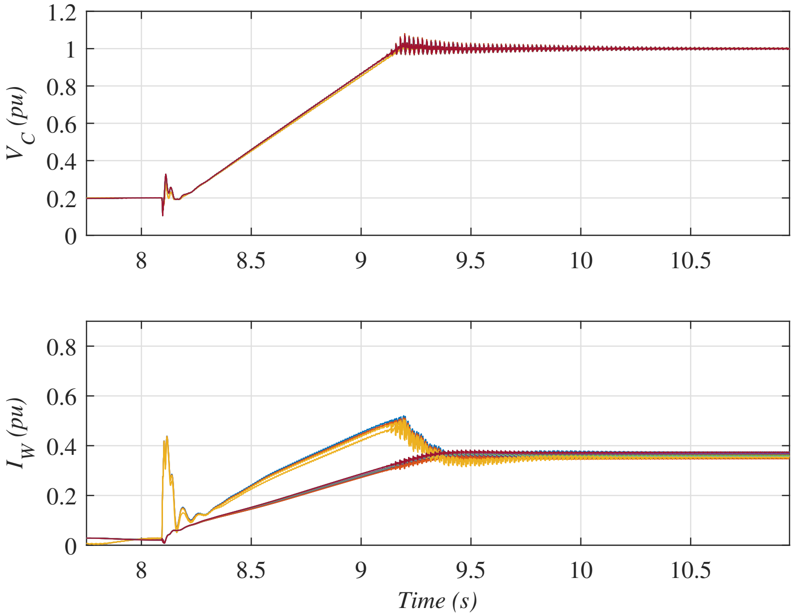

Figure 8.7: Connection of on-shore substation transformer and HVAC export cable

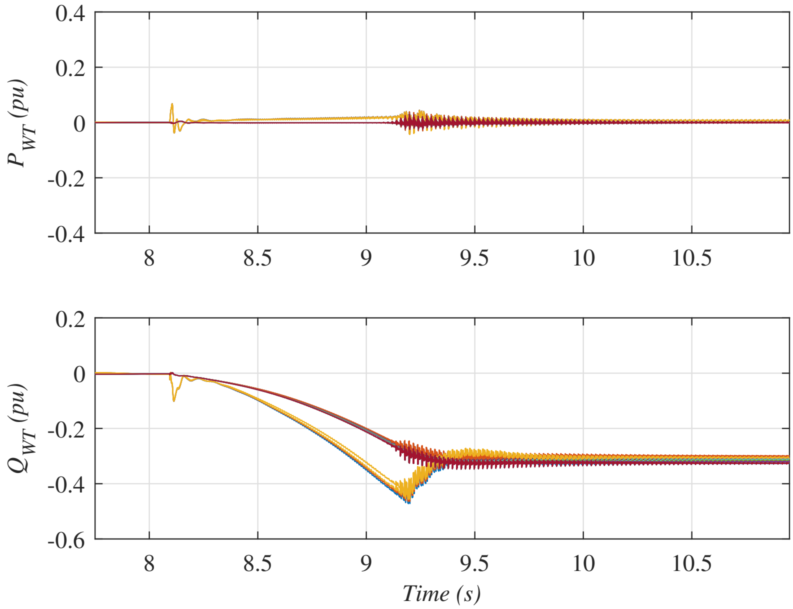

Figure 8.8: Connection of on-shore substation transformer and HVAC export cable

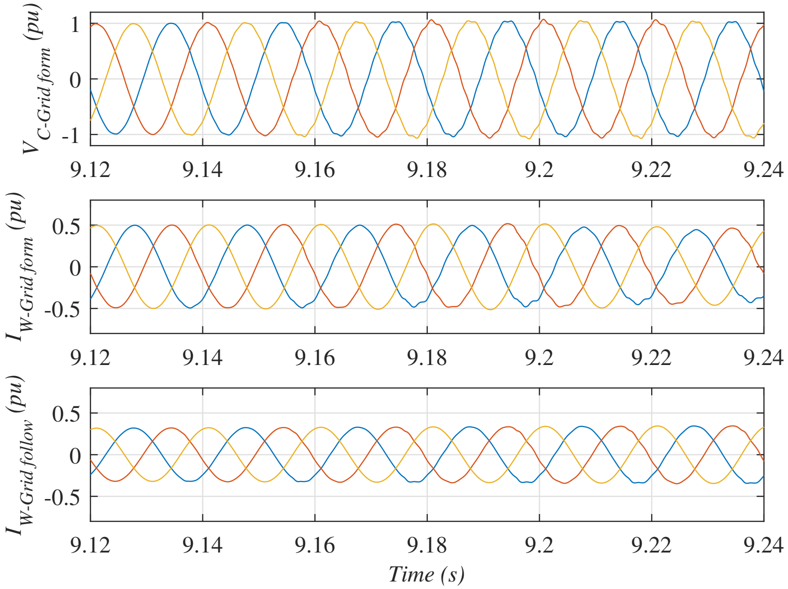

Figure 8.9: Connection of on-shore substation transformer and HVAC export cable

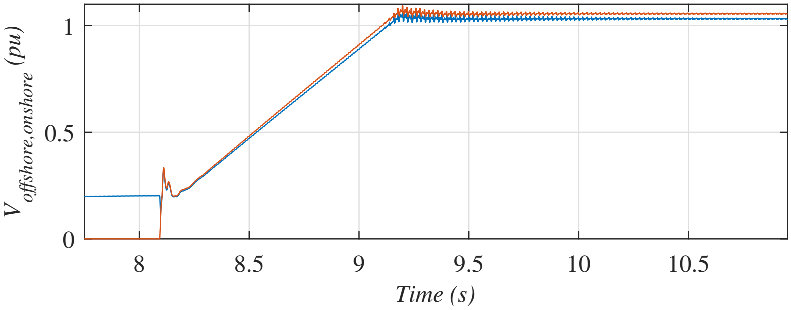

Figure 8.10: On-shore and off-shore cable end voltages

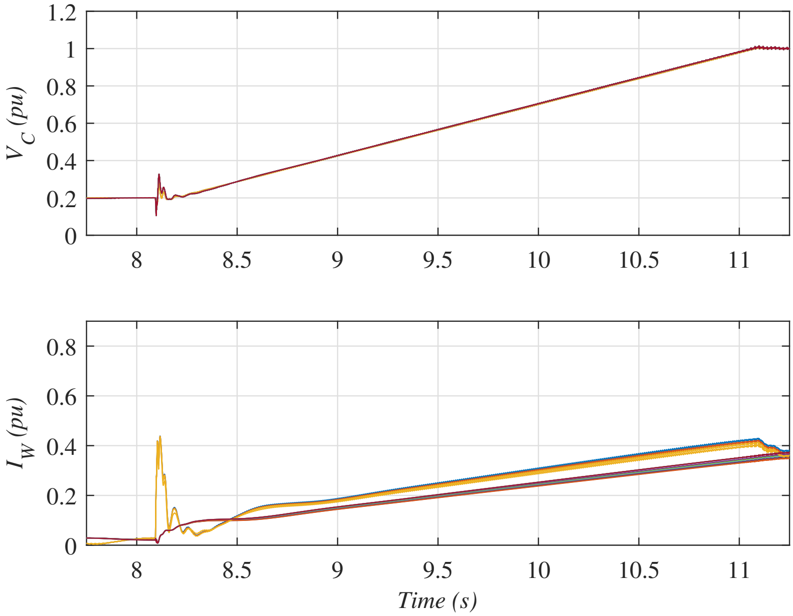

Figure 8.11: Connection of on-shore substation transformer and HVAC export cable

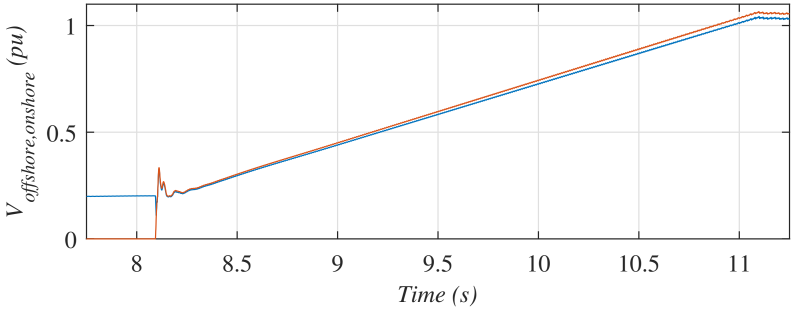

Figure 8.12: On-shore cable voltage

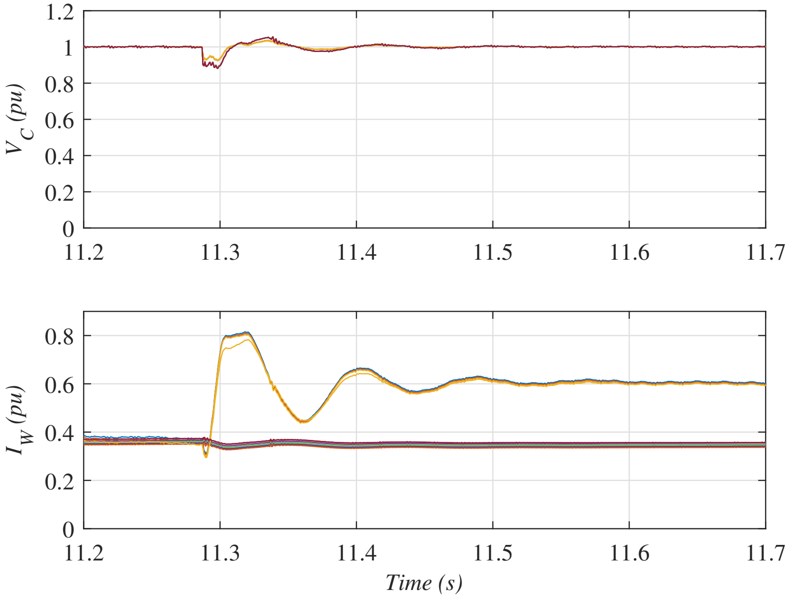

Figure 8.13: Connection of on-shore load. On-shore compensation only

imately. In-rush currents and overvoltages affect both grid-forming and grid following wind turbines, as clearly seen in fig. 8.10.

Also, it can be clearly seen that grid following wind turbines contribute to overall reactive power requirements, albeit with much slower dynamics.

A slower voltage ramp rate can be used in order allow the dc-flux in the transformer to disappear and hence prevent transformer saturation when a high voltage is reached. The results are shown in figs. 8.11 to 8.12. Clearly, in this case, oscillations due to transformer saturation and cable interaction are practically eliminated, in the voltage and current magnitudes at the wind turbines and also in the voltages at both ends of the cable.

8.4.5 Results: On-shore load energisation

Finally, a 0.1 pu on-shore resistive load is connected by closing its breaker, in this way, the voltage dynamic response of the complete system can be assessed. Figure 8.13 shows the voltage and current magnitude of the wind turbines. Clearly, grid forming wind turbines are the ones to increase their active power in reaction to the voltage drop caused by the resistive load.

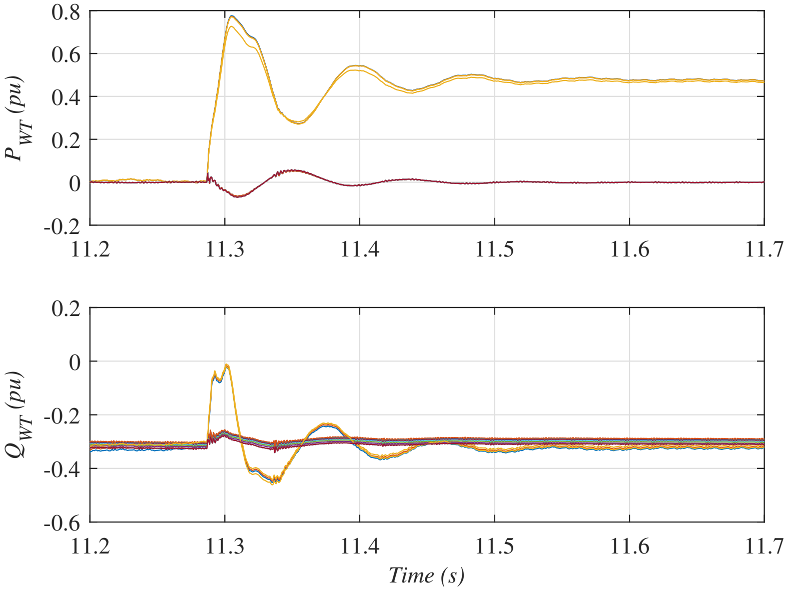

Figure 8.14: Connection of on-shore load. On-shore compensation only

During the direct connection of the load, the voltage V_C drops to a maximum of 0.9 p.u., at the expense of grid forming wind turbine currents increasing up to 0.8 p.u (fig. 8.13). Voltage profiles on-shore show that maximum drop is around 10%.

Figs. 8.13 and 8.14 show that the grid following wind turbines contribute to overall reactive power requirements.

Figures 8.15 and 8.16 show the behaviour of the system during block load connection when both on-shore and off-shore compensation are connected.

The graph shows how the initial 0.1 p.u. step load is absorbed by the grid forming wind turbines (t=11.29 s). Once the steady state operation is reached, the wind farm controller rises the active power reference of the grid following wind turbines to 0.13 p.u. After approx. 1 second, the load is now fed by the grid following wind turbines. At this point, another step block load of a 0.1 p.u. is applied (so a total of 0.2 pu load is now connected on-shore). The time to transfer the load from the grid forming to the grid following WTGs is set to 1 sec to keep reasonable simulation times. In practice, ramp time would be generally slower and would depend on maximum allowable rate of rise of active power and pitch actuator speed.

Maximum voltage drop is consistently smaller than 10%. However, current in fig. 8.15 shows smaller oscillations and settles at a smaller value than that in fig. 8.13. The peak current to be delivered by the wind turbine converters is now 0.7 p.u., slightly smaller than when

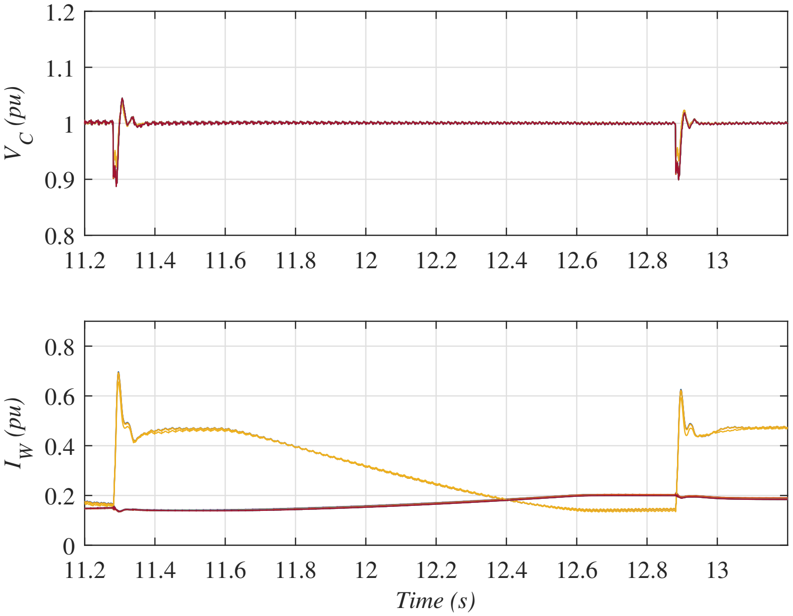

Figure 8.15: On-shore block load connection. Both end cable compensation

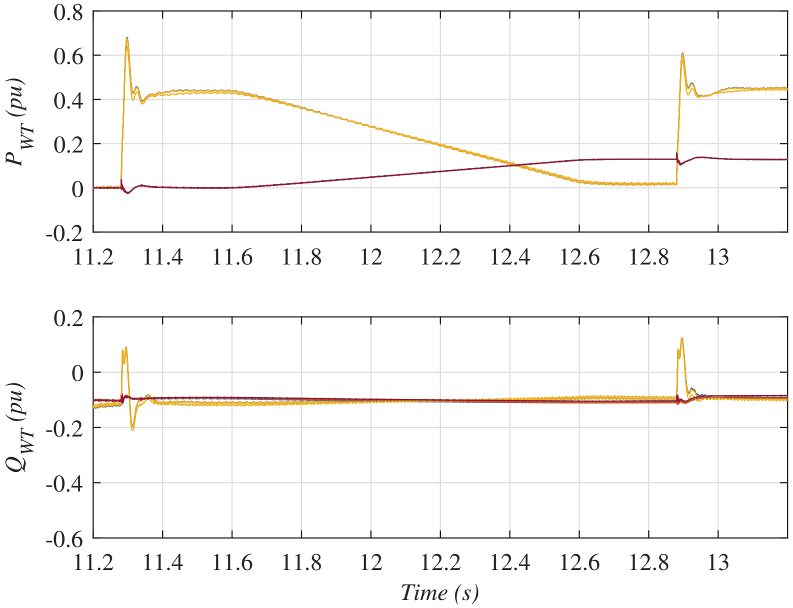

Figure 8.16: On-shore block load connection. Both end cable compensation

Table 8.1: Characteristics for different grid forming power

Grid forming power	40MW	48MW	**96MW**	192MW
% step load block	100%	120%	**240%**	480%
Gearbox extreme load	1 pu	0.6 pu	**0.25 pu**	0.125 pu
Minimum wind speed	11.4 m/s	10.6 m/s	**8.7 m/s**	6.9 m/s

only on-shore side compensation is considered. Reactive power requirements in fig. 8.16 are clearly smaller than those in fig. 8.14.

Table 8.1 shows the gearbox extreme load and the minimum wind speed required for black start operation for different grid forming power, covering 100% to 480% of the considered step block load (40MW).

8.5 Discussion and Conclusions

This paper shows a case study of the technical viability for off-shore grid self-start operation and on-shore grid service restoration, with the aim of studying the grid forming to grid following ratio for black start operation. Stable operation has been found provided that there is enough grid forming power to cope with energisation transients.

Particular attention has been paid to load rejection and export cable energisation.

The strategy used for sub-station transformer and export cable energisation consisted on connecting both cable and on-shore transformer at a reduced voltage of 0.2 pu and then ramp up the voltage to 1 p.u. with a rate that ensures the transformer dc-flux does not cause saturation at high voltage, thus avoiding voltage oscillations.

Regarding load rejection, grid forming wind turbines voltage control loops have been designed for a maximum 10% voltage drop for a 0.1 p.u. on-shore resistive load connection. This case represents a worst-case scenario, as the connection of such large loads would be carried out gradually or in smaller steps, however, it has been selected to show the grid forming wind turbine performance in a demanding black start scenario.

Moreover, the mechanical impact of step load connection to the wind turbine has been carried out by means of EMT-aeroelastic co-simulation.

When cables are compensated at both ends, maximum current through grid forming wind turbines is 0.7 pu, so required grid forming power would be around 20%. Smaller amounts of grid forming power can be used if load is connected at smaller steps or voltage sag requirements are relaxed.

Chapter 9

$\mathcal{H}_\infty$ controller design for grid forming Offshore Wind Power Plants Connected to a HVDC-Diode Rectifier system

Note: this chapter proposes a controller design procedure for grid forming WTGs. The controller is obtained using $\mathcal{H}_\infty$ synthesis.It achieves resonant behaviour. The chapter contents are published on:

Martínez-Turégano, Jaime; Sala, Antonio; Blasco-Gimenez, Ramon (2019). $\mathcal{H}_\infty$ controller design for grid forming Offshore Wind Power Plants Connected to a HVDC-Diode Rectifier system. EN 13th International Conference on Modeling and Simulation of Electric Machines, Converters and Systems (ElectrIMACS 2019). Salerno, Italy.

Abstract

The use of Diode Rectifiers units (DRU) is an alternative for the HVDC connection of off-shore wind power plants to the on-shore grid. DRUs are passive converters, therefore, grid forming wind turbine generators (WTG) are required for their operation. This paper shows how $\mathcal{H}_\infty$ synthesis can improve both WTG dynamic response and harmonic mitigation. The designed stationary frame $\mathcal{H}_\infty$ controller achieves zero steady state error to sinusoidal voltage references at the synchronous frequency. The response of the proposed controller is compared with that of a reasonably designed proportional-resonant controller, both in terms of dynamic response and on harmonic mitigation. The results have been validated by means of detailed PSCAD simulations.

9.1 Introduction

HVDC Diode Rectifier (DR) stations have been proposed by different authors as a technical solution that reduce significantly the cost of the off-shore wind power plant (WPP), while increasing the overall efficiency and robustness of the entire system [14, 11, 12, 13, 15]. Indeed, Siemens states that the use of HVDC DR stations could reduce the WPP connection cost up to 30% [6, 109].

The use of DR stations for HVDC links requires wind turbine generators (WTGs) capable of creating the off-shore ac-grid. Several control alternatives have been proposed for this purpose [11, 12, 13, 110, 93, 6, 105, 81, 109, 90].

This paper proposes a new control alternative that uses $\mathcal{H}_\infty$ based design to improve the WTG dynamic performance. Moreover, this control strategy allows for the design of the WTG harmonic impedance and hence contribute to both reduce the overall harmonic distortion while improving stability margins.

Furthermore, the $\mathcal{H}_\infty$ robust control techniques can be used to achieve zero steady state error at the synchronous frequency. In addition, the use of $\mathcal{H}_\infty$ control techniques allows to consider unmodelled dynamics arising from changes in the structure of the system, as connection/disconnection of strings/WTGs/cables, which change system impedance.

This paper is structured as follows. Firstly, the paper justification of this paper is described. The second section shows a description of the system used to validate the proposal control. The third section describes the system model and the controller design. The fourth section shows a comparison of the results of the $\mathcal{H}_\infty$ synthesis controller with that of a reasonably tuned PR controller. The last section includes the conclusions of this paper.

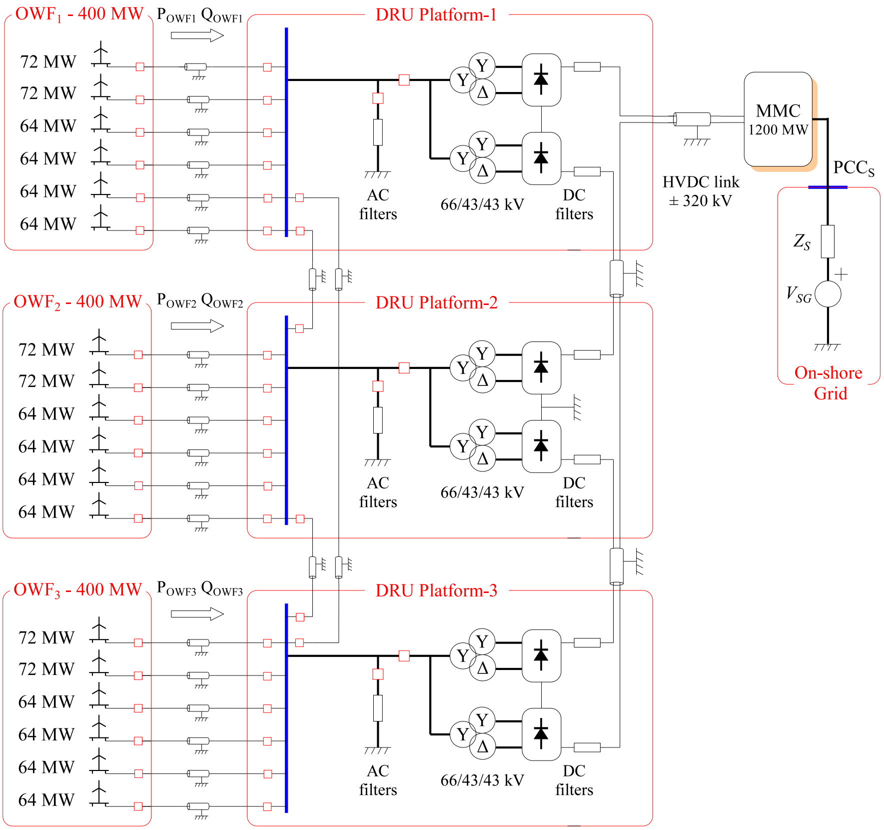

Figure 9.1: OWFs connected to the on-shore ac-grid via a diode-based HVDC link.

9.2 System description

Fig. 9.1 shows the diagram of the entire system. It considers a 1200 MW off-shore WPP distributed in there clusters of 400 MW each one. The WPP is connected via a diode-rectifier HVDC link to a full-bridge on-shore Modular Multi-level Converter (MMC). Each cluster OWF is composed of fifty 8 MW rated WTGs. The complexity of each cluster has been reduced using an aggregated wind turbine for each string, as shown in Fig. 9.1. The WTG aggregation technique used is the proposed in [65]. The aggregation of each string allows a reasonable computational cost reduction. All transformer models (WTG and diode rectifier units (DRU)) consider saturation.

The system also includes three DRU platforms [6]. Every platform consists of two 12-pulse DRU of 200 MW each, that are connected in parallel on the ac-side, while their dc-side is connected in series.

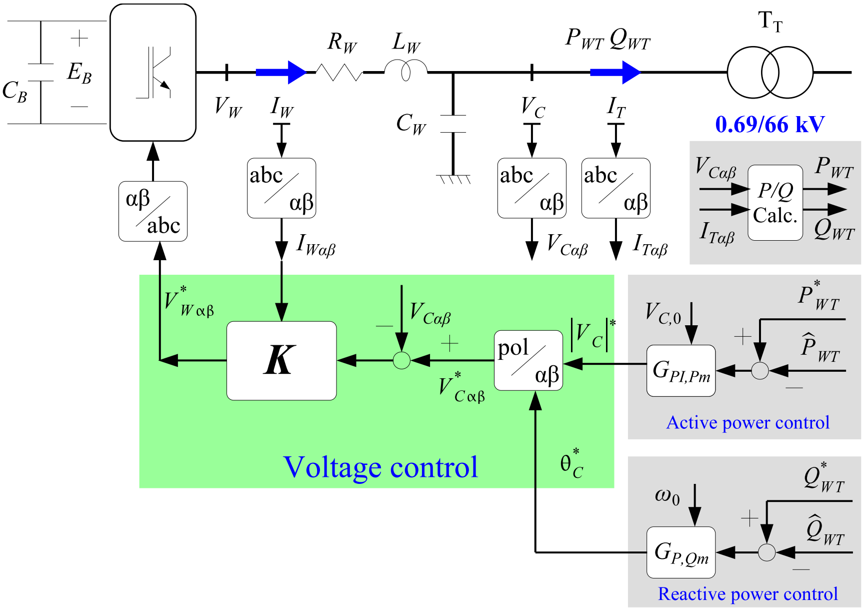

Figure 9.2: Control strategies for grid forming WTGs.

As Fig. 9.1 shows, the wind farms OWF-i ($i = 1, 2, 3$) are connected to the corresponding DRU platform by means of the off-shore ac-grid. Additionally, ac and dc filters are placed in each DRU platform. All ac-cables considered in the system are modelled using lumped π-parameters.

The export HVDC cable connecting the DRU stations to the on-shore MMC converter is modelled considering distributed, frequency dependant parameters.

System parameter values are shown in the Appendix.

9.3 System model and Control strategies

Fig. 9.2 shows the WTG model considered in this paper and its control strategy. The dynamics of the LC filter in Fig. 9.2 can be written as

$$V_W = R_W I_W + L_W \frac{dI_W}{dt} + V_C \tag{9.1}$$

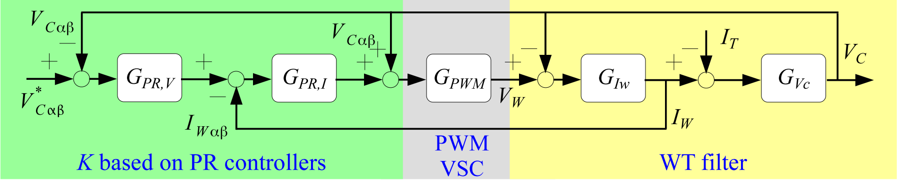

Figure 9.3: Block diagram of the closed-loop VSI for voltage control based on PR regulators.

$$I_W - I_T = C_W \frac{dV_C}{dt} \tag{9.2}$$

The control system includes an active and reactive power control based on well known P/V Q/ω droops [25, 94]. The control of the WTG grid side converter is also included in Fig. 9.2, where $\mathbf{K}(s)$ is:

$$V^*_{W\alpha\beta}(s) = \mathbf{K}(s) \begin{pmatrix} V^*_{C\alpha\beta}(s) - V_{C\alpha\beta}(s) \\ I_{W\alpha\beta}(s) \end{pmatrix} \tag{9.3}$$

All controllers have been designed in continuous time and discretised using the bilinear approximation with a sampling time of 250 μs. The main aim of this paper is the design of controller $\mathbf{K}(s)$.

9.3.1 Active and reactive power control

The power control has been design following the methodology in [25, 30, 94].The considered active and reactive power controllers are:

$$|V^*_C| = \left(K_P + \frac{K_I}{s}\right)(P^*_{WT} - P_{WT}) \tag{9.4}$$

$$\delta = \left(K_P + \frac{K_I}{s} + K_D s\right)(Q^*_{WT} - Q_{WT}) + \omega_0 \frac{1}{s} \tag{9.5}$$

9.3.2 Voltage Control based on Proportional-Resonant regulators

The PR based voltage control consists of a cascaded control with an inner current loop and an outer voltage loop. The voltage and the current controllers have been designed following the considerations in [28]. Furthermore, both voltage and current controls have been designed as a PI controller in a rotating frame of reference, considering a given settling time and overshoot and then frequency shifted to a PR structure using (9.6) [113, 89]:

$$G_{AC}(s) = G_{DC}(s - j\omega) + G_{DC}(s + j\omega) \tag{9.6}$$

Fig. 9.3 shows the block diagram of the closed loop used for PR controller design, where G_{PWM} considers the PWM effect and the measurement delay, G_{I_W} represents the inductor dynamics and G_{V_C} the filter capacitor. G_{PWM}, G_{I_W} and G_{V_C} are:

$$G_{PWM}(s) = \frac{1}{1 + 1.5T_s s} \tag{9.7}$$

$$G_{I_W}(s) = \frac{1}{L_W s + R_W} \tag{9.8}$$

$$G_{V_C}(s) = \frac{1}{C_s s} \tag{9.9}$$

The inner current controller has been tuned to achieve a setting time of 6.5 ms and an overshoot less than 10%, considering the PWM converter delays (G_{PWM}).

The outer voltage controller is designed taking into account the current loop closed loop transfer function and aiming at a setting time of 25 ms and an overshoot less than 10%.

Then, both controllers are frequency shifted using (9.6) to obtain the parameters of the equivalent PR controller. The parameters of both current and voltage PR controllers are listed in the appendix.

Therefore, the voltage controller $\mathbf{K}(s)$ based on PR regulators is:

$$K_{PR} = \begin{bmatrix} G_{PR,V}(s) * G_{PR,I}(s) & -G_{PR,I}(s) \end{bmatrix} \tag{9.10}$$

where $G_{PR,V}(s)$ and $G_{PR,V}(s)$ are

$$G_{PR,V}(s) = K_{P,V} + \frac{K_{R,V} \cdot s}{s^2 + \omega_0^2} \tag{9.11}$$

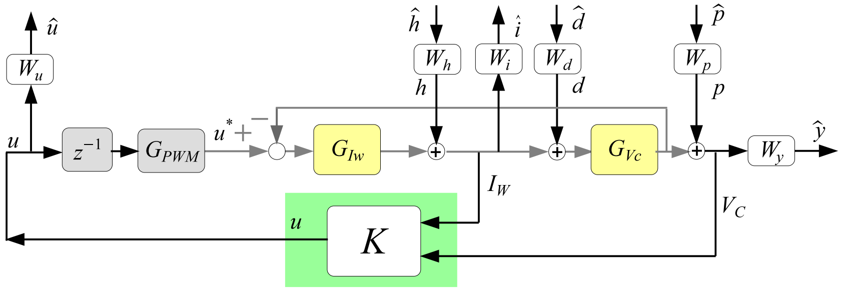

Figure 9.4: Control strategies for grid forming WTGs.

$$G_{PR,I}(s) = K_{P,I} + \frac{K_{R,I} \cdot s}{s^2 + \omega_0^2} \tag{9.12}$$

The PR controllers have been implemented using the double integrator form presented in [115].

9.3.3 Voltage Control based on $\mathcal{H}_\infty$ synthesis

The voltage control based on $\mathcal{H}_\infty$ synthesis has been obtained following the next steps. The effect of the PWM is considered by discretising the plant in (9.1) and (9.2) using the zero-order hold (ZOH) approximation with a 0.25 ms sampling rate and a time delay z^{-1} in order to consider the computational delay. Finally, a continuous-time model has been obtained by using the bilinear transformation [161]. As the bilinear transformation preserves the frequency response magnitude, it is well known that the resulting continuous-time controller, when discretised again, guarantees the same $\mathcal{H}_\infty$ performance proven in the continuous domain.

The next step is to obtain the generalised plant using the obtained model before. Fig. 9.4 shows the generalised plant, including the output weights W_u, W_i and W_y as the control objectives, and the input weights W_h, W_d and W_p.

Note that optimal $\mathcal{H}_\infty$ does not explicitly include uncertainty, and it must be "plugged in" in the weights (for instance, it is well known that the weight on the output of the generalised plant assigned to the control action provides robustness against unstructured additive uncertainty).

Fig. 9.5 shows the chosen weights to obtain the $\mathcal{H}_\infty$ controller. The weights W_u, W_h, W_d and W_p have the same structure of (9.13).

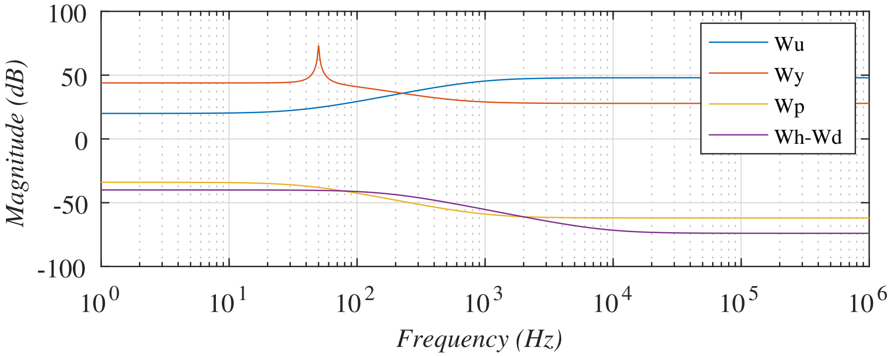

Figure 9.5: Weights for $\mathcal{H}_\infty$ design.

$$W = \frac{K_W\,(s+b)}{s+a} \tag{9.13}$$

Considering that the model described in (9.1) and (9.2) has p.u., the accepted stationary error is chosen to be below 2 % for frequencies within the bandwidth of 180Hz. So, the gain of W_p for low frequencies is set to 0.02. In addition, W_p adds 10 times lower gain at high frequencies.

The weights W_h and W_d are related to the added uncertainty of the inductor filter L_w and the disturbance I_T respectively. The gain for high frequencies is 50 times lower than for low frequencies.

The weights relating to the control objectives have been designed as follows. The maxim voltage applied in V_W is 1.1 pu, so the dc gain of W_u may have a maximum value of 10, however, in order to reduce the control effort, it has been set to a value of 5. The gain for frequencies higher than 180 Hz is chosen to be 10 times smaller than that for low frequencies.

The current I_W has been limited with the weight W_i; it is chosen as a constant gain with a value of 100.

The weight Wy has been designed as Eq.(9.14) shows.

$$W_y = (K_{Low} + W_{yres}) \cdot W_{High} \tag{9.14}$$

where K_{Low} is the gain for low frequencies, W_{yres} is a resonant weight and W_{High} is the gain for high frequencies.

W_{yres} has been obtained as follows. A weight as (9.13) has been adjusted with a gain for low frequencies equal to the inverse of the accepted error (0.02) multiplied by 100. The gain

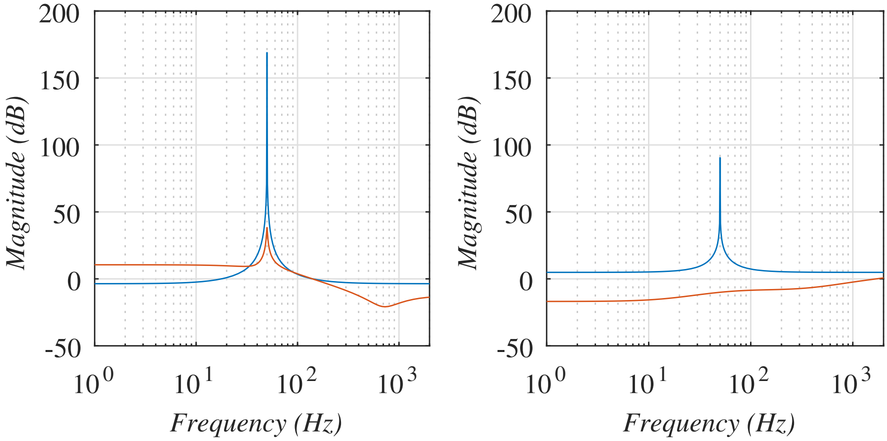

Figure 9.6: Controller frequency response (left: K_V; right: K_I): blue: PR based controller; red: $\mathcal{H}_\infty$ based controller.

for frequencies higher than 50 Hz has been set to a value 200 times lower. Then, the weight has been transformed to a resonant form at 50 Hz using (9.6). Additionally, K_{Low} improves the disturbance rejection of the voltage with frequencies lower than 50 Hz. K_{Low} has been set 100. Finally, W_{High} reduces the control effort for frequencies higher than 50 Hz. W_{High} has the same structure than Eq.(9.13).

The final $\mathcal{H}_\infty$ controller shown in Eq.(9.15) has been obtained using the described weights and the Matlab's `hinfsyn` function. The whole set of generalised-plant weights is included in the Appendix. With the considered weight selection, the obtained closed-loop $\mathcal{H}_\infty$ norm is less than 1, which means that we ensure that all generalised-plant's outputs have a frequency response below the inverse of their respective weights when the generalised-plant's disturbances have an input spectrum below the designed weights.

The resulting two-input controller $K(s)$ can be split in a voltage-feedback component and a current-feedback one:

$$K(s) = \begin{bmatrix} K_{\mathcal{H}_\infty,V} & K_{\mathcal{H}_\infty,I} \end{bmatrix}. \tag{9.15}$$

9.3.4 Comparison between $\mathcal{H}_\infty$ and Proportional-Resonant controllers

Both $\mathcal{H}_\infty$ and PR controllers have been implemented as digital controllers with a rate of 4 kHz. Both controllers have been discretised using Matlab's *d2c* function considering a bilinear approximation and a frequency prewarp of 50 Hz.

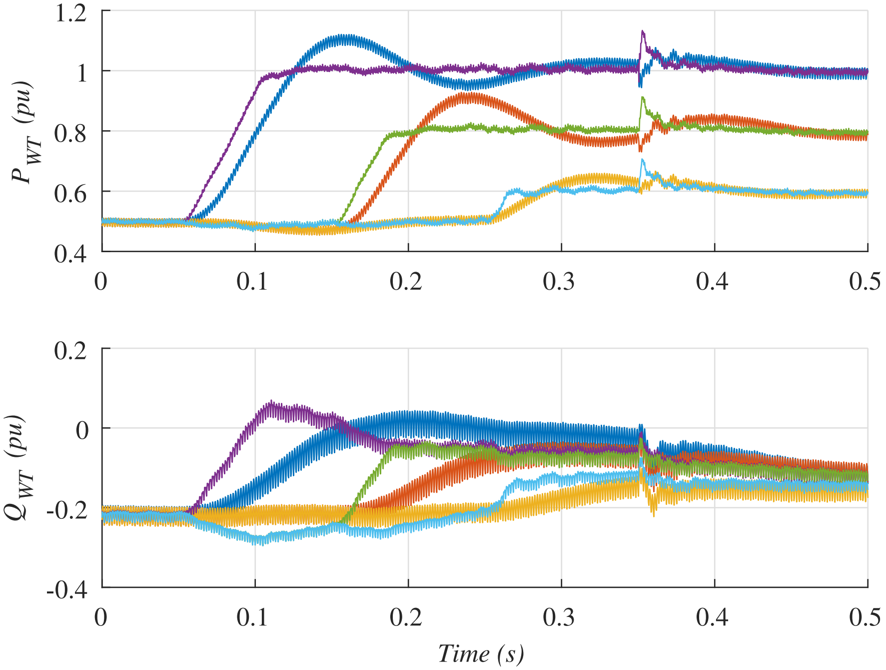

Figure 9.7: Active and reactive powers P_{WT} and Q_{WT}: Response with PR controller:Blue, red and yellow; Response with $\mathcal{H}_\infty$ controller: purple, green and cyan.

Fig. 9.6 shows the frequency response of both controllers. Note that the voltage response of the $\mathcal{H}_\infty$ controller has a bigger gain for low frequencies, a lower resonant peak, and a lower gain for high frequencies. By contrast, the current response of $\mathcal{H}_\infty$ controller does not have resonant peak and is lower in all frequencies.

In this work, normalised coprime factor uncertainty margin [162] has been used to assess *a posteriori* the overall level of robustness of the designs to the said uncertainty structure. This is implemented in Matlab's `ncfmargin` function. The achieved margins for our $\mathcal{H}_\infty$ and the PR option are: 0.32 and 0.06 respectively. It validates that the $\mathcal{H}_\infty$ controller is 5 times more robust than the controller based on PR regulators.

9.4 Results

The validation of the correct operation of the designed controllers is carried out by means of a PSCAD simulation. Considered test includes a change of each cluster‘s active power reference (OWF_1: from 0.5 to 1 pu; OWF_2: from 0.5 to 0.8 pu; OWF_3: from 0.5 to 0.6 pu) every 100 ms and the connection of a 15% rated restive load at $t = 0.35$s.

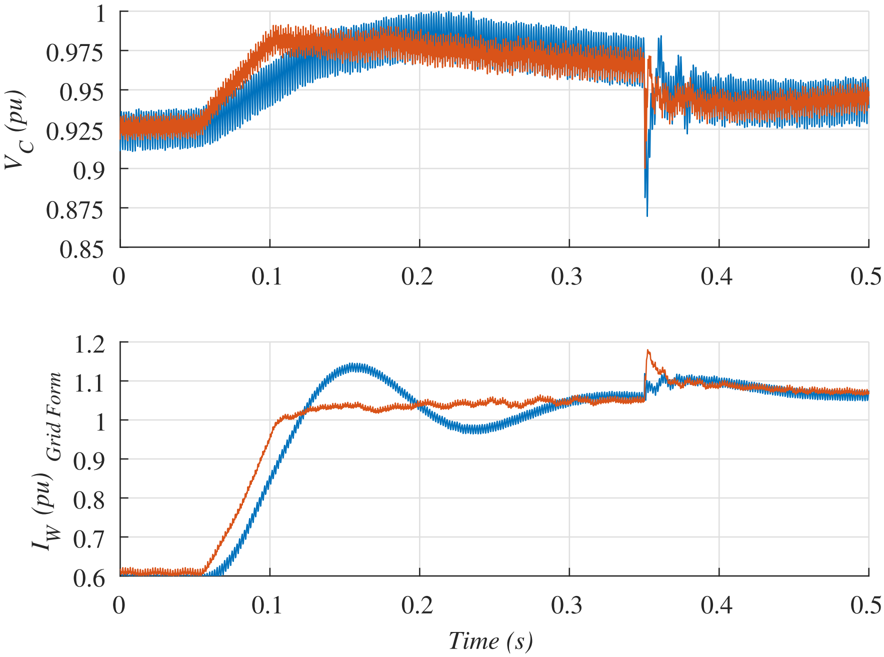

Figure 9.8: Voltage and current V_C and I_W: Response with PR controller:Blue; Response with $\mathcal{H}_\infty$ controller: red.

Fig. 9.7 shows the response of the active and reactive powers during the test carried. Note that the response with $\mathcal{H}_\infty$ controller has lower oscillations. Those oscillations are produced by the DRUs and are of 600 Hz (12^{th} harmonic). Finally, the overshoot and the setting time are lower with the $\mathcal{H}_\infty$ based controller.

Fig. 9.8 shows the magnitude of the voltage and the current during the test. Note that the voltage ripple when using the PR controller. Furthermore, the voltage has a faster recovery time with the $\mathcal{H}_\infty$ controller when the 15% resistive load is connected. The faster voltage restoration produce a bigger current peak as shown in Fig. 9.8.

Fig. 9.9 shows the frequency of the off-shore ac-grid during the test. The traces shown have been filtered with a 10 ms low-pass filter and a 12^{th} harmonic notch filter for representation purposes. Clearly, frequency deviation during the load transient is much smaller when using the $\mathcal{H}_\infty$ controller.

The voltage and current harmonic analysis has been carried out to compare the harmonic rejection of the designed controllers. Tab. 9.1 shows that using $\mathcal{H}_\infty$ controller the voltage harmonics are halved. Additionally, the table shows that the current harmonics are independent of the controller. It validates that the DRUs can be considered harmonic current sources.

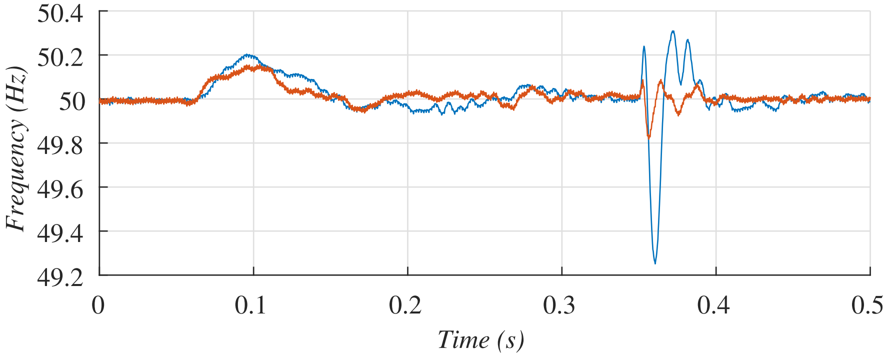

Figure 9.9: Off-shore grid frequency: Response with PR controller:Blue; Response with $\mathcal{H}_\infty$ controller: red.

Table 9.1: Harmonic analysis

harmonic	Voltage (pu)		Current (pu)	
	PR	$\mathcal{H}_\infty$	PR	$\mathcal{H}_\infty$
11^{th}	0.00902	0.00372	0.00654	0.00155
13^{th}	0.00887	0.00353	0.00733	0.00225

9.5 Conclusions

This paper has presented a voltage control methodology based on $\mathcal{H}_\infty$ techniques with a resonant behaviour. Besides, a PR controller has been obtained following a sound methodology. Both controllers have then been compared to check their robustness and dynamics.

With a suitable selection of generalised plant and associated weights, $\mathcal{H}_\infty$ controllers have been designed with a good time response, as well as a good coprime-factor uncertainty margin when compared to reasonably designed PR controllers.

Moreover, the $\mathcal{H}_\infty$ design procedure allowed for the shaping of high frequency closed loop response, leading to an improved harmonic rejection with respect to traditional PR controllers.

Appendix A

A.1 Stability analysis

The stability analysis of wind power plants for their design and integration has been carried out using some techniques. Some of them just can be used for SISO systems while others can be used for MIMO systems.

A.1.1 Nyquist stability

The first technique used to analyse the WTG stability is the Nyquist stability criterion. It consist of a graphical technique that allows to check the stability of a SISO system. The Nyquist plot shows the gain and phase stability margins that give information about the stability and robustness of the system. In [58] it is used to analyse the stability of a grid following WTG that uses a dq reference frame controller as is shown in Fig A.1. The stability of the system is analysed considering all the components of the system (controller, WTG, transformers, array cables and transport cables).

Another example is the presented in [163, 164], that considering a more complex MIMO system, separates each SISO combination to analyse the overall system stability using Nyquist curve.

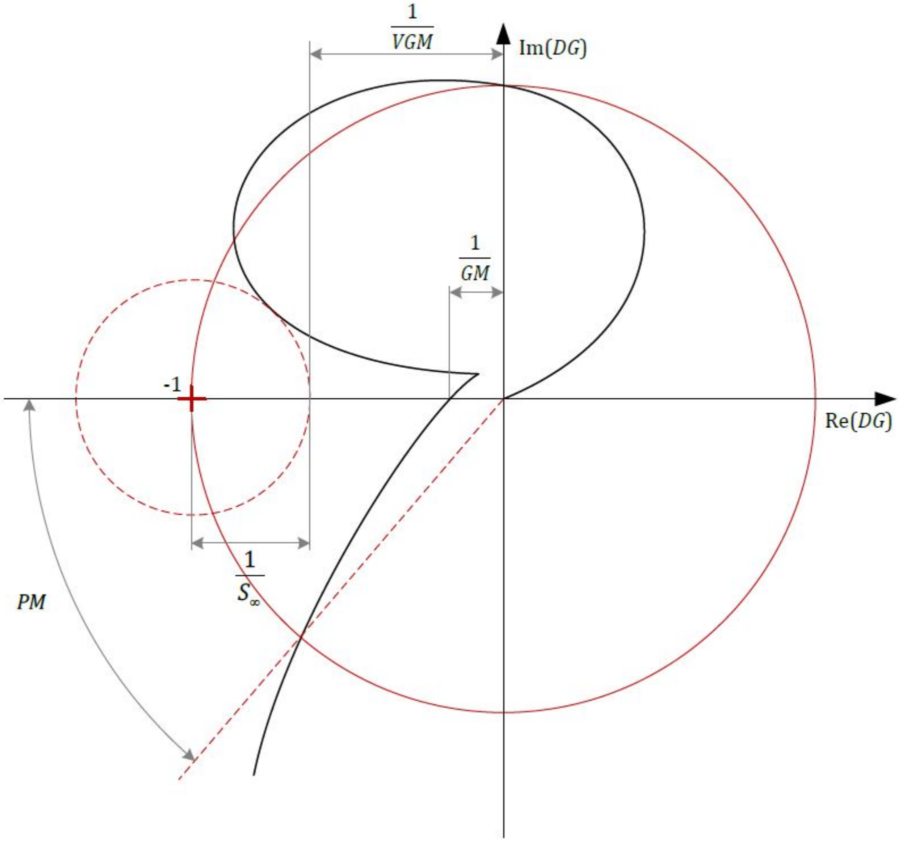

Figure A.1: Nyquist plot showing stability margins [58].

A.1.2 Impedance-based stability

The impedance-based stability method divides a system into two subsystems at a point of interest. As shows Fig A.2, one of the subsystem is considered as he source and the other as the load subsystem [165]. From this point, a feedback control can be obtained (see Fig A.2) in order to analyse the stability of the system. In the case of SISO systems the Nyquist criterion can be used for that purpose. For MIMO systems, generalised Nyquist criterion shall be used.

Moreover, this method is usefull when the frequency response of some element of the system is unknown. An example of what to do in this case is the applied in [166]. It uses this method to identify the frequency response of the WTG applying a small current disturbance

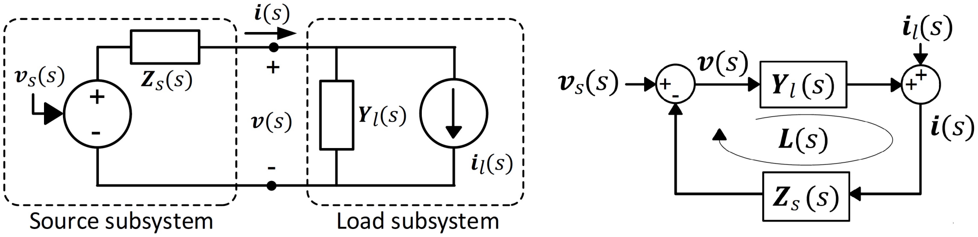

Figure A.2: Left: Impedance-based representation of grid and converter; right: Negative feedback control loop for stability analysis [166].

to the point of interest. The disturbance does a sweep in a range of frequency from 0 to 2000 Hz as shown in Fig A.3.

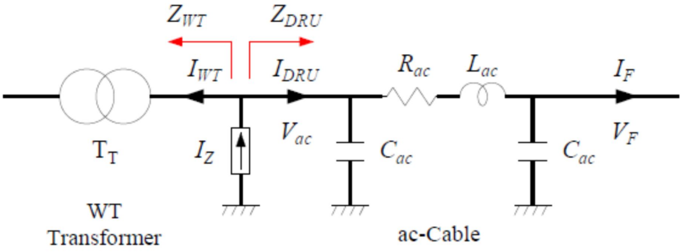

Figure A.3: Injection of a small disturbance I_Z to compute WT and DRU impedances [166].

A.1.3 Eigenvalue-based stability

The eigenvalue-based stability method allows a more exhaustive analysis of the system stability. This is probably the most interesting method to detect what is producing a non-desired behaviour in the system. Then, this method allows the next:

- The models of different components are available in the state space form.
- Eigenvalue analysis for stability (damping and frequency).
- Model some part of the system in detail and other as an equivalent impedance model.
- Controller tuning and root cause investigation based on the participation factor analysis.

In contrast, this method has the following cons:

- Everything must be modelled in state space. Non-linear state space modelling is also possible.

- Identification techniques (e.g. vector fitting) are required when only numerical data is available (e.g. look-up table).
- The system should be linearised for each operating point to apply linear analysis; critical especially for low frequency range.

In [167] the eigenvalue-based stability method is used for a system with grid forming and grid following inverters. It allows the analysis of the impact of critical parameters on system stability.

[168] uses this method to analysing the participation factors to tune a grid forming cascade controller.

[169] proposes a methodology to analyse grid forming converters that connect to a power grid. The consideration in this paper is to model the power grid as an impedance equivalent model while the grid forming converter is modeled in state-space representation (converter model and converter controller). Then both models are interconnected.

A.1.4 Passivity

Another method to analyse the stability of a system is the passivity. As defined in [170], a system is said to be a "Passive" system because the system does not "produce" anything to increase the output beyond the input. It means that a system is "Passive" if it cannot produce energy on its own, and can only dissipate the energy that is stored in it initially.

Moreover, as shown in Fig A.4 and defined in [170], the interconnection of $S_1(s)$ and $S_2(s)$ be two linear systems with passivity R-indices R_1 and R_2, respectively. If $R_1 R_2 < 1$, then the negative feedback interconnection of G_1 and G_2 is stable.

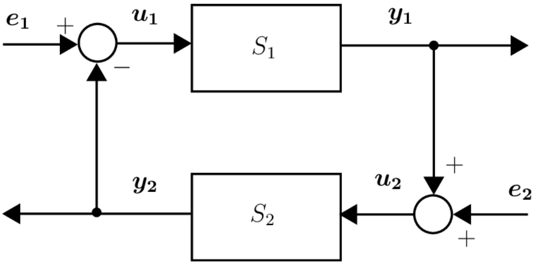

Figure A.4: Interconnection of passive systems.

From the "Passivity" concepts, a lot of studies have been proposed where the stability is guaranteed if the inverter output impedance behaves passive. a example of that is the proposed in [171, 172], that uses that concept to tune a grid forming converter that uses a cascade control loop of voltage and current. Similar studies are proposed in [173, 174, 175].

[176] evaluate the low-frequency passivity properties of grid-forming converters and its impact at the converter control loops.

[177] proposes a passivity-oriented discrete-time voltage controller for grid-forming inverters that achieves superior reference tracking performance, load disturbance rejection capability, and provides passive output impedance. It guarantees stable inverter operation under weak grid condition.

Bibliography

[1] *A European Green Deal.* European Commission - European Commission. URL: `https://ec.europa.eu/info/strategy/priorities-2019-2024/european-green-deal_en` (cit. on p. 2).

[2] *European Green Deal Call is launched.* WindEurope. Section: News. Sept. 23, 2020. URL: `https://windeurope.org/newsroom/news/european-green-deal-call-is-launched/` (cit. on p. 2).

[3] *European Green Deal.* WindEurope. URL: `https://windeurope.org/about-wind/campaigns/european-green-deal/` (cit. on p. 2).

[4] *Onshore and offshore wind.* Energy - European Commission. Apr. 21, 2020. URL: `https://ec.europa.eu/energy/topics/renewable-energy/onshore-and-offshore-wind_en` (cit. on p. 2).

[5] *Wind energy and economic recovery in Europe.* WindEurope. URL: `https://windeurope.org/data-and-analysis/product/` (cit. on p. 2).

[6] Peter Menke. "New grid access solutions for offshore wind farms". In: *EWEA Off-shore* (Mar. 2015) (cit. on pp. 3, 5, 10, 35, 62–64, 92, 128, 136, 160, 176, 177).

[7] Roland Ryndzionek and Łukasz Sienkiewicz. "Evolution of the HVDC Link Connecting Offshore Wind Farms to Onshore Power Systems". In: *Energies* 13.8 (Jan. 2020), p. 1914. DOI: `10.3390/en13081914` (cit. on p. 3).

[8] *PROMOTioN - Objectives.* URL: `https://www.promotion-offshore.net/objectives/` (cit. on p. 4).

[9] *PROMOTioN - Work Packages Structure.* URL: `https://www.promotion-offshore.net/about_promotion/work_packages_structure/` (cit. on p. 4).

[10] Nicolaos Antonio Cutululis et al. “Deliverable 3.7: Compliance evaluation results using simulations”. In: (2020). Publisher: PROMOTion - Progress on Meshed HVDC Offshore Transmission Networks (cit. on pp. 4, 35, 39, 53).

[11] R Blasco-Gimenez et al. “Uncontrolled rectifiers for HVDC connection of large off-shore wind farms”. In: *Power Electronics and Applications, 2009. EPE’09. 13th European Conference on.* IEEE. 2009, pp. 1–8 (cit. on pp. 5, 10, 62, 128, 176).

[12] R. Blasco-Gimenez et al. “Distributed Voltage and Frequency Control of Offshore Wind Farms Connected With a Diode-Based HVdc Link”. In: *IEEE Transactions on Power Electronics* 25.12 (2010). 00056, pp. 3095–3105. ISSN: 0885-8993. DOI: `10.1109/TPEL.2010.2086491` (cit. on pp. 5, 10, 35, 46–48, 50, 62, 92, 96, 128, 160, 176).

[13] R. Blasco-Gimenez et al. “Diode-Based HVdc Link for the Connection of Large Offshore Wind Farms”. In: *IEEE Transactions on Energy Conversion* 26.2 (2011). 00047, pp. 615–626. ISSN: 0885-8969. DOI: `10.1109/TEC.2011.2114886` (cit. on pp. 5, 10, 50, 62, 128, 160, 176).

[14] S. Bernal-Perez et al. “Efficiency and Fault Ride-Through Performance of a Diode-Rectifier- and VSC-Inverter-Based HVDC Link for Offshore Wind Farms”. In: *IEEE Transactions on Industrial Electronics* 60.6 (2013), pp. 2401–2409. ISSN: 0278-0046. DOI: `10.1109/TIE.2012.2222855` (cit. on pp. 5, 10, 35, 50, 62, 92, 94, 128, 148, 160, 176).

[15] R. Blasco-Gimenez et al. “LCC-HVDC Connection of Offshore Wind Farms With Reduced Filter Banks”. In: *IEEE Transactions on Industrial Electronics* 60.6 (2013), pp. 2372–2380. ISSN: 0278-0046. DOI: `10.1109/TIE.2012.2227906` (cit. on pp. 5, 10, 35, 62, 128, 160, 176).

[16] Mengran Yu et al. “Performance of hybrid power park technologies in future OFTO networks with the aim to achieve grid-forming capability”. In:

19th Wind Integration workshop. 19th Wind Integration workshop. Num Pages: 8. Dublin, Oct. 18, 2019 (cit. on p. 10).

[17] Ali Tayyebi et al. *Grid-Forming Converters–Inevitability, Control Strategies and Challenges in Future Grids Application.* AIM, June 7, 2018. ISBN: 978-2-9602415-1-8. DOI: `10.34890/412` (cit. on p. 10).

[18] T. Kawabata and S. Higashino. "Parallel operation of voltage source inverters". In: *IEEE Transactions on Industry Applications* 24.2 (Mar. 1988), pp. 281–287. ISSN: 1939-9367. DOI: `10.1109/28.2868` (cit. on p. 10).

[19] H. Beck and R. Hesse. "Virtual synchronous machine". In: *2007 9th International Conference on Electrical Power Quality and Utilisation.* ISSN: 2150-6655. Oct. 2007, pp. 1–6. DOI: `10.1109/EPQU.2007.4424220` (cit. on p. 11).

[20] Catalin Arghir, Taouba Jouini, and Florian Dörfler. "Grid-forming control for power converters based on matching of synchronous machines". In: *Automatica* 95 (Sept. 1, 2018), pp. 273–282. ISSN: 0005-1098. DOI: `10.1016/j.automatica.2018.05.037` (cit. on pp. 11, 16).

[21] B. B. Johnson et al. "Synchronization of Parallel Single-Phase Inverters With Virtual Oscillator Control". In: *IEEE Transactions on Power Electronics* 29.11 (Nov. 2014), pp. 6124–6138. ISSN: 1941-0107. DOI: `10.1109/TPEL.2013.2296292` (cit. on pp. 11, 18).

[22] X. Wang et al. "Grid-Synchronization Stability of Converter-Based Resources–An Overview". In: *IEEE Open Journal of Industry Applications* 1 (2020), pp. 115–134. ISSN: 2644-1241. DOI: `10.1109/OJIA.2020.3020392` (cit. on p. 11).

[23] M. C. Chandorkar, D. M. Divan, and R. Adapa. "Control of parallel connected inverters in standalone AC supply systems". In: *IEEE Transactions on Industry Applications* 29.1 (Jan. 1993), pp. 136–143. ISSN: 1939-9367. DOI: `10.1109/28.195899` (cit. on p. 12).

[24] Josep M. Guerrero et al. "A wireless controller to enhance dynamic performance of parallel inverters in distributed generation systems". In: *IEEE Transactions on Power Electronics* 19.5 (Sept. 2004), pp. 1205–1213. ISSN: 0885-8993. DOI: `10.1109/TPEL.2004.833451` (cit. on p. 13).

[25] J. M. Guerrero et al. “Output impedance design of parallel-connected UPS inverters with wireless load-sharing control”. In: *IEEE Transactions on industrial electronics* 52.4 (2005), pp. 1126–1135. ISSN: 0278-0046. DOI: `10.1109/TIE.2005.851634` (cit. on pp. 13, 69, 179).

[26] K. De Brabandere et al. “A Voltage and Frequency Droop Control Method for Parallel Inverters”. In: *IEEE Transactions on Power Electronics* 22.4 (July 2007), pp. 1107–1115. ISSN: 1941-0107. DOI: `10.1109/TPEL.2007.900456` (cit. on p. 13).

[27] J. M. Guerrero et al. “Control Strategy for Flexible Microgrid Based on Parallel Line-Interactive UPS Systems”. In: *IEEE Transactions on Industrial Electronics* 56.3 (Mar. 2009), pp. 726–736. ISSN: 0278-0046. DOI: `10.1109/TIE.2008.2009274` (cit. on p. 13).

[28] J. C. Vasquez et al. “Modeling, Analysis, and Design of Stationary-Reference-Frame Droop-Controlled Parallel Three-Phase Voltage Source Inverters”. In: *IEEE Transactions on Industrial Electronics* 60.4 (Apr. 2013), pp. 1271–1280. ISSN: 0278-0046. DOI: `10.1109/TIE.2012.2194951` (cit. on pp. 13, 22, 68, 179).

[29] J. M. Guerrero et al. “Hierarchical Control of Droop-Controlled AC and DC Microgrids – A General Approach Toward Standardization”. In: *IEEE Transactions on Industrial Electronics* 58.1 (Jan. 2011), pp. 158–172. ISSN: 0278-0046. DOI: `10.1109/TIE.2010.2066534` (cit. on pp. 13, 138).

[30] W. Yao et al. “Design and Analysis of the Droop Control Method for Parallel Inverters Considering the Impact of the Complex Impedance on the Power Sharing”. In: *IEEE Transactions on Industrial Electronics* 58.2 (2011), pp. 576–588. ISSN: 0278-0046. DOI: `10.1109/TIE.2010.2046001` (cit. on pp. 13, 69, 179).

[31] J. Beerten and R. Belmans. “Analysis of Power Sharing and Voltage Deviations in Droop-Controlled DC Grids”. In: *IEEE Transactions on Power Systems* 28.4 (Nov. 2013), pp. 4588–4597. ISSN: 1558-0679. DOI: `10.1109/TPWRS.2013.2272494` (cit. on p. 13).

[32] N. R. Chaudhuri and B. Chaudhuri. “Adaptive Droop Control for Effective Power Sharing in Multi-Terminal DC (MTDC) Grids”. In: *IEEE Transactions on Power Systems* 28.1 (Feb. 2013), pp. 21–29. ISSN: 1558-0679. DOI: `10.1109/TPWRS.2012.2203390` (cit. on p. 13).

[33] W. Wang et al. “Adaptive Droop Control of VSC-MTDC System for Frequency Support and Power Sharing”. In: *IEEE Transactions on Power Systems* 33.2 (Mar. 2018), pp. 1264–1274. ISSN: 1558-0679. DOI: `10.1109/TPWRS.2017.2719002` (cit. on p. 13).

[34] Y. Mi et al. “Intelligent Power Sharing of DC Isolated Microgrid Based on Fuzzy Sliding Mode Droop Control”. In: *IEEE Transactions on Smart Grid* 10.3 (May 2019), pp. 2396–2406. ISSN: 1949-3061. DOI: `10.1109/TSG.2018.2797127` (cit. on p. 13).

[35] H. Han et al. “An Improved Droop Control Strategy for Reactive Power Sharing in Islanded Microgrid”. In: *IEEE Transactions on Power Electronics* 30.6 (June 2015), pp. 3133–3141. ISSN: 1941-0107. DOI: `10.1109/TPEL.2014.2332181` (cit. on p. 13).

[36] A. Milczarek, M. Malinowski, and J. M. Guerrero. “Reactive Power Management in Islanded Microgrid-Proportional Power Sharing in Hierarchical Droop Control”. In: *IEEE Transactions on Smart Grid* 6.4 (July 2015), pp. 1631–1638. ISSN: 1949-3061. DOI: `10.1109/TSG.2015.2396639` (cit. on p. 13).

[37] A. Micallef et al. “Reactive Power Sharing and Voltage Harmonic Distortion Compensation of Droop Controlled Single Phase Islanded Microgrids”. In: *IEEE Transactions on Smart Grid* 5.3 (May 2014), pp. 1149–1158. ISSN: 1949-3061. DOI: `10.1109/TSG.2013.2291912` (cit. on p. 13).

[38] H. Mahmood, D. Michaelson, and J. Jiang. “Reactive Power Sharing in Islanded Microgrids Using Adaptive Voltage Droop Control”. In: *IEEE Transactions on Smart Grid* 6.6 (Nov. 2015), pp. 3052–3060. ISSN: 1949-3061. DOI: `10.1109/TSG.2015.2399232` (cit. on p. 13).

[39] L. Zhang, L. Harnefors, and H. Nee. “Power-Synchronization Control of Grid-Connected Voltage-Source Converters”. In: *IEEE Transactions on Power Systems* 25.2 (May 2010), pp. 809–820. ISSN: 1558-0679. DOI: `10.1109/TPWRS.2009.2032231` (cit. on p. 14).

[40] Q. Zhong and G. Weiss. “Synchronverters: Inverters That Mimic Synchronous Generators”. In: *IEEE Transactions on Industrial Electronics* 58.4 (Apr. 2011), pp. 1259–1267. ISSN: 1557-9948. DOI: `10.1109/TIE.2010.2048839` (cit. on p. 15).

[41] M. Guan et al. “Synchronous Generator Emulation Control Strategy for Voltage Source Converter (VSC) Stations”. In: *IEEE Transactions on Power Systems* 30.6 (Nov. 2015), pp. 3093–3101. ISSN: 1558-0679. DOI: `10.1109/TPWRS.2014.2384498` (cit. on p. 15).

[42] Marcelo Oñate et al. “Control of a back-to-back converter as a power transfer system using synchronverter approach”. In: *IET Generation, Transmission & Distribution* 12.9 (Jan. 12, 2018). Publisher: IET Digital Library, pp. 1998–2005. ISSN: 1751-8695. DOI: `10.1049/iet-gtd.2017.0093` (cit. on p. 15).

[43] S. Y. Caliskan and P. Tabuada. “Compositional Transient Stability Analysis of Multimachine Power Networks”. In: *IEEE Transactions on Control of Network Systems* 1.1 (Mar. 2014). Conference Name: IEEE Transactions on Control of Network Systems, pp. 4–14. ISSN: 2325-5870. DOI: `10.1109/TCNS.2014.2304868` (cit. on p. 16).

[44] Dominic Groß et al. “The Effect of Transmission-Line Dynamics on Grid-Forming Dispatchable Virtual Oscillator Control”. In: *IEEE Transactions on Control of Network Systems* 6.3 (Sept. 2019), pp. 1148–1160. ISSN: 2325-5870. DOI: `10.1109/TCNS.2019.2921347` (cit. on p. 19).

[45] *GC0062: Fault Ride Through | National Grid ESO*. Sept. 25, 2018. URL: `https://www.nationalgrideso.com/codes/grid-code/modifications/gc0062-fault-ride-through` (cit. on p. 20).

[46] Bandopant Pawar et al. “Grid-Forming Control for Solar PV Systems with Power Reserves”. In: *IEEE Transactions on Sustainable Energy* (2021), pp. 1–1. ISSN: 1949-3037. DOI: `10.1109/TSTE.2021.3074066` (cit. on p. 21).

[47] S. F. Zarei et al. “Reinforcing Fault Ride Through Capability of Grid Forming Voltage Source Converters Using an Enhanced Voltage Control Scheme”. In: *IEEE Transactions on Power Delivery* 34.5 (Oct. 2019), pp. 1827–1842. ISSN: 1937-4208. DOI: `10.1109/TPWRD.2018.2844082` (cit. on p. 22).

[48] M. S. Golsorkhi and D. D. Lu. “A Decentralized Control Method for Islanded Microgrids Under Unbalanced Conditions”. In: *IEEE Transactions on Power Delivery* 31.3 (June 2016), pp. 1112–1121. ISSN: 1937-4208. DOI: `10.1109/TPWRD.2015.2453251` (cit. on p. 22).

[49] M. Eskandari and A. V. Savkin. “On the Impact of Fault Ride-Through on Transient Stability of Autonomous Microgrids: Nonlinear Analysis and Solution”. In: *IEEE Transactions on Smart Grid* (2020), pp. 1–1. ISSN: 1949-3061. DOI: `10.1109/TSG.2020.3030015` (cit. on p. 23).

[50] B. Mahamedi et al. “Sequence-Based Control Strategy With Current Limiting for the Fault Ride-Through of Inverter-Interfaced Distributed Generators”. In: *IEEE Transactions on Sustainable Energy* 11.1 (Jan. 2020), pp. 165–174. ISSN: 1949-3037. DOI: `10.1109/TSTE.2018.2887149` (cit. on p. 23).

[51] I. Sadeghkhani et al. “A Current Limiting Strategy to Improve Fault Ride-Through of Inverter Interfaced Autonomous Microgrids”. In: *IEEE Transactions on Smart Grid* 8.5 (Sept. 2017), pp. 2138–2148. ISSN: 1949-3061. DOI: `10.1109/TSG.2016.2517201` (cit. on p. 23).

[52] F. Salha, F. Colas, and X. Guillaud. “Virtual resistance principle for the overcurrent protection of PWM voltage source inverter”. In: *2010 IEEE PES Innovative Smart Grid Technologies Conference Europe (ISGT Europe)*. 2010 IEEE PES Innovative Smart Grid Technologies Conference Europe (ISGT Europe). Oct. 2010, pp. 1–6. DOI: `10.1109/ISGTEUROPE.2010.5638965` (cit. on p. 23).

[53] M. G. Taul et al. “Current Limiting Control With Enhanced Dynamics of Grid-Forming Converters During Fault Conditions”. In: *IEEE Journal of Emerging and Selected Topics in Power Electronics* 8.2 (June 2020), pp. 1062–1073. ISSN: 2168-6785. DOI: `10.1109/JESTPE.2019.2931477` (cit. on p. 23).

[54] A. D. Paquette and D. M. Divan. “Virtual Impedance Current Limiting for Inverters in Microgrids With Synchronous Generators”. In: *IEEE Transactions on Industry Applications* 51.2 (Mar. 2015), pp. 1630–1638. ISSN: 1939-9367. DOI: `10.1109/TIA.2014.2345877` (cit. on p. 23).

[55] M. A. Awal and I. Husain. “Unified Virtual Oscillator Control for Grid-Forming and Grid-Following Converters”. In: *IEEE Journal of Emerging and Selected Topics in Power Electronics* (2020), pp. 1–1. ISSN: 2168-6785. DOI: `10.1109/JESTPE.2020.3025748` (cit. on pp. 23, 24).

[56] Ahmed Abdelrahim et al. “Modified grid forming converter controller with fault ride through capability without PLL or current loop”. In: *18th Wind Integration Workshop*. IRL, Oct. 18, 2019 (cit. on pp. 23, 24).

[57] Justino Rodrigues, Carlos Moreira, and JoÃ£o PeÃ§as Lopes. “Fault-ride-through strategies for grid-tied and grid-forming smart-transformers suited for islanding and interconnected operation”. In: *Electric Power Systems Research* 189 (Dec. 1, 2020), p. 106616. ISSN: 0378-7796. DOI: `10.1016/j.epsr.2020.106616` (cit. on p. 24).

[58] Lukasz Hubert Kocewiak. *Harmonics in large offshore wind farms*. Department of Energy Technology, Aalborg University, 2012 (cit. on pp. 26, 28, 129, 141, 187, 188).

[59] Łukasz Hubert Kocewiak, Jesper Hjerrild, and Claus Leth Bak. “Wind turbine converter control interaction with complex wind farm systems”. In: *IET Renewable Power Generation* 7.4 (2013), pp. 380–389 (cit. on pp. 26, 129).

[60] E. Muljadi et al. “Equivalencing the collector system of a large wind power plant”. In: *2006 IEEE Power Engineering Society General Meeting*. 2006, 9–pp. DOI: `10.1109/PES.2006.1708945` (cit. on pp. 26, 28, 129, 135, 141).

[61] Miguel Garcia-Gracia et al. “Modelling wind farms for grid disturbance studies”. In: *Renewable Energy* 33.9 (2008), pp. 2109–2121 (cit. on pp. 26, 129).

[62] L. M. Fernandez et al. “Equivalent models of wind farms by using aggregated wind turbines and equivalent winds”. In: *Energy conversion and management* 50.3 (2009), pp. 691–704 (cit. on pp. 26, 129).

[63] Paul Brogan. “The stability of multiple, high power, active front end voltage sourced converters when connected to wind farm collector systems”. In: *Proc. EPE Wind Energy Chapter Seminar*. 2010, pp. 1–6 (cit. on pp. 26, 27, 129, 140).

[64] Łukasz Hubert Kocewiak, Jesper Hjerrild, and C Leth Bak. “Wind farm structures impact on harmonic emission and grid interaction”. In: *European Wind Energy Conference*. 2010, pp. 1–8 (cit. on pp. 26, 129).

[65] J Martínez-Turégano et al. “Model aggregation of large wind farms for dynamic studies”. In: *IECON 2017 - 43rd Annual Conference of the IEEE Industrial Electronics Society*. 2017, pp. 316–321. DOI: `10.1109/IECON.2017.8216057` (cit. on pp. 27, 129, 136, 137, 177).

[66] R. Brayton et al. “A new algorithm for statistical circuit design based on quasi-Newton methods and function splitting”. In: *IEEE Transactions on Circuits and Systems* 26.9 (1979), pp. 784–794. ISSN: 0098-4094. DOI: `10.1109/TCS.1979.1084701` (cit. on pp. 29, 136).

[67] FW Gembicki. “Vector optimization for control with performance and parameter sensitivity indices”. In: *Ph. D. thesis, Case Western Reserve Univ.* (1974) (cit. on pp. 29, 136).

[68] PETER J. FLEMING. “Computer aided control system design using a multi-objective optimization approach”. In: *Proceedings of Control 1985 Conference, Cambridge, UK*. 1985, pp. 174–179 (cit. on pp. 29, 136).

[69] Shih-Ping Han. “A globally convergent method for nonlinear programming”. In: *Journal of optimization theory and applications* 22.3 (1977), pp. 297–309 (cit. on pp. 29, 136).

[70] *California battery’s black start capability hailed as ’major accomplishment in the energy industry’*. Energy Storage News. URL: `https://www.energy-storage.news/news/california-batterys-black-start-capability-hailed-as-major-accomplishment-i` (cit. on p. 34).

[71] *Black-start and system restoration utilizing the NEMO Modular Multilevel Converter: a practical test in the Belgian transmission system*. e-cigre. Aug. 31, 2020. URL: `https://e-cigre.org/publication/SESSION2020_B4-108` (cit. on p. 34).

[72] *Black Start | National Grid ESO*. URL: `https://www.nationalgrideso.com/black-start?technical-requirements` (cit. on p. 34).

[73] *A carbon free system: Stability Pathfinder stakeholder feedback request | National Grid ESO*. URL: `https://www.nationalgrideso.com/news/carbon-free-system-stability-pathfinder-stakeholder-feedback-request` (cit. on p. 34).

[74] I Penarrocha et al. “Synthesis of nonlinear controller for wind turbines stability when providing grid support”. In: *International Journal of Robust and Nonlinear Control* 24.16 (2014), pp. 2261–2284. ISSN: 1099-1239. DOI: `https://doi.org/10.1002/rnc.2986` (cit. on p. 34).

[75] J. Martinez-Turegano et al. “Mixed grid-forming and grid-following wind power plants for black start operation”. In: *17th International Wind Integration Workshop, Energynautics GmbH, Stockholm*. Vol. 550. 2018 (cit. on p. 34).

[76] Daniela Pagnani et al. “Overview of Black Start Provision by Offshore Wind Farms”. In: *IECON 2020 The 46th Annual Conference of the IEEE Industrial Electronics Society*. ISSN: 2577-1647. Oct. 2020, pp. 1892–1898. DOI: `10.1109/IECON43393.2020.9254743` (cit. on pp. 34, 36, 37).

[77] Anubhav Jain, Jayachandra N. Sakamuri, and Nicolaos A. Cutululis. “Grid-forming control strategies for black start by offshore wind power plants”. In: *Wind Energy Science* 5.4 (Oct. 12, 2020). Publisher: Copernicus GmbH, pp. 1297–1313. ISSN: 2366-7443. DOI: `https://doi.org/10.5194/wes-5-1297-2020` (cit. on p. 34).

[78] T. Machida et al. “Control and protection of HVDC systems with diode valve converter”. In: *Electr. Eng. Jpn. (Engl. Transl.); (United States)* 98:1 (Jan. 1, 1978). DOI: `10.1002/eej.4390980109` (cit. on p. 35).

[79] J. P. Bowles. “Multiterminal HVDC Transmission Systems Incorporating Diode Rectifier Stations”. In: *IEEE Transactions on Power Apparatus and Systems* PAS-100.4 (Apr. 1981), pp. 1674–1678. ISSN: 0018-9510. DOI: `10.1109/TPAS.1981.316562` (cit. on pp. 35, 51).

[80] S. Hungsasutra and R. M. Mathur. “Unit connected operator with diode valve rectifier scheme”. In: *IEEE Transactions on Power Systems* 4.2 (May 1989), pp. 538–543. ISSN: 1558-0679. DOI: `10.1109/59.193827` (cit. on p. 35).

[81] R Ramachandran et al. “AC Grid Forming by Coordinated Control of Offshore Wind Farm connected to Diode Rectifier based HVDC Link - Review and Assessment of Solutions”. In: *2018 20th European Conference on Power Electronics and Applications (EPE’18 ECCE Europe)*. 2018, P.1–P.10 (cit. on pp. 35, 62, 176).

[82] Daniela Pagnani et al. "Offshore Wind Farm Black Start Service Integration: Review and Outlook of Ongoing Research". In: *Energies* 13.23 (Jan. 2020). Number: 23 Publisher: Multidisciplinary Digital Publishing Institute, p. 6286. DOI: `10.3390/en13236286` (cit. on pp. 36, 37).

[83] Weipeng Liu and Yutian Liu. "Hierarchical model predictive control of wind farm with energy storage system for frequency regulation during black-start". In: *International Journal of Electrical Power & Energy Systems* 119 (July 1, 2020), p. 105893. ISSN: 0142-0615. DOI: `10.1016/j.ijepes.2020.105893` (cit. on p. 37).

[84] Andres Pena Asensio et al. "Decentralized Frequency Control for Black Start of Full-Converter Wind Turbines". In: *IEEE Transactions on Energy Conversion* 36.1 (Mar. 2021), pp. 480–487. ISSN: 1558-0059. DOI: `10.1109/TEC.2020.3011611` (cit. on p. 38).

[85] Zia Emin et al. "Transformer energization in power systems: A study guide". In: *CIGRE WG C4.307* (2014) (cit. on p. 43).

[86] A. Abdalrahman and E. Isabegovic. "DolWin1 - Challenges of connecting offshore wind farms". In: *2016 IEEE International Energy Conference (ENERGYCON)*. Apr. 2016, pp. 1–10. DOI: `10.1109/ENERGYCON.2016.7513981` (cit. on p. 43).

[87] Filipe Miguel Faria da Silva. *Analysis and simulation of electromagnetic transients in HVAC cable transmission grids.* Institut for Energiteknik, Aalborg Universitet, July 2011. ISBN: 978-87-89179-99-5 (cit. on p. 44).

[88] Ömer Göksu et al. "Deliverable 3.4: Results on control strategies of WPPs connected to DR-HVDC". In: (2018) (cit. on pp. 47, 48).

[89] Remus Teodorescu, Marco Liserre, and Pedro Rodriguez. *Grid converters for photovoltaic and wind power systems.* John Wiley & Sons, 2011. ISBN: 978-1-119-95720-1 (cit. on pp. 47, 65, 66, 68, 69, 180).

[90] L. Yu, R. Li, and L. Xu. "Distributed PLL-Based Control of Offshore Wind Turbines Connected With Diode-Rectifier-Based HVDC Systems". In: *IEEE Transactions on Power Delivery* 33.3 (2018), pp. 1328–1336. ISSN: 0885-8977. DOI: `10.1109/TPWRD.2017.2772342` (cit. on pp. 47, 62, 67, 176).

[91] Qi Hu et al. “Large Signal Synchronizing Instability of PLL-Based VSC Connected to Weak AC Grid”. In: *IEEE Transactions on Power Systems* 34.4 (July 2019), pp. 3220–3229. ISSN: 1558-0679. DOI: `10.1109/TPWRS.2019.2892224` (cit. on p. 47).

[92] Baohong Li, Shi Chen, and Tianqi Liu. “Theoretical analysis on the VSC instability caused by PLL in weak system”. In: *IET Renewable Power Generation* 14.10 (2020), pp. 1782–1788. DOI: `10.1049/iet-rpg.2019.1349` (cit. on p. 47).

[93] R. Li, L. Yu, and L. Xu. “Offshore AC Fault Protection of Diode Rectifier Unit Based HVDC System for Wind Energy Transmission”. In: *IEEE Transactions on Industrial Electronics* (2018), pp. 1–1. ISSN: 0278-0046. DOI: `10.1109/TIE.2018.2869357` (cit. on pp. 49, 62, 94, 106, 176).

[94] Slavomir Seman, Rainer Zurowski, and Christos Taratoris. “Interconnection of advanced Type 4 WTGs with Diode Rectifier based HVDC solution and weak AC grids”. In: *Proceedings of the 14th Wind Integration Workshop, Brussels, Belgium, 20th–22nd Oct.* 2015 (cit. on pp. 48, 179).

[95] Cord Prignitz et al. “FixReF: A control strategy for offshore wind farms with different wind turbine types and diode rectifier HVDC transmission”. In: *IEEE 7th International Symposium on Power Electronics for Distributed Generation Systems (PEDG).* ISSN: 2329-5767. June 2016, pp. 1–7. DOI: `10.1109/PEDG.2016.7527013` (cit. on p. 49).

[96] Miguel Angel Cardiel-Alvarez et al. “Decentralized Control of Offshore Wind Farms Connected to Diode-Based HVdc Links”. In: *IEEE Transactions on Energy Conversion* 33.3 (Sept. 2018), pp. 1233–1241. ISSN: 1558-0059. DOI: `10.1109/TEC.2018.2804662` (cit. on p. 49).

[97] S Bernal-Perez et al. “Off-shore wind farm grid connection using a novel diode-rectifier and VSC-inverter based HVDC transmission link”. In: *IECON 2011 - 37th Annual Conference of the IEEE Industrial Electronics Society.* ISSN: 1553-572X. Nov. 2011, pp. 3186–3191. DOI: `10.1109/IECON.2011.6119820` (cit. on p. 50).

[98] Soledad Bernal-Perez, Salvador Añó-Villalba, and R Blasco-Gimenez. “Stability analysis of HVDC-diode rectifier connected off-shore wind power plants”. In: *IECON 2015 - 41st Annual Conference of the IEEE Industrial*

Electronics Society. Nov. 2015, pp. 004040–004045. DOI: `10.1109/IECON.2015.7392729` (cit. on p. 50).

[99] Zheren Zhang, Yingjie Tang, and Zheng Xu. "Medium frequency diode rectifier unit based HVDC transmission for offshore wind farm integration". In: *IET Renewable Power Generation* 15.4 (2021), pp. 717–730. ISSN: 1752-1424. DOI: `10.1049/rpg2.12062` (cit. on p. 50).

[100] Ashkan Nami et al. "Active Power Filtering Embedded in the Frequency Control of an Offshore Wind Farm Connected to a Diode-Rectifier-Based HVDC Link". In: *Energies* 11.10 (Oct. 2018), p. 2718. DOI: `10.3390/en11102718` (cit. on p. 50).

[101] Ashkan Nami et al. "Frequency Control of Offshore Wind Farm With Diode-Rectifier-based HVdc Connection". In: *IEEE Transactions on Energy Conversion* 35.1 (Mar. 2020), pp. 130–138. ISSN: 1558-0059. DOI: `10.1109/TEC.2019.2949892` (cit. on p. 50).

[102] S. Bernal-Perez et al. "Connection of off-shore wind power plants to VSC-MTdc networks using HVdc diode-rectifiers". In: *2013 IEEE International Symposium on Industrial Electronics (ISIE)*. 2013, pp. 1–6. DOI: `10.1109/ISIE.2013.6563795` (cit. on pp. 51, 160).

[103] S Bernal-Perez, S Añó-Villalba, and R Blasco-Gimenez. "Stability analysis of multi-terminal HVDC with diode rectifier connected off-shore wind power plants". In: *International Journal of Electrical Power & Energy Systems* 124 (Jan. 1, 2021), p. 106231. ISSN: 0142-0615. DOI: `10.1016/j.ijepes.2020.106231` (cit. on p. 51).

[104] Behnam Nouri et al. "D2. 4 Requirement recommendations to adapt and extend existing grid codes". In: (2019). Publisher: European Commission (cit. on p. 51).

[105] Thanh Hai Nguyen, Dong-Choon Lee, and Chan-Ki Kim. "A Series-Connected Topology of a Diode Rectifier and a Voltage-Source Converter for an HVDC Transmission System". In: *IEEE Transactions on Power Electronics* 29.4 (2014), pp. 1579–1584. ISSN: 0885-8993. DOI: `10.1109/TPEL.2013.2283368` (cit. on pp. 52, 62, 176).

[106] M. von Hofen et al. "Hybrid offshore HVDC converter with diode rectifier and Modular Multilevel Converter". In: *IEEE 7th International Sympo-*

sium on Power Electronics for Distributed Generation Systems (PEDG). ISSN: 2329-5767. June 2016, pp. 1–7. DOI: `10.1109/PEDG.2016.7527085` (cit. on p. 52).

[107] R. Li and L. Xu. “A Unidirectional Hybrid HVDC Transmission System Based on Diode Rectifier and Full-bridge MMC”. In: *IEEE Journal of Emerging and Selected Topics in Power Electronics* (2020), pp. 1–1. ISSN: 2168-6785. DOI: `10.1109/JESTPE.2020.3015342` (cit. on p. 53).

[108] Y. Chang and X. Cai. “Hybrid Topology of a Diode-Rectifier-Based HVDC System for Offshore Wind Farms”. In: *IEEE Journal of Emerging and Selected Topics in Power Electronics* 7.3 (Sept. 2019), pp. 2116–2128. ISSN: 2168-6785. DOI: `10.1109/JESTPE.2018.2881768` (cit. on p. 53).

[109] Slavomir Seman, Rainer Zurowski, and Timo Christ. “Investigation of DC Converter Nonlinear Interaction with Offshore Wind Power Park System”. In: *EWEA Off-shore* (2015) (cit. on pp. 62, 176).

[110] Timo Christ, Slavomir Seman, and Rainer Zurowski. *Power generation facility and method for the operation thereof.* US Patent App. 15/741,777. 2018 (cit. on pp. 62, 176).

[111] S.V. Bozhko et al. “Control of Offshore DFIG-Based Wind Farm Grid With Line-Commutated HVDC Connection”. In: *Energy Conversion, IEEE Transaction on* 22.1 (2007). ISSN: 0885-8969. DOI: `10.1109/TEC.2006.889544` (cit. on p. 63).

[112] Jaime Martínez-Turégano et al. “Aggregation of Type-4 Large Wind Farms Based on Admittance Model Order Reduction”. In: *Energies* 12.9 (2019), p. 1730 (cit. on p. 63).

[113] R. Teodorescu et al. “Proportional-resonant controllers and filters for grid-connected voltage-source converters”. In: *IEE Proceedings-Electric Power Applications* 153.5 (2006), pp. 750–762. ISSN: 1350-2352. DOI: `10.1049/ip-epa:20060008` (cit. on pp. 66, 180).

[114] A. Timbus et al. “Evaluation of Current Controllers for Distributed Power Generation Systems”. In: *IEEE Transactions on Power Electronics* 24.3 (2009), pp. 654–664. ISSN: 0885-8993. DOI: `10.1109/TPEL.2009.2012527` (cit. on p. 66).

[115] A. G. Yepes et al. “High-Performance Digital Resonant Controllers Implemented With Two Integrators”. In: *IEEE Transactions on Power Electronics* 26.2 (2011), pp. 563–576. ISSN: 0885-8993. DOI: `10.1109/TPEL.2010.2066290` (cit. on pp. 66, 181).

[116] D. N. Zmood and D. G. Holmes. “Stationary frame current regulation of PWM inverters with zero steady-state error”. In: *IEEE Transactions on Power Electronics* 18.3 (2003), pp. 814–822. ISSN: 0885-8993. DOI: `10.1109/TPEL.2003.810852` (cit. on pp. 66, 69).

[117] S. Golestan, J. M. Guerrero, and J. C. Vasquez. “Three-Phase PLLs: A Review of Recent Advances”. In: *IEEE Transactions on Power Electronics* 32.3 (2017), pp. 1894–1907. ISSN: 0885-8993. DOI: `10.1109/TPEL.2016.2565642` (cit. on p. 67).

[118] P. Rodriguez et al. “Decoupled Double Synchronous Reference Frame PLL for Power Converters Control”. In: *IEEE Transactions on Power Electronics* 22.2 (2007), pp. 584–592. ISSN: 0885-8993. DOI: `10.1109/TPEL.2006.890000` (cit. on p. 67).

[119] Y. Guo et al. “Enhanced Voltage Control of VSC-HVDC-Connected Offshore Wind Farms Based on Model Predictive Control”. In: *IEEE Transactions on Sustainable Energy* 9.1 (2018), pp. 474–487. ISSN: 1949-3029. DOI: `10.1109/TSTE.2017.2743005` (cit. on p. 69).

[120] Paul C. Krause et al. *Analysis of Electric Machinery and Drive Systems*. Second. IEEE Press Series in Power Engineering - John Wiley & Sons, Inc., 2002. ISBN: 978-1-118-02429-4 (cit. on p. 69).

[121] Qing-Chang Zhong and Dushan Boroyevich. “Structural resemblance between droop controllers and phase-locked loops”. In: *IEEE Access* 4 (2016), pp. 5733–5741 (cit. on p. 74).

[122] Conseil international des grands réseaux électriques. Comité d’études C4. *Transformer Energization in Power Systems: A Study Guide*. CIGRÉ, 2014 (cit. on p. 79).

[123] Infineon Technologies. *Infineon Technologies*. URL: `https://www.infineon.com/cms/en/product/power/igbt/igbt-modules/igbt-modules-up-to-1600v-1700v/fz3600r17he4/` (cit. on p. 80).

[124] M. Szechtman, T. Wess, and C. V. Thio. “First benchmark model for HVDC control studies”. In: *Electra* Vol. 135.Num. 135 (Apr. 1991), pp. 54–73 (cit. on pp. 88, 126, 156).

[125] Thomas Hammer et al. “Diode-Rectifier HVDC link to onshore power systems: Dynamic performance of wind turbine generators and Reliability of liquid immersed HVDC Diode Rectifier Units”. In: *CIGRE Conference Technical Committee B4*. 2016 (cit. on pp. 92, 96).

[126] Peter Menke et al. “Second Generation DC Grid Access for Large Scale Offshore Wind Farms”. In: *14th International Workshop on Large-Scale Integration of Wind Power into Power Systems as well as on Transmission Networks for Offshore Wind Power Plants.* Brussels, Oct. 2015, pp. 1–6. ISBN: 978-3-9816549-1-2 (cit. on p. 92).

[127] Peter Menke. “Major breakthrough in DC grid access for large scale offshore wind farms”. In: *EWEA Offshore Conference.* Copenhagen, 2015 (cit. on p. 92).

[128] Xue Han et al. “Transient Characteristics Under Ground and Short-Circuit Faults in a ± 500 kV MMC-Based HVDC System With Hybrid DC Circuit Breakers”. In: *IEEE Transactions on Power Delivery* 33.3 (2018), pp. 1378–1387. DOI: `10.1109/TPWRD.2018.2795800` (cit. on p. 93).

[129] Simon Wenig et al. “On Full-Bridge Bipolar MMC-HVDC Control and Protection for Transient Fault and Interaction Studies”. In: *IEEE Transactions on Power Delivery* 33.6 (Dec. 2018), pp. 2864–2873. ISSN: 1937-4208 (cit. on p. 93).

[130] Yushuang Liu et al. “Short-Circuit Current Estimation of Modular Multilevel Converter Using Discrete-Time Modeling”. en. In: *IEEE Trans. Power Electron.* 34.1 (Jan. 2019), pp. 40–45. ISSN: 0885-8993, 1941-0107. DOI: `10.1109/TPEL.2018.2840100` (cit. on p. 93).

[131] Marius Langwasser et al. “Fault Current Estimation in Multi-Terminal HVdc Grids Considering MMC Control”. en. In: *IEEE Trans. Power Syst.* 34.3 (May 2019), pp. 2179–2189. ISSN: 0885-8950, 1558-0679 (cit. on p. 93).

[132] Nadew Adisu Belda, Cornelis Arie Plet, and Rene Peter Paul Smeets. “Analysis of Faults in Multiterminal HVDC Grid for Definition of Test Requirements of HVDC Circuit Breakers”. en. In: *IEEE Trans. Power De-*

livery 33.1 (Feb. 2018), pp. 403–411. ISSN: 0885-8977, 1937-4208 (cit. on p. 93).

[133] Geng Tang and Zheng Xu. “A LCC and MMC hybrid HVDC topology with DC line fault clearance capability”. en. In: *International Journal of Electrical Power & Energy Systems* 62 (Nov. 2014), pp. 419–428. ISSN: 0142-0615. DOI: `10.1016/j.ijepes.2014.04.045` (cit. on p. 93).

[134] Hong Rao et al. “Key technologies of ultra-high voltage hybrid LCC-VSC MTDC systems”. In: *CSEE Journal of Power and Energy Systems* 5.3 (Sept. 2019), pp. 365–373. ISSN: 2096-0042. DOI: `10.17775/CSEEJPES.2019.01140` (cit. on p. 93).

[135] Zhe Zhu et al. “HIL Testing of an LCC-MMC Multi-terminal HVDC System in Various Operating Modes”. In: *Proceedings of the International Conference on Power Systems Transients 2019 (IPST 2019)*. Perpignan, June 2019 (cit. on p. 93).

[136] Naushath M. Haleem et al. “Investigation of Fault Ride-Through Capability of Hybrid VSC-LCC Multi-Terminal HVDC Transmission Systems”. In: *IEEE Transactions on Power Delivery* 34.1 (Feb. 2019), pp. 241–250. ISSN: 1937-4208. DOI: `10.1109/TPWRD.2018.2868467` (cit. on p. 93).

[137] CENELEC. *CLC/TS 50654-1:2020 "HVDC Grid Systems and connected Converter Stations - Guideline and Parameter Lists for Functional Specifications - Part 1: Guidelines"*. 2020 (cit. on p. 94).

[138] Mian Wang et al. “Pole Rebalancing Methods for Pole-to-Ground Faults in Symmetrical Monopolar HVDC Grids”. In: *IEEE Transactions on Power Delivery* 34.1 (Feb. 2019), pp. 188–197. ISSN: 1937-4208. DOI: `10.1109/TPWRD.2018.2853704` (cit. on p. 94).

[139] P. Rault et al. “Real-time simulation with an industrial DCCB controller in a HVDC grid”. In: *Proceedings of the International Conference on Power Systems Transients 2019 (IPST 2019)*. Perpignan, June 2019 (cit. on pp. 94, 108).

[140] Salvador Añó-Villalba et al. “Wind power plant integration in voltage source converter HVdc grids with voltage droop control”. In: *Mathematics and Computers in Simulation* 146 (Apr. 2018), pp. 186–199. ISSN: 0378-4754. DOI: `10.1016/j.matcom.2016.12.007` (cit. on p. 94).

[141] R. Li et al. "DC Fault Protection of Diode Rectifier Unit Based HVDC System Connecting Offshore Wind Farms". In: *2018 IEEE Power Energy Society General Meeting (PESGM)*. ISSN: 1944-9933. Aug. 2018, pp. 1–5. DOI: `10.1109/PESGM.2018.8586510` (cit. on p. 94).

[142] S Dennetière et al. "Modeling of modular multilevel converters for the France-Spain link". In: *Proceedings of the International Conference on Power Systems Transients (IPST'13)*. Vancouver, Canada, July 2013, pp. 1–7 (cit. on pp. 97, 100).

[143] Ricardo Vidal-Albalate et al. "Analysis of the Performance of MMC Under Fault Conditions in HVDC-Based Offshore Wind Farms". In: *IEEE Transactions on Power Delivery* 31.2 (Apr. 2016), pp. 839–847. ISSN: 0885-8977. DOI: `10.1109/TPWRD.2015.2468171` (cit. on pp. 98, 106).

[144] W. Leterme et al. "Overview of Grounding and Configuration Options for Meshed HVDC Grids". In: *IEEE Transactions on Power Delivery* PP.99 (2014), pp. 1–1. ISSN: 0885-8977. DOI: `10.1109/TPWRD.2014.2331106` (cit. on p. 104).

[145] Lei Shi et al. "Enhanced Control of Offshore Wind Farms Connected to MTDC Network Using Partially Selective DC Fault Protection". In: *IEEE Journal of Emerging and Selected Topics in Power Electronics* (2020), pp. 1–1. ISSN: 2168-6785. DOI: `10.1109/JESTPE.2020.2985129` (cit. on p. 106).

[146] Tim Augustin et al. "Transient behaviour of VSC-HVDC links with DC breakers under faults". In: *2017 19th European Conference on Power Electronics and Applications (EPE'17 ECCE Europe)*. ISSN: null. Sept. 2017, P.1–P.10. DOI: `10.23919/EPE17ECCEEurope.2017.8099248` (cit. on p. 108).

[147] A. Semlyen and A. Deri. "Time Domain Modelling of Frequency Dependent Three-Phase Transmission Line Impedance". In: *IEEE Transactions on Power Apparatus and Systems* PAS-104.6 (1985), pp. 1549–1555. ISSN: 0018-9510. DOI: `10.1109/TPAS.1985.319171` (cit. on p. 130).

[148] N. Garcia and E. Acha. "Transmission line model with frequency dependency and propagation effects: A model order reduction and state-space approach". In: *2008 IEEE Power and Energy Society General Meeting - Conversion and Delivery of Electrical Energy in the 21st Century*. 2008, pp. 1–7. DOI: `10.1109/PES.2008.4596875` (cit. on p. 130).

[149] J. Beerten, S. D'Arco, and J. A. Suul. "Frequency-dependent cable modelling for small-signal stability analysis of VSC-HVDC systems". In: *IET Generation, Transmission & Distribution* 10.6 (2016), pp. 1370–1381. ISSN: 1751-8687. DOI: `10.1049/iet-gtd.2015.0868` (cit. on p. 130).

[150] Carlos Ruiz et al. "Frequency-Dependent Pi Model of a Three-Core Submarine Cable for Time and Frequency Domain Analysis". In: *Energies* 11.10 (2018), p. 2778. DOI: `10.3390/en11102778` (cit. on p. 130).

[151] R. Pena, J.C. Clare, and G.M. Asher. "A doubly fed induction generator using back-to-back PWM converters supplying an isolated load from a variable speed wind turbine". In: *IEE Proceedings-Electric Power Applications* 143.5 (1996), pp. 380–387. ISSN: 1350-2352. DOI: `10.1049/ip-epa:19960454` (cit. on p. 160).

[152] Enrique Belenguer et al. "Analysis of Control Alternatives for Offshore Wind Farms Connected through a VSC-HVDC Link". In: *11th International Workshop on Large-Scale Integration of Wind Power into Power Systems as well as on Transmission Networks for Offshore Wind Power Plants.* Lisboa, 2012. ISBN: 978-3-9873870-5-6 (cit. on p. 160).

[153] E. Belenguer et al. "Control strategy for islanded operation of offshore wind power plants connected through a VSCHVDC link". In: *IECON 2013 - 39th Annual Conference of the IEEE Industrial Electronics Society.* Nov. 2013, pp. 5254–5259. DOI: `10.1109/IECON.2013.6699989` (cit. on p. 160).

[154] R Vidal-Albalate et al. "Simultaneous Connection of Type-3 and Type-4 Off-shore Wind Farms to HVDC Diode Rectifier Units". In: *Proc. of the 15th International Workshop on Large-Scale Integration of Wind Power into Power Systems as well as on Transmission Networks for Offshore Wind Power Plants.* Vienna: Energynautics, Nov. 2016 (cit. on p. 160).

[155] Paul Brian Brogan et al. "Control Method for Self-Commutated Converter for Controlling Power Exchange". German (DE). WO/2015/024583. Feb. 2015 (cit. on p. 160).

[156] R. Blasco-Gimenez, R. S. Pena, and R. Cardenas. "Control Of Three Phase Parallel Compensators with Non-Sinusoidal Unbalanced Supply". In: *Proceedings of the 9th European Conference on Power Electronics and Applications.* Graz, Aug. 2001, pp. 1–6. ISBN: 90-75815-06-9 (cit. on p. 163).

[157] R. Blasco-Gimenez et al. “Connection of Large Off-Shore Wind Farms Using Diode Based HVDC Links”. In: *Wind Energy Conversion Systems. Technology and trends.* London: Springer-Verlag, 2012. ISBN: 978-1-4471-2200-5 (cit. on p. 163).

[158] F. S. Young, R. L. Schmid, and P. I. Fergestad. “A Laboratory Investigation of Ferroresonance in Cable-Connected Transformers”. In: *IEEE Transactions on Power Apparatus and Systems* PAS-87.5 (May 1968), pp. 1240–1249. ISSN: 0018-9510. DOI: `10.1109/TPAS.1968.292213` (cit. on p. 167).

[159] R. A. Turner and K. S. Smith. “Transformer Inrush Currents”. In: *IEEE Industry Applications Magazine* 16.5 (Sept. 2010), pp. 14–19. ISSN: 1077-2618. DOI: `10.1109/MIAS.2010.937440` (cit. on p. 167).

[160] I. Arana et al. “Energization of Wind Turbine Transformers With an Auxiliary Generator in a Large Offshore Wind Farm During Islanded Operation”. In: *IEEE Transactions on Power Delivery* 26.4 (Oct. 2011), pp. 2792–2800. ISSN: 0885-8977. DOI: `10.1109/TPWRD.2011.2163648` (cit. on p. 167).

[161] Santiago Cóbreces et al. “Robust admittance shaping approach to grid current harmonic attenuation and resonance damping”. In: *IEEE Transactions on Industry Applications* 54.5 (2018), pp. 5039–5053. DOI: `10.1109/TIA.2018.2845358` (cit. on p. 181).

[162] Kemin Zhou and John Comstock Doyle. *Essentials of robust control.* Vol. 104. Prentice hall Upper Saddle River, NJ, 1998 (cit. on p. 184).

[163] H. Zhang et al. “SISO Transfer Functions for Stability Analysis of Grid-Connected Voltage-Source Converters”. In: *IEEE Transactions on Industry Applications* 55.3 (May 2019), pp. 2931–2941. ISSN: 1939-9367. DOI: `10.1109/TIA.2019.2898978` (cit. on p. 187).

[164] H. Zhang et al. “Stability Analysis of Grid-Connected Voltage-Source Converters Using SISO Modeling”. In: *IEEE Transactions on Power Electronics* 34.8 (Aug. 2019), pp. 8104–8117. ISSN: 1941-0107. DOI: `10.1109/TPEL.2018.2878930` (cit. on p. 187).

[165] J. Sun and H. Liu. “Sequence Impedance Modeling of Modular Multilevel Converters”. In: *IEEE Journal of Emerging and Selected Topics in Power Electronics* 5.4 (Dec. 2017), pp. 1427–1443. ISSN: 2168-6785. DOI: `10.1109/JESTPE.2017.2762408` (cit. on p. 188).

[166] Salvador Añó-Villalba et al. "Impedance-based Stability Analysis for HVDC Diode-Rectifier Connected Off-shore Wind Farms". In: *IECON 2019 - 45th Annual Conference of the IEEE Industrial Electronics Society.* Vol. 1. Oct. 2019, pp. 2389–2394. DOI: `10.1109/IECON.2019.8927634` (cit. on pp. 188, 189).

[167] L. Ding et al. "Region-based Stability Analysis of Resilient Distribution Systems with Hybrid Grid-forming and Grid-following Inverters". In: *2020 IEEE Energy Conversion Congress and Exposition (ECCE).* ISSN: 2329-3748. Oct. 2020, pp. 3733–3740. DOI: `10.1109/ECCE44975.2020.9236196` (cit. on p. 190).

[168] T. Qoria et al. "Tuning of Cascaded Controllers for Robust Grid-Forming Voltage Source Converter". In: *2018 Power Systems Computation Conference (PSCC).* 2018 Power Systems Computation Conference (PSCC). June 2018, pp. 1–7. DOI: `10.23919/PSCC.2018.8443018` (cit. on p. 190).

[169] F. Zhao et al. "A General Integration Method for Small-Signal Stability Analysis of Grid-Forming Converter Connecting to Power System". In: *2020 IEEE 21st Workshop on Control and Modeling for Power Electronics (COMPEL).* ISSN: 1093-5142. Nov. 2020, pp. 1–7. DOI: `10.1109/COMPEL49091.2020.9265697` (cit. on p. 190).

[170] Hassan K. Khalil. *Nonlinear control.* Pearson Higher Ed, 2014 (cit. on p. 190).

[171] H. Wu and X. Wang. "Passivity-Based Dual-Loop Vector Voltage and Current Control for Grid-Forming VSCs". In: *IEEE Transactions on Power Electronics* (2020), pp. 1–1. ISSN: 1941-0107. DOI: `10.1109/TPEL.2020.3048239` (cit. on p. 190).

[172] Y. Liao, X. Wang, and F. Blaabjerg. "Passivity-Based Analysis and Design of Linear Voltage Controllers For Voltage-Source Converters". In: *IEEE Open Journal of the Industrial Electronics Society* 1 (2020), pp. 114–126. ISSN: 2644-1284. DOI: `10.1109/OJIES.2020.3001406` (cit. on p. 190).

[173] J. Watson et al. "Stability of power networks with grid-forming converters". In: *2019 IEEE Milan PowerTech.* June 2019, pp. 1–6. DOI: `10.1109/PTC.2019.8810506` (cit. on p. 190).

[174] Y. Liao and X. Wang. “Passivity Analysis and Enhancement of Voltage Control for Voltage-Source Converters”. In: *2019 IEEE Energy Conversion Congress and Exposition (ECCE)*. Sept. 2019, pp. 5424–5429. DOI: `10.1109/ECCE.2019.8912790` (cit. on p. 190).

[175] L. Harnefors et al. “Asymmetric Complex-Vector Models With Application to VSC-Grid Interaction”. In: *IEEE Journal of Emerging and Selected Topics in Power Electronics* 8.2 (June 2020). Conference Name: IEEE Journal of Emerging and Selected Topics in Power Electronics, pp. 1911–1921. ISSN: 2168-6785. DOI: `10.1109/JESTPE.2020.2972070` (cit. on p. 190).

[176] M. Beza, M. Bongiorno, and A. Narula. “Impact of control loops on the low-frequency passivity properties of grid-forming converters”. In: *2020 22nd European Conference on Power Electronics and Applications (EPE’20 ECCE Europe)*. Sept. 2020, P.1–P.10. DOI: `10.23919/EPE20ECCEEurope43536.2020.9215823` (cit. on p. 191).

[177] H. Yu et al. “Passivity-Oriented Discrete-Time Voltage Controller Design for Grid-Forming Inverters”. In: *2019 IEEE Energy Conversion Congress and Exposition (ECCE)*. Sept. 2019, pp. 469–475. DOI: `10.1109/ECCE.2019.8912988` (cit. on p. 191).